Star Formation in Cygnus X

by

Soumen Deb

A thesis submitted in partial fulfillment of the requirements for the degree of

Doctor of Philosophy

Department of Physics
University of Alberta

Abstract

In astrophysics, stellar evolution is one of the most discussed topics. Although a significant amount of research and advancement of instrumentation over the last few decades have contributed to this field greatly, our understanding of the pre-main sequence evolution remains largely incomplete. The general model for the formation of protostars within the ISM is the virial instability in cold molecular gas resulting in spontaneous gravitational collapse. However, the complete understanding of this instability requires a set of other physical factors, including the hydrodynamic turbulence in the ISM, local magnetic field strength, and feedback from surrounding high-mass stars, not all of them are well-understood. This work investigates the effect of stellar feedback on local star formation and the extent of energy support for molecular clouds provided by protostellar outflows within them.

I first look into a specific case of potentially triggered star formation in Cygnus X, being one of the most active star-forming regions in the Milky Way. Using multi-line submillimetre emissions as well as radio continuum and infrared data, I measure the properties of two highly energetic molecular outflows near the massive stellar complex Cygnus OB2 complex. I show structure, physical conditions, and timescale of the outflows and the associated photoionized rim are consistent with a triggering scenario.

I further investigate 13 such molecular outflows in Cygnus X and measure their properties using multi-line data which I find are similar to the previous surveys of outflows throughout the galaxy. Additionally, I develop and test a method to measure the same properties using single spectral line emission. This is useful in surveys where optically thin line data are not available.

Next, I implement our method to estimate outflow properties in a large-scale survey of 82 outflows, many of which were previously unknown, based on single spectral-line observations. I use machine learning to fill out missing information on protostellar luminosity using existing catalogues and investigate the comparative predictive powers of line emission and radio continuum data on local outflow formation. Next, by comparing outflow power to turbulent dissipation power I show that single-generational outflows cannot provide enough energy support for the surrounding molecular clouds. Finally, I search for evidence of large-scale triggering of star formation and find that an ionization front can perhaps trigger local star formation where molecular gas emission is high, however, find no evidence for this effect to be strong.

Preface

This thesis is an original work by Soumen Deb, under the supervision of Dr. Erik Rosolowsky and Dr. Roland Kothes.

Chapter 2 of this thesis is published as Deb et al. 2018: "A case study of triggered star formation in Cygnus X", Monthly Notices of the Royal Astronomical Society, Volume 481, Issue 2, December 2018, Pages 1862–1872.

Chapter 3 of this thesis is published as Deb et al. 2021: "Characterizing outflows in the Cygnus X region", Monthly Notices of the Royal Astronomical Society, Volume 503, Issue 1, May 2021, Pages 1264–1275.

Chapter 4 of this thesis has been submitted to Monthly Notices of the Royal Astronomical Society as Deb et al. 2022: "A Large Scale Survey of Protostellar Outflows in the Cygnus X Region".

Nature and Nature's laws lay hid in night: God said, "Let Newton be!" and all was light.

– Alexander Pope, 1726.

...It did not last: the devil, howling "Ho! Let Einstein be," restored the status quo!

– J.C. Square, 1957.

This work is dedicated to the memory of my dad, Dr. Priyaranjan Deb, who inspired me throughout my childhood to study fundamental sciences.

Acknowledgements

I would like to express my gratitude to my supervisors, Dr. Erik Rosolowsky and Dr. Roland Kothes, for all their help and advice with my research, as well as their support outside work. I would also like to thank my advisory committee member Dr. Sharon Morsink for her valuable input. A big thanks to my mother and my brother for constantly encouraging me, and without them this would have not been possible. Finally, I greatly appreciate all the love and support I have received from Pamela during my long recovery from a major accident and continuing with academic work.

Table of Contents

List of Tables

List of Figures

List of Plates

Chapter 1

Introduction

In astrophysics, the formation of stars is one of the most discussed topics. This is important because the formation and evolution of stars is the prime component in the evolution of galaxies, which shapes the universe, and the spacetime distribution; and on a small-scale, stellar and protoplanetary disk formation are closely connected to our existence. Although rapid improvement of instrumentation over the last few decades has contributed to this field greatly, our understanding of the early phase (phase before nuclear fusion in a star begins) or the pre-main sequence evolution remains largely incomplete. The formation of stars in the filamentary gas structures in a galaxy happens through the evolution of dense cold molecular (hydrogen) gas clouds that involve several intermediate stages such as fragmentation of the cloud, formation of denser and more compact cloud cores, and finally the emergence of prenatal stars or protostars. The general model for the formation of protostars is that the virial instability in cold molecular cloud cores results in spontaneous gravitational collapse. However, the instability requires a set of other physical factors of influence. These factors include hydrodynamic turbulence in the interstellar medium (ISM), local magnetic field strength, feedback from surrounding high-mass stars in terms of radiation pressure, and shockwaves. Not all of these factors are well understood.

The study of star formation has three main aspects: the physical and dynamical conditions in interstellar gas clouds necessary for the formation of stars, the particular processes involved in star formation; and the properties of newly born stars. We have no means of

knowing if stars are going to form in a gas cloud, and unless stars form much more quickly than any current theories indicate, the first two aspects cannot be observed directly. This is because the time-scale of star formation is too long (compared to the human lifetime) to produce observational data for a particular cloud core that goes through all evolutionary phases and forms protostars. All our relevant astronomical data come from observations of the dynamics of stars after they have formed, and from observations of interstellar gas clouds which may, or may not, be in a state in which stars can form in them.

1.1 The Interstellar Medium

Stars are born in regions of dark dense cold molecular gas. also known as the molecular clouds, in the vast space of matter and radiation fields between the stars, called the interstellar medium (ISM). The process of star formation is complex. Observations provide snapshots of different phases of this process. An extensive study of physical processes, namely, thermodynamics, radiative transfer, magnetohydrodynamics, and quantum mechanics is required to understand how the various material and radiation components of the ISM interact with each other and form pre-stellar structures. Star formation is also thought of as a recycling process of matter in the interstellar medium. Stars are born in the ISM and during their life, most of the material is returned to the ISM through stellar feedback or supernovae or planetary nebulae after their death.

This makes the ISM one of the most important components in any galaxy. Excluding the dark matter mass (which accounts for 90% of the total galactic mass), mass-wise (baryonic), the ISM is filled with mostly gas and dust that determine how the galaxies appear visibly. At the early stages of the Universe, the visible or baryonic mass in galaxies was in diffuse gas produced in the photon epoch after the Big Bang. The early matter was mostly composed of isotopes of hydrogen and helium, with trace amounts of lithium, beryllium, and boron. As galaxies evolved, the ISM converted gas into stars. Stellar nucleosynthesis started to produce heavier elements that were added to the ISM as stellar feedback or

through novae, supernovae. Most of the interstellar matter at present, especially that of heavier elements, has been recycled many times through stellar interiors. Part of the gas was also ejected out of the ISM as galactic winds or stripped off by the warm-hot intergalactic medium (WHIM) and in some cases, mass was added to the ISM from the WHIM.

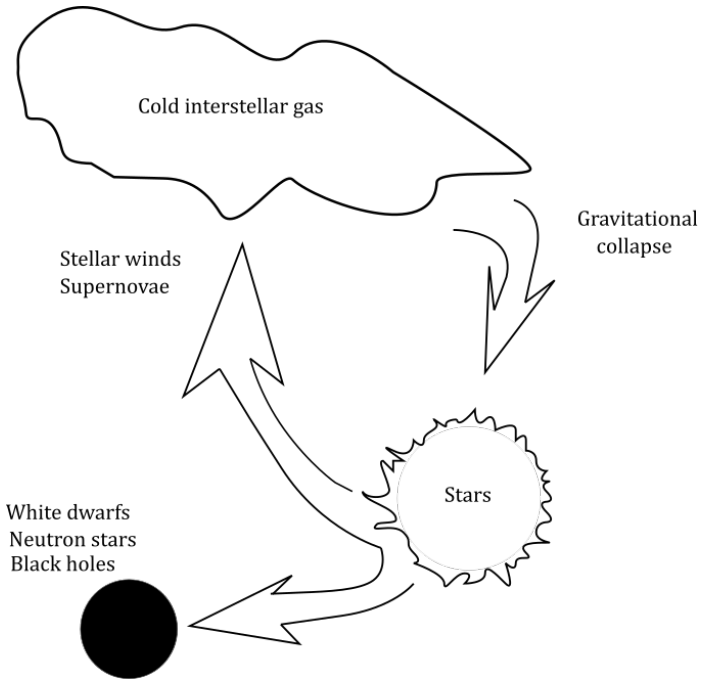

Plate 1.1: A schematic of recycling of matter in the interstellar medium.

At the current epoch, the baryonic interstellar matter is composed of largely hydrogen and helium but also includes heavier elements. Fig 1.1 shows a schematic of this process. Initial interstellar gas (hydrogen, helium) condenses, fragments, and collapses to form the first generation of stars. As stars form, lighter elements fuse to form heavier 'metals' in stellar cores through nuclear processes. As stars age and die, nuclear fuel gets exhausted, and depending on the initial mass, stars end up as white dwarfs, neutron stars, or black holes. During this phase, initial diffuse gas is ejected back into the ISM, as stellar winds or supernovae, along with the newly produced heavier elements. This process has been repeated many times and gave the present appearance of the galaxies.

The visible mass-wise, interstellar medium consists of 70% hydrogen, 28% helium, and 2% heavier elements. Interstellar gas is mostly hydrogen and helium which altogether

account for almost 99% of the mass and the rest 1% is dust (Boulanger et al., 2000). Moreover, hydrogen gas is found in the mass ratio of 3:1:1 for atomic (HI), molecular (H_2), and ionized (HII) forms (Draine, 2011). The particle number density within the ISM varies largely, from 10^{-4} per cm^3 in hot ionized gas to 10^{10} per cm^3 in molecular cloud cores.

The components of the interstellar medium that interact with each other and control the dynamics of the ISM include(Draine, 2011),

- *Interstellar gas*

  Mostly hydrogen gas in atomic, molecular, or ionic forms, helium, and other elemental and molecular gases. Interstellar gas particles approximately follow thermal velocity distribution.

- *Interstellar dust*

  There are solid particle grains, of size roughly of the order of 1 micron, mixed with gas. Interstellar dust grains are much smaller than terrestrial dust particles. A dust grain has three parts, namely, core, mantle, and surface. Dust grain core is about 0.05 μm across, usually composed of iron, carbon, and silicate. The mantle is $0.5-1.0\,\mu$m across and made of ice molecules of water, CH_4, CO_2, and NH_3. The thin surface is mostly made of organic compounds. Dust grains are cold, with temperatures varying around 20 K (Krumholz, 2015).

- *Cosmic rays*

  In addition to gas and dust, a third kind of matter particle is found in the ISM, with highly energetic ions and electrons. They are known as cosmic rays. They have nearly the same composition as ordinary interstellar gas, except for kinetic energies much greater than thermal energy. Most of the cosmic rays are hydrogen nuclei (protons) stripped of their accompanying electron. Helium (alpha-particles) and heavier nuclei (HZE ions) constitute less than 10% . About 1% of cosmic rays are electrons or positrons. These particles are often relativistic, typically moving at the speed of

0.9c.

- *Electromagnetic radiation*

  Electromagnetic radiation fields of various sources play a crucial role in the dynamics of the interstellar medium. Such radiations include visible and ultraviolet starlight, a broad spectrum of radiation emitted by interstellar atoms, molecules, and ions, thermal infrared emission from dust, gamma rays from nuclear transitions, thermal bremsstrahlung radiation from hot ionized gas, magnetic bremsstrahlung or synchrotron emission produced by relativistic particles, and cosmic microwave background radiation.

- *Interstellar magnetic field*

  The magnetic field is also a significant component that can direct cosmic rays and interstellar ions, contribute to interstellar turbulence, and have an important contribution to the star formation process.

- *Gravitational field*

  Gravity is undoubtedly the most important factor in star formation and the evolution of the ISM. The gravitational field is generated by all the mass that is present in the galaxy, including interstellar gas and dust, stars and stellar remnants, and also the dark matter particles (discussion of dark matter contribution to the interstellar gravitational field is beyond our scope here. Also, the interaction of them with visible mass is weak and largely unclear till date).

1.1.1 Phases of the Interstellar Medium

We limit our discussion of characteristics of the interstellar medium to the ISM in spiral galaxies, in particular the Milky Way galaxy, since we are interested in star formation in a region in our galaxy. Most of the visible matter in a spiral galaxy like the Milky Way is within a thin gaseous disk, distributed more or less symmetrically about the disk mid-

plane. This gaseous disk encompasses the interstellar medium. Although the ISM slowly diffuses away with distance from the midplane, most of the interstellar gas and dust is found within 500 pc across the disk. This gives rise to the current estimate of the half-thickness of the galactic disk which is about 250 pc near the Sun (Draine, 2011). The Sun, at the current epoch, is located at a distance of 8.5 kpc from the galactic center and is approximately at the mid-plane. So the disk thickness in the solar neighborhood in the galaxy is about 2.9% of the disk size. The (baryonic) interstellar matter, confined in this thin disk, is found to have dynamically varying density and temperature ranges throughout the different regions in the galaxy. That said, most matter (gas and dust) particles in the ISM belong to certain characteristic states associated with particular temperature values. These characteristic states are called *phases* of the ISM.

Six major phases have been observed in the ISM (Draine, 2011),

1. *Coronal gas*

   This is hot, collisionally ionized, low-density ($\sim$ 0.004 cm^{-3}) plasma with ions of heavier elements (OVII, for example). Characteristic temperature is 300, 000 K, obtained by shock-heating of gas by supernova blast waves. The term is used following the similarity in the ionization state of the gas and temperatures to those found in the solar corona. The gas in this state is also called the hot ionized medium (HIM). Since the gas faces shock fronts moving outwards, coronal gas is found above and below the galactic disk. Gas in this phase cools by adiabatic expansion and by emitting X-rays and is observed in UV, X-ray, and radio wavelengths.

2. HII *gas*

   Ultraviolet radiation from young massive O- and B-type stars in the interstellar molecular clouds photoionizes hydrogen gas. The ionized hydrogen gas (HII, temperature $\sim 10^4$ K) is found in two main types, dense ($\sim 10^4$ cm^{-3}) ionized gas near molecular clouds, called the HII *regions*. and much less dense *diffuse* HII ($\sim$ 0.3 cm^{-3}) found in the intercloud medium. Dense HII regions are often observed in optical lines, as

bright rims around molecular gas. The low-density diffuse photoionized hydrogen gas is much less visually present, and hence termed as the *warm ionized medium* (WIM) but contributes significantly more to the total mass of ionized hydrogen gas in the galaxy. The cooling mechanism is dominated by radiative recombination and thermal bremsstrahlung emissions.

3. *Warm* HI *gas*

   A large fraction of the disk gas volume is occupied by warm hydrogen gas in atomic form, characterised by temperatures around 5000 K and densities around 0.6 cm^{-3}. This phase is also known as the *warm neutral medium* (WNM), often heated by photoelectrons from dust grains. WNM can be further ionized by cosmic rays and stellar photoionizing radiation to form HII gas. Optical line emission is one of the primary cooling mechanisms for warm neutral gas. WNM can be observed against both 21-cm line absorption and emission.

4. *Cool* HI *gas*

   Gas in this phase is chemical composition-wise the same as above, but with much lower temperature ($\approx 10^2$ K) and higher density (≈ 30 cm^{-3}). This phase is also referred to as the *cold neutral medium* (CNM), which accounts for about 1% of the interstellar gas volume. The cooling mechanism and observation technique are similar to the WNM.

5. *Diffuse molecular gas*

   Diffuse H_2 gas is also similar to the cool neutral medium gas in most aspects, except for a significantly higher density of 100 cm^{-3}. Gas in this phase provides the shielding from ionizing radiation and heating effects to the molecular gas that is in the interior of the molecular clouds.

6. *Dense Molecular gas*

   This phase of dense molecular hydrogen gas found in dark clouds that are gravitation-

ally bound and serves as the "womb" for stellar birth. Density in such star-forming clouds ranges from 10^3 to 10^6 cm^{-3}. It is worth noting that the high-density values in such clouds are extremely low compared to the average sea level air particle density on earth ($\approx 2.7 \times 10^{19}$ cm^{-3}). The column density in the dense molecular clouds can reach high enough to cause large visual extinction. Gas in this phase is often very cold (10 to 20 K), and dust grains in such clouds are found to have mantles of ices of different molecular species. The main cooling mechanism includes CO line emission and CI fine structure line emission. Due to the low temperature, molecular H_2 gas is extremely difficult to observe directly, and often dust infrared emission is used as a proxy observation technique.

Although many aspects of the interstellar medium are unexplained, in general, the ISM is a dynamic system and far from being in thermodynamic equilibrium. The gas in the ISM is thought to be composed of distinct phases in approximate pressure equilibrium. The interstellar matter goes through thermal and chemical processes to convert from one phase to another. Cosmic rays and photoionization can heat the cold molecular hydrogen gas and photodissociate it to form atomic and HI gas. Cool neutral gas receives heating by photo-electrons and cosmic rays and starlight and becomes warm and finally hot ionized hydrogen gas. On the other hand, radiative recombination of electrons and other cooling mechanisms allow the hot ionized gas to become cool HII, and eventually, H atoms recombine to form cold molecular gas. Molecular gas undergoes gravitational collapse to form protostars, and finally stars which eject material back into the ISM in molecular and ionized forms.

1.1.2 Molecular Clouds

It has been established from observations that star formation occurs in the densest and coldest gas regions in the ISM where gravity is more likely to dominate the thermal energy of the gas, local turbulence, and magnetic field. In particular, molecular clouds (mean temperature $\sim 10 - 20$ K) are the sites for almost all cases of star formation in our galaxy

(except possibly for the very old population II stars typically found in globular clusters or the galactic halo). Galactic molecular gas is observed to have various size scales from 0.05 parsec for denser sub-clouds or cloud cores to 200 parsecs for giant molecular clouds (GMC) or GMC complexes. Molecular clouds are found to have complex filamentary structures (resembling the terrestrial cirrus clouds, except for extremely low density in molecular clouds). Within these clouds, there are dense and cold clumpy structures, masses ranging from 10 $M_\odot$ for cores to 10^6 $M_\odot$ for GMCs, and density values from 10^5 cm^{-3} for cloud cores to 100 cm^{-3} for typical clouds. Here, density is given by the number of molecules per unit volume in clouds which mostly contain H_2 gas, with some amount of He, dust grains, and CO molecules.

Molecular clouds were first discovered in the eighteenth century when Herschel found dark patches lacking stars in his Milky Way star counting observations. This is now understood as a result of the obscuration of starlight or extinction of visible light by the dust and gas in molecular clouds. This phenomenon is still effective in determining the structure of molecular clouds. Based on their appearance against background optical light, molecular clouds are typically categorized into four groups, namely, diffuse, translucent, dark, and infrared dark clouds (Draine, 2011). Visual extinction A_V for diffuse and translucent molecular clouds are the lowest, less than 1 and between 1 and 5 respectively. These clouds are kept stable by surface pressure (from background UV radiation) with occasional support from self-gravity. Usually, the dark clouds have extinction $A_V \approx 10$. Extinction magnitude exceeds 20 for very opaque dark clouds, which are often opaque in even infrared frequencies with extinction values around 100. Infrared dark clouds (IRDC) are often observed against background emission at 8 μm from interstellar PAHs (Draine, 2011).

Clouds are also separated into categories based on their mass and size. *Dark molecular clouds* and *giant molecular clouds (GMC)* are the primary categories. Dark clouds are typically from 0.3 up to 6 pc in size and of mass ranging from $5M_\odot$ up to $500M_\odot$. However, much galactic molecular gas is found in larger clouds or the GMCs (size ~20 pc). The

Category	Size (pc)	Mass ($M_\odot$)	n (cm^{-3})	Linewidth (km s^{-1})	A_V (mag)
GMC complex	25 – 200	10^5 – $10^{6.8}$	50 – 300	4 – 17	3 – 10
Dark Cloud complex	4 – 25	10^3 – $10^{4.5}$	10^2 – 10^3	1.5 – 5	4 – 12
GMC	2 – 20	10^3 – $10^{5.3}$	10^3 – 10^4	2 – 9	9 – 25
Dark cloud	0.3 – 6	5 – 500	10^2 – 10^4	0.4 – 2	3 – 15
Star-forming clump	0.2 – 2	10 – 10^3	10^4 – 10^5	0.5 – 3	4 – 90
Core	0.02 – 0.4	0.3 – 10^2	10^4 – 10^6	0.3 – 2	30 – 200

Table 1.1: Molecular clouds and substructures (Draine, 2011)

largest structures of molecular gas in the galaxy are the *dark cloud complexes* and the *giant molecular cloud complexes* which are gravitationally bound structures of distinct dark clouds or GMCs. For example, the Orion Molecular Cloud complex is the nearest GMC complex to the Sun, located in the galactic plane at galactic longitude $l \approx 210^\circ$ at a distance of 414 pc from the Sun. The OMC consists of six giant molecular clouds gravitationally bound in it, with a total mass of $3{\times}10^5 M_\odot$. The largest star-forming region Cygnus X in the local arm of the Milky Way galaxy consists of a number of GMCs and isolated and connected molecular clouds. I will discuss this in detail in a later section.

There are substructures of higher densities within the molecular clouds or GMCs that are self-gravitating. They are described as *clumps*. Clumps that have the favorable condition in them for star formation are called *star-forming clumps*. *Cores* are high-density substructures within star-forming clumps which undergo gravitational collapse to form a single or binary star. Cores are essentially the stellar embryos in molecular clouds. Table 1.1 describes some of the key properties of these structures.

Although, molecular clouds can be found isolated, in most cases they are found in groups or complexes. Almost all large clouds have a substructure which sometimes makes it observationally difficult to separate a cloud from a cloud complex. Usually, a structure or substructure is identified using the dispersion in the radial velocity of gas or molecular line

width (of typically CO ($J = 1 \rightarrow 0$) transition), since velocity dispersion in turbulent gas increases with characteristic size scale as size power one-third ($\sigma_v \propto L^{1/3}$), following the Kolmogorov model for turbulence in incompressible fluid (Krumholz, 2015). In addition, the transition is optically thick, and the luminosity is proportional to the total mass of the molecular cloud. Assuming a particular rotation curve, and an adopted value of CO to H_2 conversion factor, cloud mass can be estimated. Cloud mass can also be estimated using far-infrared and sub-millimeter dust thermal emission (Draine, 2011).

There are more than one way how atomic hydrogen combined together to form molecular hydrogen in the cold interstellar medium. In the absence of dust, which was the case in the early universe, the primary way of H_2 formation is radiative association followed by associative detachment (Draine, 2011),

$$\begin{aligned} \mathrm{H} + e^- &\rightarrow \mathrm{H}^- + h\nu \\ \mathrm{H}^- + \mathrm{H} &\rightarrow \mathrm{H}_2 + e^- + \mathrm{KE} \end{aligned} \tag{1.1}$$

However, H_2 formation rate in this process is very low, because of symmetry in homonuclear molecules. Most of galactic H_2 formation occurs in presence of dust. Dust grains act as catalysts for molecular hydrogen formation. The grain surface serves as a site for the diffusion or random walk of an H atom. Since dust grains are efficient emitters of heat, low thermal fluctuations (T~20 K) lowers the expected dispersion of such a two-dimensional random walk of the H atom and it becomes bound to the surface. The same fate happens to other H atoms. In other words, each of them eventually encounters another H atom that is already bound to the grain surface and they combine to form an H_2 molecule in the ground state. The energy released in the reaction (ΔE=4.5 eV) is much greater than the atom-grain binding energy so the newly formed molecule no longer sticks to the grain and is ejected into the cloud.

The binding energy of H_2 molecule in its ground state is 4.48 eV, which is easily available in the cold interstellar medium. So it would be tempting to infer that a simple photodissociation $H_2 + \gamma \rightarrow H + H$ would be sufficient to destroy the molecular hydrogen.

This is however much more complex than that. Such transition is forbidden in quantum mechanics because the symmetry in linear homonuclear diatomic molecules like hydrogen (reactant, initial bound state) and the H atoms (final unbound state, also symmetric) result in lack of dipole moment which does not allow emission of dipole radiation. Hence the production of atomic hydrogen via this channel is insignificant in the molecular gas. If the H_2 molecule is in excited state it becomes asymmetric and such transition is then possible, so is the case when one of the resultant H atoms is produced in an excited state. Typically H_2 molecules in clouds are almost always in ground state, and an excited H atom production requires 14.5 eV which is not common either in cold molecular clouds shielded by neutral hydrogen.

The main photodissociaiton channel carried out by UV photons involves ro-vibrational excited states of hydrogen molecule. The molecular orbital of H_2 has electronic ($u = 1, 2, 3, ..$), rotational ($J = 0, 1, 2, ..$), and vibrational ($v = 0, 1, 2, ..$) eigenstates. An initial state of H_2 molecules absorb photons to transition from an initial level $X(v, J)$ of electronic ground state (here $X, B, C, ..$ denote the electronic states in order) to another level $B(v', J')$ first electronic state or that of the second electronic excited state $C(v', J')$ via a permitted absorption line. The photoexcitation is followed by radiative decay via which the molecule transitions back to vibrationally excited levels $X(v', J')$ of the electronic ground state (Draine, 2011).

For instance, consider the electronic ground state of the hydrogen molecule with the lowest ro-vibrational energy, denoted by $X^1\Sigma_g^+$, which corresponds to the zero-point vibrational energy (slightly above the absolute bottom of the electronic potential well in its ground state) and has both electrons in the lowest σ_g orbital. This molecule can get photoexcited via absorption lines in two ways.

First, it can absorb a photon that has its electric field vector parallel to the internuclear axis of the hydrogen molecule and one of the electrons jumps into the orbital σ_u and the molecule transitions into the level $B^1\Sigma_u^+$ of the first electronic excited state. The photon

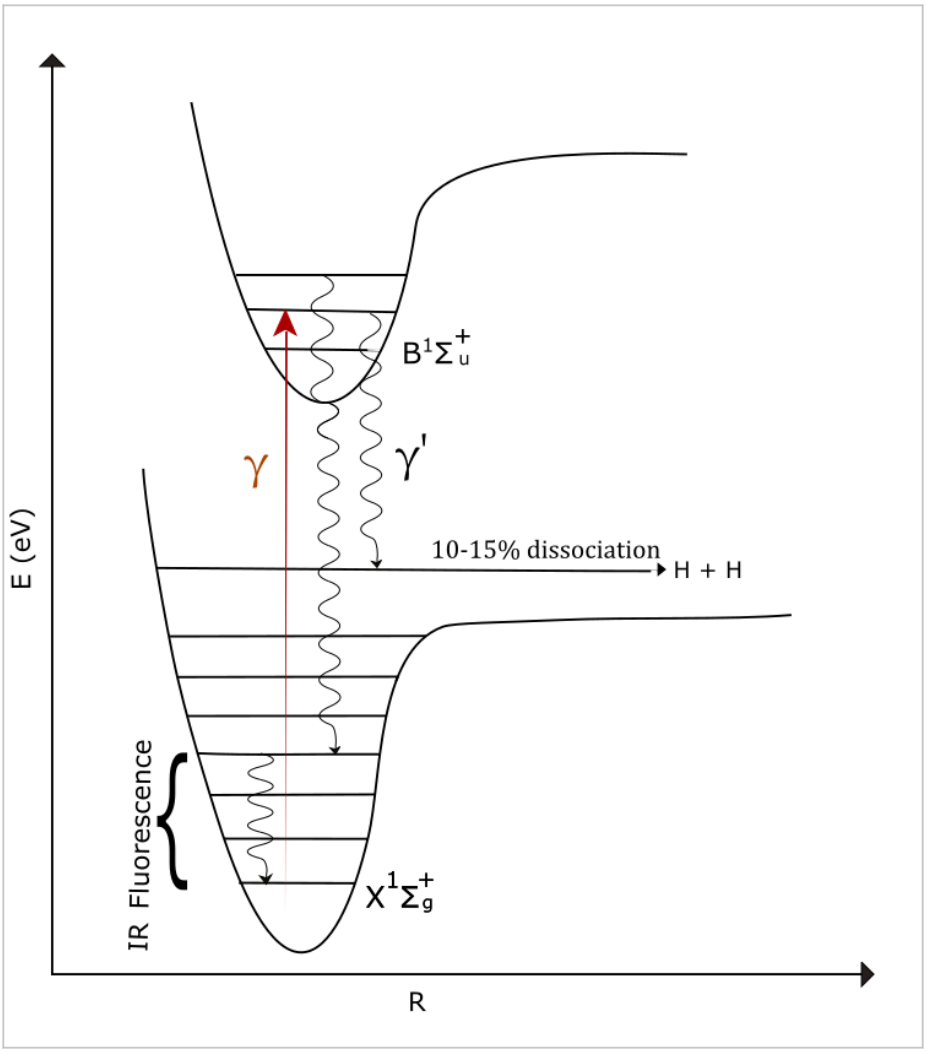

Figure 1.1: Schematic view of photodissociation of H_2 via uv-pumping. Vertical axis (not scaled, shown for the purpose of explanation) denotes effective potential energy E of a quantum harmonic oscillator with rigid rotor approximation plotted against internuclear separation R in H_2 molecule *(adapted from Hollenbach & Tielens 1999 and Draine 2011)*.

for this transition must have minimum energy of 11.2 eV and the corresponding absorption lines belong to the *Lyman band*. Second, a photon with its electric field orthogonal to the internuclear axis can excite the molecules into the $C^1\Pi_u$ level of the second electronic excited state by exciting one of the electrons into π_u orbital. Such photons have at least 12.3 eV energy and the corresponding band is known as the *Werner band*.

These energy values are much greater than the binding energy of hydrogen molecule (4.48 eV), the Lyman and Werner absorption bands result in dipole-allowed radiative decay to a number of different ro-vibrational levels in the ground electronic state in a cascading manner, bound states in most cases as a consequence of UV-pumping of H_2. Decaying back to $X^1\Sigma_g^+$ causes UV emission, and excited vibrational states of the electronic ground state results in infrared emission which is referred to as H_2 *fluorescence*. Figure 1.1 elaborates these photoexcitation and decay channels. However, there is also 10-15% probability that the spontanous decay of an excited level will end up in an unbound state or the vibrational continuum of the electronic ground state, in which case the molecule will be dissociated into H atoms (figure 1.1). The photodissociated via uv-pumping can then be summarized as (Hollenbach & Tielens, 1999),

$$H_2(X^1\Sigma_g^+) + \gamma \rightarrow H_2(B^1\Sigma_u^+ \text{ or } C^1\Pi_u) \rightarrow 2H(1s_{1/2}) + \gamma \tag{1.2}$$

Stars are born in molecular clouds, and young massive stars produce a high amount of ionizing UV radiation that irradiates the parent molecular cloud or clouds in the neighborhood, resulting in photodissociation and photoionization of neutral gas. Similar to the destruction of H_2 gas by incoming UV radiation, as discussed above, other molecular species in the cold ISM or particularly in molecular clouds can also get photodissociated and photoionized by the UV radiation field. particularly, CO and O_2 molecules. CO is the most common observed molecular species in the ISM that is used for tracing molecular (H_2) gas in galactic as well as extragalactic regions. The ionization front faces atomic hydrogen first that usually envelops inner molecular regions, and consequently, a region of photoionized gas (HII region) is pushed towards the molecular region by the ionization front. The inter-

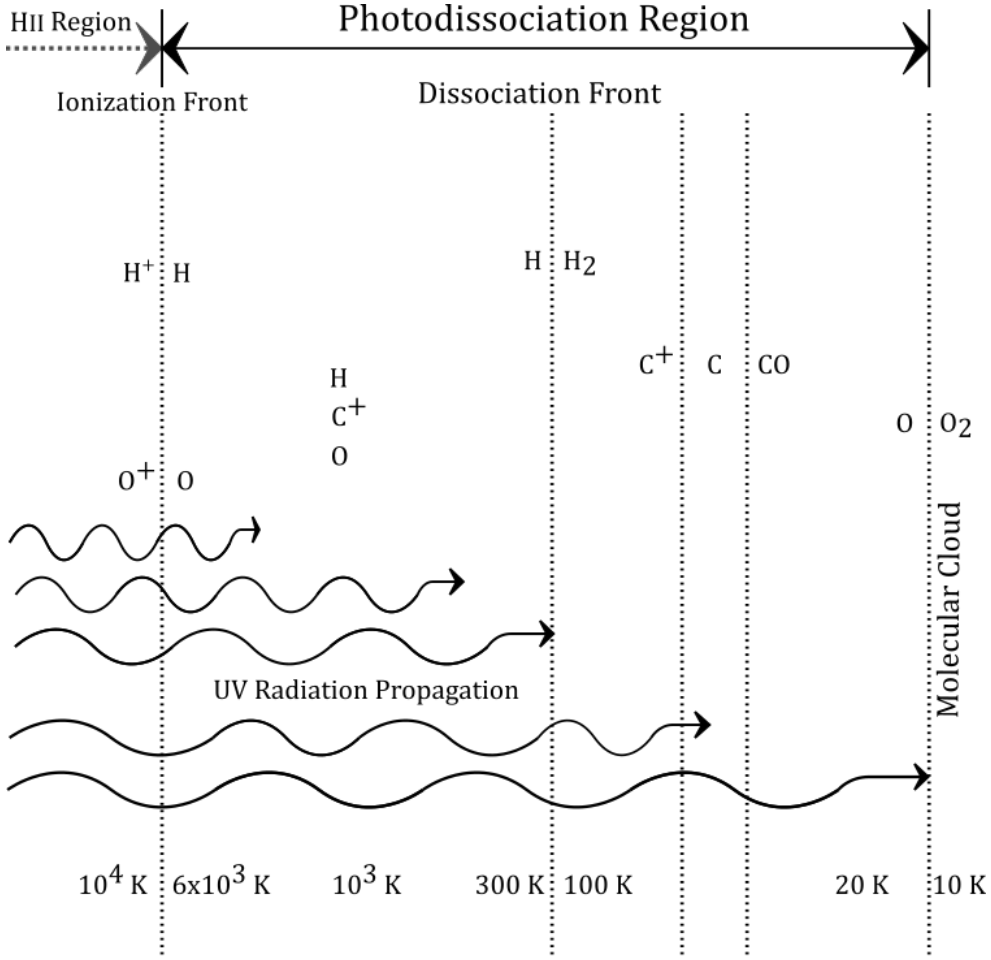

Figure 1.2: Schematic view of a non-stationary photodissociation region structure *(adapted from Draine 2011)*.

face between the moving hot HII region and the cold molecular cloud is referred to as the *photodissociation region* (PDR) because in PDRs, molecular species get dissociated and finally ionized as the HII region proceeds towards the molecular gas.

The structure of photodissociation region is primarily maintained by stellar far-UV radiation (6 eV – 13.6 eV) (Hollenbach & Tielens, 1999). The ionization front sets the boundary of the PDR, the surface at which hydrogen is 50% ionized by mass as the Lyman continuum radiation curves into the neutral hydrogen gas (Draine, 2011). There is a photodissociation front in the PDR, the surface that separates atomic and molecular hydrogen. It is the surface where UV-pumping causes H_2 to create H atoms, and hence the photodissociation front propagates into molecular regions. In a reference frame co-moving with

the photodissociation front, molecular gas flows towards this surface, and H atoms after being dissociated at the surface flow away from it and towards the ionization front where the atomic gas becomes ionized. Photodissociation of CO and ionization of C results in the presence of C^+ in the deep interior of the photodissociation region. Far-UV flux also keeps O atoms in high abundance within the entire region (Hollenbach & Tielens, 1999). Figure 1.2 shows a schematic of a PDR. The average gas temperature gradient along the direction of radiation propagation in different sub-regions is also shown, a negative value of which depicts the hydrogen self-shielding effects in the interior of molecular clouds.

Observations strongly indicate that the internal temperature of molecular clouds can be as low as 10 K. Such cold conditions are achieved via efficient cooing processes. The Heating processes are also an important part of the thermodynamics of the ISM. For atomic gas, the most dominant channel of heating is the dust photoelectric effect. Dust grains are bombarded with starlight far-UV (FUV) photons ($h\nu \sim 8 - 13.6$ eV) and which eject energetic electrons. These electrons in turn collide with gas atoms and increase thermal energy in interstellar gas. A typical rate of such heating via a photoelectric effect in the interior of clouds ranges around 10^{29} erg s^{-1} per H nucleus (Krumholz, 2015). Heating rates can be much greater near the cloud surface. It also depends on the proximity of the radiation field.

The second most common source of heating, particularly for molecular gas, is cosmic rays. The cosmic ray particles with relativistic speeds are much more likely to penetrate the interior of clouds, where FUV photons can not, due to the self-shielding effect. The high-energy particles displace electrons from the molecular orbital in the following fashion $CR + H_2 \rightarrow H_2^+ + e^- + CR$ which can have energies up to 30 eV (Krumholz, 2015). These electrons have sufficient energy to ionize or photodissociate H_2, but as we have already discussed, although the binding energy is low (4.48 eV), a direct dissociation of the form $e^- + H_2 \rightarrow 2H + e^-$ does not occur with substantial probability.

An alternative channel is a free electron that excites a hydrogen molecule without dis-

sociation, which encounters another H_2 and de-excites collisionally. The excess energy, if any, is shared between the two molecules as recoil energy, and the gas is heated.

$$H_2 + e^- \rightarrow H_2^* + e^-$$

$$H_2^* + H_2 \rightarrow 2H_2$$

Chemical heating is another process where cosmic rays create H_2^+ ions which interact with other molecules present in the ISM, often following exothermic reaction chains such as the following (Krumholz, 2015) (as CO is the most commonly observed molecular species),

$$H_2^+ + H_2 \rightarrow H_3^+ + H$$

$$H_3^+ + CO \rightarrow HCO^+ + H_2$$

$$HCO^+ + e^- \rightarrow CO + H$$

Reactions like this result in high dispersion of recoil speeds in these heavier ions which translates as thermal energy and is shared among the participating molecules which heat up the entire gas. Combing all mechanisms, cosmic ray heating rate per H nucleus is estimated as (1 molecule=2 H nuclei),

$$\Gamma_{CR} \sim 2 \times 10^{-27} \text{ erg s}^{-1}. \tag{1.3}$$

So, the cosmic ray heating rate dominates in the interior of molecular gas clouds, over the photoelectric heating mechanism that is much more prominent at the cloud surface.

The two primary cooling processes in molecular clouds include dust thermal radiation and molecular line emission. Dust grains work as an excellent cooling agent in molecular clouds. Dust grains are solid particles as opposed to molecular and neutral gas which is why dust grains are much better thermal emitters. In molecular clouds, H_2 and dust have to be thermally coupled for the grains to cool hydrogen gas. This is achieved via grain-gas collisional coupling and the collision rate is only significant when the cloud density is greater than 10^4 cm^{-3} (Krumholz, 2015). Dust thermal emission, generally in the ISM, is optically thin for $\lambda > 300\,\mu$m. This is, however, not a common occurrence in typical clouds or GMCs (table 1.1). Substructures like star-forming clumps and cores usually fulfill this

criterion and consequently dust thermal cooling becomes significant in the gravitational collapse in such clouds.

In larger clouds or GMCs cooling mechanism is dominated by line emission (rotational) from CO molecules which is a result of inelastic collisions between CO and hydrogen molecules. Typical low temperatures in molecular clouds, only rotational transitions are likely, in particular the highly occupied low eigenstates ($J = 0, 1$) of CO molecules. Higher J transition lines are optically thin as those photons are capable of escaping the cloud (not very many CO would be in the $J - 1$ state to reabsorb them), but such excited states of high rotational levels are not common in low-temperature clouds and consequently, the lines are too weak to be significant in cooling. On the other hand, the lower level transition lines ($J = 1 \rightarrow 0$) are optically thick, particularly in the deeper regions (photons are more likely to escape the cloud near the surface before getting reabsorbed), which results in no net cooling at the lower CO lines in the interior regions. However, the Doppler broadening of CO lines effectively widens the frequency band and can increase the photon escape probability.

This location-dependent cooling suppression effect for $J = 1 \rightarrow 0$ line combined with high J excited transitions effectively results in a molecular line cooling mechanism that is dominated by a single marginally thin emission line, which is associated with a population of molecules approximately in local thermal equilibrium. Although the exact transition J to $J - 1$ depends on velocity dispersion of the gas and the CO column density, the most common values in the galaxy vary between $J = 2 \rightarrow 1$ and $J = 5 \rightarrow 4$ (Krumholz, 2015) and the typical cooling rate for such cases is roughly 10^{-27} erg s^{-1} assuming a 10 K cloud (Krumholz, 2015). This is in close agreement with the heating rate and thus supports an equilibrium temperature to be maintained in molecular clouds. Thermodynamics in molecular clouds plays a critical role in cloud evolution and dynamics. The heating mechanisms by photoelectric effect and cosmic rays do not require the temperature sensitivity on heating rate variations. The cooling mechanisms, however, are related to local temperature

variations. (Krumholz, 2015) has argued cooling timescale is much shorter than the cloud crossing timescale, which implies gas will return to the equilibrium temperature if it gets out of equilibrium by hydrodynamic effects in the cloud, much before the cloud experiences any mechanical motion of the gas. This conclusion can be interpreted as molecular clouds being approximately isothermal systems.

1.1.3 Turbulence in Molecular clouds

The gas motion in the cold interstellar medium is thought to be turbulent. The degree of turbulence can, however, depend on the size scale of fluid motion. Although the interstellar medium is magnetized, the un-magnetized hydrodynamic model can still shed light on useful conclusions about the large-scale fluid motion in the ISM. The two basic equations are the ones in the conservation of mass and momentum (Krumholz, 2015),

$$\begin{aligned} \frac{\partial}{\partial t}\rho &= -\nabla \cdot (\rho \mathbf{v}) \\ \frac{\partial(\rho \mathbf{v})}{\partial t} &= -\nabla \cdot (\rho \mathbf{v}\mathbf{v}) - \nabla P + \rho\nu\nabla^2\mathbf{v}. \end{aligned} \tag{1.4}$$

The first equation relates the positive (negative) change in mass density ρ at a point in the ISM to the mass flow in (out) of an infinitesimal volume around that point. The second equation, momentum conservation, has the equivalent term $\rho\mathbf{v}\mathbf{v}$ (tensor product) denoting in or outflow of momentum (referred as *momentum advection*). ∇P indicates the influence of pressure on the fluid, and the final term $\rho\nu\nabla^2\mathbf{v}$ denotes momentum redistribution rate by viscous forces, ν being kinematic viscosity. Using the momentum conservation equation with an order of magnitude calculation we can perform a dimensional analysis of the nature of the interstellar hydrodynamic flow. If we consider a gas volume of characteristic length scale L and characteristic fluid velocity V, the time scale becomes of the order of $\frac{L}{V}$. Then replacing the derivatives by natural length and time scales we re-write the equation as,

$$\begin{aligned} \frac{\rho V^2}{L} &\sim \frac{\rho V^2}{L} + \frac{\rho c_s^2}{L} + \rho\nu\frac{V}{L^2}, \\ 1 &\sim 1 + \frac{c_s^2}{V^2} + \frac{\nu}{VL}, \end{aligned} \tag{1.5}$$

since the pressure in gas can be written in terms of the speed of sound in the medium $P = \rho c_s^2$. The last two terms in the RHS can be equated to (dimensionally) two important quantities in fluid dynamics, namely, the Mach number and the Reynolds number,

$$\begin{aligned} \mathcal{M} &\sim \frac{V^2}{c_s^2} \\ \mathcal{R}e &\sim \frac{VL}{\nu} \end{aligned} \tag{1.6}$$

It is evident from equation 1.5 if the Mach number $\mathcal{M} \ll 1$ the pressure term is important and the motion is subsonic. If $\mathcal{M} \gg 1$, pressure force is unimportant and the fluid motion is supersonic. $1/\mathcal{R}e$ measures the degree of viscosity which is only important if $\mathcal{R}e \ll 1$. If we consider a fluid element, viscosity would measure the diffusion of momentum (or the dissipation of energy) in or out of the surface enclosing the fluid element. A large value of Reynolds number (= insignificant viscosity) would then mean a low-dissipation fluid motion, which in turn would mean the gas is turbulent.

The sound speed can be written as $c_s = \sqrt{\frac{kT}{\mu m_{\rm H}}}$, where μ is mean mass per particle in molecular gas. In a typical molecular cloud, $\mu = 2.33$ considering H : He $\approx$ 10 : 1, $T \sim 10$K, $L \sim 10$ pc, and $V \sim 5$ km s^{-1}. Then $\mathcal{M} \sim \frac{V}{c_s} \approx 28$ implies the gas is supersonic and pressure forces are not of much significance in molecular clouds. For molecular clouds, usual values of the Reynolds number are of the order of 10^9, which indicates viscosity is unimportant and the large-scale motions in molecular clouds are turbulent. However, turbulence itself is not modeled well in the context of molecular clouds.

1.1.4 Magnetic Field in Molecular Clouds

As we have mentioned before, the magnetic field is an important component of the ISM. In particular, most molecular clouds are magnetic. The source of the interstellar magnetic field is not modelled very well. Here we discuss some important aspects of interstellar magnetic field structure, particularly in the context of molecular gas dynamics. The induction equation which governs magnetic field evolution in plasma (molecular clouds are

considered to be weak plasmas) is given by,

$$\frac{\partial \mathbf{B}}{\partial t} + \nabla \times (\mathbf{B} \times \mathbf{v}) = -\nabla \times (\eta \nabla \times \mathbf{B}),$$

where $\mathbf{B}$ is the magnetic field intensity, $\mathbf{v}$ denotes the ion velocity field, and η is the magnetic diffusivity. Assuming η to be approximately constant in the ISM (uniform ion density) and using $\nabla \cdot \mathbf{B} = 0$ (no magnetic monopoles!) the above equation can be re-written as,

$$\frac{\partial \mathbf{B}}{\partial t} + \nabla \times (\mathbf{B} \times \mathbf{v}) = \eta \nabla^2 \mathbf{B}. \tag{1.7}$$

Similar to the case of momentum conservation, the last term $\eta \nabla^2 \mathbf{B}$ measures the redistribution or diffusion of the magnetic field. We can carry out a similar dimensional analysis with scaling and the above equation becomes

$$\frac{BV}{L} + \frac{BV}{L} \sim \eta \frac{B}{VL} \text{ or } 1 \sim \frac{\eta}{VL}.$$

The last term is dimensionally equal to the reciprocal of the *magnetic Reynolds number*,

$$\mathcal{R}m \sim \frac{VL}{\eta} \tag{1.8}$$

Clearly, magnetic diffusion is significant when $\mathcal{R}m \lesssim 1$, similar to the hydrodynamic case. Using the same scaling $L \sim 10$ pc, $V \sim 5$ km s^{-1}, $B \sim 10\mu$G, and $\eta \sim 10^{22}$ cm^2 s^{-1}, typical values found in molecular clouds (Krumholz, 2015), $\mathcal{R}m$ turns out to be of the order of 10^3. This implies on large scales, magnetic diffusion is not significant. This result can be extended using Stokes theorem (Krumholz, 2015), that the magnetic flux in a fluid is conserved for any infinitesimal volume, which can be interpreted as that magnetic field lines move with the fluid in molecular clouds. This is referred to as *flux-freezing*, suggests that the interstellar hydrodynamic turbulence must be magnetized, hence the momentum conservation equation needs a correction factor for the magnetic field,

$$\frac{\partial (\rho \mathbf{v})}{\partial t} = -\nabla \cdot (\rho \mathbf{v}\mathbf{v}) - \nabla P + \rho \nu \nabla^2 \mathbf{v} + \frac{1}{4\pi} (\nabla \times \mathbf{B}) \times \mathbf{B}. \tag{1.9}$$

This is the case of ideal MHD (*magneto-hydrodynamic*) flow in molecular clouds. Again, we re-write the above equation using the order of magnitude scaling (Krumholz, 2015),

$$\begin{aligned} \frac{\rho V^2}{L} &\sim -\frac{\rho V^2}{L} + \frac{\rho c_s^2}{L} + \frac{\rho \nu V}{L^2} + \frac{B^2}{L} \\ 1 &\sim 1 + \frac{\rho c_s^2}{V^2} + \frac{\nu}{VL} + \frac{B^2}{\rho V^2} \end{aligned} \tag{1.10}$$

The second and third terms are dimensionally equal to the Mach and Reynolds numbers. The last term gives rise to another quantity, the *Alfvénic Mach number*,

$$\mathcal{M}_A \sim \frac{V}{v_A}, \tag{1.11}$$

where $v_A = B/\sqrt{4\pi\rho}$ is called the *Alfvén speed*, a magnetic analogue of the thermal sound speed in gas. $\mathcal{M}_A$ characterizes magnetized turbulence in the ISM. If $\mathcal{M}_A \gg 1$ (super Alfvénic flow), from equation 1.10, magnetic forces are insignificant. If $\mathcal{M}_A \ll 1$ (sub Alfvénic flow) magnetic forces are important. Using typical values for molecular clouds as before, and $n_H \sim 100$, $v_A \approx 2$ km s^{-1} and hence $\mathcal{M}_A \sim 1$ (trans-Alfvénic) so the magnetic forces in molecular clouds can not be ignored.

However, ideal MHD is only an approximation for molecular clouds and not a very good approximation. This is because in most cases the ISM has a fairly low ion fraction of 10^{-6} or less. Unlike the ions, neutral gas found in the cold ISM (with low ferromagnetic fraction and H_2 or He lack unpaired orbital electrons) interacts with the magnetic field indirectly, through ion-neutral collisional coupling. This coupling is not strong due to the low ion fraction and flux freezing implies only the ions move with the magnetic field lines. Neutral particles tend to slip off the field lines and essentially drift across the direction of motion of the ions. The flow of neutral particles is largely dominated by gravitational force. This non-ideal MHD effect is called ion-neutral drift or *ambipolar diffusion*. The drift velocity field is given by (Krumholz, 2015),

$$\mathbf{v}_{\text{drift}} = \frac{1}{4\pi\gamma\rho_n\rho_i}(\nabla \times \mathbf{B}) \times \mathbf{B} \tag{1.12}$$

ρ_n and ρ_i denote densities of neutral gas and ions, γ is called drag force coefficient, specific to the plasma under consideration.

1.1.5 HII Regions

In addition to its atomic and molecular counterparts, hydrogen exists in an ionized state in the ISM. Some of this gas is found in the HII regions surrounding individual O- and B-type stars. HII regions are created when young, massive stars ionize nearby gas clouds with high-energy UV radiation. The typical temperature of ionized hydrogen gas being of the order of 10,000 K, HII regions can vary in size from compact $\sim$ fraction of a pc to extended regions $\sim$ 100 pc. This also implies they can have a large range of number density values, from a few cm^{-3} up to 10^6 cm^{-3}. HII regions are associated with active star formation in two ways, they surround young stars, and they induce the formation of new generations of stars. Hence, dense HII regions may also be used as tracers of star formation and they are also concentrated in the spiral arms of the galaxy.

In all cases, when the ionization front arrives, the edge of the already 'shocked' molecular cloud that faces the radiation front forms globules in the shape of a comet or a pillar (refer to section 1.5). Protostars tend to form in clusters along the propagation of such radiation front inside the globules. This spatial asymmetry may suggest a causality. In addition to this, the energetic photons cross the radiation front and start to ionize the gas leading to photoevaporation of the cloud. This effect is observed as a narrow rim of ionized gas around the globule that is visible in Hα and radio continuum emissions. The famous 'Pillars of Creation in the Eagle Nebula is an excellent example (Figure 1.3).

The gas temperature in the HII region around a young massive star ranges between 7000 K and 15000 K. This depends on the gas metallicity and spectral class of the star. High energy photons (mostly ultraviolet and $h\nu > 13.6$ eV), emitted by the young star that is initially embedded in a neutral cloud, start molecular dissociation and ion production in the medium around the star. This ionization zone expands with time and the moving edge is called the ionization front. The edge of the ionization front forms a narrow rim, as it propagates through the neutral medium.

The ionization releases free electrons that radiatively recombine with newly created ions

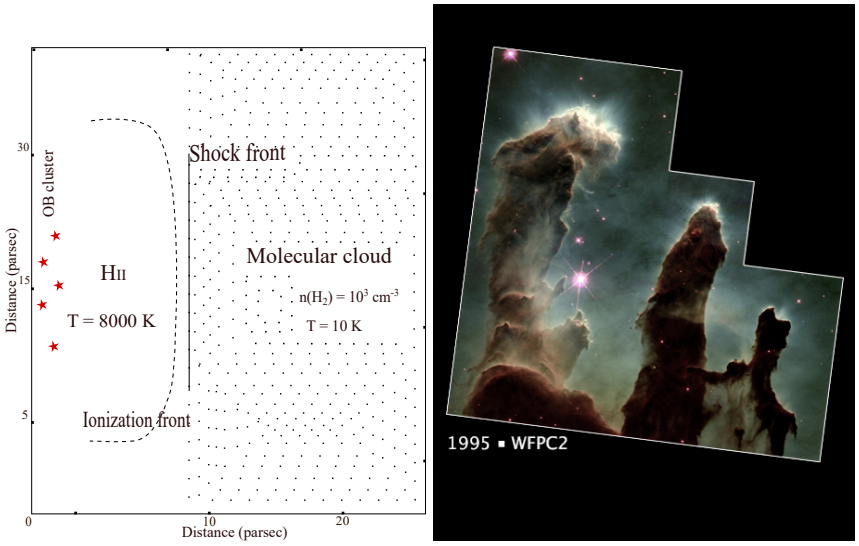

Figure 1.3: Left: a schematic diagram of shock front propagation though molecular cloud followed by ionizing radiation front (*adapted from Bodenheimer 2011*). Right: optical image of the Pillars of Creation, the molecular globule formation in the Eagle Nebula. The glowing photoionized exteriors are irradiated by incoming ionizing radiation from the above of the pillars (*credits*: NASA, ESA, STScI, (Hester et al., 1996)).

in a cascading manner down the energy levels, resulting in Hα emission (Balmer $3 \rightarrow 2$). This is why the Hα line is the most commonly used emission to observe and resolve HII regions. In the beginning, the recombination is no match for the enormous amount of ionizing photons coming out of the star. The excess photons reach the ionization front quickly without being absorbed and cross the boundary, ionize additional neutral gas (photodissociate if molecular) and the ionization front expands. If It is evident that in this phase the front propagates rapidly due to the imbalance between dissociation and ionization. Figure 1.4 provides a schematic of how this happens.

Let q_0 be the ionizing photon flux reaching the edge R at time t. As the photons cross the boundary, let us assume the front propagates to an additional distance ΔR in an additional time Δt, dissociating $n_{\mathrm{H}_2}\Delta R$ molecules per unit area which requires the same number of photons of each having the energy of at least 14.7 eV (direct dissociation of hydrogen molecule). This creates $2n_{\mathrm{H}_2}\Delta R$ neutral hydrogen atoms, each of which in turn gets ionized by a photon of energy of at least 13.6 eV. Since three photons are needed to ionize one

H_2 molecule, the total number of photons supplied for this process is $q_0\Delta t$ per unit area which can ionize $q_0\Delta t/3$ molecules. Equating this cosmic supply and demand relation we get (Stahler & Palla, 2004),

$$\frac{q_0\Delta t}{3} = \frac{2n_{H_2}\Delta R}{2}$$

This gives the ionization front propagation speed as,

$$\frac{dR}{dt} \approx \frac{\Delta R}{\Delta t} = q_0/3n_{H_2} = 2q_0/3n_H^0 \tag{1.13}$$

where n_H^0 is the number density of atomic hydrogen. Since the ratio is very high at the beginning the ionization front expands rapidly ($\sim$ 1000 km s^{-1} on a time average). However as the region grows and so does the recombination rate, the expansion speed decreases. If the molecular material around the star is approximately uniform the expansion of the ionized region becomes isotropic and spherically symmetric. With time this sphere achieves a balance between ionization and recombination. At this point the expanding region becomes the Strömgren sphere. The expansion asymptotically stops when the radius reaches the Strömgren radius.

The steady state inside the sphere implies every photoionization $H + h\nu \rightarrow H^+ + e^-$ is associated with a radiative recombination $H^+ + e^- \rightarrow H + h\nu$. If Q_0 is the rate of ionizing photon production, R_{SO} is the radius of the expanding Strömgren sphere and n_{H^+}, n_e denote densities of HII and free electrons in the plasma respectively, the equilibrium between radiative recombination and photoionization implies,

$$Q_0 = \frac{4\pi}{3}R_{SO}^3\alpha n_{H^+}n_e = \frac{4\pi}{3}R_{S0}^3\alpha n_e^2 \tag{1.14}$$

α is the recombination coefficient which can have two types based on the ionization environment (Draine, 2011).

Case A: HII region is optically thin to $h\nu = 13.6$ eV. Most ionizing photons in this case escape the region during the recombination. Recombination coefficient is given by

$$\alpha_A(T) = \sum_{n=1}^{\infty}\sum_{l=0}^{n-1}\alpha_{nl} \tag{1.15}$$

where α_{nl} is the rate coefficient for recombination of electron to hydrogen level nl (n and l denote the principal and the azimuthal quantum numbers).

Case B: HII region is optically thick to ionizing photons released during recombination to $n = 1$ level, because they get reabsorbed readily due to high density of neutral hydrogen. This happens usually in photoionized medium around O or B spectral type stars. Recombination coefficient for this case is given by

$$\alpha_B(T) = \sum_{n=2}^{\infty} \sum_{l=0}^{n-1} \alpha_{nl} \tag{1.16}$$

The approximate values for hydrogen are provided in (Draine, 2011),

$$\begin{aligned} \alpha_A(T) &\approx 4.13 \times 10^{-13} T_4^{-0.71} \quad \mathrm{cm^3 s^{-1}} \\ \alpha_B(T) &\approx 2.56 \times 10^{-13} T_4^{-0.83} \quad \mathrm{cm^3 s^{-1}}. \end{aligned} \tag{1.17}$$

During this early phase of expansion, the temperature in the ionized region is on the order of 10^4 K compared to 10 - 40 K in the surroundings so the pressure difference becomes very large. The mass density, however, remains approximately the same inside and outside the HII region, because the ionization front moving at a speed much greater than 11 km s^{-1}, the isothermal speed of sound in the ionized region, does not allow the perturbation in pressure to readjust the density after ionization (Stahler & Palla, 2004). As the radius of HII region approaches Strömgren radius, the expansion exponentially declines to become stationary. In reality, when the radiation front slows down to the speed of sound, the perturbation crosses the boundary of the (slowly) expanding HII region and propagates as a shock front through the much cooler molecular region followed by the ionization front moving at the same speed.

The shock compresses matter particles in its path forming a narrow shell of neutral gas. The inner boundary of this shell is the ionization front encompassing the HII region (Figure 1.4).The material in the shell maintains a low temperature similar to the exterior cloud via isothermal cooling. The inner edge of the shell from a very thin rim of significantly hotter (order of 10000 K) ionized gas.

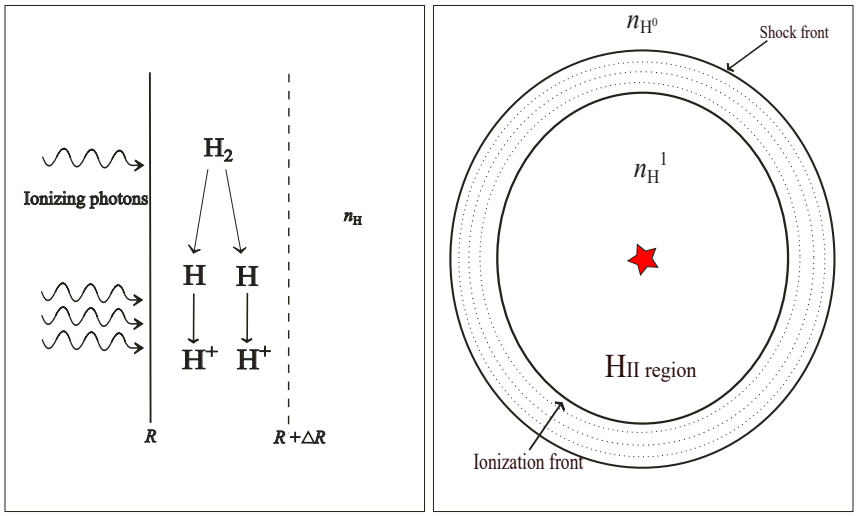

Figure 1.4: *Left*: dissociation of H_2 as ionization front propagates. *Right*: expansion of HII region after reaching Strömgren radius. n_{H^1} denotes the number density inside the ionized region (*adapted from Stahler & Palla 2004*).

1.2 Star forming Process

Molecular clouds are the most massive reservoirs of interstellar gas and dust, particularly the giant molecular clouds are among the most massive objects in the galaxy. The densest regions within the cold interiors of these clouds with a characteristic temperature of 10 K are the stellar nurseries. The first step in the process of forming stars formation of self-gravitating dense cores within a clump of molecular gas and dust. Due to internal turbulence, density fluctuations, and gravity gas and dust particles fall onto the core. The gravitational force of the infalling gas eventually gets strong enough to dominate the gas motions completely over other forces present such as turbulence governed pressure, magnetic force, and thermal motion. Matter in the core then undergoes a rapid collapse (free-fall), with the fast increase of core density.

The intrinsic turbulence present in the clump provides an initial angular momentum to the collapsing core. The conservation of angular momentum implies that the core would be spinning faster with the contracting matter in it. As it spins, the gas and dust would infall onto the core in directions where the spinning rates are less. The least preferred direction would be along the equatorial plane (assuming a spherical geometry), and the infalling

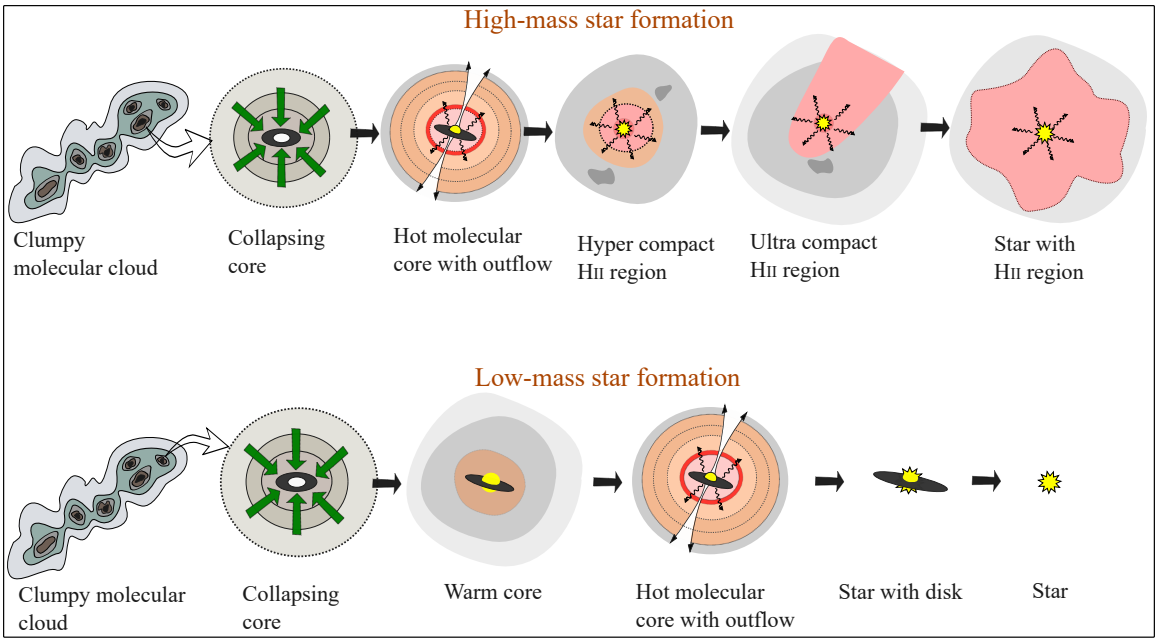

Figure 1.5: Schematics of star formation (*adapted from Ginsburg 2019, original credit: Cormac Purcell*).

matter would form a spinning disk around the collapsing core. The collapsing core is in this phase is called a *protostar*, and the disk as the *accretion disk* or the *protostellar disk*.

Although embedded in an envelope of infalling cold material, as it contracts, the collapsing core (protostar) converts gravitational energy into kinetic energy and it becomes hotter. In this phase, the protostar is obscured by the dust envelope and only detected as the source of infrared emission from the dust envelope. The distribution of such emission intensity over the IR frequencies determines the evolutionary stage of the protostar (section 1.4.1). The accreting core (protostar) with the disk continues to collapse until it becomes hot enough to start fusing hydrogen nuclei into helium and comes to be known as a star. Radiation from (low-mass) stars disperses away the remaining disk, gas, and dust around it and become visible in optical wavelengths. In addition to this, a high-mass star creates an expanding HII region around it since the amount of ionizing radiation is much higher for massive stars. Both cases of star formation are shown in figure 1.5.

The two characteristic features of protostellar accretion are the disk and the outward flow of molecular matter in opposite directions along the rotation axis. Observation has

revealed narrow jets streaming out similarly in the later phases of protostars, known as T-Tauri stars. These jets, which often emit visible light and are referred to as *Herbig-Haro (HH) objects* are, however, fast-moving and contain ionized particles as opposed to the slow-moving wide angled molecular outflows.

Additionally, in molecular clouds, collapsing cores tend to produce a large number of smaller stars with a higher likelihood, as explained by their *initial mass function* (sec 1.2.3), over a single star of a very large mass, comparable to the initial core mass. This suggests that contracting cores must fragment during the collapse and the most likely characteristic size scale of core-collapse (into protostars) must be related to the dynamics of the fragmented sub-cores. At this point, we attempt to understand the hydrodynamics of the ISM, particularly that in star-forming clumps, and identify the major forces that influence the collapse.

1.2.1 Collapsing Molecular Clouds

Lack of thermodynamic equilibrium, the influence of magneto-hydrodynamic (MHD) turbulence, and large density variation result in the formation of structures of a wide range of length scales in the ISM, from 50 pc in enormous regions of dust and gas also known as giant molecular clouds (GMC) down to less than a parsec in dense cloud cores. The clouds or the dense gas clumps, irrespective of their sizes, are typically filamentary in structure. The large masses of the clouds with high molecular densities lead to high gravitational potential energy which plays the most significant role in the process of star formation. However, most molecular gas clouds are not collapsing readily. Whether the gravitational contraction of the cloud, which would form a dense core and ultimately protostar formation, can overcome the support of internal gas pressure depends on the virial condition of the particular cloud.

To find the viral condition for molecular clouds, let us consider a cloud of a fixed volume V, with surface of the cloud denoted by $\mathcal{S}$. A volume element inside this surface has

density ρ with velocity field vector $\mathbf{v}$. Then the MHD equations, without the viscosity and diffusivity terms (since for large molecular clouds neither is significant), but with gravity, become (Krumholz, 2015),

$$\begin{aligned} \frac{\partial \rho}{\partial t} &= -\nabla \cdot (\rho \mathbf{v}) \\ \frac{\partial}{\partial t}(\rho \mathbf{v}) &= -\nabla \cdot (\rho \mathbf{v}\mathbf{v}) - \nabla P + \frac{1}{4\pi}(\nabla \times \mathbf{B}) \times \mathbf{B} - \rho \nabla \phi \end{aligned} \tag{1.18}$$

where $-\rho\nabla\phi$ represents the gravitational force per unit volume, with ϕ being the gravitational potential.

Now, by defining the moment of inertia for this volume as $I = \int_V \rho r^2 dV$ and following (Krumholz, 2015), the virial theorem for this cloud can be written as

$$\frac{1}{2}\ddot{I} = 2(\mathcal{T} - \mathcal{T}_S) + \mathcal{B} + \mathcal{W} \text{ (virial equation)} \tag{1.19}$$

where $\mathcal{T}$ represents the total kinetic and thermal energy of the cloud, $\mathcal{T}_S = \int_S rP d\mathcal{S}$ denotes the pressure on the cloud surface $\mathcal{S}$, $\mathcal{W}$ is the gravitational binding energy, $\mathcal{B} = (1/8\pi)\int_V (B^2 - B_0^2) dV$ is the difference between the magnetic pressure inside the volume which supports the cloud again gravitational collapse and magnetic pressure and tension on the surface that try to crunch it (assuming a constant background magnetic field B_0). Finally, the quantity $\ddot{I}$ represents the rate of change in the contraction (or expansion) of the cloud (Krumholz, 2015).

If the surface pressure and magnetic forces are insignificant, we get

$$\frac{1}{2}\ddot{I} = 2\mathcal{T} + \mathcal{W}$$

Then for a stable cloud $\ddot{I} = 0$, and the viral ratio may be defined as

$$\alpha_{\text{vir}} = \frac{2\mathcal{T}}{|\mathcal{W}|} \tag{1.20}$$

where $\alpha_{\text{vir}} < 1$ implies collapse and $\alpha_{\text{vir}} = 1$ implies the gas pressure and kinetic energy support against gravity, in other words, the cloud is in virial equilibrium.

For such an isothermal isolated gas cloud of mass M, radius R and temperature T,

$$\begin{aligned} \mathcal{T} &= \frac{3}{2} N k_B T = \frac{3}{2} M c_s^2 \\ \mathcal{W} &= -a \frac{GM^2}{R} \end{aligned} \tag{1.21}$$

with $N = \frac{M_c}{\mu m_H}$ is the total number of particles in the cloud and $c_s = \sqrt{\frac{k_B T}{\mu m_H}}$ is the thermal sound speed in the cloud. It is notable that the internal kinetic energy has only thermal pressure term, ignoring other possible supporting forces. Then the virial condition $\alpha_{\rm vir} \approx 1$ yields the critical mass as

$$M_J \approx \left(\frac{3}{2aG}\right)^{3/2} \left(\frac{3}{4\pi\rho_0}\right)^{1/2} c_s^3 \approx \left(\frac{81}{32a^3\pi}\right)^{1/2} \frac{c_s^3}{\sqrt{G^3\rho_0}} \quad , \tag{1.22}$$

where ρ_0 is the initial density of the cloud. This mass is famously known as the Jeans mass. The factor a depends on the geometry and internal density structure of the cloud, but it is a factor of order unity. With some more simplifications,

$$M_J \approx (0.9\ \mathrm{M}_\odot) \left(\frac{c_s}{0.13\ \mathrm{km\ s^{-1}}}\right)^3 \left(\frac{n}{10^3\ \mathrm{cm^{-3}}}\right)^{-1/2} \tag{1.23}$$

where n denotes the number density in the collapsing cloud clump. Using typical values found in molecular clouds or star-forming clumps ($r \sim 1$ pc, $n \sim 10^4$ cm^{-3}, M$\sim 10^4$ M$_\odot$) both of the above forms of Jeans mass lead to values of the order of 10 M$_\odot$. A cloud with mass greater than the Jeans mass will undergo a spontaneous isothermal gravitational collapse.

Using equations 1.20 and 1.21, we can also provide the characteristic length scale for collapse,

$$\lambda_J \approx 0.6 \frac{c_s}{\sqrt{G\rho}} \approx (2.3\ \mathrm{pc}) \left(\frac{c_s}{0.13\ \mathrm{km\ s^{-1}}}\right) \left(\frac{n}{10^3\ \mathrm{cm^{-3}}}\right)^{-1/2}, \tag{1.24}$$

which yields a value of the order of 2 pc.

If the cloud stays optically thin such that gravitational energy released during the process is radiated out causing the gas remain isothermal and the internal pressure gradient is

insignificant, the collapse essentially becomes pressure-less and continues to happen on a free-fall timescale

$$t_{\rm ff} = \sqrt{\frac{3\pi}{32G\rho_0}} \quad \text{(for a spherically symmetric cloud)} . \tag{1.25}$$

Using the above values from a star-forming clump, $t_{\rm ff} \sim 0.3$ Myr. However, most clouds are centrally concentrated, so the free-fall collapse is more effective in the inner layers of the cloud. The density near the core will undergo a faster increase than the outer parts. Collapse like this is referred as *inside-out*.

If we add the $\mathcal{T}_{\mathcal{S}}$ term to the virial equation which accounts for external thermal gas pressure in equilibrium at the surface of the volume, the critical mass above changes by a factor of order unity and becomes the Bonnor-Ebert mass, given by (Krumholz, 2015)

$$M_{\rm BE} = 1.18 \frac{c_s^3}{\sqrt{G^3\rho_0}}. \tag{1.26}$$

The forces that affect gravitational collapse in the virial equation 1.19 are turbulence and magnetic field. Turbulent support contributes to the term $\mathcal{T}$ in the virial equation and works against gravity but turbulence is poorly understood in the context of gravitational collapse in molecular clouds. The existing model is that supersonic turbulence can result in the spatial variation of shock in a cloud core. This can theoretically create irregular density fluctuations in the molecular gas compressed by the shock which can, in turn, destabilize high-density regions and bring about the onset of the collapse. The timescale is of the order of 1 Myr (Krumholz, 2015).

The Magnetic field term $\mathcal{B}$ in the virial equation generally supports the collapse. To see how B-field influences the collapse, we consider a spherical cloud of radius R with uniform magnetic field $\mathbf{B}$ and a background field $\mathbf{B_0}$ outside the cloud ($\mathbf{B} \gg \mathbf{B_0}$). Then the magnetic flux passing through the cloud is given by $\Phi_{\mathbf{B}} = \pi B R^2$ and the magnetic term in the virial equation can be written as,

$$\mathcal{B} \approx \frac{\Phi_B^2}{6\pi^2 R}$$

Comparing this to the gravitational energy term $\mathcal{W} = -\frac{3GM^2}{5R}$ ($a = 3/5$ for sphere),

$$\mathcal{B} + \mathcal{W} \approx \frac{\Phi_B^2}{6\pi^2 R} - \frac{3GM^2}{5R} = -\frac{3G}{5R}\left(M_\Phi^2 - M^2\right), \tag{1.27}$$

where

$$M_\Phi = \sqrt{\frac{5}{2}}\left(\frac{\Phi_B}{3\pi G^{1/2}}\right) \tag{1.28}$$

is called the magnetic critical mass (Krumholz, 2015). If we assume ideal MHD, Φ_B remains constant while the cloud contracts, because of flux-freezing, and hence M_Φ does not change either. Clouds that have masses greater than the magnetic critical mass are called magnetically supercritical ($M > M_\phi$). For such clouds, $\mathcal{B} + \mathcal{W} < 0$ and gravity dominates over the magnetic field. Magnetic forces can not stop their gravitational collapse in them.

On the other hand, for magnetically subcritical clouds ($M < M_\phi$), $\mathcal{B} + \mathcal{W}$ is positive and gravity is outperformed by magnetic force. In this case, if there other factors like external pressure on the cloud surface help gravity to initiate a collapse ($\mathcal{T}_\mathcal{S}$ in the virial equation being sufficiently negative), eventually magnetic force will halt the collapse since $\mathcal{B} + \mathcal{W} \propto 1/R$, and assuming the pressure forces are finite. This term will increase without a bound as the cloud contracts and R get smaller.

For subcritical clouds, collapse can occur only if we drop the ideal MHD approximation, and consider non-ideal MHD effects that allow deviation from flux freezing. Ambipolar diffusion or ion-neutral drift is one such effect (section 1.1.4). Although, it allows magnetic flux change though fluid elements, the timescale for ambipolar diffusion is given by,

$$t_{\rm AD} = \frac{2R}{v_{\rm drift}} \approx 10\ {\rm Gyr}\left(\frac{n}{10^4\ {\rm cm}^{-3}}\right)\left(\frac{B}{10\,\mu{\rm G}}\right)^{-2}\left(\frac{R}{1\ {\rm pc}}\right)^2 \tag{1.29}$$

which vary from a few Myr to a few tens of Myr thus can exceed free-fall timescale by 1 to 2 orders of magnitude. The longer collapse time may negatively affect star formation in the particular clump, as we shall in section 1.5, that photoionizing radiation from nearby young massive stars can destroy a molecular cloud before any significant star formation can occur if the collapse timescale is not shorter than the photoevaporation time.

Fortunately, observations suggest that atomic gas in the ISM is subcritical but molecular gas in most cases is supercritical (Crutcher, 2012). So magnetic field in molecular clouds is not strong enough to stop the gravitational collapse.

The third most important factor that can initiate virial instability followed by gravitational collapse of cloud cores, especially those that are otherwise stable against collapse, is the triggering effect by ionizing radiation from nearby massive stars or shock fronts from supernovae. External shock can also be generated by collisions between clouds or by galaxy mergers. These forces contribute to the $\mathcal{T}_S$ term in the virial equation and since it's negative it indicates contraction of the virial surface or gravitation collapse. I will discuss this factor in section 1.5.

1.2.2 Fragmentation of Collapsing Cores

The large sizes of molecular clouds result in masses larger than Jeans mass, hence protostars of very large initial masses are likely to form. This is not supported by observational evidence though, which shows stars form in clusters and preferably with smaller masses than larger. This implies cores must fragment during their collapse.

Molecular clouds are thought to be mostly turbulent, magnetized, self-gravitating approximately isothermal gas. The primary cooling source is thermal emission by dust grains that is collisionally well-coupled with gas, which is the case at densities $n \sim 10^5 - 10^6$ cm^{-3} (or $\rho \sim 10^{-18}$ g cm^{-3}) typically found in cloud cores. The isothermal assumption is valid for a collapsing core if the gas is optically thin for the thermal emission because then the cooling rate by thermal emission is given by (Krumholz, 2015),

$$\Lambda_{\rm thin} = 4\kappa_{\rm P}\sigma_{\rm SB}T^4, \tag{1.30}$$

where $\sigma_{\rm SB}$ is the Stephen-Boltzmann constant and $\kappa_{\rm P}$ is the opacity of the gas dust mixture.

Additionally, as the gas collapses, heating occurs via compression and is given by,

$$\begin{aligned} \Gamma &= -p\frac{d}{dt}\left(\frac{1}{\rho}\right), \\ \Gamma &= C_1 c_s^2 \sqrt{4\pi G\rho}, \end{aligned} \tag{1.31}$$

where C_1 is a constant which depends on the collapse model, usually of order unity (Krumholz, 2015). As long as $\Gamma \lesssim \Lambda$, the gas is isothermal. In fact, cooling rate should be greater than the rate of heating via pure compression because a collapsing core is also exposed to cosmic rays and external radiation fields, and both cause additional heating.

The density in a collapsing core increases rapidly, and consequently, the opacity for dust thermal emission rises as well. This is evident from the opacity surface density relation $\tau_\nu \approx \kappa_\nu \Sigma$, dust density reaches high enough that it starts to block all radiations out of the clump. This in turn leads to the breaking down of the isothermal assumption. At this stage cooling rate drops below the heating rate. The gravitational energy during the collapse $dU = pdV$ is retained within the collapsing core, it begins to heat the gas, and the collapse becomes adiabatic. Using typical values for the parameters, found in cloud cores, the characteristic density is estimated to be $\rho \sim 10^{-13}$ g cm^{-3} at which the transition from isothermal to adiabatic becomes evident (Krumholz, 2015).

If we consider purely isothermal collapse, from equation 1.23, $M_J \propto \rho^{-1/2}$, because $c_s \sim T^{1/2}$ is constant, under the isothermal assumption. As density rises, M_J drops (decreasing function of ρ), which means smaller-scale individual gravitational collapses are now allowed within the original collapsing core. As a result, the core fragments. This process can continue if the core remains isothermal.

However, as seen above, isothermal to adiabatic transition happens at $\rho \sim 10^{-13}$ g cm^{-3}. Since T is no longer treated as constant,

$$M_J \propto T^{1/2} n^{-1/2}.$$

For a purely adiabatic collapse the ideal gas law yields $T = K'' \rho^{\gamma-1}$ (K'' being a constant). Here $\gamma = C_p/C_v$ is the ratio of specific heats for the gas. Using $c_s \propto T^{1/2} \propto \rho^{(\gamma-1)/2}$,

$$M_J \propto \rho^{\frac{3}{2}(\gamma-\frac{4}{3})}. \tag{1.32}$$

The Jeans mass is an increasing function of ρ if $\gamma > 4/3$. For molecular clouds consisting mostly of diatomic H_2, γ is 7/5 or 5/3 depending on the gas temperature and excitation

state of the molecules (Krumholz, 2015). So the Jeans mass increases with density, hence a lower limit on M_J applies. In reality, a collapse is neither purely adiabatic nor isothermal. Between the two processes, the core will fragment at a characteristic scale of mass, usually of the order of typical-sized stellar masses, and free-fall collapse will halt as thermal pressure increases against gravity. At this mass, it will become a protostar, of sizes (including disk) of the order of $10 - 100$ AU. This also implies only a small fraction of collapsing mass ends up producing protostars.

1.2.3 The Initial Mass Function

Observations related to star formation in our galaxy have revealed that in star-forming regions in molecular clouds less high mass than low mass stars form. Although the actual fraction varies from one cluster to another, the general trend is the same. This indicates if we group observed stars from a single stellar cluster into several mass intervals, the number (frequency of occurrence) of stars per interval would depend on the mass of the interval. More generally, the number (or relative fraction) of stars per mass interval per unit area in the plane of the galactic disk is largely mass-dependent. This functional relationship between stellar mass and the number of stars is referred to as the *initial mass function* or the IMF.

Regions of the galaxy rich in molecular gas determine the properties of the stars and gas composing them and thus influence the rate at which stars in different mass ranges are formed. The observed luminosity function provides the basic data on the numbers of stars of different masses formed. As we have mentioned in section 1.2.2, low mass stars form in abundance but high stars are relatively rare. In any case, the determination of the mass function, and its dependence on the properties of the gas out of which stars form, is a central observational problem.

Although various theories and numerical simulations have produced initial mass functions in good agreement with observations, it remains unclear which mechanism dominates.

The function itself is determined from observations of main-sequence stars in the field in the solar neighborhood (field stars) and forms stars in clusters by using mass-luminosity relation (Krumholz, 2015). Comparison of the positions of stars in the H-R diagram with theoretical pre-main-sequence evolutionary tracks is also useful, particularly for young stellar clusters.

The IMF is defined as the infinitesimal change in the number of stars per unit change in log stellar mass. The general form of the IMF is fairly flat in the range 0.1–1$M_\odot$, with a peak at about 0.2$M_\odot$. It drops off at low and high masses, and above 1$M_\odot$ the drop-off has the well-defined slope of $dN/(d\log M) \propto M^{-1.35}$ (Bodenheimer, 2011). There are of course statistical fluctuations from cluster to cluster, but even the oldest stars, in globular clusters, show mass function similar to the nearby field stars and open clusters.

The functional form of the initial mass function can be parameterized in a number of ways. Two of the most popular are from Kroupa (2002) and Chabrier (2005). The functional form of Chabrier IMF is

$$\frac{dn}{d\,\log\,m} \propto \begin{cases} \exp\left[-\frac{((\log\ m - \log\ 0.22))^2}{2\times 0.57^2}\right], & \text{if } m < 1 \\ \exp\left[-\frac{(-\log\ 0.22))^2}{2\times 0.57^2}\right] & \text{if } m \geqslant 1 \end{cases} \tag{1.33}$$

and the functional form of Kroupa IMF is gven by,

$$\frac{d}{d\,\log\,m} \propto \begin{cases} \left(\frac{m}{m_0}\right)^{-\alpha_0}, & \text{if } m_0 < m < m_1 \\ \left(\frac{m}{m_0}\right)^{-\alpha_0}\left(\frac{m}{m_1}\right)^{-\alpha_1}, & \text{if } m_1 < m < m_2 \\ \Pi_{i=1}^{n}\left(\frac{m}{m_0}\right)^{-\alpha_0} & \text{if } m_n < m < m_{n+1} \end{cases} \tag{1.34}$$

where

$$\begin{aligned} \alpha_0 &= -0.7 \pm 0.7, m_0 = 0.01 \\ \alpha_1 &= 0.3 \pm 0.5, m_1 = 0.08 \\ \alpha_2 &= 1.3 \pm 0.3, m_2 = 0.5 \\ \alpha_3 &= 1.3 \pm 0.7, m_3 = 1, m_4 \to \infty \end{aligned} \tag{1.35}$$

In both cases, m is in the units of solar masses (Krumholz, 2015).

The observed IMFs show that higher masses have relatively few stars. Based on observations in the Milky Way galaxy, stars can be as massive as 50 $M_\odot$. On the other hand, low-

mass main-sequence stars range in 0.3−1 $M_\odot$. Using the Chabrier IMF, a sample probability calculation shows the relative abundances of stars in different mass groups (table 1.2). Stars of the size of the sun or with lower masses are comparatively abundant, Stars smaller than the Sun are much more common than the ones with much higher masses. Very high-mass stars are extremely rare. High mass stars are also short-lived, which potentially contributes to their observational rarity. The precise statistics for low-mass stars are uncertain because they are faint and hard to detect.

The theoretical basis for the IMF is not completely clear. The same applies to whether the IMF of the Milky Way galaxy represents the IMF in general in the universe. It has been proposed that the relative abundance of heavier elements in a collapsing cloud is one of the factors that modify the IMF (Bodenheimer, 2011). The idea of a universal mass function has been an open question, and recent efforts to test this idea, have been possible thanks to sensitive instrument sensitivity to much fainter stellar objects. Stars of different masses have different atmospheres, resulting in the emission of different spectral lines. In that sense, modern improvement in spectroscopy technique provides useful insights into stars of different masses of a distant cluster whose individual stars could not be resolved otherwise.

Mass ($M_\odot$)	%age of stars
$\leqslant 0.1$	26.9
0.1 – 0.8	57.0
0.8 – 1.5	9.4
1.5 – 8	6.1
8 – 20	0.5
20 – 49.5	0.1
49.5 – 50	0.0008

Table 1.2: Relative frequency distribution of stellar population according to Chabrier IMF

An interesting observation regarding the IMF in various star-forming regions, where the cores have not formed stars yet, is that the mass function of the molecular cloud cores ($n \approx 10^4$ cm^{-3}) shows functional resemblance with the form of IMF, although scaled up in location by a factor of 3. This leads to the question if the core mass function (CMF) is a predecessor of the IMF and what factors influence the CMF. Turbulent shock compres-

sion and the resulting fragmentation are among the proposed factors (Bodenheimer, 2011; Krumholz, 2015). It can also represent a statistical distribution around the critical Bonnor-Ebert mass at the given temperature and pressure of the molecular cloud region (Krumholz, 2015).

There is a universal efficiency factor of 1/3, independent of mass, involved in the conversion of the cores into stars. This factor can qualitatively be attributed to the fact that some of the core mass is later ejected in the form of bipolar outflows, and some of it is left behind in the form of a circumstellar disk, to be dissipated later. The similarity of the CMF to the IMF suggests that cores form first, survive for a few free-fall times, and then collapse. This model applies to stars that form in relative isolation.

However, if stars form in relatively dense clusters, the picture becomes more complicated, because the individual protostars interact with each other, through a number of different encounters such as mergers, outflows, feedback, competitive accretion, and component ejection, etc. In that case, the model mentioned above does not explain how the core mass function evolves into the initial mass function.

1.3 High-mass Star Formation

A star is considered high-mass when its zero-age main sequence (ZAMS) mass is greater than 8 $M_{\odot}$. ZAMS is the earliest phase of newborn stars where they have just begun hydrogen burning in stellar cores to create helium. The time to collapse onto this phase is inversely proportional to the stellar mass.

High-mass stars belong to spectral types O, B0, and B1 (Bodenheimer, 2011). Although they do not contribute significantly to the number in overall stellar population in a region, as seen in section 1.2.3, they dominate the total energy budget of all stars through their very high luminosities ($L \sim M^{1/3}$).

High-mass stars play a crucial role in the physics of the ISM. First of all, high-mass stars end their life as supernovae, which eject heavy elements into the ISM as feedback.

These heavy elements act as excellent cooling agents for the molecular gas in the ISM and not only facilitate star formation in the long run, but also contribute to life formation in the Universe. Additionally, shock waves from supernovae and stellar winds from massive stars produce interesting dynamics within the ISM. This can accelerate the local star formation rate by providing radiation pressure which promotes gravitational collapse. However, stellar feedback can also suppress star formation rate by eroding (photoevaporation) molecular cloud material in the neighborhood, particularly when the free-fall timescale is well below the photoevaporation time. I will discuss these effects in a later section. Strong observational evidence for the latter case is yet to be found.

Although high-mass stars are naturally very luminous, they are also at large distances from the sun, $\sim 0.5 - 3$ kpc, which causes lower spatial resolution, as well as obscurity in the optical radiation due to large extinction by interstellar dust columns. Altogether these factors make high-mass stars difficult to observe. On the other hand, Emissions from extra-galactic low-mass stars would be too weak to be useful. High-mass stars are almost the only cases possible in extra-galactic observations, and they are extrapolated to conclude extra-galactic stellar research. Facilities such as ALMA have capabilities to observe structures at higher spatial resolution (down to ~ 0.05"), which can shed more light on the nature of distant massive stars.

The formation process for massive stars is still a very active area of research. In most cases, the cores have masses much larger ($\sim$ 100 $M_\odot$)than the Jeans mass which allows them to fragment and form clusters of low-mass stars. This does not always happen. The combined effects of magnetic field and radiative transfer can suppress fragmentation of such cores and leads to the formation of massive protostars (Commercon et al., 2013). The short gravitational collapse timescale ($\sim$ 100 yr) results in early hydrogen-burning during the protostellar phase, even while the core is still accreting (Bik et al., 2012). This implies that strong radiation pressure generated in the nuclear fusion will resist the remaining infalling gas.

There are two main solutions to this problem. First, the accretion of gas is made possible through a much higher accretion rate than that in low-mass protostellar disks (Kuiper et al., 2011). The accretion disks are also much larger, of the order of 100 to 1000 AU. The other solution is that since massive stars typically form in clusters, a collective envelope is formed during their competitive accretion, and the inflow of matter occurs on the disk. In this scenario, radiation pressure is thought to be carried away in cavities from the central spinning core in opposite directions perpendicular to the plane of rotation (Vaidya et al., 2009). In reality, a combination of both mechanisms likely governs the accretion of high-mass stars.

1.4 Cluster and Association Formation

High-mass stars typically form in clusters, along with a large number of associated low-mass stars as suggested by observations. There are roughly 4 separate categories of present locations massive stars (Bodenheimer, 2011). The first group of these massive stars is observed in gravitationally bound OB clusters. Examples of this group include the Orion Nebula Cluster, the dense cluster associated with the galactic HII region NGC 3603, and the R136 cluster in the 30 Doradus star-forming region in the Large Magellanic Cloud (LMC) (Bodenheimer, 2011).

The second group of massive stars is OB associations, for example, Scorpius OB2 and Orion OB1. The stars are between 1 and 10 pc apart, much larger than the dense clusters, and the associations are gravitationally unbound. There can be a possible relationship between the bound OB clusters and the associations. A larger bound cluster forms with a low star formation efficiency. After a considerable amount of remaining gas is scattered away, a large fraction of the stars becomes unbound and forms an expanding association. A smaller fraction of stars, those near the center of the initial cluster, can remain as a bound cluster, smaller than the original one.

The third category is called the 'runaway' OB stars, which are individual stars with

velocities greater than 40 km s^{-1}. These are often thought to have been ejected from a cluster or association. Finally, the fourth group consists of a few OB stars (less than 10% of all massive stars) in the field that cannot be traced back to an origin in a cluster or association. It is likely that they may have formed independently.

1.4.1 Protostellar Classification

There are three observationally distinct phases of prestellar evolution (Bodenheimer, 2011). The first is the formation of dense cores in massive molecular clouds and subsequent gravitational collapse. These cores are cool and detectable in molecular lines (CO for example). Next is the protostellar phase, with the accretion of matter and disk formation. Large density values and high temperature are the characteristics of this phase. Visible in infrared and submillimeter. The last phase is known as the contraction phase. In this phase, the protostellar core has enough internal gas pressure to reach equilibrium with gravity and close to the nuclear fusion stage to appear as a zero-age main sequence (ZAMS) star and to be visible in optical and near-infrared.

After the collapse has set in, the dense core in the protostellar phase becomes major source of IR or sub-mm emission, due to the abundance of dust grains around it, and the core itself comes to be known as a protostar or young stellar object (YSO), until when it enters into the contraction phase.

In the literature, the spectral energy distribution (SED) is the prime tool for observational classification of these YSO's. This begins by defining the *spectral index* (Bodenheimer, 2011),

$$\alpha = - d\log(\nu F_\nu)/d\log \nu,$$

where F_ν is the flux density, at frequency ν, measured in units of erg s^{-1} cm^{-2} Hz^{-1}. The value of α is calculated at a wavelengths around 2.2μm.

Depending on the spectral index value, protostars are categorized into four classes, namely, I, II, III, and flat-spectrum (Table 1.3), class I being the earliest evolutionary stage

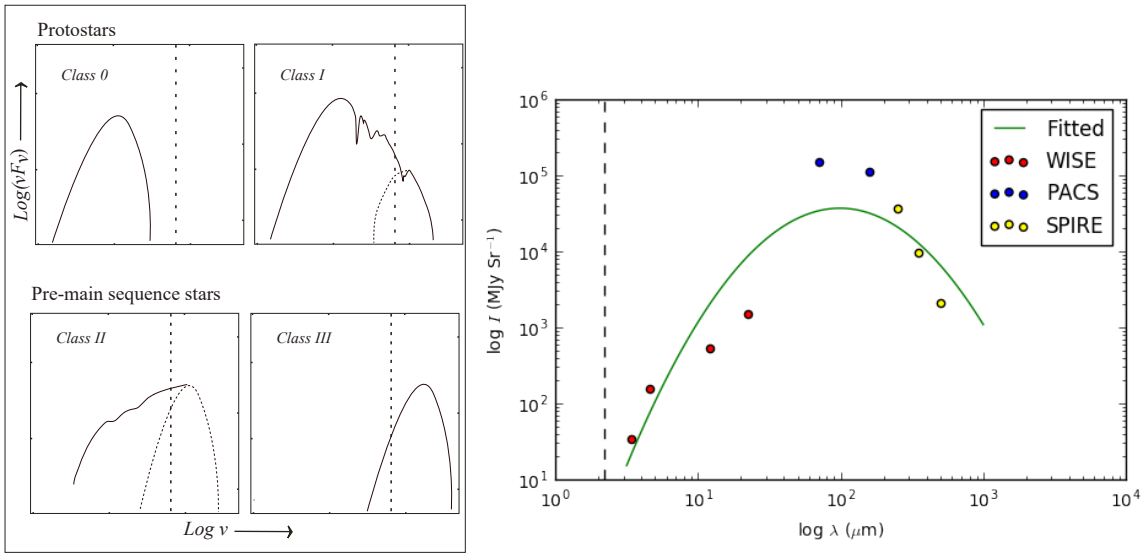

Figure 1.6: *Left*: Protostar (YSO) classification using spectral energy distribution. The vertical line is drawn at 2.2 μm, the wavelength often used for class identification (*adapted from Bodenheimer 2011*). *Right*:Spectral energy distribution of a class I embedded infrared source.

Class	Spectral Index (α)
I	$\alpha \geqslant 0.3$
Flat	$0.3 > \alpha \geqslant -0.3$
II	$-0.3 > \alpha \geqslant -1.6$
III	$-1.6 > \alpha$

Table 1.3: Protostar classification (Bodenheimer, 2011)

among the four, and class III being the latest stage. The α values also put them in specific frequency ranges in their spectral energy distribution. Protostellar SED is an effective way to identify their class as illustrated in Figure 1.6. As a protostar evolves, its SED becomes wider and moves to shorter wavelengths.

There are also class 0 sources that are not associated with an α value. They belong to an earlier stage of protostellar evolution, earlier than class I. The distinction between class 0 and class I is not always clear. Figure 1.6 (right) also shows an example of an SED of a class I protostar found in Cygnus X.

As the protostellar core approaches achieving hydrostatic equilibrium like a stellar core,

it forms a rotating disk, known as the accretion disk. Cooler material infall onto the disk from the envelope. A protostar in this phase belongs to either class 0 or class I depending on the mass accretion rate. Dust continuum emission dominates this stage.

1.5 Stellar Feedback and Triggered Star Formation

Observations suggest that star formation has been influenced both ways by previous generations of high-luminosity stars. The ultraviolet radiation starts to dissociate molecular gas into neutral and neutral gas into ionized gas. This results in the formation of a HII region inside the HI gas in the cloud.

The expanding hot HII region around a massive star or stellar cluster appears supersonic to the much cooler molecular gas in the surroundings. As a result, a shock wave is generated which is followed by an ionizing front (Figure 1.3). In the beginning, this is essentially a free expansion but once the shell between the shock front and the ionization front has swept up the gas of mass comparable to the HII mass inside the expanding bubble, the shell becomes cool and dense enough to not only stop free expansion but also destabilize the material in the shocked region leading to gravitational collapse.

Since high-mass stars are formed in clusters, the overwhelming amount of ionizing photon production can significantly increase radiation pressure in the surrounding gas which tends to ionize and disperse the cloud material. The loss of mass can make the cloud, which originally had the potential to generate low-mass protostars, gravitationally unbound, ruptured and in effect, ionizing radiation can suppress star formation rate in the cloud. An example of such a scenario is found in Carina Nebula, 3 kpc away from the sun in the southern Milky Way. Eta Carina, an emission-line supergiant ($\sim$100 $M_{\odot}$) of spectral type O, located within the nebula, along with other nearby young stars, produces enough ionizing radiation to disrupt the birth of their low-mass siblings in the region. Carina Nebula itself is being shredded by the strong stellar wind and ionizing radiation these sources (Smith, 2008).

On the other hand, molecular clouds that are originally below the threshold of gravita-

tional instability can be compressed by the effects of radiation pressure; and subsequent lowering of their Jeans mass can onset a collapse. This is called triggered star formation. There are several observations of star formation near OB clusters or high-pressure ionized regions that are considered the result of triggering. Examples include the Rosette Nebula, M16, or the Eagle Nebula, Cygnus region (Elmegreen, 1998).

As mentioned in section 1.1.3, The expansion of the Strömgren sphere can cause dynamical instabilities in the molecular cloud and mold it into a globule and form a thin envelope of hot ionized gas around the globule, compelling it to collapse by providing mechanical pressure. This happens when the shock-compressed globule cools down isothermally and lowers the value of the virial ratio favoring a forced or triggered collapse. The ionization front arrives later and provides additional (thermal) pressure on its virial surface because of the excessively hot rim of ions and electrons ($\sim$ 8000 K). The thermal pressure can be very large and can cause virial instability (the term $\mathcal{T}_S$ in equation 2) even if the shock was not unable to cause enough compression. It is possible that the globule is already existing and has even started collapsing when the ionizing front arrives. In that case, the effects of a shock wave, and/or thermal pressure in the rim facilitate the process.

It is a good spot here to remind us that for the thermal pressure by the ionized rim to even mold the gas clump into a globule and trigger a collapse, the mass has to be magnetically supercritical. No finite external pressure can help a clump achieve gravitational collapse. Additionally, The direction of ionizing radiation relative to the magnetic lines in the pre-existing molecular cloud cores plays an important role. Elmegreen (1998) proposed three distinct categories for triggering scenarios.

For small-scale triggering, pressure from ionizing radiation provides direct and surrounding compression of cloud cores or globules such as proplyds (**Pro**to **Pl**anetar**y** **D**isks), cometary globules, and pillars. Furthermore, observations indicate the gas structure exposed to high radiation and mechanical pressure under this model can have distinct geometry, which includes isolated molecular gas globules or pressurized cloud clumps, elongated

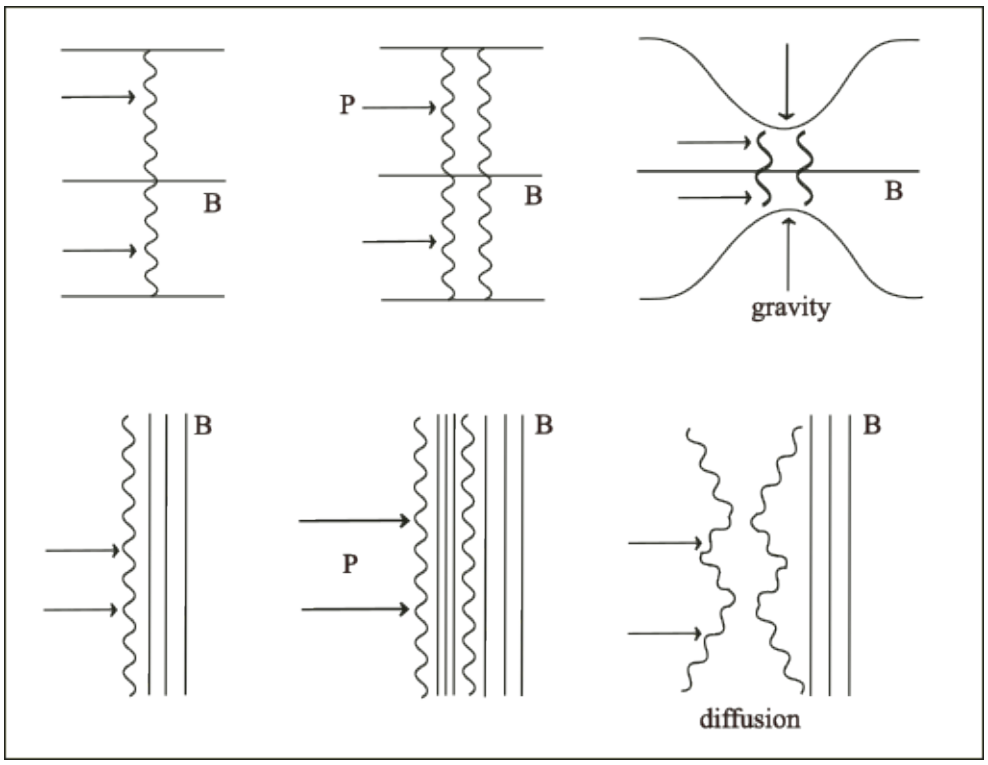

Figure 1.7: Cases of compression parallel (top) and perpendicular (bottom) to magnetic field (*adoated from Elmegreen 1998*).

pillar structures or cometary globules, and bright rims with short or no tails and denser head connected to a bigger cloud. The triggering begins with squeezing the globule/clump through high pressure at the tip of the globule. Since they are usually magnetic the basic condition for triggering, in this case, is that the globules must be magnetically supercritical as mentioned in section 1.2.2.

In addition, the direction of radiation pressure must be parallel to the magnetic field lines in the clump in order to start a collapse (Elmegreen, 1998). This is because if the clump mass is much greater than the critical mass, the motion caused by the pressure can be parallel to the magnetic field lines. If the clump is subcritical, a large fraction of gas motion caused by compression happens in the perpendicular direction relative to the magnetic field lines. Since the (internal) magnetic field strength increases with magnetic flux-freezing this means compression perpendicular to the field lines increases the internal magnetic pressure and does not contribute to triggering, under the ideal MHD assumption.

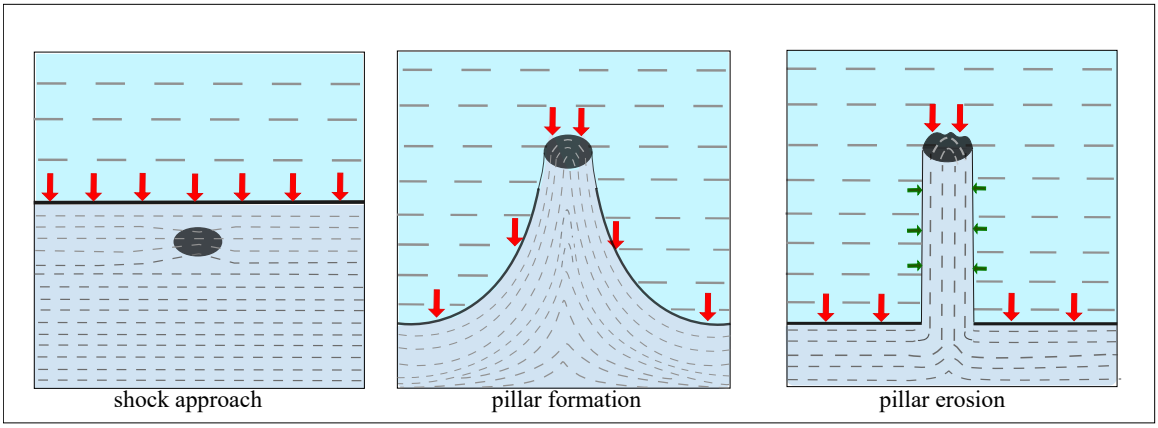

Figure 1.8: Evolutionary stages of photoevaporating pillars (*adapted from Pattle et al. 2018*).

However, as the magnetic field diffuses away, internal pressure drops, and collapse can set in. This might increase the collapse time significantly (as the case in ambipolar diffusion) and depending on other factors including rim pressure, molecular gas mass, and radiation propagation timescale, may or may not disfavor a triggered collapse. Figure 1.7 schematically shows the two cases.

Pattle et al. (2018) found support for this model of alignment of gas motion induced by radiation pressure-induced and magnetic field lines internal to evolving pillar structure compressed by radiation in their magnetic field study of M16 or the Eagle Nebula. Using high-resolution 850 microns dust polarization observations from the JCMT BISTRO survey, they mapped magnetic field structure in the molecular gas in the Pillars of Creation in the Eagle Nebula. The authors showed magnetic field vectors are approximately along the longer axis of Pillar 2, which is also the direction of propagation of photoionization front outside the pillars.

This gives rise to the evolutionary model where the ionization front (HII region) from a nearby cluster encounters neutral gas with a dense molecular gas cloud core embedded in it and molds it into a pillar structure. The initially perpendicular magnetic field lines realign with the pillar axis and get compressed radially, as a result of the flux-freezing effect. The ionizing front continues to erode and compress the pillar via photoevaporation leading

to (or promoting) gravitational collapse and subsequent star formation. The re-aligned magnetic field vectors cannot support against the erosion but provides support radially and maintain the elongated structure of the pillar (figure 1.8).

Intermediate scale triggering occurs when a cloud is compressed from one side resulting in a ridge of moving dense gas which accumulates into denser cloud cores and eventually causes the formation of stellar clusters. This process is also known as the collect-and-collapse model. Expanding HII region sweeps up neutral gas, eventually collects a large amount of such gas, and dumps it when the HII front runs into a denser nebular ridge of molecular gas. This forms thin layers of dense gas along the length of the ridge which can be unstable due to magnetic, internal gravitational, and kinematic factors. The instability leads to collapse, likely into filaments and eventually into cores inside the filaments (Elmegreen, 1998). The time scale for this process is typically greater than the first case of globule compression. This is because, unlike the small-scale triggering, there are no pre-existing dense cores in this case.

On the other hand, collect-and-collapse triggering is more universal. Aging and expanding HII regions can find residual molecular clouds in the path of expansion more or less everywhere. Moreover, since this process causes a collapse in filaments, it can form star clusters of the "collected mass" into the compressed thin layer is large enough, which is often the case. Elmegreen (1998) complies several examples of observations belonging to small and intermediate-scale triggering scenarios.

The third category is the large-scale triggering, where a central pressure can cause a giant shell of HI gas, size of the order of a few 100 pc, to expand around it. Stars are formed in the shell as a result of gravitational instability which depends on the pressure in the shell and external gas density. These expanding superstructures are often thought of as a result of shockwaves from supernovae (Tenorio-Tagle & Bodenheimer, 1988).

Particularly in the first case of small-scale triggering, there is a spatial correlation between the morphology of molecular gas clump and expanding rim of ionizing radiation.

In other words, the cometary or elongated pillar shape of collapsing globules is present in all cloud clumps exposed to the ionization front. As mentioned in section 1.1.3, photoevaporation is evident in such cases of compression of globules scenarios of triggered star formation.

Clumps	Mean Radius $\langle r \rangle$ (pc)	Number density $\langle n \rangle$ cm^{-1}	Avg. Mass $\langle M \rangle$ ($M_\odot$)	Avg. Temperature $\langle T \rangle$ (K)
Pillars	0.6	5.0×10^3	500	18
Globules	0.6	1.2×10^4	500	18
EGGs	0.1	2.2×10^4	10	17
Proplyds	0.2	1.5×10^4	30	17
Condensations	0.1	5.5×10^4	35	-

Table 1.4: Molecular cloud clumps (Schneider et al., 2016)

Schneider et al. (2016) performed a study of triggered star formation (small scale) in the Cygnus OB2 region. They defined a list of objects belonging to the bigger class of molecular clumps, particularly the characteristic structures of the evolutionary phases of a collapsing cloud core under the influence of Cyg OB2 (Table 1.4). Pillars are the largest among all. Globules are comparable in size but they have well-defined denser heads and less dense tail features. Evaporative gaseous globules (EGGs) and proplyds (evaporating circumstellar disks) are relatively smaller objects with high particle densities.

During the evolution of photoevaporating cloud cores, pillars form, fragment, and evolve into globules, and smaller structures like EGGs, proplyds, or condensations, and eventually stars are born in them. The exact path of evolution depends on the initial density conditions and size of the photoevaporating cores (Schneider et al., 2016). Observational evidence can found in figure 4.1 which shows cometary features (pillar and globule structures) found in Cygnus X north (Gottschalk et al., 2012). The structures point towards the stellar cluster C114 which indicates a possible triggering scenario.

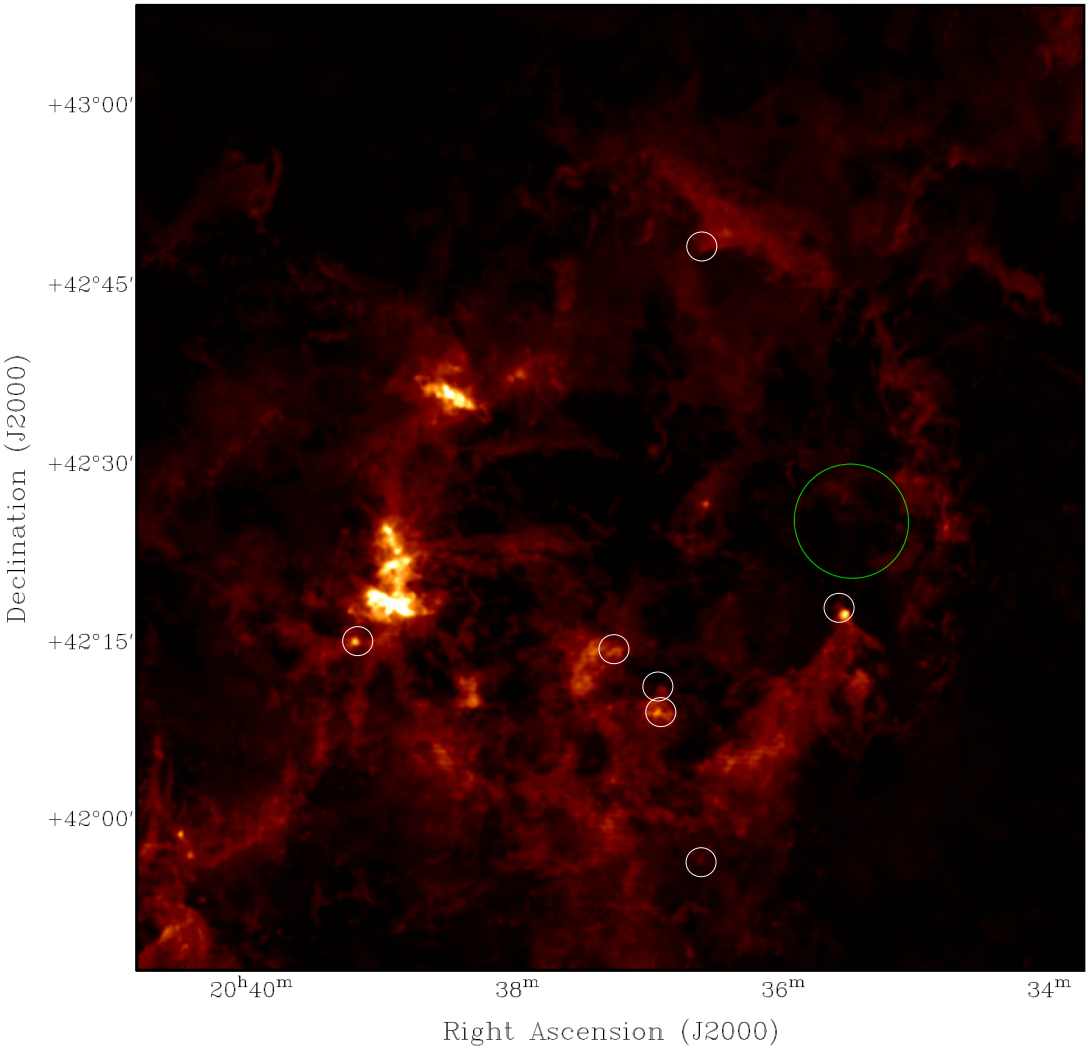

Figure 1.9: Molecular gas ring structure with pillars and globules around young stellar cluster C114 (green circle) in Cygnus X north revealed in ^{12}CO(3-2) emission (Gottschalk et al., 2012). The white circles indicate the location of several cometary features where radiative feedback has blown molecular material away from a dense core.

During the evolution process, the ionized rim (section 1.1.3) creeps deeper into the globule (or similar structures) causing a continuous erosion of matter via photoevaporation which can potentially shred and destroy the cloud. However, the timescale of collapse vs photoevaporation timescale will determine whether the ionization front will trigger the birth of protostars or disperse the gas away before that. There is more than one way to estimate the time to completely evaporate a molecular globule. We use the photodissociation mass loss rate estimate given by (Schneider et al., 2016),

$$\dot{M} = 9.5 \times 10^{-9} \phi_{49}^{1/2} r_{14}^{3/2} d_{17}^{-1} \tag{1.36}$$

where $\phi_{49} = q_0/(10^{49}$ photons $s^{-1})$, R_{14}=$R/(10^{14}$ cm), and d_{17}= $d/(10^{17}$ cm) is the distance between the ionizing source and the globule. In that case, $M/\dot{M}$ will provide an estimate for the photoevaporation time, which can then be compared with equation 1.25.

Smaller globules of gas mass on the order of solar mass would be destroyed completely even if they had internal gravitational collapse going on when the ionization front arrived. Most pillars or cometary globules are, however, observed to have masses of a few hundreds of solar masses. For them, the gravitational timescale is much shorter than the photoevaporation time which indeed favors a triggering scenario.

1.6 Radiative Processes

Radiative processes are the collection of physical processes by which a medium releases energy in the form of electromagnetic radiation. This involves the emission of photons by elementary particles, as the result of various interactions with other particles or fields. Continuum emission as a result of radiative processes can be both thermal and non-thermal. Thermal emissions include black-body radiation and thermal bremsstrahlung emission. Cyclotron, and synchrotron or magnetic bremsstrahlung radiations are examples of non-thermal emission. Additionally, there are spectral line emissions, which are the results of quantum transitions between energy levels in atoms, molecules, or ions. Almost anything

we know about the Universe is based on observations that are made via electromagnetic radiation received on earth (also the gravitational waves now). The vast range of electromagnetic radiation is a product of various radiative processes occurring in the interstellar medium and anywhere in the Universe. This makes the study of radiative processes important.

1.6.1 Radiative Transfer Equation

As light rays pass through matter in the ISM energy can both be added or subtracted to the medium by emission or absorption. The energy carried by individual rays is measured by the quantity *flux density* F which is defined as the infinitesimal energy dE per area element dA in the normal direction of the radiation per unit time dt. So, $dE = F\, dA\, dt$. However, rays of different frequencies carry different energies. Thus, a better way to express energy carried by rays of a particular frequency is to consider all rays in the infinitesimal frequency range $d\nu$ passing through dA in a direction perpendicular to dA within a solid angle $d\Omega$ in time dt. In this case,

$$dE = I_\nu\, dt\, dA\, d\Omega\, d\nu \tag{1.37}$$

I_ν is called the specific (monochromatic) flux density or the specific intensity or brightness which is measured in the units of ergs s^{-1} cm^{-2} sr^{-1} Hz^{-1}.

As a beam of light rays pass through a medium, specific intensity can change. Energy can be added to the beam via emission photons by the particles present in the medium. The spontaneous monochromatic emission coefficient j_ν is defined as the energy emitted per unit time per unit solid angle per unit volume per unit frequency, $dE = j_\nu\, dV\, d\Omega\, dt\, d\nu$. If a beam traverses a distance ds normal to its cross-section area dA, the volume it goes through will be $dV = dA\, ds$. The increase in the intensity of the beam will be

$$dI_\nu = j_\nu\, ds \tag{1.38}$$

The loss of intensity in a beam is measured by the absorption coefficient α_ν. Energy is absorbed by the particles in the medium and the change in specific intensity is given by

(Rybicki & Lightman, 1986)

$$dI_\nu = -\alpha_\nu \, I_\nu \, ds \tag{1.39}$$

Here, α_ν is positive when energy is lost from the beam.

The change in specific intensity along the direction of a ray, due to both emission and absorption, is given by the radiative transfer equation

$$\frac{dI_\nu}{ds} = -\alpha_\nu I_\nu + j_\nu \tag{1.40}$$

If we consider pure emission, i.e., $\alpha_\nu = 0$, the above equation has the solution

$$I_\nu(s) = I_\nu(s_0) + \int_{s_0}^{s} j_\nu(s')ds' \tag{1.41}$$

For $j_\nu = 0$ or only absorption, the transfer equation becomes $\frac{dI_\nu}{ds} = -\alpha_\nu I_\nu$. The solution to this is

$$I_\nu(s) = I_\nu(s_0)e^{-\int_{s_0}^{s} \alpha_\nu(s')ds'} \tag{1.42}$$

The combined transfer equation becomes much easier to solve if we make a variable transformation defined as $d\tau_\nu = \alpha_\nu ds$ where the new quantity τ_ν is called the optical depth of the medium. In this case,

$$\tau_\nu(s) = \int_{s_0}^{s} \alpha_\nu(s')ds' \tag{1.43}$$

In all of the above cases, the integration path is along the direction of light rays but the initial point s_0 is taken arbitrarily to make $\tau_\nu(s)$ at s_0 to be zero. Using this, the transfer equation 1.40 becomes

$$\frac{dI_\nu}{d\tau_\nu} = -I_\nu + S_\nu \tag{1.44}$$

where $S_\nu = \frac{j_\nu}{\alpha_\nu}$ is called the source function, a characteristic of the medium which the beam is passing through. From equation 1.44, it is evident if $I_\nu < S_\nu$ $\frac{dI_\nu}{d\tau_\nu} > 0$ and I_ν increases in the direction of the beam. I_ν decreases if $I_\nu > S_\nu$. This implies if the optical depth is high enough I_ν becomes the source function. Re-writing equation 1.44 as

$$\frac{dI_\nu}{d\tau_\nu} + I_\nu = S_\nu \tag{1.45}$$

and multiplying the equation by an integrating factor $\exp[\int_0^{\tau_\nu} d\tau_\nu] = \exp[\tau_\nu]$,

$$\begin{aligned}
&\frac{dI_\nu}{d\tau_\nu}e^{\tau_\nu} + I_\nu e^{\tau_\nu} = S_\nu e^{\tau_\nu} \\
&d(I_\nu e^{\tau_\nu}) = S_\nu e^{\tau_\nu} d\tau_\nu \\
&\int_0^{\tau_\nu} d(I_\nu(\tau'_\nu)e^{\tau'_\nu}) = \int_0^{\tau'_\nu} S_\nu(\tau'_\nu)e^{\tau'_\nu} d\tau'_\nu \\
&I_\nu(\tau_\nu) = I_\nu(0)e^{-\tau_\nu} + \int_0^{\tau_\nu} S_\nu(\tau'_\nu)e^{-(\tau_\nu - \tau'_\nu)} d\tau'_\nu
\end{aligned} \tag{1.46}$$

This is the general solution to the transfer equation. If we consider a constant source function, the solution becomes

$$I_\nu(\tau_\nu) = I_\nu(0)e^{-\tau_\nu} + S_\nu(1 - e^{-\tau_\nu}) \tag{1.47}$$

The ISM is filled with dust and particularly in the dense molecular clouds where stars are born. Dust particles contribute significantly to thermal radiation. Blackbody radiation is an important part of thermal radiation, particularly when the medium is in thermal equilibrium with itself. Matter particles are kept at a fixed temperature T and in an environment approximately in local thermodynamic equilibrium.

1.6.2 Local Thermodynamic Equilibrium (LTE)

Thermodynamic equilibrium is maintained in a medium if the matter within the medium satisfies the three following conditions,

1. Thermal equilibrium: no net heat transfer into or out of the medium
2. Mechanical equilibrium: no pressure gradient present in the system
3. Chemical equilibrium: forward and backward reactions have the same rate

For a global thermodynamic equilibrium, intensive parameters remain constant throughout the system. If the intensive parameters vary at a very slow rate in space and time, thermodynamic equilibrium in the immediate neighborhood of any point in the medium can be

assumed. This is often the case in interstellar gas and dust, the matter is in thermal equilibrium with itself but not necessarily with the radiation field through it. This is known as the local thermodynamic equilibrium (LTE). The molecules or atoms under thermal equilibrium follow the Maxwell-Boltzmann velocity distribution.

If we consider electronic, rotational, and vibrational transitions in atoms or molecules present in the medium that is in thermodynamic equilibrium, the transition rate from a lower state l to an upper state u, should be the same as that from the upper state to the lower state. If n_l and n_u denote number densities of particles in the lower and upper levels of transition respectively, the ratio is given by (Rybicki & Lightman, 1986),

$$\frac{n_l}{n_u} = \frac{g_l}{g_u} \exp\left(\frac{h\nu}{kT}\right) \tag{1.48}$$

The is the mathematical condition of LTE.

The temperature T characterises transitions (which is in equilibrium) in the medium and is constant. T is referred as the excitation temperature and denoted by T_{ex}. In this case $S_\nu = B_\nu(T_{ex})$.

1.6.3 Brightness Temperature and Flux Density

In order to make our further analyses simpler, we can replace the flux density or the specific intensity in equation 1.47 with a quantity called the brightness temperature, denoted by T_b. The advantage of this is having a simpler unit of Kelvin instead of erg s^{-1} cm^{-2} Hz^{-1} sr^{-1} and T_b indicates the physical property of the sources of emission. The brightness temperature $T_b(\nu)$ of an emitting source for a certain frequency is defined as the temperature of a black body that has the same specific intensity or brightness I_ν at that frequency. In other words,

$$I_\nu = B_\nu(T_b) \tag{1.49}$$

where

$$B_\nu(T) = \frac{2h\nu^3}{c^2} \frac{1}{\exp\left(\frac{h\nu}{kT}\right) - 1} \tag{1.50}$$

is the Planck function.

1.6.4 Continuum Emission

For objects without a background source, the radiative transfer equation associated with continuum emission can be written as

$$I_\nu = B_\nu(T)(1 - e^{\tau_\nu}) \tag{1.51}$$

Radio sources in astrophysics are generally categorized into two types, based on whether the emission mechanism is thermal or nonthermal. There are a number of mechanisms belonging to each category but we will discuss only a few of them.

- **Thermal Bremsstrahlung**

  In thermal Bremsstrahlung (German for "braking radiation") an electron is inelastically scattered from one free state to another free state when moving close to a much heavier ion. In such a process, electrons decelerate or are braked by positive ions and release continuum photons.

  In astrophysics, bremsstrahlung radiation indicates the presence of hot thermal plasma (temperature ranges from 10^3 to 10^8 K) where the ionized gas particles approximately follow Maxwell-Boltzmann velocity distribution. Such plasmas are found everywhere in the interstellar and intergalactic media, stellar atmospheres, and central regions in active galactic nuclei (AGN). Bremsstrahlung emission ranges from radio frequency up to x-rays. For example, an HII region surrounding a young massive star(s) is ionized by the UV photons from the star and the signature of the hot ionized gas is found in bremsstrahlung emission from the optical to the radio range. On the other hand, in galaxy clusters, the energy of electrons is high enough that they produce x-ray emissions when they are "braked" by the proton field.

  Although, bremsstrahlung can be non-thermal, we limit our discussion to thermal bremsstrahlung. For an electrons with a single speed v the total emission per unit

time per unit volume per unit frequency is given by (Rybicki & Lightman, 1986)

$$\frac{dW}{d\omega dV dt} = \frac{16\pi e^6}{3\sqrt{3}c^3 m^2 v} n_e n_i Z^2 g_{ff} \tag{1.52}$$

where the Gaunt factor g_{ff} is for quantum mechanical correction and given by,

$$g_{ff} = \frac{\sqrt{3}}{\pi} \ln\left(\frac{b_{\max}}{b_{\min}}\right), \qquad b_{\max} = v/\omega, \;\; b_{\min} = h/mv \tag{1.53}$$

For thermal bremsstrahlung, the ionized particles are assumed to have Maxwell Boltzmann distribution so the probability of a particle belonging to velocity range $(\mathbf{v}, \mathbf{v} + d^3\mathbf{v})$ is

$$dP \propto \exp\left(-\frac{mv^2}{2kT}\right) d^3\mathbf{v} = v^2 \exp\left(-\frac{mv^2}{2kT}\right) dv \tag{1.54}$$

Now we can compute the average emission over the speed distribution as a function of frequency and gas temperature using the statistical weight given by equation 1.54. For the range of integration we can not use $0 \leqslant v < \infty$ because the speed of the electrons should be able to produce photons of that frequency, which means $1/2mv^2 \geqslant h\nu$ or $v_{\min} = \sqrt{2h/m}$. Then the expression for the average emission becomes,

$$\frac{dW}{dV dt d\omega}(T, \omega) = \frac{\int_{v_{\min}}^{\infty} \frac{dW}{dV dt d\omega}(v, \omega) v^2 \exp\left(\frac{-mv^2}{2kT}\right) dv}{\int_0^{\infty} \exp\left(\frac{-mv^2}{2kT}\right) dv} \tag{1.55}$$

The integral in the denominator can be written in terms of gamma function if we substitute $t = \alpha v^2$ where $\alpha = m/2kT$,

$$\int_0^{\infty} \exp\left(\frac{-mv^2}{2kT}\right) dv = \frac{1}{2\alpha} \int_0^{\infty} \left(\frac{t}{\alpha}\right)^{1/2} e^{-t} dt = \frac{1}{2}\alpha^{-3/2}\Gamma(3/2) = \frac{\sqrt{\pi}}{4}\alpha^{-3/2}$$

The numerator can be simplified as,

$$\int_{v_{\min}}^{\infty} \frac{dW}{dV dt d\omega}(v, \omega) v^2 \exp\left(\frac{-mv^2}{2kT}\right) dv = \int_{v_{\min}}^{\infty} \frac{16\pi e^6}{3\sqrt{3}c^3 m^2 v} n_e n_i Z^2 g_{ff} v^2 e^{-\frac{mv^2}{2kT}} dv$$

$$= \frac{16\pi e^6}{3\sqrt{3}c^3 m^2 v} n_e n_i Z^2 g_{ff} \int_{v_{\min}}^{\infty} v e^{-\alpha v^2} dv = \frac{16\pi e^6}{3\sqrt{3}c^3 m^2 v} n_e n_i Z^2 g_{ff} \frac{e^{-\frac{h\nu}{kT}}}{2\alpha}$$

Combing the two, equation 1.55 becomes,

$$\frac{dW}{dV dt d\omega}(T, \omega) = \left(\frac{16\pi e^6}{3\sqrt{3}c^3 m^2 v} n_e n_i Z^2 g_{ff} \frac{e^{-\frac{h\nu}{kT}}}{2\alpha}\right)\left(\frac{1}{\frac{\alpha^{-3/2}\sqrt{\pi}}{4}}\right) = \frac{2^4 e^6}{3mc^3}\sqrt{\frac{2\pi}{3mk}} T^{-1/2} n_e n_i Z^2 g_{ff} e^{-\frac{h\nu}{kT}} \tag{1.56}$$

Finally, expressing in terms of frequency instead of angular frequency $\omega = 2\pi\nu$, total emission per unit time per unit volume per unit frequency is,

$$\frac{dW}{dVdtd\omega}(T,\nu) = \frac{dW}{dVdtd\omega}(T,\omega)J\left(\frac{\omega}{\nu}\right) = \frac{2^5\pi e^6}{3mc^3}\sqrt{\frac{2\pi}{3mk}}T^{-1/2}n_e n_i Z^2 \bar{g}_{ff} e^{-\frac{h\nu}{kT}} \quad (1.57)$$

where $\bar{g}_{ff} \equiv \bar{g}_{ff}(T,\nu)$ is the Gaunt factor averaged over speed.

In order to get the total power of thermal bremsstrahlung per unit volume is then given by (Rybicki & Lightman, 1986)

$$\frac{dW}{dtdV}(T) = \int_0^\infty \frac{dW}{dVdtd\omega}(T,\nu)d\nu = \left(\frac{2\pi kT}{3m}\right)^{1/2} \frac{2^5\pi e^6}{3hc^3m} Z^2 n_e n_i \bar{g}_B \quad (1.58)$$

where $\bar{g}_B = \int_0^\infty \bar{g}_{ff}(T,\nu)d\nu$. It is to be noted here for thermal bremsstrahlung emission, power $\propto n_e n_i T^{1/2}$ which implies the density of the plasma or HII region is more important than the temperature of the gas.

- **Synchrotron Radiation**

  Synchrotron radiation, also known as magnetic bremsstrahlung, is generated due to the relativistic motion of charged particles in a magnetic field. It is non-thermal in nature. Charged particles, mostly electrons, spiral around magnetic field lines at speeds close to that of light, they continuously change direction and as a result of such accelerated motion, they emit photons in narrow cones in the direction of motion. The resultant synchrotron spectrum is the combination of all emission spectra from individual accelerating charged particles.

  Individual charged particles (electrons) have frequencies depending on the speed of that electron at that instant and how fast it travels around the field lines. This is because $h\nu = \Delta E = \frac{p}{\sqrt{p^2 - m^2c^2}}\Delta p$. The flux density of synchrotron emission depends on the frequency through $S_\nu \propto \nu^\alpha$ producing a characteristic spectrum with α being called the spectral index for that particular emission. Observed α values are used for the identification of the sources that produced the emission.

Synchrotron emission is also polarized in the normal plane to the magnetic field lines. The angle of polarization is determined by the strength of the magnetic field.

- **Dust thermal emission**

  Interstellar dust plays a very crucial role in molecular clouds by acting as an efficient emitter of electromagnetic radiation and regulator of temperature. Dust grains are about the same size as the wavelength of blue light. This implies light passing through a dust cloud has its blue component absorbed, making the light appear redder. Additionally, dust grains absorb the excess amount of energy during H_2 molecule formation in a HI gas cloud, as well as absorb the energy of ionizing UV radiation from nearby stars. This way the dust grains keep the cloud cool and also re-emit the absorbed energy as IR radiation. This also makes dust clouds transparent to IR emissions.

  Hence, dust grains can be heated to temperatures between about 10 and 200 K, depending on several factors including the spectrum and intensity of the radiation field, the size and optical properties of the grains, etc. However, it is the cold dust grains ($\sim$ 10 - 30 K) that constitute most of the dust mass. At this temperature, the emitted radiation belongs to the sub-millimeter or far-infrared regime. Since dust grains serve as a great catalyst in molecular hydrogen formation, dust emission is also an excellent proxy for molecular hydrogen detection. Unlike the gas, the dust emission process is thermal, with a modified blackbody spectrum, given by equation 1.51.

  Since dust is optically thin for longer wavelengths, the specific intensity of dust thermal emission can be re-written as

$$I_\nu \approx B_\nu(T)(1 - 1 + \tau_\nu) = \tau_\nu B_\nu(T) \tag{1.59}$$

  where $\tau_\nu = \int \kappa_\nu \rho ds$ is the frequency-dependent optical depth of the cloud , ρ is the matter density, κ_ν is called the opacity at the frequency ν and the path of integration is along the line of sight. If the opacity remains constant along the propagation of

the ray, $\tau_\nu = \kappa\Sigma$, where Σ is the surface density of the dust cloud. In that case, the specific intensity of the dust emission becomes (Krumholz, 2015),

$$I_\nu = \kappa_\nu \Sigma B_\nu(T) \tag{1.60}$$

In many cases, resolved images of dust clouds are not available, and within reasons, a volume-averaged description of the opacity as a function of frequency is assumed: $\kappa_\nu \propto \nu^\beta$. Usually β lies in the range (1,2), with $\beta \sim 2$ at longer wavelengths and $\beta \sim 1$ at shorter wavelengths (Hildebrand, 1983).

- **Polarized emission and spinning grains**

  In addition to absorption and efficient emission of light rays passing through them, interstellar dust grain can also polarize light. This is because most dust grains are thought to have non-spherical geometry, in particular, dust grains are elongated. Starlight extinction efficiency depends on the grain's cross-section which is effectively higher along the longitudinal axis of an elongated grain than along the transverse or perpendicular axis. This means the electric component ($\vec{E}$) of light rays oscillating parallel to the longitudinal axis of grain will face a greater extinction than the rays with their electric components oscillating perpendicular to the long axis. In the ISM, transverse or the shorter axes of dust grains are also globally aligned with the large-scale magnetic field lines present. As a result, when unpolarized light waves (electric field vectors oscillating in random directions) pass through interstellar dust, part of the light waves, whose electric component vectors are aligned with the elongated dust grains (or the magnetic field lines), will get absorbed that and the transmitted light waves will become polarized with the $\vec{E}$ components parallel to the magnetic field.

  It is to be noted that, the absorbed light is re-emitted as thermal blackbody radiation, as we discussed in the previous section, preferentially along the longitudinal axes of the dust grains making the thermal dust emission polarized perpendicular to the

magnetic field.

Thermal and superthermal processes in the interstellar medium cause elongated dust grains to spin rapidly at angular frequencies ranging between 0.1 MHz and 10 MHz, sometimes in addition to the grains being electrically charged by interstellar ionizing UV radiation. If the (electric) dipole moment vector makes an angle with the spin axis, the dipole component perpendicular to the spin axis emits dipole radiation in microwave frequencies (10-100 GHz). This can be accompanied by magnetic dipole radiation if the grains are already ferromagnetic, due to high iron content, for example. The dipole emissions cause rotational damping which depends on the grain size. This leads to a distribution of spin rates of dust grains where the angular frequency follows a Maxwell-Boltzmann distribution (Draine & Lazarian, 1997).

The dipole emission of spinning grains also overlaps with the CMB radiation which peaks at 160.4 GHz, observed as a foreground component to the CMBR (Kogut et al., 1996).

1.6.5 Line Emission

- **Recombination lines**

  The process opposite to photoionization is radiative recombination, in which an energetic free electron is captured in a bound state n by an ion. A photon is released in the process, resulting in a discrete line emission of typical energy less than the photoionization energy of $h\nu = 13.6eV$, lines of higher wavelengths. The electron can further cascade down to lower energy states, all the way down to the ground state. In all such electron transitions, photons of specific frequencies are emitted producing a set of recombination lines. This is more evident, particularly in an environment where the photoionization rate is low, implying the time interval between two subsequent photoionizations of the same atom is longer than the electronic down transition time steps. Even when the photoionization rate is significant, recombination lines are

still produced because electrons often recombine into an excited state rather than the ground state. This results in the release of photons with $h\nu << 13.6eV$ that cannot ionize another atom.

Later stages of Strögren sphere expansion, the HII region in rim between ionization front and the shock front produces recombination lines (section 1.1.3). Another example might be planetary nebulae which are much older than the usual HII regions and are visible in radiative recombination lines (Wilson et al., 2013). The most common recombination emissions are Hα (656 nm) and Hβ (486 nm) visible spectral lines in the Balmer series which are produced by the electronic transitions 3$\rightarrow$ 2 and $4 \rightarrow 2$ in the hydrogen atom. Other prominent examples include Paschen α ($4 \rightarrow 3$) and β ($5 \rightarrow 3$) producing 1.87 microns and 1.28 microns in the infrared spectra.

HII regions are found around young massive stars (10-20 $M_{\odot}$), as well as at the sites of triggered star formation. Like molecular gas, HII regions have a (positive) spatial correlation with star formation. Since radiative recombination lines are directly related to ionized hydrogen gas, these spectral lines can work as an excellent tracer of star-forming regions. Observed line strength or luminosity can be used to compute recombination rate in the HII region, by equating which to the photoionization rate can lead to obtaining photon flux from the source and spectral type of the star or cluster.

- **Molecular emission lines**

  Suppose $I_{\nu}(0)$ denotes specific intensity coming from an arbitrary reference point along a line of sight that only contains some background intensity and I_{ν} denotes specific intensity along a line of sight that has the molecular line source of interest. Since the background intensity is present in all directions, spectral line intensity is often measured after subtracting the pure background intensity from that along the

molecular line. In other words(Mangum & Shirley, 2015),

$$\Delta I_\nu = I_\nu - I_\nu(0) = I_\nu(0)e^{-\tau_\nu} + S_\nu\,(1 - e^{\tau_\nu}) - I_\nu(0) \tag{1.61}$$

Since we are considering LTE, $S_\nu = B_\nu(T_{ex})$. Furthermore, owing to equation 1.49 we can replace I_ν with $B_\nu(T_{bg})$, where T_{bg} is the equivalent temperature of the background emission. Then, the above equation can be written as,

$$\Delta I_\nu = [B_\nu(T_{ex}) - B_\nu(T_{bg})]\,(1 - e^{\tau_\nu}) \tag{1.62}$$

At this point, we define two quantities (Mangum & Shirley, 2015). The first one is the Rayleigh-Jeans equivalent temperature given by,

$$J_\nu(T) = \frac{h\nu/k}{\exp\left(\frac{h\nu}{kT}\right) - 1} \tag{1.63}$$

and the second one is the radiation temperature which is the equivalent observable temperature of the source, given by

$$T_R = \frac{c^2}{2k\nu^2}\Delta I_\nu \tag{1.64}$$

It is easy to see that $B_\nu(T) = \frac{2k\nu^2}{c^2}J_\nu(T)$. Then, substituting I_ν from equation 1.62 in equation 1.64,

$$\begin{aligned} T_R = \frac{c^2}{2k\nu^2}[B_\nu(T_{ex}) - B_\nu(T_{bg})]\,(1 - e^{\tau_\nu}) &= \frac{c^2}{2k\nu^2}\left[\frac{2k\nu^2}{c^2}J_\nu(T_{ex}) - \frac{2k\nu^2}{c^2}J_\nu(T_{bg})\right](1 - e^{\tau_\nu}) \\ &= [J_\nu(T_{ex}) - J_\nu(T_{bg})]\,(1 - e^{\tau_\nu}) \end{aligned} \tag{1.65}$$

- **21 cm emission**

  The 21 cm line emission is the prime characteristic of neutral hydrogen gas (HI) ubiquitous to the interstellar and intergalactic space. Cold HI gas in the ISM do not possess enough energy to be detected in optical bands through electronic transitions. It is rather detected via a rotational transition of the electron in HI atom, called the spin-flip transition, which emits radio waves.

This transition occurs between hyperfine structure levels of HI atom, namely from the state $1s^2, l_0, S_{+1/2}$ to $1s^2, l_0, S_{-1/2}$. The spin of the only electron in a neutral hydrogen atom can be either parallel or anti-parallel with that of the proton. When the spin of the electron is aligned with the proton the atom has slightly higher energy. The electron can spontaneously flip its spin to be misaligned with the spin of the proton and as a result transition to a lower energy state. The very small amount of energy released in this spin-flip transition is emitted as a photon of a precise wavelength of 21 (or 1420.2 MHz frequency) cm which is detected as long radio waves. Although the spontaneous transition occurs on a 10 Myr timescale, HI gas is the most abundant species in the ISM. This means despite the probability of spin-flip transition being very low, the overall high volume of the gas makes the detection possible.

1.7 Observations

1.7.1 Heterodyne observation of spectral lines

Heterodyning is a digital signal processing (analogue as well) technique that combines (mixes) two frequencies and creates a new frequency. The two input frequencies are mixed in a nonlinear signal-processing unit or a *mixer* (diode, transistor, vacuum tube, etc.). This mixing produces two frequencies, generally termed heterodynes, which are stronger and easier to process than the weak input signal received at the antenna. A major application of this is the superheterodyne radio receiver circuit, which is used in all modern radio telescopes for observing molecular spectral lines at high resolution.

Radio signals detected at a radio telescope are considered superpositions of simple harmonic functions of time. In addition, signals are represented as stationary random processes $x(t)$ (stationary time series). Different values of $x(t)$ from a random process that acts on the signal at the detector (raw observational data) at different times. The similarity between observations is measured statistically using the Autocorrelation function (ACF) which depends on the time lag between two realizations of the time series. The ACF is defined by

$R_T(\tau) = \mathscr{E}[x(t-\tau)x(t)]$ where $\mathscr{E}[x]$ denotes statistical expectation and τ is the time-lag between signals detected (sampled). Here T denotes the time period of signal detection or sampling. Stationarity implies

$$R_T(\tau) = \mathscr{E}\left[x(t-\tau)x(t)\right] = \mathscr{E}\left[x(s)x(s+\tau)\right]. \tag{1.66}$$

Moreover, using the Weinner-Khinchin theorem total power of any physical signal can be described as a distribution of the frequency components composing the signal,

$$R(\tau) = \int_{-\infty}^{\infty} S(\nu) e^{2\pi i \nu \tau} d\nu \tag{1.67}$$

where

$$S(\nu) = \int_{-\infty}^{\infty} R(\tau) e^{-2\pi i \nu \tau} d\tau \tag{1.68}$$

This is simply a Fourier transform pair of the signal ACF $R(\tau)$ and the *Power spectral density (PSD)* $S(\nu)$. PSD describes the spectral energy distribution per unit time at a given frequency. The final output PSD can be interpreted as spectral line data or the spectral energy distribution of a continuum, which depends on whether the backend of the particular instrument (called a *receiver*) is connected to a spectrometer or a continuum bolometer.

Figure 1.10 illustrates the main components of a typical superheterodyne receiver. The leftmost part denotes the physical signal arriving at the receiver. The rightmost part has two possible options. In this section, we focus on the component shown at the bottom (sampler). There are three major components of signal processing for spectral line data, namely, amplification, mixing, and sampling. A radio receiver should be able to detect the faintest signal. The input signal produces an output voltage as a function of time which is amplified before it passes through the mixer. In the mixer, The input band is mixed with a monochromatic stable signal produced locally (*Local Oscillator*) to create a lower (intermediate) frequency (IF).

One way to do this is using the non-linear relation between current produced and input voltage. $I = \alpha U^2$. If we denote the frequency of the input signal by ν_S and that from

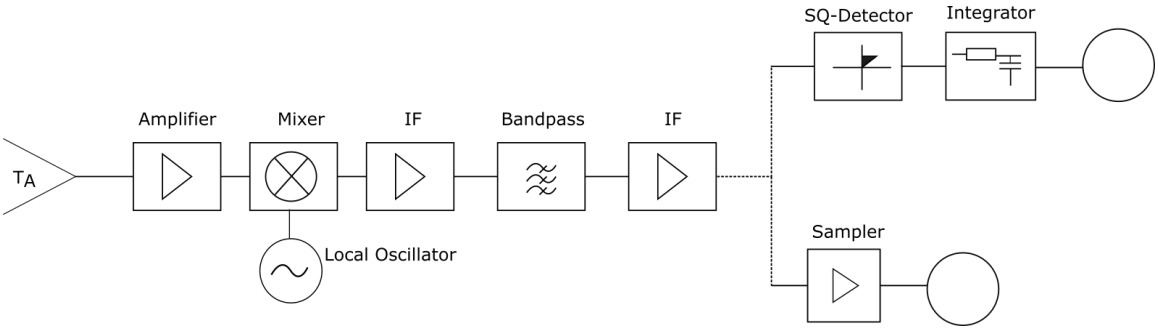

Figure 1.10: a schematic showing the main parts of a heterodyne receiver (*partly adapted and modified from Wilson et al. 2013*).

the local oscillator by ν_L, U be the sum of input signal and that from the local oscillator, $U = E\sin(2\pi\nu_S + \delta_S) + V\sin(2\pi\nu_L + \delta_L)$, δ denoting the phase of the corresponding signal, the output signal can be written as (Wilson et al., 2013),

$$\begin{aligned} I &= \alpha[E\sin(2\pi\nu_S t + \delta_S) + V\sin(2\pi\nu_L t + \delta_L)]^2 \\ &= \frac{1}{2}(\alpha E^2 + V^2) - \frac{1}{2}\alpha E^2\sin(4\pi\nu_S t + 2\delta_S + \frac{\pi}{2}) - \frac{1}{2}\alpha V^2\sin(4\pi\nu_L t + 2\delta_L + \frac{\pi}{2}) \\ &+ \alpha EV\sin[2\pi(\nu_S - \nu_L)t + (\delta_S - \delta_L + \frac{\pi}{2})] - \alpha EV\sin[2\pi(\nu_S + \nu_L)t + (\delta_S + \delta_L + \frac{\pi}{2})]. \end{aligned} \tag{1.69}$$

It is to be noted that the output is a superposition of components of different frequencies, also referred to as image frequencies. The difference and sum of signal and LO frequencies are called the lower sideband (LSB) and the upper sideband (USB). Also, the amplitudes are proportional to the first power of the input signal.

All output components except for the one with $\nu_{IF} = \nu_S - \nu_L$ is suppressed using an appropriate bandpass filter in a single sideband (SSB) receiver which is the case in a heterodyne spectrometer. This is because for spectral line measurement the line is usually in one sideband and the other sideband in that case becomes a source of extra noise. Mixers that allow both sidebands are used in single-dish continuum measurement since both sidebands contain the desired signal.

For a practical receiver in which the backend is a digital autocorrelation spectrometer, the receiver has to be an SSB since the frequency channel width (resolution) $\delta\nu$ is very small and only one of the sidebands contains the PSD information of the spectral line

radiation. The desired spectral density outcome can be achieved in two ways. The receiver backend is designed for this purpose and can either be a digital Fourier spectrometer or an autocorrelation spectrometer. They are equivalent in terms of producing the power spectral density of the received signal.

As shown earlier in this section, Fourier analysis of a signal can be done considering the signal as a time series $\{y(t)\}$ (represents the IF signal in this case),

$$V(t) = \int_{-T/2}^{T/2} y(t) e^{-2\pi i \nu t} dt$$

T denotes total time of signal integration. This in turn, is squared in terms of mean-square expectation value given by (Westpfahl, 1999)

$$\mathscr{E}_T[|V(\nu)|^2] = \mathscr{E}_T[V(\nu) * V(\nu)] = \mathscr{E}\left[\int_{-T/2}^{T/2}\int_{-T/2}^{T/2} y(s)y(t)e^{-2\pi i\nu(t-s)} ds\ dt\right]$$

The power spectral density is defined by,

$$S(\nu) = \lim_{T\to\infty} \frac{1}{T}\mathscr{E}_T[|V(\nu)|^2] \tag{1.70}$$

Using equation 1.66 it can be shown that PSD defined above is equivalent to that defined using the Wiener-Khinchen theorem (equation 1.68).

For a real receiver, the limit $T \to \infty$ leads to a non-existent Fourier transform, and sampling must be done. This amounts to measuring the continuous signal $\{y(t)\}$ every Δt seconds and the sampled signal becomes a discrete time series $\{y(n\Delta t)\}, (n = 0, 1, 2, ..)$ where Δt is referred as the sampling period or the sampling interval. Consequently, $f_s = 1/\Delta t$ is called the sampling frequency or the sampling rate. In order for the sampled signal to faithfully represent the physical signal, a receiver has to follow the *Nyquist sampling* which means the sampling rate must be greater than twice the highest frequency B in the observed band,

$$\begin{aligned} B &< f_s/2 \\ \text{or, } \Delta t &< \frac{1}{2B} \end{aligned} \tag{1.71}$$

Hence, the Fourier transform defined above changes to a discrete-time Fourier transform $V(t) = \lim_{T\to\infty} \int_{-T/2}^{T/2} y(t)e^{-2\pi i\nu t}dt \approx \sum_{n=-\infty}^{\infty} \Delta t\, y(n\Delta t)\, e^{-2\pi i\nu n\Delta t}$ and is carried out using a finite series fast Fourier transform (FFT) defined as (Westpfahl, 1999),

$$V(\nu) = \sum_{n=0}^{N-1} y_n e^{-2\pi i\nu n/N} \tag{1.72}$$

where $y_n,\ n = 0(1)N$, denotes the ordinates of the signal sampled at time intervals Δt.

Finally, the PSD defined in equation 1.70 is obtained using specific FFT spectrometers connected to the backend of heterodyne receivers and is saved as a spectral distribution over a narrow band (velocity channels) of the observed line for spectral analysis.

1.7.2 Continuum emission

The top branch in the rightmost segment of the schematic diagram in figure 1.10 represents the working of a continuum receiver or a *bolometric radiometer*. In this case, the receiver has a double sideband operation (DSB) since, for continuum measurements, both side bands contain information. The bandpass allows signals from both upper side band (LSB) and lower side band (USB) components $\alpha EV\sin[2\pi(\nu_S - \nu_L)t + (\delta_S - \delta_L + \frac{\pi}{2})]$ and $\alpha EV\sin[2\pi(\nu_S + \nu_L)t + (\delta_S + \delta_L + \frac{\pi}{2})]$ as a linear combination of both. This makes the output signal broadband. This signal passes through a square-law detector defined by $y(t) = ax(t)^2$. The ACF of the output signal is $R_y(t) = a^2[R_x^2(0) + 2R_x^2(\tau)]$ (τ being the time lag of the ACF). Using Wiener-Khinchin theorem, the power spectral density can be written as (Wilson et al., 2013)

$$S_y(\nu) = a^2R_x^2(0)\delta(\nu) + 2a^2 \int_{-\infty}^{\infty} S_x(\nu')S_x(\nu - \nu')d\nu' \tag{1.73}$$

Clearly, the output power density is of the order of the second power of the input power density. The next component of the receiver, the integrator computes the time average of the power density over the frequency band over measurement period.

Finally, the operation of a bolometer is similar to an R-C circuit. The incident power causes an increase in its temperature which results in a change in the resistance R of an

absorptive element present in the bolometer, usually a thin layer of metal. This temperature variation measures the intensity of the radiation or in this case, the absorbed power of the output signal. The absorbed power raises the bolometer temperature which is connected to a heat sink kept at a constant temperature T_0 to $T_0 + \Delta T$. This temperature response to absorbed power depends on other properties of the bolometer, such as thermal capacity $\mathscr{C}$ and thermal conductance $\mathscr{G} \sim 1/R$ (Wilson et al., 2013)

$$|\Delta T| = \frac{P_0}{\mathscr{G}\sqrt{1 + (2\pi\nu_{\rm IF}\tau)^2}} \tag{1.74}$$

where $\tau = \mathscr{C}/\mathscr{G}$, and P_0 denotes the (average) power input. This thermal effect has a weak dependence on the signal frequency which makes bolometers essentially a broadband unit for producing a spectral distribution of continuum emission.

1.7.3 Facilities

- **JCMT**

  The James Clerk Maxwell Telescope (JCMT) situated at the summit of Mauna Kea in Hawaii is the largest single-dish (15 m in diameter) sub-mm radio telescope in the world. The active research fields using the JCMT data include solar system studies, star formation, galaxy evolution, and cosmology.

  The current JCMT receivers have an IF of 4 GHz (RxA) or 5 GHz (HARP). JCMT is capable of detecting both continuum and line emissions. The Heterodyne Array Receiver Program (HARP) istrument on JCMT is a spectral line heterodyne receiver. It has 16 independent detectors in a 4×4 array that can be tuned between 325 and 375 GHz, with a spatial resolution of 30″ and velocity resolution of 55 m s^{-1}. The Auto Correlation Spectral Imaging System (ACSIS) is a digital autocorrelation spectrometer used as the backend for HARP. The target molecular spectral lines include ^{12}CO($J = 3 \rightarrow 2$), ^{13}CO($J = 3 \rightarrow 2$), C^{18}O($J = 3 \rightarrow 2$), ^{12}CS($J = 7 \rightarrow 6$), HCN($J = 4 \rightarrow 3$) etc. The second heterodyne instrument RxA (bandwidth 211-272

GHz) was for spectral lines ^{12}CO($J = 2 \rightarrow 1$), ^{13}CO($J = 2 \rightarrow 1$), C^{18}O($J = 2 \rightarrow 1$), ^{12}CS($J = 5 \rightarrow 4$), HCN($J = 3 \rightarrow 2$), but was retired in 2018.

Sub-millimetre Common-User Bolometer Array 2 (SCUBA-2) is the JCMT instrument for mapping continuum emission, with 4 32×40 arrays of detectors. The receiver is tuned at 450μm and 850 μm simultaneously. In addition, there is POL-2, a linear polarimeter attached to SCUBA-2 detectors, designed for measuring magnetic field strength and orientation.

- **Herschel**

  Herschel Space Observatory was part of the Horizon 2000 program primarily operated by the European Space Agency (ESA). It was a space-based telescope working in sub-mm and far-infrared wavelengths, operating between 2009 and 2013. *Herschel* had a detection range of 60-670 μm which made it possible to produce observations related to dust-obscured objects and cold objects not observed previously. The mission objective of *Herschel* included, non exhaustively, investigation of the formation and evolution of galaxies, galactic and extra-galactic star formation and stellar-ISM interaction, planet atmosphere, and comets in the solar system. The space telescope had three major instruments on board, SPIRE and PACS both photometers, and a high-resolution heterodyne spectrometer HIFI.

  Photodetector Array Camera and Spectrometer (PACS) was primarily a photometer with an associated low resolution ($\sim$ 150 km s^{-1}) spectrometer. PACS, when operational in photometry mode, was capable of observing either in 60-90 μm or 90-130 μm simultaneously with the band 130-210 μm. Spectral and Photometric Imaging Receiver (SPIRE) was capable of observing in three bands centering at 250, 360, and 520 μm. The third instrument was Heterodyne Instrument for the Far Infrared (HIFI), a spectrometer with a velocity resolution much higher than PACS and SPIRE. HIFI detectors had an emission range of 157-625 μm covered by seven bands, with the

highest range of velocity resolution of 90-54 m s^{-1} (source: *herschel*-caltech.edu).

- **Spitzer**

  The Spitzer Space Telescope or the SST is a space-based telescope operated in infrared bands from 2003 to 2020. Spitzer has three major instruments, namely, IRAC, IRS, and MIPS. The infrared Array Camera (IRAC) is capable of observing four bands centering at 3.6, 4.5, 5.8, and 8 μm simultaneously. An infrared Spectrograph (IRS) is a spectrometer that has the observing wavelength ranges of 5.3-14 μm, 14-40 μm, 10-19 v, and 19-37 μm. The last two modules have much higher resolution than the first two. Multiband Imaging Photometer for Spitzer (MIPS) can detect three emission bands centering at 24, 70, and 160 μm.

  One of the prime missions is the Cygnus X Spitzer Legacy, a survey of 24 degree^2 regions of Cygnus X, using the IRAC bands and MIPS 24 and 70-micron bands. Mission objectives included analysis of high mass protostellar evolution, significance stellar clustering in high mass star formation, low mass star formation in large molecular clouds affected by nearby O/OB associations, production of an unbiased survey of Cygnus X to be investigated along with other studies (Beerer et al., 2010).

  Among other missions, the Galactic Legacy Infrared Mid-Plane Survey Extraordinaire, or GLIMPSE, is an infrared survey of the inner Milky Way galaxy covering a region of 300 degree^2, using the IRAC bands, and MIPSGAL covering 278 degree^2 area of the same using the MIPS instrument (Churchwell et al., 2009).

- **Hα observatories**

  The first transition in the Blamer series (3→2) of electronic transition in the hydrogen atom, produces Hα or 656.28 nm visible (red) spectral line. In HII regions, ionization releases free electrons which radiatively recombine with the ions, in a cascading manner down the electronic energy levels. This process releases Hα lines half of the time. This is why Hα is the most common way to observe and resolve HII regions.

One of the astronomical observatories for Hα map is the Wisconsin H-Alpha Mapper (WHAM), used for studying wide-spread, diffuse optical emission from the warm ionized hydrogen in the ISM (Madsen et al., 2001). This program is run by the University of Wisconsin–Madison. It is a 0.6 m optical telescope located in northern Chile.

Using the Isaac Newton Telescope (INT), a 2.54 m optical telescope in the Canary Islands, Spain, the INT Photometric H-Alpha Survey (IPHAS) maps the all of northern plane of the Milky Way within the latitude range of $-5^\circ < b < 5^\circ$. The survey uses two broad-band filters and a narrow H-alpha filter (centered at 656.8 nm with a bandwidth of 9.5 nm) of resolution $1''$ to obtain deep images of many targets, including low-mass young stellar objects, Be stars, rapidly evolving post-AGB stars, hydrogen-rich white dwarfs, HII regions, main-sequence A stars, and compact planetary nebulae (Corradi et al., 2008; Sale et al., 2014).

- **DRAO-ST**

  The Synthesis Telescope at the Dominion Radio Astrophysical Observatory (DRAO-ST) is a ground-based aperture synthesis radio telescope located in the Okanagan Valley, Canada. DRAO-ST can perform moderate resolution ($1'$) observations at the 21-cm spectral line as well as in radio continuum emission in two bands centering at 408 MHz and 1420 MHz, with its seven antennas of variable separations and with the aid of three digital correlator systems S21, C21, and C74 which match the signal delay time among the receivers. The main focus of the telescope is galactic and extragalactic objects including the ISM (Landecker et al., 2000), the Canadian Galactic Plane Survey (CGPS) is among the most significant surveys produced by DRAO-ST.

  The 21-cm HI spin-flip transition line comes from neutral hydrogen gas and the 1420 MHz and 408 MHz radio continuum from thermal bremsstrahlung and synchrotron

emission in the ionized gas in the interstellar medium. The Synthesis Telescope can observe the two continuum bands and the spectral line simultaneously and hence can map the two major components of the ISM, namely, the atomic hydrogen gas and HII regions. The angular resolution of the synthesis telescope is comparable to VLA, for example, but it produces significantly better performance compared to single antenna telescopes. Particularly, the $1'$ resolution becomes equivalent to 0.6 to 3 pc at for survey planes at 2 to 10 kpc, which proves valuable for studying detailed filamentary structures in the galactic plane and at high latitudes (Landecker et al., 2000). A continuum image produced by DRAO-ST as part of the Canadian Galactic Plane Survey (Taylor et al., 2003a) is in figure 1.13 (section 1.7.1) showing some of the important features in the local arm (Orion spur) and also objects along the line of sight that belongs to a further spiral arm of the galaxy.

1.8 Molecular Outflows

As it was mentioned in section 1.2, during the protostellar phase, collapsing cores launch molecular outflows. Protostellar accretion is characterized by two features, disk formation and the launch of outflowing gas in opposite directions orthogonal to the protostellar disk. Outflow activity can vary and there can be several 'active' and quiescent periods during the existence of the class 0/I phase. Outflows can emit a range of wavelengths, from radio to ultraviolet. In this section, I focus on the molecular component of outflows that is typically observed in spectral line emissions from rotational molecular transitions. Outflows are bipolar, massive, and wide-angled. They can inject a significant amount of momentum and energy into the surrounding cloud. For this reason, the outflow-cloud interaction is an active area of research and one of the objectives of this work.

Fast-moving collimated jets and low-velocity, wide-angled outflows exist in the very early phases of protostellar formation. The collimation factor (length/width) can be as low as 3 (slow-moving molecular outflows) and exceeding 20 (fast-moving jets) (Arce et al., 2010). Outflows consist of molecular gas around the core, that is pushed outward by matter (jets) ejected by the spinning core (Krumholz, 2015). Although jet velocities can range between 100 and 300 km s^{-1} (Bodenheimer, 2011), the molecular outflows themselves are much slower moving ($\sim$ 10 km s^{-1}) (Krumholz, 2015). However, due to their large masses, these slow-moving components carry most of the outflow momentum.

Bipolarity implies that outflows have two (usually symmetrical) lobes of molecular gas moving away in opposite directions from the rotating central object (YSO). Unless they are perpendicular to the line of sight on the plane of the sky, they are observed as blue- and red-shifted lobes due to Doppler shift. Like the disks, how protostars power up the bipolar molecular outflows is an active topic of research. The protostar-accretion disk system loses mass and momentum through jets and outflows. This gives rise to the possibility, as suggested by Königl (1991) and Shu et al. (1994), that the surplus amount of momentum that is transferred from the cloud to the disk, is centrifugally transported out of the disk

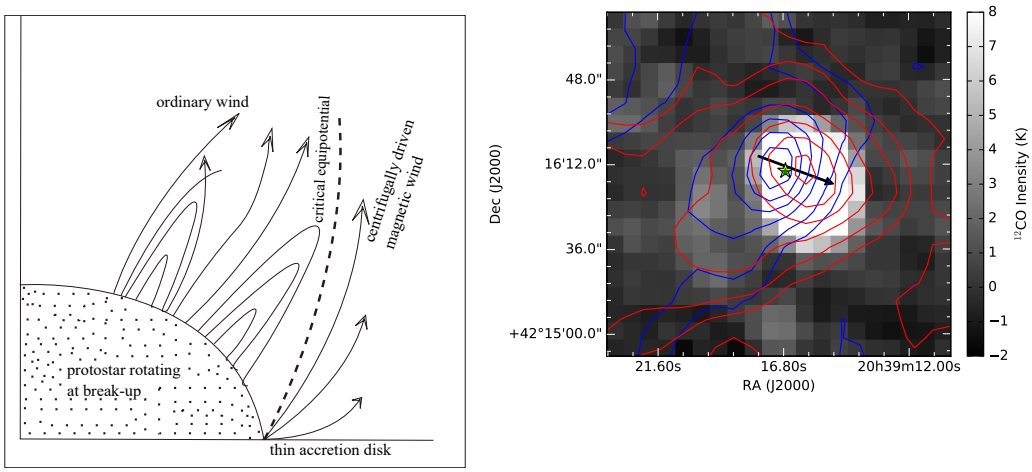

Figure 1.11: *Left*: Magnetically driven wind and outflow generation. The effective potential is zero on the surface of the critical equipotential line. Outside this line, gas flows away from the disk-protostar system creating a molecular outflow (*adapted from Shu et al. 1994*). *Right*: ^{12}CO(3-2) line emission reveals the blue- and red-shifted components of an outflow in Cygnus X. The location of the infrared source (protostar) is shown as a green star as found in the catalouge of Kryukova et al. (2014a).

under the influence of magnetic field present in the cloud. This magnetic field can be either primordial or generated by the central protostar.

The precise origin of outflows and jets from a protostar-disk system is still not completely clear, but it is generally accepted that the process involves a dynamical interaction between the protostar-disk magnetic field and accretion (Frank et al., 2014). One model suggests the launch is the result of the combined influence of gravitational potential of the central protostar, centrifugal potential arising from the rotation of the disk, and magnetic field lines passing through the disk (Krumholz, 2015). These field lines, denoted by $\mathbf{B} = (B_R, B_\phi, B_z)$ (cylindrical coordinates), are assumed to be going out of the plane of rotation without looping back.

We consider the motion of a fluid element, launched at a radius R_0 on the disk, in a reference frame rotating at the same angular speed as a central protostar. Since the disk rotation is Keplarian, this angular speed is given by $\Omega = (GM_*/R_0)^{1/2}$, M_* being the mass of the protostar. If the position of this displaced element is (R, z) in this frame, the gravitation

potential is given by

$$\psi_g = -\frac{GM_*}{\sqrt{R_0^2 + z^2}}$$

and the centrifugal potential (due the frame of choice) by,

$$\psi_c = -(1/2)\Omega^2 R^2 = -(1/2)GM_*\frac{R^2}{R_0^2}.$$

Combining the two, total potentials at (R, z) is

$$\psi = -\frac{GM_*}{R_0}\left[\frac{1}{2}\left(\frac{R}{R_0}\right)^2 + \frac{R_0}{\sqrt{R^2 + z^2}}\right] \tag{1.75}$$

Then the force on the fluid element can be calculated using $\mathbf{F} = -\nabla\psi$ (Krumholz, 2015).

The magnetic field in the rotating frame makes an angle θ with disk plane, where $cos\theta = \frac{B_R}{\sqrt{B_R^2+B_z^2}}$. If the fluid element is displaced by an infinitisimal distance ds from the starting point $(R_0, 0)$ to the new position $(R = R_0 + \cos\theta ds, z = \sin\theta ds)$, the force component in the direction of magnetic field lines is given by(Krumholz, 2015)

$$dF_{\mathbf{B}_{(R,\phi)}} = \frac{GM_*}{R_0^3}(3\cos^2\theta - \sin^2\theta)ds. \tag{1.76}$$

For $\theta < 60^0$, this component is positive. This implies a complex geometry of closed and open magnetic field lines leading to outflow generation. The open field lines making an angle below 60^0 will cause a magnetically driven wind of gas pushed by centrifugal force, which will result in the observed wide-angled molecular outflow in opposite directions. The situation is illustrated on the left of Figure 1.11.

Molecular outflows as protostellar feedback can impact the internal dynamics of its host cloud. The energy injection into the cloud can disrupt local gas as well as contribute to the large-scale turbulence energy support in a giant molecular cloud (GMC). Although the importance of the outflow feedback is disputed in the literature (Henning, 1989), outflow energy injection can be a significant source of local turbulence driving force (Matzner & McKee, 2000). Also, since molecular outflows are always associated with protostars in the initial phase, outflows are essential in studying the accretion history of the star formation

process Arce et al. (2010). The accretion efficiency of the infalling mass can be measured as accretion power, which depends on the mass of the central object (protostar), rate of infalling mass, and the inner disk radius or the protostellar radius: $L_{\rm acc} \approx GM_{\rm ps}\dot{M}_{\rm ps}/R_{\rm ps}$. A fraction of this power drives outflows and returns matter and energy to the cloud, which, depending on the outflow driving efficiency and then the mass of the accreting material, can be large. The contribution of outflow kinetic energy relative to the total cloud turbulence energy may depend on the length-scale associated. Although older outflow studies mostly focused on outflow feedback on its immediate surroundings, more recent observations have been able to study outflow interactions at a wider range of length scales. In particular, there might be 3 scales of interest, namely, disk scale $\sim 0.1 - 10^2$ AU, envelope scale $\sim 10^2 - 10^5$ AU, and cloud scale $\sim 10^5 - 10^6$ AU (Frank et al., 2014).

The disk scale is where accretion happens and planets form. Energy driven from outflow feedback can thus greatly impact the initial masses of the (proto)planets. The envelop scale is of the order of the distance between two protostars. The energy from the outflow can disperse the gas around the accreting protostar hence lowering the final stellar mass. This is measured by the core-to-star efficiency. Outflow interaction with the gas determines the value of the efficiency. Envelop destruction leads to lower core-to-star efficiencies, hydrodynamic simulations indicate about 30% to 50% (Frank et al., 2014; Machida & Hosokawa, 2013).

The cloud scale is essentially a parsec scale since the typical distance between two protostars forming in a cluster is of the order of 1 pc $\approx 2 \times 10^5$ AU. Whether the energy from outflows is relevant on this scale can be verified by noting that within the protostellar time-scale (~0.1 Myr) fast-moving, collimated jets (~200 km/s) can carry momentum up to $\sim$ 20 pc. For slower-moving outflows $\sim$ 20 km/s, this can reach up to 2 pc. Parsec-scale outflow feedback is feasible. At this scale, turbulence energy in the cloud becomes relevant. For this reason, a number of studies have focused on the relative contribution of outflow feedback towards the cloud turbulent support against gravitational collapse. Turbulence

in molecular clouds or in GMCs is supersonic and dissipates quickly, on the order of one crossing time, defined by, $T_{\rm cross} = \ell/\sigma_v$, where σ_v is the average velocity dispersion in a cloud of size ℓ (Stone et al., 1998). This is why turbulence requires constant energy injection. Also, turbulence energy transfer cascades down on length-scale, from GMC to parsec scales. At smaller scales, supersonic turbulence in cloud cores is capable of driving local and isolated star formation by rapidly creating density fluctuations via shocks, which can provoke gravitational collapse. Since turbulence, at these scales, dissipates on time scales that are comparable to but shorter than the free-fall time, this can in turn further facilitate star formation. The presence of turbulence in the later phase of collapse (e.g., due to outflow feedback in the neighborhood) otherwise could have disrupted the process. So, outflow feedback may have greater significance at smaller scales, by determining local star-forming efficiency. Wang et al. (2010) showed that high-mass star formation is driven by accretion at larger scales, which implies that in a stellar cluster outflow feedback from lower mass protostars can disrupt accreting material in the nearby molecular gas deposit that is essential for further accretion of the high-mass star. This can lead to lower Star formation efficiency (SFE) and lower masses of individual stars in the cluster.

1.9 Cygnux X

1.9.1 Overview

The process of star formation is among the most important factors influencing the structure and evolution of a galaxy. This process, however, is itself influenced by several factors within the galaxy. As discussed earlier in this chapter, the triggering effects of massive stars are among the most important external forces that constantly re-shape molecular clouds in the ISM and promote new generations of star formation. In order to develop a model of triggered star formation, we must choose a region, possibly nearby, where different phases of the ISM are observed, a region that is gas-rich, particularly molecular hydrogen, and has sources of shockwaves and ionizing radiation that cause triggering.

In the Milky Way galaxy, there are a number of gas-rich complexes that also are sites for large clusters of young massive stars. We have studied a specific region, called Cygnus X, within a $\sim 7^\circ \times 7^\circ$ field of view approximately centered at $20^h\ 31^m$, $+40^\circ 20'$, located in the Cygnus constellation in the local arm (Orion Spur) of the Milky Way galaxy (figure 1.12), near the galactic tangent at $l = 80^\circ$. Cygnus X, being at a distance of about 1.4 kpc from the sun, is one of the richest known regions of star formation in the galaxy and fulfills all of the above criteria. The name "Cygnus-X" was first assigned by J.H. Piddington and H. C. Minnett in 1952 who detected Cygnus X for the first time. 'X' stands for "extended", in order to distinguish it from the powerful radio galaxy Cygnus A. At the time, the authors found Cygnus X to be the first "radio nebula" detected. They identified the radio emission in Cygnus X as being from clouds of ionized interstellar gas (Piddington & Minnett, 1952). Additionally, their location and size estimates are close to those in modern observations.

Cygnus X contains as many as 800 distinct HII regions, a number of Wolf-Rayet and O stars and several OB associations, and Cygnus Rift in the foreground, a dark lane of interstellar matter that obscures the stars behind it. Cygnus X is among the largest molecular gas reserves in the Milky Way that could be as high as $4.7 \times 10^6 M_\odot$ (Schneider et al., 2006).

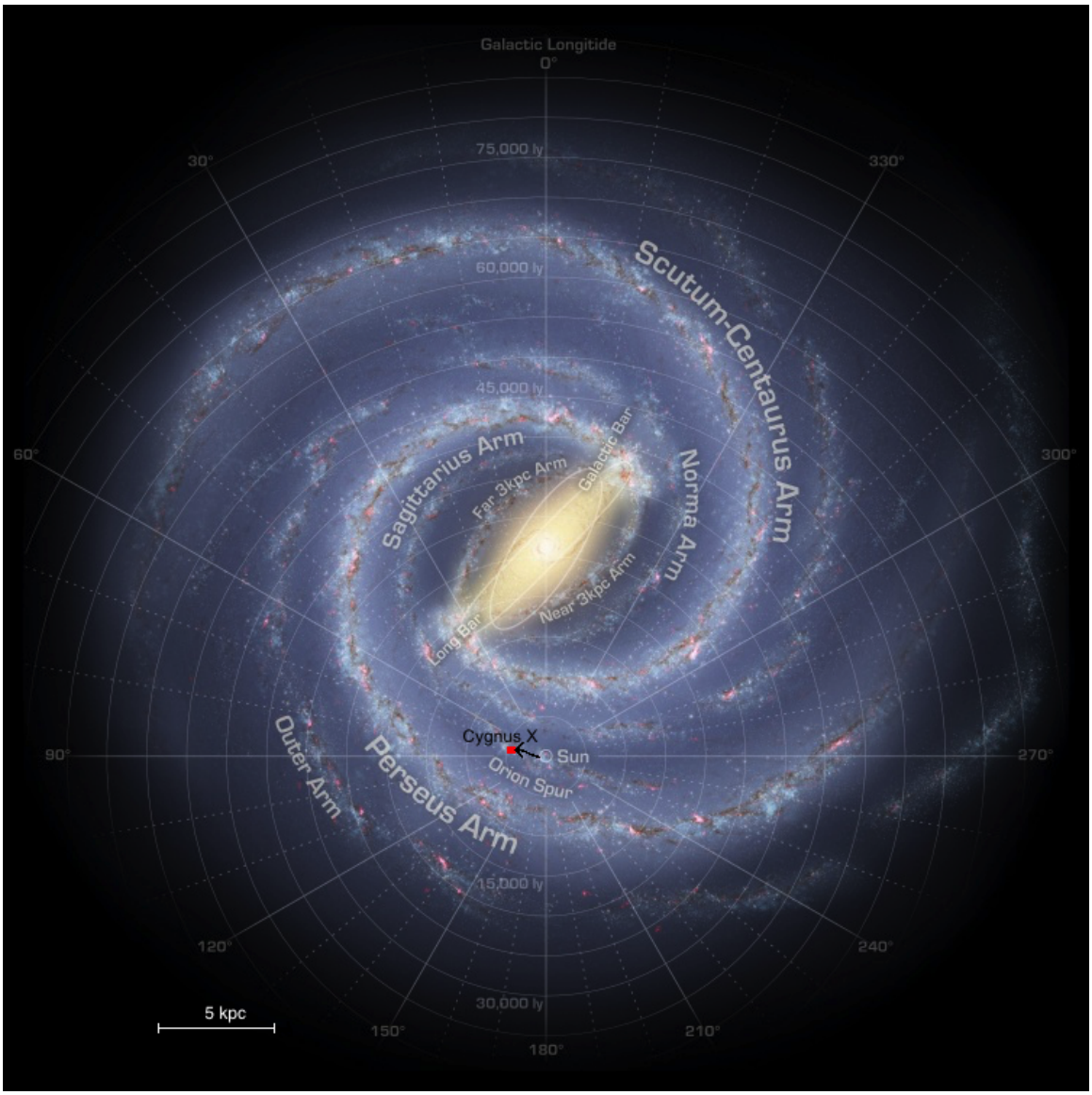

Figure 1.12: An illustration of the Milky Way galaxy along with spiral arms as seen from the galactic north pole. Approximate location of Cygnus X region is denoted by a red square (*illustration credit: R. Hurt (SSC), JPL-Caltech, NASA. Survey credit: GLIMPSE*). The square is shown in detail in figures 1.15 and 3.1.

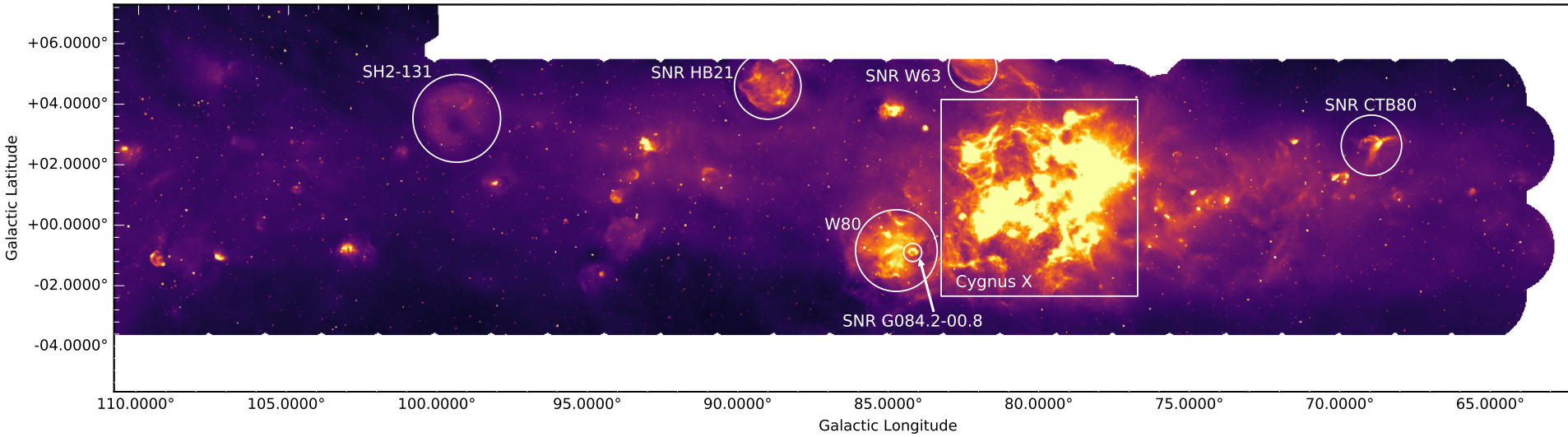

Figure 1.13: Local spiral arm in radio continuum emission, with a few interesting features including supernova remnants and HII regions. Location of Cygnus X is highlighted with a squar. Cygnus Rift in the foreground of Cygnus X, possibly covering most of the emission from Cyg X.

Previously, Dickel et al. (1969) argued that Cygnus X was a superposition of a number of star-forming regions. However, using a detailed comparison of ^{13}CO(2→1) and ^{13}CO(1 → 0) emissions, Schneider et al. (2006) concluded that the molecular clouds in Cygnus X are connected groups. Infrared observations indicate that Cygnus OB2, located at the center of Cygnus X, contains about 2600 ± 400 OB stars and 100 O-type stars (Knödlseder, 2000; Comerón et al., 2002). Additionally, Cygnus OB2 and OB9 associations are heating and affecting the molecular gas in Cygnus X (Schneider et al., 2006).

Arguably, the majority of objects seen in this region are located at the same distance, i.e., that of the stellar clusters OB2, OB1 and OB9 associations at ∼ 1.4 kpc. This includes molecular clouds DR21 and S106. Cygnus X is largely composed of a single 200 pc diameter, one of the most massive complexes in the nearby Galaxies. Roughly, it has 3 times the combined mass of the molecular clouds within 500 pc of the Sun, in a region of one-fifth the size. Cygnus X is the most active, molecular gas-rich, massive star-forming complex within a 2 kpc radius from the Sun. In addition, the close association of OB clusters with a massive molecular complex is exceptional, particularly the OB2 association that is growing while still embedded in its molecular complex (Comerón & Pasquali, 2012).

All of the above characteristics make Cygnus X the best nearby subject for an extensive study of star formation in general. Moreover, With large molecular clouds within it that are being bombarded with ionizing radiation coming from the growing large OB associations, particularly make it an ideal candidate for our study of triggered star formation.

1.9.2 Structure of Cygnus X

The study of the Cygnus X region is almost as old as radio astronomy itself. With the improvement of instrumentation and access to better technology and resolving power, the pic of the Cygnus X region has improved significantly. However, the region, being the biggest star-forming complex within the 2 kpc of the solar neighborhood, is still understudied. Several authors have added information to the structure and dynamics of this big

$7^\circ \times 7^\circ$ region in the galactic coordinate frame (figure 1.13) over decades, but a complete picture of Cygnus X will still require an extensive amount of work. Figure 1.13 (data from the CGPS of DRAO-ST) shows the location of Cygnus X in the galactic plane along with other objects belonging to the same local arm, which includes several HII regions and supernova remnants, except for the HII region W80 which is possibly in Perseus Arm in the background of the supernova remnant G084.2-00.8.

One of the most discussed issues is the ongoing debate on Cygnus X being a single complex of physically connected star-forming regions vs being superposed layers of distinct star-forming complexes along the line of sight. To develop a reliable model of star formation in Cygnus X, we must attempt to address this issue. In general, the internal physical states of molecular clouds are described by quantities including mass, size, material density, and temperature as well as external factors such as the interaction between clouds and with their environments that determine the evolution, and subsequently the star formation efficiency in a region. For this reason, it is important that we investigate the structure of Cygnus X and whether the individual star-forming regions are connected (and influence each other) or independent. Accurate distance and proper space velocity measurements can provide a way to resolve the issue.

Several authors have identified several star-forming regions within Cygnus X along with their distance estimates. Schneider et al. (2006) suggested most of the significant objects in Cygnus X are located at roughly the same distance. The authors used ^{12}CO ($J = 2 \rightarrow 1$)and ^{13}CO ($J = 3 \rightarrow 2$) data from KOSMA sub-mm telescope in combination with MSX 8.3 μm emission and found more than 90 cloud clumps. They mapped Cygnus X into 5 distinct groups. The results are shown in Table 1.5.

The group Cygnus Rift is a diffuse gas in the foreground of Cygnus X ($\sim$ 800 pc) and is of the size close to Cygnus X itself. In addition to the above major dense gas cloud cores that harbor young stars as well as embedded protostars, there are several star clusters or OB associations (Cygnus OB2 and OB9, for example) and HII regions. Schneider et al. (2007)

Groups	Clouds and associations	Combined mass ($M_\odot$)	Galactic latitude l	v_{radial} (km s^{-1})
I	DR20, DR21, DR22, DR23	167,000	80.5° to 82°	-7, +1
II	W75N, DR17, AFGL2620	54,500	80.5° to 82°	+6 to +20
III	Cyg OB2, DR7, DR12, DR15 DR18, DR20, AFGL2591	37,000	-	-11 to 13
IV	DR4,5,9,13,15	420,000	77.4° to 80°	-5 to +3
V	Cygnus Rift	10,000	-	+3 to +7

Table 1.5: Groups in Cygnus X (Schneider et al., 2006)

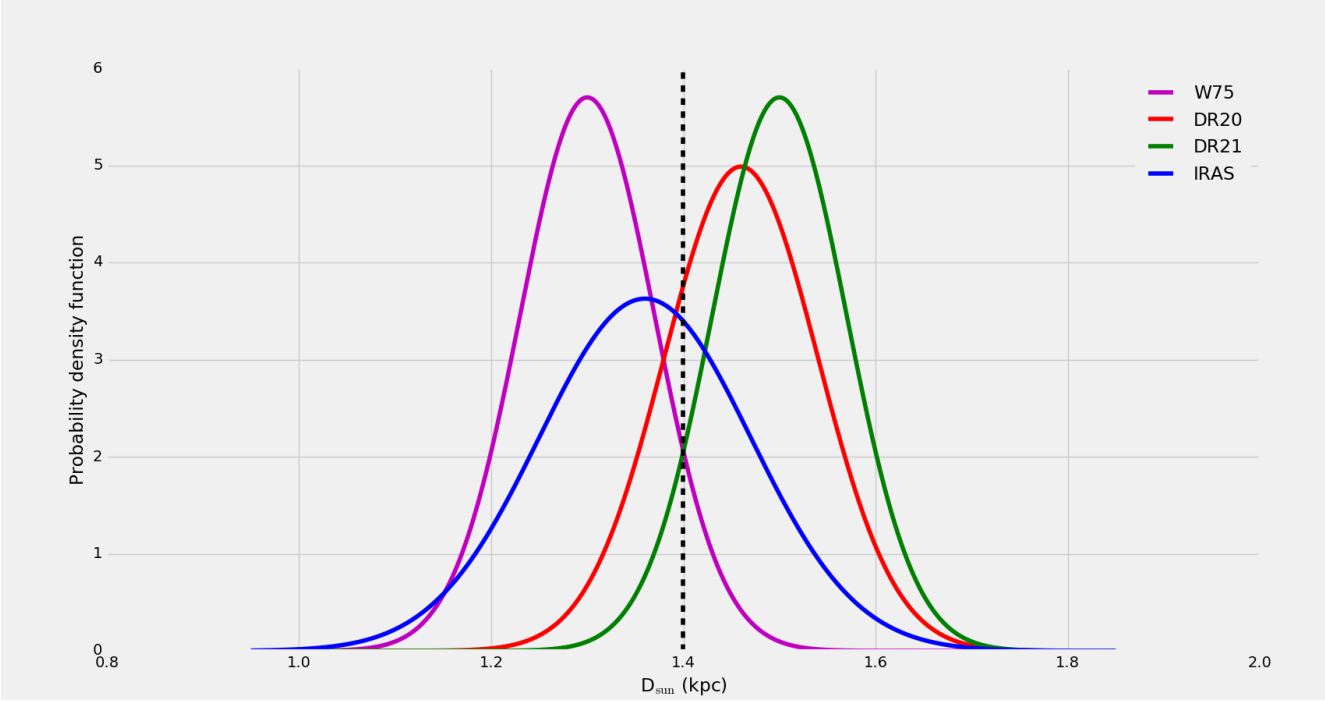

Figure 1.14: Overlapping distance uncertainties of major sub-regions of Cygnus X

added the molecular cloud/HII region associated with the previously known bipolar nebula S106 to be in Cygnus X south and at a distance of 1.7 kpc, same as the associations OB2 and OB1 (see figures 1.15, 3.1). Schneider et al. (2006) supported the previous claims of Landecker et al. (2000) that the cloud complexes in Cygnus X being at a single distance of 1.7 kpc are connected to each other and with OB2 and OB9. Furthermore, Cygnus X is an expanding Strömgren bubble as the effects of OB associations within it.

Using parallaxes and proper motion, Rygl et al. (2012) provides the distances of the five largest star-forming regions that are thought to belong to Cygnus X. Among them, W 75N, DR 20, DR 21, and IRAS 20290+4052 are found to have overlapping distance measurement errors (figure 1.14) which indicate that they are consistent with a single distance value of 1.4±0.08 kpc which the authors stated as an average of their mean value distances as the distance of Cygnus X North. The relative locations are shown in figures 1.15 and 3.1.

The fifth region appears to be at a much larger distance compared to the rest. Although, it was previously thought the first 3 regions in the above table were in Cygnus X north and the last two in Cygnus X south, the distance measurement, as well as the proper motion values for these sources, indicate AFGL 2591 might not be a part of Cygnus X (Rygl et al., 2012). W 75N, DR 20, DR 21, and IRAS 20290+4052 are physically related star-forming regions within Cygnus X North. In that sense, Cygnus X North can be considered a star-forming complex of connected regions. Thus they support the first claim of Schneider et al. (2006).

There are two proposed explanations for Cygnus X to be a connected region. As mentioned before, Landecker et al. (2000) and Schneider et al. (2006) argued Cygnus X to be a single expanding Strögren sphere, where the molecular clouds or star-forming regions and HII regions are located at the front and back surfaces of this shell, around Cygnus OB2 and Cygnus OB9 stellar associations and mainly created by the ionizing radiation from Cyg OB2. It is worthwhile to note here that the conclusion by Schneider et al. (2006) on Cyg X south being a connected group and their conjecture on both the north and south regions

Regions	D_{Sun}(kpc)
W 75N	$1.30^{+0.07}_{-0.07}$
DR 20	$1.46^{+0.09}_{-0.08}$
DR 21	$1.50^{+0.08}_{-0.07}$
IRAS 20290+4052	$1.36^{+0.12}_{-0.11}$
AFGL 2591	$3.33^{+0.11}_{-0.11}$

Table 1.6: Distances of major star-forming regions in Cygnus X (Rygl et al., 2012)

being 'dynamically' connected makes Cygnus X the largest giant molecular cloud in the Milky Way galaxy. However, Rygl et al. (2012) used UVW space motion data to show the individual clumps within Cygnus X have dissimilar proper motions on the galactic plane, which disfavors the idea of a common expanding surface for this region.

The second claim of a single connected Cygnus X was a theory of 'Cygnus Super Bubble' (CSB) caused by the Cygnus Loop supernova remnant (Walsh & Brown, 1955). Uyanıker et al. (2001) rejected the claim by showing that the so-called supernova remnant is nothing but a projection of unrelated X-ray emissions along the line of sight.

Dickel et al. (1969), Wendker et al. (1991) argued the large number of observed features including cloud clamps (star-forming regions), OB associations, and of course, Cygnus Rift is distributed in separate layers along the line of sight that appear superposed to be one big region of Cygnus X. They suggested the distances of different features in Cygnus X varies from 800 pc to 4 kpc.

This conclusion is supported by Gottschalk et al. (2012) who, by using position-velocity diagrams (P-V slices) of ^{12}CO($J = 3 \rightarrow 2$) spectral line, showed what appears to be Cygnus X has three separate layers along the line of sight at different distances. The authors identified layer 1 to be associated with radial velocity range (with respect to the Local Standard of Rest frame) -10 km s^{-1} $\leqslant v_r \leqslant$ 0 km s^{-1} which is the HII and molecular clouds associated with the star-forming region DR 21, at a distance of 1.5 kpc.

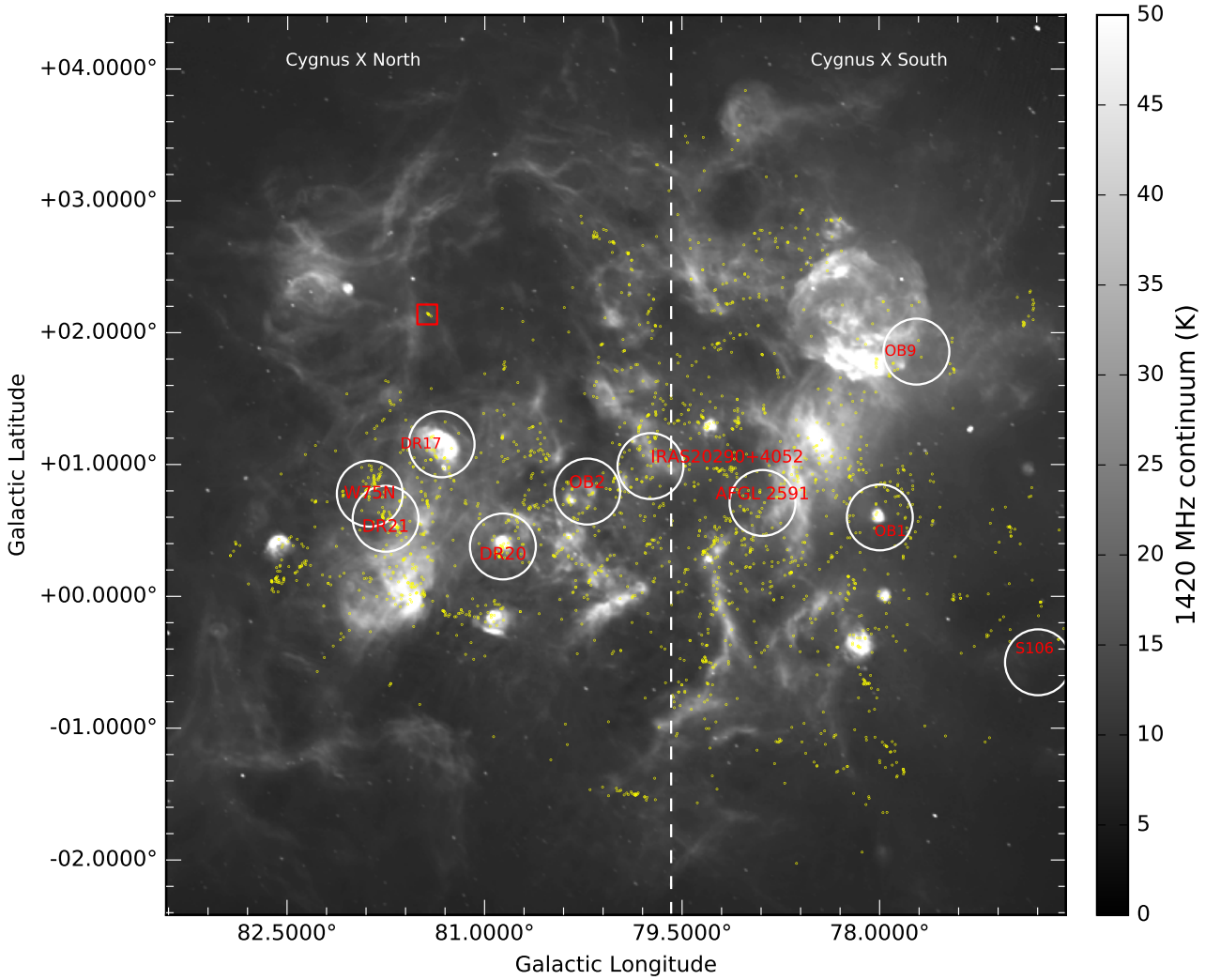

Figure 1.15: Radio continuum emission at 1420 MHz reveals the hot ionized gas in Cygnus X. Protostars from Kryukova et al. (2014a) catalogue are shown in yellow dots. The red dot denotes the location of the cometary feature in Deb et al. 2018.

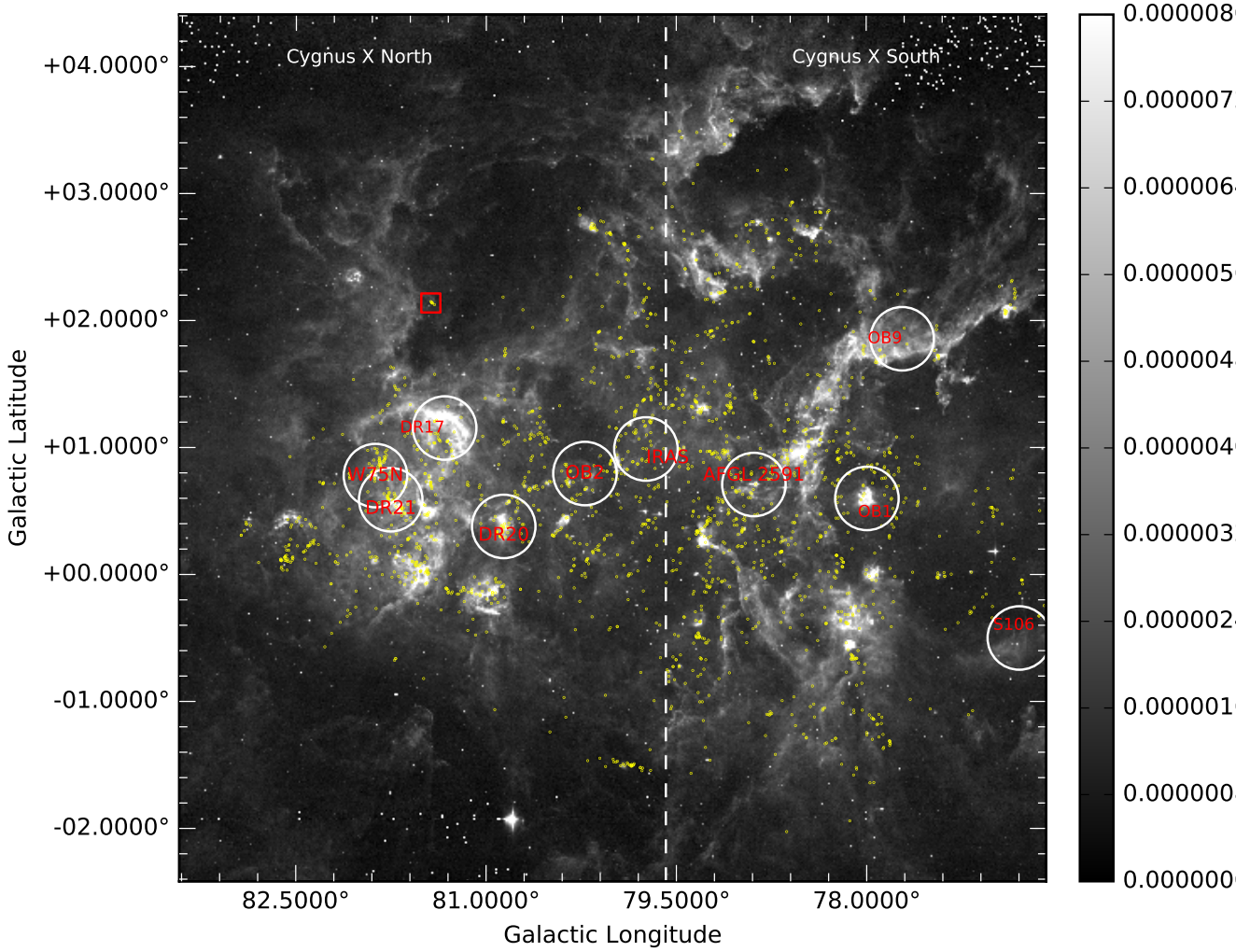

Figure 1.16: Cygnus X dust thermal emission at 8 μm showing molecular gas in Cygnus X. Protostars from Kryukova et al. (2014a) catalogue are shown in yellow dots. The red dot denotes the location of the cometary feature in Deb et al. 2018.

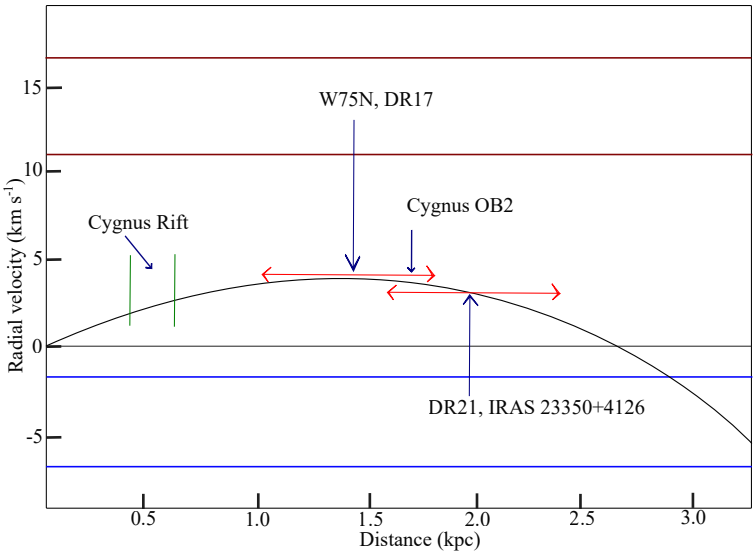

Figure 1.17: Locations of major components of Cygnus X in the line-of-sight distance-radial velocity space (*adapted from Gottschalk et al. 2012*).

Layer 2 is on the other hand, a large cloud of diffuse and cold gas with a low positive LSR radial velocity at a distance of 500 to 800 pc (Gottschalk et al., 2012). This region is called Cygnus Rift and almost covers the entire Cygnus X region that is behind Cygnus Rift causing large visual extinction for the stars and absorbing spectral emissions, coming from the clouds behind, that fall in the velocity range of Cygnus Rift. Gottschalk et al. (2012) also showed the maximum radial velocity along the line of sight towards Cygnus X can be 4 km s^{-1} in the LSR frame. The low positive velocity of Cygnus Rift confirms its location very close to the tangent point where kinematic distance ambiguity vanishes as orbital velocity coincides with radial velocity. Figure 1.17 shows locations and velocity ranges for objects in Cygnus X, as proposed by Gottschalk et al. (2012).

Gottschalk et al. (2012) associated layer 3 with regions at the same distance of 1.3 kpc as W 75N, radial velocity being $v_r \geqslant 8$ kms^{-1}. Although DR 21 and W75N are spatially overlapping regions along the line of sight (figures 1.15 and 3.1), they have disjoint radial velocity ranges. The authors showed that the (background) emission from molecular outflows associated with DR 21 gets absorbed by the (foreground) clouds associated with W 75N, but not the other way. This confirms these two layers are completely separate.

DR 21 in the background is moving towards us ($v_{\rm LSR}$ being negative) and W 75N in the foreground is moving away (positive $v_{\rm LSR}$) implies these two complexes are moving towards each other and will possibly interact collisionally in the future and become a single star-forming layer. The factors causing this relative motion are largely unclear. Possibility includes shockwaves from ancient supernovae remnants or stellar clusters that do not exist anymore. However, no observations are found to support this idea.

The individual clouds in Cygnus X have molecular outflows associated with possible star formation sites. Gottschalk et al. (2012) identified 47 of them in their pilot study of Cyg X, which only counts for 15% of the entire region. Most molecular outflows are still uncatalogued. Molecular outflows are generally associated with infrared sources that are typically protostars. Kryukova et al. (2014a) identified 1800 such protostellar candidates in Cygnus X using the *Spitzer Legacy Survey* data from the two instruments Infrared Array Camera (IRAC) and Multiband Imaging Photometer for *Spitzer* on *Spitzer Space telescope*. Their criteria for protostellar classification are based on the calculation of spectral index α in the wavelength interval of 3.6 to 24 microns (Kryukova et al., 2012).

The authors identified protostars associated with rising SED (class 0 or I), flat spectrum SEDs and more evolved SEDs corresponding to class II protostars (section 1.2.3 for classification based on the spectral index) between 4.5 and 24 microns.

The authors constructed a luminosity function based on the sample of protostars from the data and compared individual luminosity functions for Cygnus X north and Cygnus X south. Based on these distribution functions, they showed the two regions are statistically different. Moreover, the luminosity function shows negative skewness, in particular, protostars with higher luminosity are more likely to form in molecular gas. This implies luminosity function is dependent on the protostellar birth environment in molecular clouds. Locations of these protostellar candidates (Kryukova et al., 2014a) in Cygnus X north and south regions are also shown in figures 1.15, and 3.1.

With this background, in the next few chapters, which are published results, I will dis-

cuss the details of my work focusing on molecular outflows and associated star formation in Cygnus X. In chapter 2, I will present a specific case of triggered star formation in Cygnus X. In chapter 3, I will discuss a method developed to infer outflow properties using single-line data. In chapter 4, I will present a study of the contribution of outflow feedback at different length scales in the context of Cygnus X, and investigate whether a large-scale triggered star formation is likely in Cygnus X.

Chapter 2

A case study of triggered star formation in Cygnus X

As a specific case of potential triggering scenario, we analyzed the structure and the energetics of a feature in the shape of a comet found in a pilot survey by Gottschalk et al. (2012). This cometary feature is located about 50 pc north of Cygnus OB2 complex and has 2 very strong molecular outflows (Makin & Froebrich, 2018) with 6 embedded protostars (Kryukova et al., 2014b). The specific geometry resembling pillar structure in M16 or the Eagle Nebula, which is an established case of triggered star formation (Pattle et al., 2018), and close proximity to the OB2 star forming complex make the cometary feature an ideal candidate for a triggering investigation.

We observed CO(3-2) line emission data of the region along with Hα, infrared, and radio continuum data.

This chapter is published as Deb et al. 2018: "A case study of triggered star formation in Cygnus X", Monthly Notices of the Royal Astronomical Society, Volume 481, Issue 2, December 2018, Pages 1862–1872.

2.1 Abstract

Radiative feedback from massive stars can potentially trigger star formation in the surrounding molecular gas. Inspired by the case of radiatively driven implosion in M16 or

Eagle Nebula, we analyze a similar case of star formation observed in the Cygnus X region. We present new JCMT observations of ^{13}CO(3-2) and C^{18}O(3-2) molecular lines of a cometary feature located at 50 pc north of the Cyg OB2 complex that was previously identified in ^{12}CO(3-2) mapping. These data are combined with archival Hα, infrared, and radio continuum emission data, from which we measure the mass to be 110 $M_{\odot}$. We identify Cyg OB2 as the ionizing source. We measure the properties of two highly energetic molecular outflows and the photoionized rim. From this analysis, we argue the external gas pressure and gravitational energy dominate the internal pressure. The force balance along with previous simulation results and a close comparison with the case of Eagle Nebula favours a triggering scenario.

2.2 Introduction

Cygnus X is among the most active star forming regions in our Galaxy. It contains hundreds of distinct H II regions, numerous Wolf-Rayet and O-type stars, and several OB associations with Cygnus OB2 at the heart of the region (Figure 2.1). Cygnus X was long considered to be the local spiral arm, the Orion Spur, seen end-on with superimposed emission from objects along a large range of distances (e.g., Wendker et al., 1991). This is partly correct, but as shown by Gottschalk et al. (2012), there are three major concentrations of material towards the centre of Cygnus X. The great Cygnus Rift, responsible for the strong absorption in this direction is located at a distance of 500 to 800 pc and is the only major component along this line of sight that is following normal Galactic rotation (Gottschalk et al., 2012). The second component, which is connected to star forming region W75N, is located at a distance of 1 to 1.8 kpc. The distance to W75N was later refined by Rygl et al. (2012) to 1.3 kpc with trigonometric parallax measurements. This component contains material at a high positive local-standard-of-rest (LSR) velocity, which is not allowed assuming a flat rotation curve for our galaxy. This implies that all the material related to W75N was

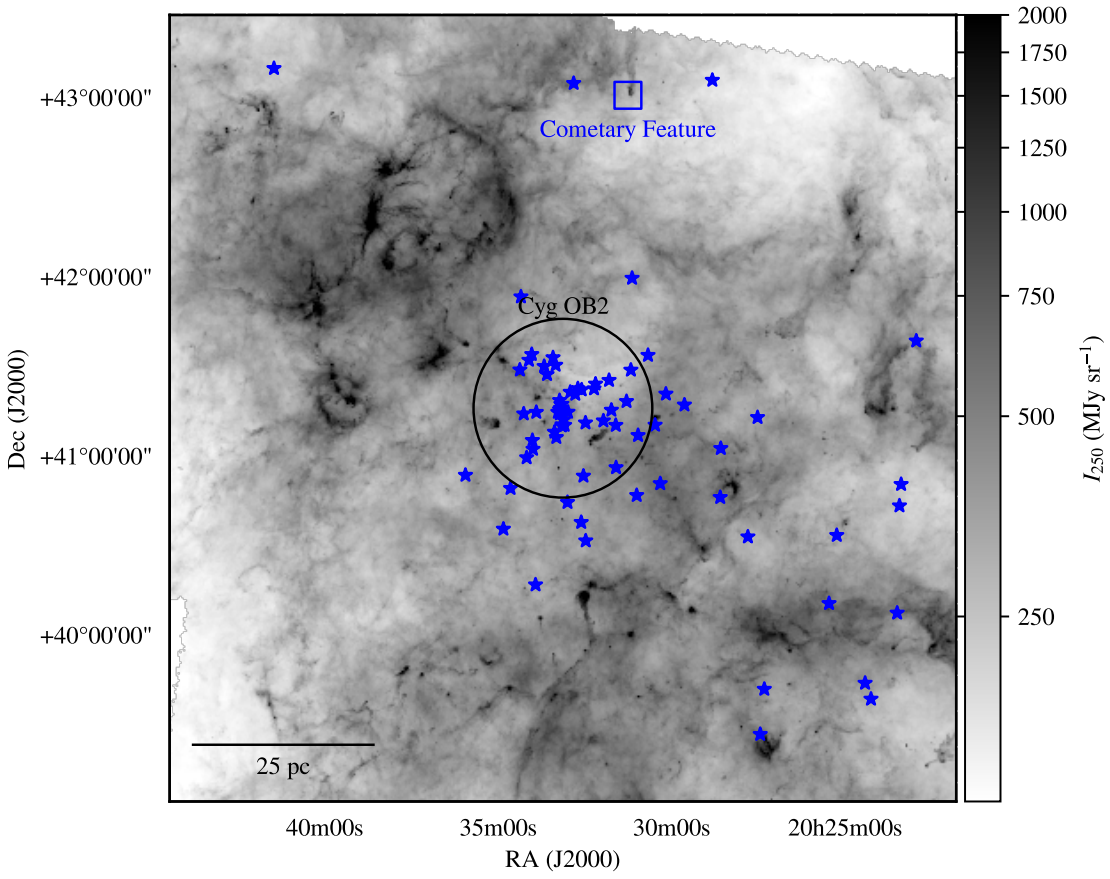

Figure 2.1: *Herschel* 250 μm map of the Cygnus OB2 region illustrating the ISM structure in the region. The locations of O stars in the catalog of Comerón & Pasquali (2012) are indicated with blue star symbols. The location of Cyg OB2 is highlighted as is the location of the cometary feature we are studying. The scale bar on the figure assumes a distance of 1.4 kpc.

pushed away from us by some force, indicating a triggered origin for this star formation complex. The third component found by Gottschalk et al. (2012) is related to DR21 at a distance of 1.5 to 2.5 kpc. This was later refined by Rygl et al. (2012) to 1.5 kpc. Material connected to this component shows an unusually low LSR velocity, in the low negatives, which in this direction of our galaxy would indicate a distance beyond 2.5 kpc. This layer must have been pushed towards us by some force, again, indicating a triggered origin.

In a JCMT CO(3-2) pilot study of Cygnus X, Gottschalk et al. (2012) detected 47 molecular outflows; 27 of these were previously unknown and suggested widespread sequentially-triggered star formation. Most of those outflows and the possibly triggered star formation are related to the aforementioned layers found at unusual LSR velocities. One feature, discovered in the pilot study by Gottschalk et al. (2012), is in the shape of a comet with two molecular outflows inside, which is suggestive of triggered star formation for the protostars. This object is found north of Cygnus OB2 (Figure 2.1). There is a chain of 6 protostellar sources inside this cometary structure (Kryukova et al., 2014b), two of which produce the two distinctive molecular outflows. The outflows are identified as G81.424+2.140 and G81.435+2.147. These outflows are also visible in shocked H_2 emission in the infrared observations of Makin & Froebrich (2018), who also cite the region as a candidate for investigation in the context of triggered star formation. The cometary feature shows a bright limb of emission around the "head" of the comet in both Hα and the radiocontinuum, implying strong photodissociation and ionization of the molecular gas. Here we use the wide-area CO observations of Gottschalk et al. (2012), new data from the James Clerk Maxwell Telescope, and a wealth of archival information to explore this feature as an exemplar of star formation in the neighbourhood of high mass stars. This work focuses on exploring the interplay between the strong radiation field and winds of the massive stars and how these affect the local star formation in this region.

The question of whether the star formation in this feature has been triggered by external effects is natural given the location of the feature on the edge of the ionized region that is

centred on the Cygnus OB2 association of young, high mass stars. The pillar-like geometry of the feature is frequently cited as being indicative of triggered star formation (Dale et al., 2015), drawing analogy to the well studied "Pillars of Creation" in M16 (Hester et al., 1996). Such features are thought to be formed where a dense region of a molecular cloud casts a shadow with respect to an ionizing radiation field. The ionizing radiation field can drive an implosion of the dense region at the tip of the forming cometary feature (Lefloch & Lazareff, 1994; Klein et al., 1994) and the imploding cloud can then go on to form stars. Hence, the mere presence of cometary features are often taken as evidence of triggering (Dale et al., 2015, and extensive references therein).

It is difficult to explicitly identify a region as having had its star formation triggered, mostly because observations lack the ability to evaluate how star formation would have proceeded in a given region under the alternative hypothesis, namely the lack of the strong local ionizing radiation field. Simulations, however, enjoy the ability to actively conduct experiments, studying star formation with and without feedback. Observations can only make a case for some physical effect locally increasing the star formation rate. However, the expected outcomes of star formation are only well-defined on large scales where the star formation law and initial mass function become well defined (Kennicutt & Evans, 2012). Thus, the case for triggering of star formation on small scales (< 10 pc) are particularly fraught (Dale et al., 2015) and must be approached with a careful study.

In this work, we examine the cometary feature in detail using new observations of CO isotopologues to characterize the outflows in this region. We present these new data in Section 2.3 and calculate the physical properties of the feature as as whole as well as the outflows in Section 2.4. In Section 2.5, we discuss the implications of these measurements in the context of triggering.

2.3 Observations

We observed ^{13}CO (3-2) and C^{18}O (3-2) emission with the James Clerk Maxwell Telescope (JCMT), located at the summit of Mauna Kea in Hawai'i, using the Heterodyne Array Receiver Program (HARP) instrument and the Auto Correlation Spectral Imaging System (ACSIS) spectrometer (project code M11AC10). HARP consists of 16 independent receptors in the focal plane of the instrument, separated by 30″ on the sky. We observed the region using the JIGGLE4 scan pattern, which samples a grid of positions covering the region filling in the positions between the individual receptors at sub-Nyquist sampling. We collected sixteen jiggle maps at two offset pointing centres to make a deep map of the outflows. The receiver system observed two bands centred at 330.58 GHz and 329.33 GHz for ^{13}CO(3-2) and C^{18}O (3-2) transitions respectively with a velocity resolution of 0.055 km s^{-1}. Over the course of the observations (July 2011), the mean atmospheric opacity at 225 GHz was τ_{225} = 0.041, corresponding to Band 2 weather in JCMT operations. We reduced the data using the Starlink software package (Currie et al., 2014) and the standard JCMT reduction recipes for narrow emission line data. We then combined the data into a mosaic (position-position-velocity) data cube for each molecular species with central coordinates at RA(J2000) = 20$^{\rm h}$31$^{\rm m}$12.5$^{\rm s}$, Dec(J2000) = +43°05′33.8″. We used nearest-neighbour gridding to map the positions of the spectra into the final data cube. We fit and subtracted a third-order baseline from each position in the data cubes, using emission-free regions defined by eye in the ^{13}CO data. The beam size for the observations is 15.2″. Since the data are sampled on a 7.5″ rectilinear grid, only spatial scales larger than $2\sqrt{(2)}\cdot 7.5'' = 21.2''$ are fully sampled in all directions. The small-scale spatial distribution of the emission is systematically uncertain, but the primary conclusions of this study rest primarily on the integrated spatial properties of the molecular emission, which will be less affected. We corrected the emission to the $T_{\rm MB}$ scale using the observatory values for the beam efficiency: $\eta_{\rm MB}$ = 0.64. The noise level in the final cubes is 130 mK in a 0.055 km s^{-1} channel, when measured on the $T_{\rm MB}$ scale. In this work, we also use the ^{12}CO(3-2) data

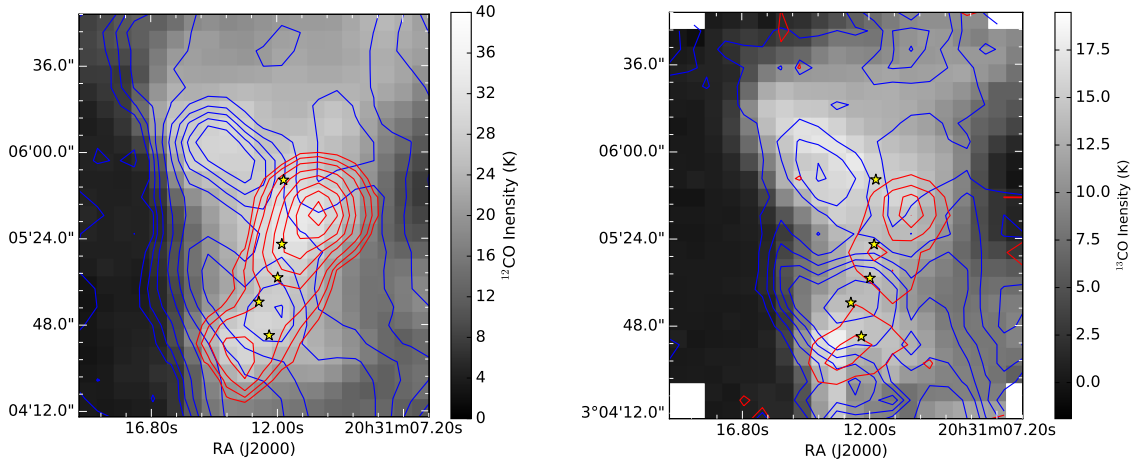

Figure 2.2: Integrated intensity of (a) ^{12}CO and (b) ^{13}CO line emission to highlight the spatial distribution of the molecular gas. Red and blue contours represent the red- and blue-shifted wings of the emission in the corresponding tracers, plotted over the background of total emission (gray-scale). Yellow stars indicate the locations of the protostars in the catalouge of Kryukova et al. (2014b). The gray-scale shows the integration over the entire spectral line, but the blue and red contour sets indicate emission over the velocity ranges of $v_{\rm LSR} = -15$ to -5 km s^{-1} and $v_{\rm LSR} = 0$ to 10 km s^{-1} respectively.

from Gottschalk et al. (2012), which we align and re-sample to be on the same coordinate grid as the ^{13}CO and C^{18}O data.

Figure 2.2 shows integrated intensity maps for the ^{12}CO and ^{13}CO emission. The contour sets highlight the two bipolar outflows. The emission wings for the northern outflow are significantly brighter than the southern outflow. Yellow stars indicate sources in the catalogue of Kryukova et al. (2014b). The northern outflow position is consistent with driving by J203111.98+430507.74 but the southern outflow is more confused. However, all of these sources have a positive spectral index indicating they are relatively young and embedded.

The bipolar outflows are clearly visible in the spectra shown in Figure 2.3, which shows two spectra for each outflow. The red and blue spectra are sampled at positions containing the red- and blue-shifted lobes of the outflow respectively. The line wings that indicate the outflow are clearly present in the high-opacity ^{12}CO emission line, but the line profile

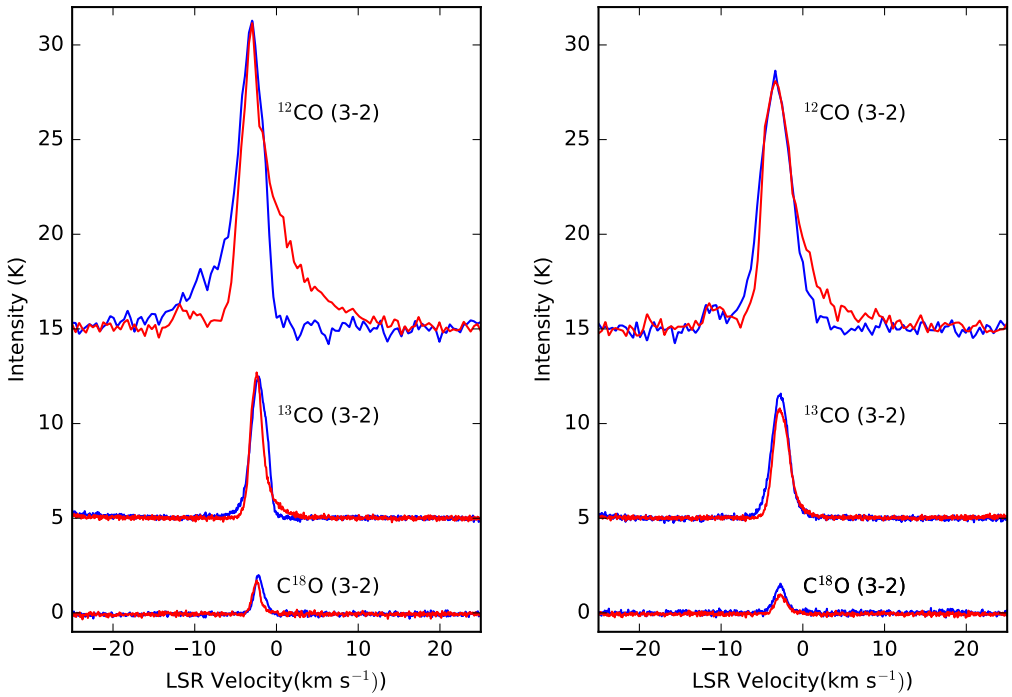

Figure 2.3: A side-by-side comparison between the outflows G81.435+2.147 (left) and G81.424+2.140 (right) in ^{12}CO (offset +15 K), ^{13}CO (offset +5 K), and C^{18}O lines. The asymmetry of the intensity around the central velocity indicates the strength of the outflow. The red and blue colours denote spectra taken through the redshifted and blueshifted components of the outflow. The wing features that indicate the outflow are present in the high opacity ^{12}CO line but the line profile is symmetric in the optically thin C^{18}O line.

becomes more symmetric in the lower-opacity ^{13}CO and C^{18}O emission. We will use these different opacities to estimate outflow properties in section 2.4.3.

We combine the CO emission line data with archival data from the dust continuum emission as observed by *Herschel*[1] as part of the Hi-GAL program (70 to 500 μm; OBSIDs 1342244170, 1342244171; Molinari et al., 2016), Hα emission from the Isaac Newton Telescope Photometric Hα Survey (IPHAS; Barentsen et al., 2014), and the 21-cm radio continuum from the Canadian Galactic Plane Survey (CGPS; Taylor et al., 2003b). The infrared and radio data were obtained as fully calibrated images from their respective archives. We process the IPHAS data to produce Hα image by subtracting off a scaled *R*-band image to remove the stellar continuum. We adopt the photometric calibration provided in the IPHAS metadata. Figure 2.4 shows the cometary feature as seen in these archival data. The infrared data highlight the column density of the neutral medium and reveal a limb-brightened cometary feature in the 70 μm data. The Hα and radio continuum data show emission from the ionized gas at the boundary of the cometary feature. The comet head is directed south towards Cygnus OB2 and with the "tail" pointed directly away from the OB2 association.

2.4 Results

2.4.1 Mass of the cometary feature

We measure the mass of the cometary feature using dust emission. Specifically, we use the *Herschel* SPIRE (250, 350, and 500 μm) and PACS (70 and 160 μm) observations of the region (Molinari et al., 2016), which we obtained from the Herschel archives. Since the calibrated data were at different resolutions, we used a Gaussian kernel to convolve the short-wavelength data to match the 37$''$ resolution of the 500 μm data (Figure 2.5).

[1]Herschel is an ESA space observatory with science instruments provided by European-led Principal Investigator consortia and with important participation from NASA.

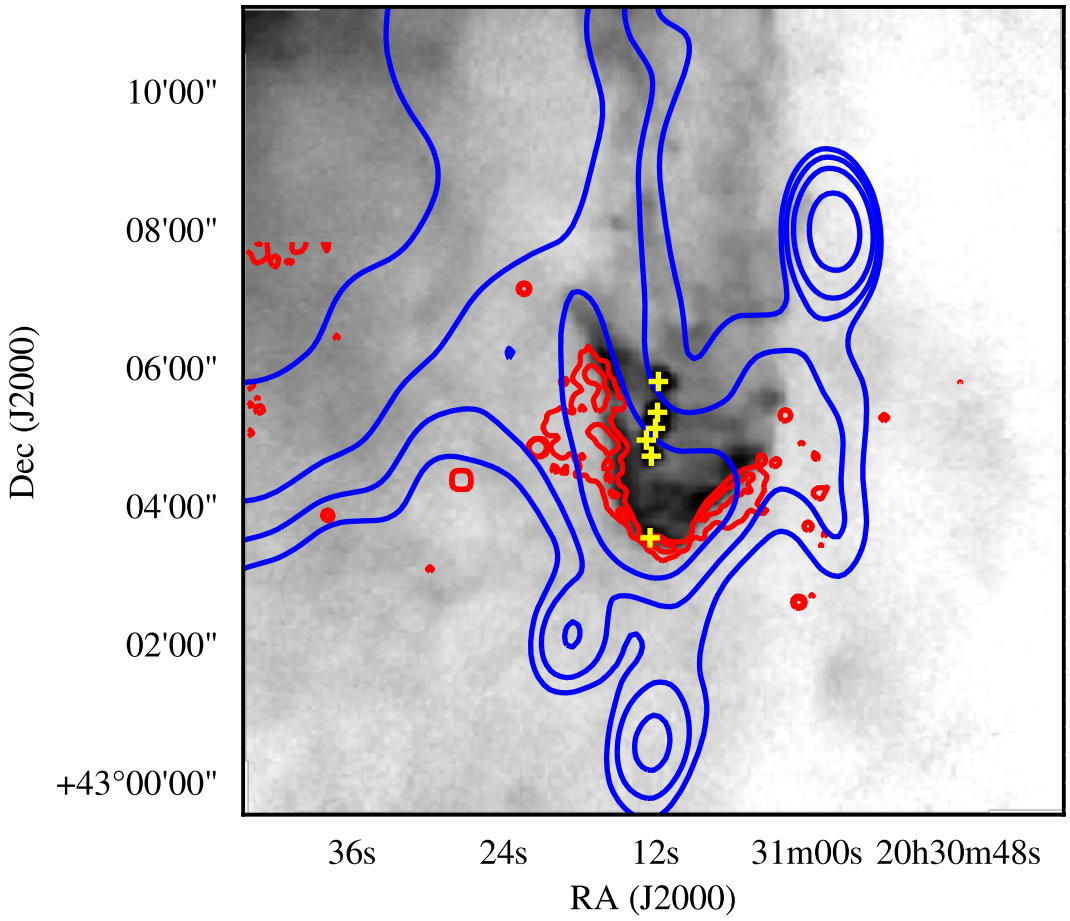

Figure 2.4: Structure of the cometary feature seen in multiple wavebands. The gray-scale image shows the PACS 70 μm data for the region on an arcsinh stretch, where darker colours indicate more intense emission. The red contours show the Hα flux with contour levels at 6 and 9 $\times$ 10^{-17} erg s^{-1} cm^{-2} and the blue contours show the CGPS 21-cm radio continuum image with contours at 14.25, 14.75, 15.6 and 18 K. The yellow + signs indicate the six protostellar sources identified in Kryukova et al. (2014b).

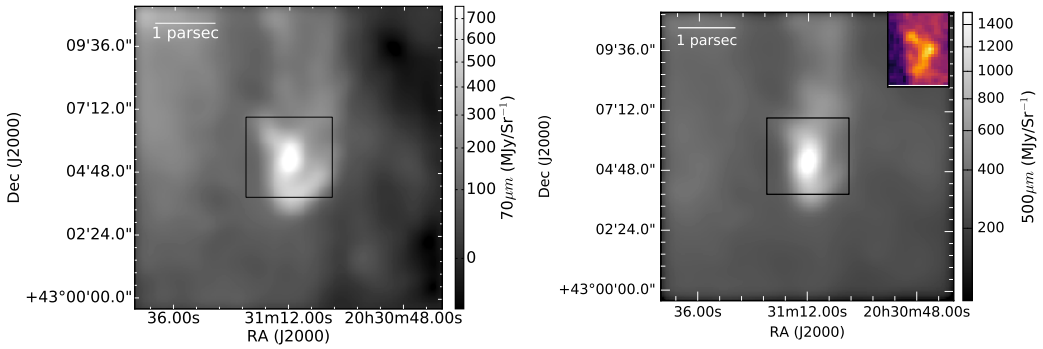

Figure 2.5: Far infrared imaging of the cometary feature from *Herschel* data showing the distribution of matter in the feature for wavelengths of 70 and 500 μm emission, in the left and right panels respectively. The data are convolved to the resolution of the 500 μm data. The square in each figure shows the extent of the CO line mapping. The upper right corner of the right panel shows the integrated intensity image for the ^{13}CO data. The figure shows the overall structure of the cometary feature, highlighting the enhanced short wavelength emission at the "head" of the comet and the tail of cooler, low column density gas behind the feature.

Assuming the dust emission is optically thin, we model the emission from each band as

$$I_\nu = \Sigma_{\rm gas} \kappa_\nu B_\nu(T) \tag{2.1}$$

where B_ν is the Planck function, $\Sigma_{\rm dust}$ is the surface density derived from dust and κ_ν is the opacity of the dust grains per unit gas mass. We assume κ is constant along the line of sight. We adopt κ_ν from (Hildebrand, 1983),

$$\kappa_\nu = 0.1 \frac{\rm cm^2}{\rm g} \left(\frac{\nu}{1\ {\rm THz}} \right)^\beta, \tag{2.2}$$

which includes a gas-to-dust ratio of 100 by mass to convert to an effective gas surface density and we assume $\beta = 2$.

We have two parameters Σ and T in our model, which we estimate by fitting the model (Equation 2.1) to each position in the data. Figure 2.5 shows that the region contains spatially varying background emission. We define a background level from a region near the cometary feature in each image and subtracting the average in that region from the data. On examining the spectral energy distributions of different positions (e.g., Figure 2.6), we find that the 70 μm data are not well represented by a single dust temperature

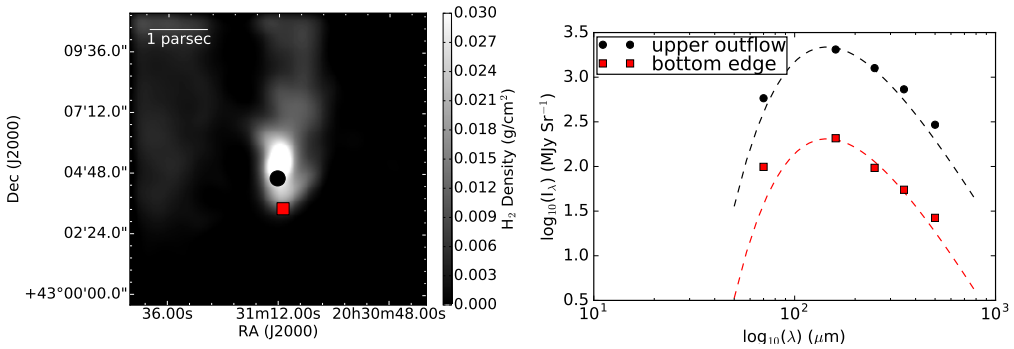

Figure 2.6: (left) Surface density map of dust emission of the cometary region with background emission removed (right) Spectral Energy Distribution: fitted (dashed lines) and observed (squares/circles) for the second outflow source ($20^{\rm h}31^{\rm m}12.31^{\rm s}$, $+43°04'43.61''$) and the bottom edge of the cometary feature ($20^{\rm h}31^{\rm m}12.19^{\rm s}$, $+43°03'07.25''$). Positions are shown in black circles and red squares respectively in the left panel. The SED at the bottom edge shows that the 70 μm data sits above the fit for the rest of the curves, indicating the presence of a second hot dust component.

model, with the bright 70 μm emission found at the limb of the comet (see also the full resolution image in Figure 2.4). We thus omitted the 70 μm data from the fit and adopted a fixed dust temperature of $T = 20$ K, which should trace the bulk of the mass in the star forming comet. Under these assumptions, we derive the column density map (Figure 2.6) and find the mass of the feature to be $M = 110$ M$_\odot$, assuming a distance of 1.4 kpc.

2.4.2 CO line Emission: Optical Depth and Column Density

We also derive the column density of the CO isotopologues using the multi-line observations. Specifically, we assume local thermodynamic equilibrium so the spectral line emission is modelled as (Mangum & Shirley, 2015):

$$T_{\rm R} = f[J_\nu(T_{\rm ex}) - J_\nu(T_{\rm bg})](1 - e^{-\tau_\nu}). \tag{2.3}$$

Here $T_{\rm R}$ is the observed radiation temperature, $T_{\rm ex}$ is the molecular excitation temperature, $T_{\rm bg}$ is taken as the cosmic microwave background temperature (≈ 2.73 K), $J_\nu(T) = (h\nu/k)/(\exp[h\nu/(kT)] - 1)$ is the compensated radiation temperature, and τ is the optical depth. The factor f corresponds to the beam dilution factor, which we assume is 1 (i.e., the emission is beam-filling).

As ^{12}CO is a much more abundant species in molecular clouds, compared to ^{13}CO and C^{18}O, we assume the emission is optically thick in ^{12}CO emission, particularly at the line centre. In that case,

$$J_\nu(T_{\rm ex}) - J_\nu(T_{\rm bg}) \approx T_{\rm max}, \tag{2.4}$$

where $T_{\rm max}$ is the maximum radiation temperature of the ^{12}CO emission along each line of sight. In that case, the molecular excitation temperature becomes

$$T_{\rm ex} = \frac{h\nu/k}{\ln\left[1 + \frac{h\nu/k}{T_{\rm max} + J_\nu(T_{\rm bg})}\right]} \tag{2.5}$$

We assume the ^{13}CO and C^{18}O have the same excitation temperature as ^{12}CO, and that the C^{18}O emission is optically thin. We can then express the column density for the top state of the C^{18}O transition as:

$$\begin{aligned} N_u &= \frac{8\pi\nu_0^3}{c^3 A_{ul}} \frac{1}{e^{\frac{h\nu_0}{kT_{\rm ex}}} - 1} \int \tau_\nu d\nu, \\ &= \frac{8\pi\nu_0^3}{c^3 A_{ul}} \frac{1}{e^{\frac{h\nu_0}{kT_{\rm ex}}} - 1} \frac{\int T_{\rm R} d\nu}{J_\nu(T_{\rm ex}) - J_\nu(T_{\rm bg})}. \end{aligned} \tag{2.6}$$

Here, ν_0 is the equivalent frequency and A_{ul} is the Einstein coefficient for $u = 3$ to $l = 2$ transition. We extrapolate to the total column density of the species using the partition function (Q), which is well approximated as

$$Q \approx \frac{kT}{hB_0} \exp\left(\frac{hB_0}{3kT}\right). \tag{2.7}$$

With these assumptions, the total column density is

$$N_{\rm tot} = \frac{Q}{g_u} \exp\left(\frac{E_u}{kT_{\rm ex}}\right) N_u. \tag{2.8}$$

For this calculation, the Einstein coefficient $A_{ul} = 6.011 \times 10^{-7}$ s^{-1}, $\nu_0 = 330.588$ GHz and the rotational constant $B_0 = 54891.42$ MHz, with values from the LAMDA[2] (Schöier et al., 2005) and NIST[3] databases.

[2] http://home.strw.leidenuniv.nl/~moldata/

[3] https://physics.nist.gov/PhysRefData/MolSpec/

The ^{13}CO line is not necessarily optically thin. In this case, Equation 2.3 implies

$$\tau_\nu = -\ln\left[1 - \frac{T_{\rm R}}{J(T_{\rm ex}) - J(T_{\rm bg})}\right] \tag{2.9}$$

We compute a total column density of ^{13}CO (Equation 2.8) using $A_{ul} = 6.038 \times 10^{-7}$ s^{-1}, $\nu_0 = 330.588$ GHz and $B_0 = 55101.01$ MHz.

Fig. 2.7 shows the correlation between the H_2 and the CO column densities. We convolve the molecular line column density maps to match the 37″ resolution of the dust map. This figure shows typical fractional abundances of 10^{-6} and 1.5×10^{-7} for the ^{13}CO and C^{18}O respectively, which are comparable to the canonical values (Wilson & Rood, 1994). However, the ^{13}CO emission shows a shallower increase with increasing column density compared to the C^{18}O. At large values of the dust column density, both species appear to saturate indicating some depletion onto dust grains.

2.4.3 Properties of the Outflows

We also estimate the mass, momentum and kinetic energy of the molecular outflows from the line emission data. In particular, we use ^{13}CO column density data for this purpose. Using Equation 2.8 in the previous section, the column density of ^{13}CO as a function of position and velocity is:

$$N_{^{13}\rm CO}(x, y, v) = \frac{8\pi\nu_0^3 Q_{\rm rot}}{7c^3 A_{ul}} \frac{e^{\frac{E_u}{kT_{\rm ex}}}}{e^{\frac{h\nu_0}{kT_{\rm ex}}} - 1} \tau_\nu(\mathbf{x}, v)\, \delta v. \tag{2.10}$$

Here, $\mathbf{x}$ is the position along a position-velocity (PV) slice, running through the blue and red shifted region of an outflow. We have also used $\int \tau_\nu(\mathbf{x}, v) dv \approx \tau_\nu(\mathbf{x}, v)\, \delta v$ where δv is the channel width, and $g_u = 2J_u + 1 = 7$. Using our typical fractional abundance of ^{13}CO derived from dust in section 2.4.2, the column density of H_2 is $N_{\rm H_2}(x, y, v) = 10^6 N_{^{13}\rm CO}(x, y, v)$. This expression gives us an estimate of the mass as a function of position offset and velocity by assuming a mean particle mass of $\mu = 2.4 m_{\rm H}$, where we include the mass of helium.

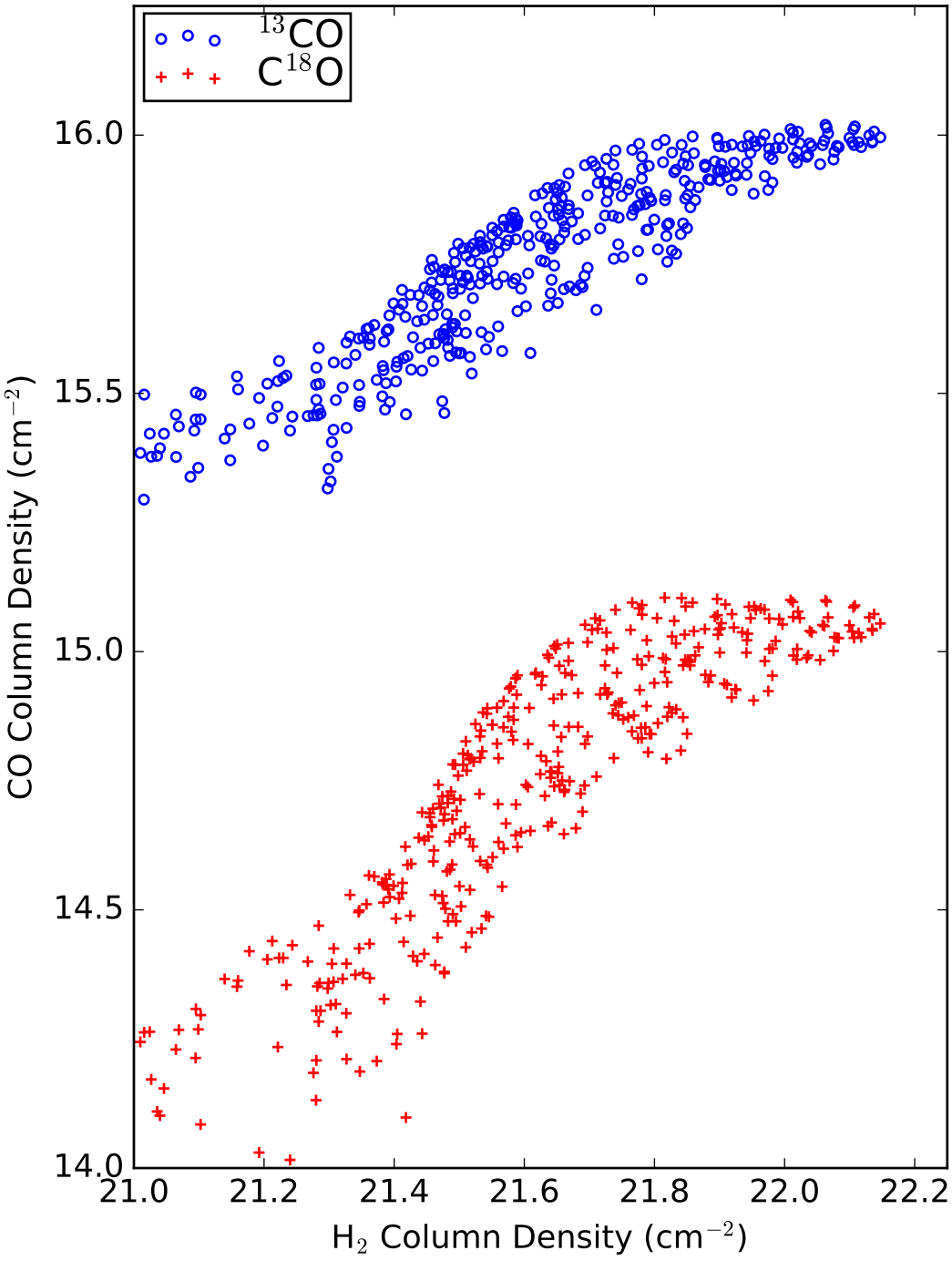

Figure 2.7: CO isotopologue column densities relative to H_2 column density estimate obtained from dust continuum emission. Both species show typical fractional abundances, and some signs of depletion onto dust grains at the highest dust column densities. This figure shows our estimates of the different column densities are broadly consistent with expectations for a typical cloud of star forming molecular gas.

Property	Outflow 1	Outflow 2
RA (J2000)	20:31:12.5	20:31:12.3
Dec (J2000)	+43:05:42	+43:04:53
PA (°)	48.01	141.34
M_o ($M_\odot$)	12	3.6
$p_o \cos i$ ($M_\odot$ km s^{-1})	26	8.5
$E_o \cos^2 i$ (10^{44} erg)	8.8	2.5

Table 2.1: Properties of molecular outflows found in the cometary feature.

The signal-to-noise ratio of the ^{13}CO emission is low in the wings of the outflows, so we infer the brightness of the ^{13}CO from the brighter ^{12}CO data (Arce & Goodman, 2001). First, we estimate the line centre by fitting a Gaussian to the C^{18}O data extracted on the same PV slice. Then we fit a quadratic function to the ^{12}CO/^{13}CO line ratio separately for blue and red-shifted regions. Again following Arce & Goodman (2001), we assume a minimum value of the line ratio is found in the optically thin case where the relative abundance of the species, assumed to be 65 (Wilson & Rood, 1994), sets the ratio.

With these assumptions, we calculate the mass at every position and velocity in the outflow. We calculate the total mass in the outflow by summing the contributions over the region, subtracting off the contribution associated with the main molecular cloud as defined by the C^{18}O. We also calculate the projected momentum ($p \cos i = \sum M|v - v_0|$) and energy ($E \cos^2 i = \sum M(v - v_0)^2/2$) for the outflows and give the results in Table 2.1. We also list the position angle (PA) along which the the position-velocity slice is extracted, measured in degrees east of north. The $\cos i$ factor accounts for the inclination of the outflow with respect to the line of sight. For comparison, the two outflows are at the upper end of momentum and energy distributions compared to the population of outflows seen in the nearby Perseus molecular cloud (Arce et al., 2010), but the outflows in Cygnus X are not exceptional.

2.5 Discussion

Here we discuss the properties of the star forming molecular feature in the context of the broader star forming environment of the Cygnus X region.

2.5.1 Ionizing Sources

The cometary feature shows a rim of radio continuum emission (Fig. 2.4) visible at 1420 MHz in the Canadian Galactic Plane Survey (CGPS, Taylor et al., 2003b) and the NRAO VLA Sky Survey (NVSS, Condon et al., 1998), outlining the CO and IR emission of the cometary feature. Assuming this is free-free emission from the hot ionized gas at the edge of the cometary feature, we can calculate the ionizing flux, required to maintain this thermal emission.

The radio continuum emission is only marginally resolved, so we calculate the plasma properties of the region using the flux density of emission and assuming a geometry based on the Hα emission. The total integrated flux density S_ν at a frequency of $\nu = 1420$ MHz results in 60 ± 6 mJy. Using the expression for the brightness temperature from Wilson et al. (2013), the flux density for a source of optically-thin, free-free emission is:

$$S_\nu = 2.553 \text{ mJy} \left(\frac{E_V}{\text{pc}^3 \text{ cm}^{-6}} \right) \left(\frac{d}{\text{kpc}} \right)^{-2} \left(\frac{T_e}{\text{K}} \right)^{-0.35} \left(\frac{\nu}{\text{GHz}} \right)^{-0.1}, \tag{2.11}$$

where T_e is the electron temperature, d is the distance to the source, and E_V is the volume emissivity:

$$E_V = \int n_e^2 dV. \tag{2.12}$$

For an electron temperature of 8000 ± 2000 K (e.g., Osterbrock & Ferland, 2006) and a distance of 1.4 kpc to the cometary feature we calculate a volume emissivity of

$$E_V = 1100 \pm 200 \text{ pc}^3 \text{ cm}^{-6}. \tag{2.13}$$

Since the radio data does not fully resolve the rim of thermal emission, we use the IPHAS image to determine the location of the ionized gas. The resolution of the CGPS

images is about 1′ and of the NVSS images about 45″, while the rim of ionized gas is about $\Delta r = 5''$ to $10''$ wide when viewed in the IPHAS data (see Fig. 2.4). We model the region as a thin, hemispherical shell with radius of $r = 1.5' = 0.6$ pc. We then calculate the typical electron density as $n_e \approx [E_V/(2\pi r^2 \Delta r)]^{1/2} = 110 \pm 10$ cm^{-3}. We also estimate the mass of ionized gas as $M = m_{\rm H} n_e 2\pi r^2 \Delta r \sim 0.2\ M_\odot$.

We also calculate the required ionizing flux using the IPHAS image of the region (Barentsen et al., 2014). To make this estimate, we measure the average brightness of the cometary feature in a continuum subtracted Hα image finding $\langle f \rangle = 2 \times 10^{-16}$ erg s^{-1} cm^{-2} coming from each 0.33 arcsec pixel, which implies an emergent intensity of $3{\times}10^{-5}$ erg s^{-1} cm^{-2} sr^{-1}. Assuming no extinction, this measurement in turn implies an emission measure of EM = 1000 pc cm^{-6} using the calibration of Haffner et al. (1998), again taking $T_e = 8000$ K. Using our model as before, the path length is determined by the distance through the shell, where the typical path length is $\gtrsim 2\Delta r$. In this case, the typical electron density is $n_e \approx [{\rm EM}/(2\Delta r)]^{1/2} \approx 100 \pm 20$ cm^{-3}, consistent with the estimate from the radio continuum emission.

We explore what sources could be providing ionizing flux that maintains the thermal emission by setting the recombination rate for the region equal to the geometrically diluted ionizing photon flux for a source that is a distance d away. Expressing this condition in terms of the Case B recombination coefficient α_B, the emission measure and the ionizing photons produced per second (Q_0) yields the steady-state requirement that:

$$\mathrm{EM}\, \alpha_B = \frac{Q_0}{4\pi d^2} \equiv q_0. \tag{2.14}$$

Taking $\alpha_B \approx 2.56{\times}10^{-13} T_4^{-0.83}$ cm^3 s^{-1}, where $T_4 = (T_e/10^4\ \mathrm{K})$ gives $q_0 = 1{\times}10^9$ cm^{-2} s^{-1} for $T_4 = 0.8$ (Draine, 2011).

We evaluate the possible ionizing sources that could be powering this feature. We explore the catalog of Comerón & Pasquali (2012), searching for O and B stars near the cometary feature. For each star in the catalog, we calculate the number of ionizing photons produced using the model atmospheres of Sternberg et al. (2003). For stars with spectral

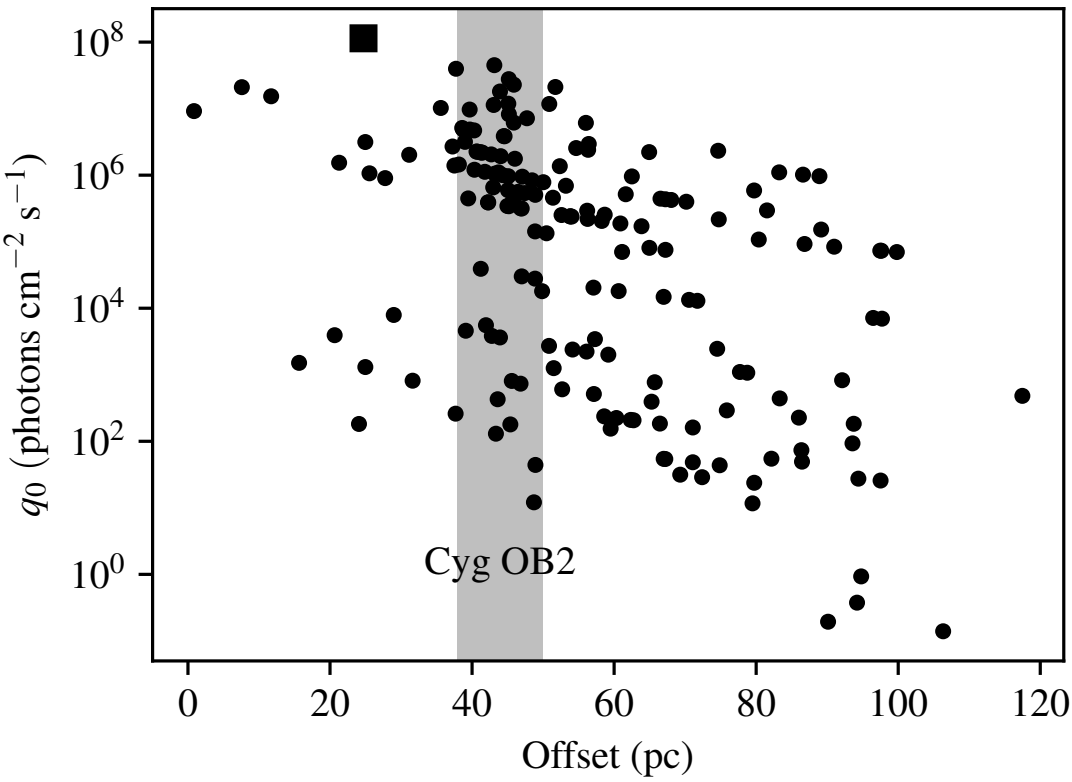

Figure 2.8: Maximum flux of ionizing photons at the location of the cometary feature based on the catalog of Comerón & Pasquali (2012). The largest contribution to the modelled flux from an individual star arises from BD+43 3654, indicated with a filled square. The dominant fraction of the emission comes from the collective action of the Cyg OB2 complex.

types later than B0, we estimate the ionizing photons by extrapolating the $T_{\rm eff}$ vs Q_0 curves to lower temperatures. However, these stars produce so few ionizing photons that they could not contribute significantly to the ionization. For each star, we calculate the maximum possible flux at the location of the cometary feature by assuming the stars are at the same distance as the feature and there is no extinction between the star and the cometary feature. We plot the results of this analysis in Fig. 2.8. The total ionizing flux provided by all cataloged stars is $q_0 = 5 \times 10^8$ photons cm^{-2} s^{-1}, close to the required budget based on the emission measure. In this simple model, the star BD+43 3654, an O4If star at a projected offset of 24 pc provides 22% of the total flux at the source. However, BD+43 3654 is located to the north of the cometary feature, and the Hα and radio geometry imply illumination from the south. Thus, BD+43 3654 is unlikely to be the primary ionizing source. It cannot be at the same projected distance as the cometary feature or else the ionization limb would not have the orientation that it does. Other, nearer stars also have unfavourable geometries. In contrast, the collective action of stars in Cyg OB2 provide $>$ 50% of the total possible photons in our model and are oriented in the correct direction to shape the cometary feature. Given the number of ionizing photons is of order the amount provided by Cyg OB2, we regard the cometary feature as likely being photoevaporated by radiation from the Cyg OB2.

We attribute the lack of a perfect agreement between the ionizing photon budget required to maintain the emission and that provided by the known stars to the incompleteness of the OB star catalogues in this regions. Many sources of ionizing photons could be obscured by dust screens from our perspective, rendering the catalogues incomplete.

2.5.2 Internal conditions of the cometary feature

While frequently correlated, the causal connection between cometary features and the triggering of star formation by feedback from local massive stars is not clear (Dale et al., 2013), particularly for gravitationally bound cloud fragments. The star formation could be

proceeding because of spontaneous gravitational collapse or compression caused by nearby supernova blast waves. To assess the likelihood of the star formation being triggered, we must look at the dynamical quantities in the cometary feature. In particular, the feedback-driven implosion of the globule requires that the thermal pressure in the surrounding HII rim and the external radiation pressure due to the ionizing flux from OB2 complex to dominate the gravitational energy of the cometary feature.

We parameterize the different physical effects in terms of the energy densities and pressures to evaluate what effects govern the evolution of the feature. For global quantities we convert energies to energy densities by assuming a spherical geometry for the object. Taking the distance to be 1.4 kpc, we estimate the radius as $R \approx 0.31$ pc. The gravitational potential energy density, assuming uniform density is $u_{\rm grav} = 9GM^2/(20\pi k_{\rm B} R^4) \approx 4.0 \times 10^6$ K cm^{-3}. We also calculate the internal pressure from the velocity dispersion in the molecular gas. We estimate the line width from $C^{18}O$ (3-2) data by fitting a Gaussian profile to the mean spectrum over the mapped region, finding $\sigma_v \approx 0.68$ km s^{-1}. We use the $C^{18}O$ since the line is the most optically thin tracer of the molecular gas and is unaffected by the line broadening due to outflows. Then the internal gas pressure is $P_{\rm int}/k_{\rm B} = \rho\sigma_v^2/k_B \approx 1.9 \times 10^6$ K cm^{-3}.

For thermal and radiation pressures we use the values calculated in Section 2.5.1. We obtain thermal pressure in the ionized gas as $2n_{\rm e}T_{\rm e} \approx 2.24 \times 10^6$ K cm^{-3} and radiation pressure as $P_{\rm rad} = h\nu q_0/(ck_{\rm B}) \approx 1.25 \times 10^4$ K cm^{-3}, where $T_{\rm e}$ and $n_{\rm e}$ are the electron temperature and mean electron number density in the ionized rim, q_0 is the incident ionizing flux density. We also estimate the contributions to the energetics of the cloud by taking the energy for the molecular outflows (Table 2.1) and dividing by the volume of the object. This represents an upper limit since the molecular outflows are not likely to contribute all this energy to the support of the region. The outflow wing velocities ($v_{\rm wing} \sim 5$ km s^{-1}) are significantly larger than the escape speed for the cometary feature ($v_{\rm esc} = 1.2$ km s^{-1}).

Considering these relative energy densities and pressures, the cometary feature is grav-

itationally bound with kinetic energies comparable to the binding energy, specifically $K = 0.75U_g$. However, the external pressure is comparable to the internal pressure for the feature, which will encourage gravitational collapse. The line widths of the feature are larger than expected from a virialized object and could be indicative instead of free-fall collapse or radiative driven implosion (Lefloch & Lazareff, 1994).

For full consideration of the energetics, we write the virial theorem for the cometary feature,

$$\frac{1}{2}\ddot{I} = U_g + 2K - \oint_A rPdA + \frac{1}{8\pi}\int (B^2 - B_0^2)dV, \tag{2.15}$$

where the terms $U_g = -3GM^2/(5R)$ and $K = 3M\sigma_v^2/2$ represent the potential and kinetic energies of the cometary feature, the values of which can be found in Table 2.2, as $U_g = -2 \times 10^{45}$ erg, $2K = 3 \times 10^{45}$ erg. The third term is the mean external pressure at the virial surface. Assuming a spherical geometry, we calculate $\oint_A rPdA = 1.7 \times 10^{45}$ erg over 2π sr representing the hemisphere bounded by the ionizing gas. If the magnetic field term (i.e., the last term) in this equation is zero, then $\ddot{I} < 0$ and the feature will collapse on a free-fall time.

The last term represents the unknown total magnetic energy of the cometary feature (B) minus that due to the background field (B_0). Given the other physical effects that are governing the energetics of this feature, we calculate the field strength required to achieve virial balance ($\ddot{I} = 0$) as 70 μG, taking $B^2 \gg B_0^2 = (5\ \mu\text{G})^2$ (Crutcher, 2012). A high magnetic field strength in a collapsing region favours the possibility of external influence such as photoevaporation. While reasonably strong, fields of this strength or larger are seen in cometary features (Pattle et al., 2018), where observations suggest a value between 170 and 320 μG with field lines aligned with the photoevaporative flow. Whether the field can support the feature under discussion against collapse depends on its geometry and strength, neither of which can be further assessed without dedicated observations.

Property	Expression	Cometary Feature	Eagle Nebula Pillar II
Mass ($M_\odot$)	M	110	250
Size (pc)	R	0.31	0.15
Electron density in ionized rim (cm^{-3})	n_e	140	4000
Potential energy density (K cm^{-3})	$9GM^2/(20\pi k_B R^4)$	3.8×10^6	$3.7{\times}10^8$
Internal pressure (K cm^{-3})	$\rho\sigma_v^2/k_B$	1.9×10^6	$1.2{\times}10^8$
Incoming ionizing flux (cm^{-2} s^{-1})	q_0	2.1×10^9	$4.6{\times}10^{11}$
Radiation pressure (K cm^{-3})	$h\nu q_0/(ck_B)$	1.2×10^4	$2.7{\times}10^6$
Thermal pressure at the tip (K cm^{-3})	$2n_eT$	2.2×10^6	$6{\times}10^7$
Outflow energy density (K cm^{-3})	$E_o \cos^2 i/(\frac{4}{3}\pi R^3)$	$< 1.7 \times 10^6$	...
Binding energy (10^{45} erg)	$3GM^2/5R$	2	21
Photoevaporation mass-loss rate ($M_\odot$ Myr^{-1})	$\dot{M}$	15	70
Photoevaporation lifetime (Myr)	$M/\dot{M}$	7	3

Table 2.2: Comparison of dynamical properties between the cometary feature and Eagle Nebula

2.5.3 Timescales for Evolution of the Cometary Feature

While Cygnus OB2 is the likely candidate for illuminating the limb of the cometary feature, the process of star formation is currently ongoing inside the cold cloud. To evaluate whether Cyg OB2 could have triggered the formation of stars inside the region, we examine the timescales for star formation to be triggered within the cometary feature. We consider a triggering scenario where Cygnus OB2 forms, creates an ionization front in a neutral cloud that then propagates to the location of the cometary feature, prompting an increase in the star formation in this region.

Source of Triggering: The study of Wright et al. (2015) argues that massive star formation occurred in Cyg OB2 continuously between 1 and 7 Myr ago, so that the region has been producing significant amounts of ionizing radiation. Considering only the stars in the Comerón & Pasquali (2012) catalog found in the central Cyg OB2 region, the current production of ionizing photons is $10^{50.8}$ s^{-1}, and the photon rate over the past few Myr is likely declining as the stellar population ages. Therefore, this value should be considered a lower limit.

Travel Time for the Ionization Front: The radiation front from Cyg OB2 propagates through the ISM between it and the cometary feature at a speed of about 20 km s^{-1}, which is the speed of sound in ionized medium. This gives a simple estimate for the propagation time as (50pc)/(20km s^{-1}) $\approx$ 2.5 Myr. This is consistent with a more sophisticated model where we consider the expansion of the Strömgren sphere created by the stellar wind in ionized medium (Draine, 2011).

Timescale for Star Formation in the Cometary Feature: To get an estimate of the timescale for protostar formation in the cometary feature, we note that the spectral index for the six protostars in the cometary feature lies between 0.79 and 2.12, which identifies them as rising-SED protostars or class 0/I (Kryukova et al., 2014b). According to Evans et al. (2009), the lifetimes for protostellar classes 0 and I have values of 0.10 and 0.44 Myr or a maximum lifetime of 0.54 Myr.

Kinematic Timescale for Outflows: We esimate the kinematic timescale of the outflows as the spatial extent of the outflow divided by the outflow velocity to get (1 pc)/(0.7 km s^{-1}) ≈ 0.03 Myr.

Looking to the future, two other timescales are relevant to describe the evolution of this feature.

Free-fall Collapse Time: We calculate the free-fall collapse time for the feature given its mean density: $\sqrt{3/(32\pi G\rho)} \approx 0.3$ Myr.

Photoevaporation Timescale: We also calculate the rate at which photodissociation will destroy the feature, following the scaling in Schneider et al. (2016),

$$\dot{M} = 9.5 \times 10^{-9} \phi_{49}^{1/2} r_{14}^{3/2} d_{17}^{-1} \tag{2.16}$$

where $\phi_{49} = q_0/(10^{49}$ photons s$^{-1})$, R_{14}=$R/(10^{14}$ cm), and d_{17}= $d/(10^{17}$ cm) is the distance between the ionizing source and the feature. Plugging in values from Table 2.2, we estimate the time for the cloud to evaporate due to radiation to be $M/\dot{M} \approx 7$ Myr. Clearly, the photo-evaporation timescale is very long relative to all other timescales, so the cloud will collapse well before the material is dispersed by radiation.

We lay out these timescales in Figure 2.9. It is evident that the ionizing radiation front has arrived between 1 Myr ago and the present, which is consistent with the radiation front being originated from Cyg OB2. Ideally, in a triggering scenario, the ionization front would arrive slightly before (to left of) the −0.5 Myr mark so its arrival predates the collapse to form the protostars that we see. If the ionization front is not launched until relatively late in the evolution of the Cyg OB2 region (in the past 3 Myr), the front would arrive after stars start to form and there would be no triggering. However, such timing disagrees with the expected star formation history of the Cyg OB2 region (Wright et al., 2015). Thus, the timescales are consistent with a triggering scenario but cannot, by themselves, confirm that the region has been triggered by the ionization front.

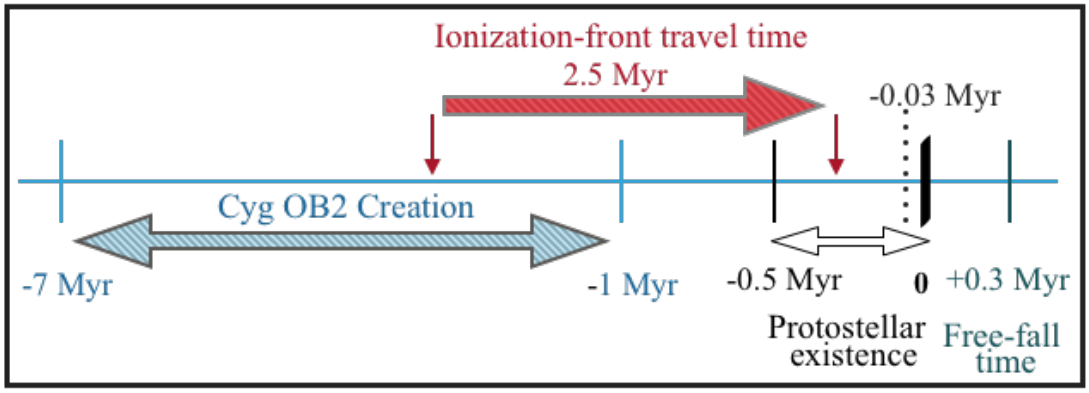

Figure 2.9: Schematic of the associated timescales for the cometary feature. The dark bold solid vertical line marks the present time. The markers on the left denote time lines in the past. The gray dotted line marks the beginning of the outflows.The solid big red arrow denotes the progress of ionization front in time with fixed length but variable ends marked by small vertical red arrows.

2.5.4 The Case for Triggering

This feature shows several indicators that the star formation may have been triggered by the ionizing radation from Cyg OB2. Given $P_{\rm ion} > P_{\rm mol}$, we are in the domain of radiatively-driven implosion from the pressure in the ionized gas. The illuminated bright rim as observed in Hα and radio continuum is evidence of a strong influence of the ionization front at the edge of the cloud. As discussed in sec 4.1, the pillar structure of the cometary feature with the tail pointed towards Cyg OB2 indicates radiation or shock waves coming from OB2, as it is the most likely source present in the vicinity. In addition, we have shown in section 4.3 that the timing is consistent with triggering.

This feature is similar to the classic triggered star formation scenario seen in the Eagle nebula. We compare characteristics of the two regions in Table 2.2. For the Eagle Nebula, total flux emitted by its ionizing source (1.9 pc away) is about $2{\times}10^{50}$ photons s^{-1} (Hester et al., 1996) which makes the total ionizing flux received at the tip of the pillars

$\left(q_0 = Q_0/4\pi d^2\right)$ much higher than that at the tip of the cometary feature, in which case $10^{50.8}$ photons s^{-1} are emitted by the possible ionizing source Cyg OB2 located at a much greater distance (50 pc). However, the gas mass is also much higher for the Eagle Nebula's pillar II. Therefore, this does not rule out the possibility of a collapse in the cometary feature imposed by the radiation front of Cygnus OB2. The relative profile of energy densities in the Eagle Nebula is quite comparable to that in the cometary feature as shown in Table 2.2, which also supports the case for triggering.

Although, Dale et al. (2015) clearly demonstrate that even with the above ensemble of circumstantial evidence the case for triggering cannot be made conclusively. Two features argue consistency with triggering as measured in simulations, namely, timing (refer to sec 4.3) and spatial correlation between the locations of the stars and the ionization front. The latter implies that in a large sample of cases of star formation, the distance between the ionizing front and the protostellar objects in a collapsing cloud serves as a (probabilistic) measure of confidence for triggered star formation. This result is shown in Fig. 4 of Dale et al. (2015).

We estimate that the protostars in the cometary feature have offsets of < 0.2 pc from the ionized rim. The statistical analysis of simulations given in Dale et al. (2015) implies that such small separations indicate the protostar formation was likely (Probability > 0.5) triggered by the ionizing front. However, without full knowledge of the previous evolution we are unable to make the case conclusively for this individual object.

While we cannot conclusively infer the past behaviour, there are some implications for future evolution of the region. The internal support for the region is relatively weak compared to the combined effects of self-gravity and external ionized gas pressure. The free-fall collapse time is short for the global region, particularly when compared to the photo-

evaporative timescale. Thus, the global collapse of this region seems inevitable. However, the region only requires a magnetic field of 70 μG to provide support and mitigate the collapse. Polarimetric observations of the dust continuum would be able to resolve the geometry and field strength to confirm the possibility of magnetic support.

2.6 Summary

This paper presents new JCMT ^{13}CO(3-2) and C^{18}O(3-2) mapping of a cometary feature in the Cygnus X star forming region. We use these new data and archival imaging to study the effects of radiative feedback on the cometary feature, evaluating whether the star formation was triggered by the ionization front. We calculated the properties of the region in detail, including molecular outflows being driven by protostars in the region. We report the following results:

- Using SED fits to the dust emission, we find the cometary feature has a mass of $M = 110$ M$_\odot$. Prior observations reveal that the source hosts the formation of at least 6 Class 0/I sources that are seen in the infrared (Kryukova et al., 2014b).

- Assuming LTE, we calculate the column densities of the CO isotopologues using the molecular line data. The fractional abundances of CO isotopologues are consistent with previous studies of molecular clouds with ^{13}CO/H$_2$ $\approx 10^{-6}$ and C^{18}O/H$_2$ $\approx 1.5 \times 10^{-7}$. The CO emission shows some signs of molecular depletion at the centre of the cometary feature.

- There are two molecular outflows present in the cometary feature (see Table 2.1). The outflowing mass is large ($M \approx 20$ M$_\odot$) but the properties of the outflow are comparable to massive outflows found in other systems. The velocities of the outflow are significantly larger than the escape speed of the clump, so outflowing gas will not provide significant energy or momentum support to the cometary feature.

- Using the radiocontinuum and the Hα emission, we estimate the conditions in the ionizing gas at the limb of the cometary feature, finding an electron density of n_e = 140 cm^{-3} assuming T_e = 8 000 K. Given the inventory of massive stars in the region, the most likely source providing the ionizing radiation to illuminate the edge of the cometary feature is the Cygnus OB2 complex of stars.

- The combination of external gas pressure and gravitational binding energy dominate the internal thermal pressure and outflow energies, which should prompt the cometary feature to completely collapse on a free-fall timescale (0.3 Myr). However, the strength and geometry of the magnetic field in the region is unknown and a field with a characteristic strength of $B \gtrsim 70$ μG could easily support the feature against collapse. We note that the clump is comparable to the cometary feature seen in M16, where the magnetic field is $B \sim 170$ μG (Pattle et al., 2018).

After reviewing the physical conditions of the molecular clump and the timescales and sources for a potential triggering scenario, we conclude that a radiatively driven implosion triggering the ongoing star formation is certainly plausible. However, numerical simulations show that is difficult to evaluate individual, small-scale triggering scenarios and come to a firm conclusion (Dale et al., 2015). In the light of those simulations and the detailed study presented here, we regard radiative triggering as the likely cause for the star formation observed here.

We acknowledge the support of the Natural Sciences and Engineering Research Council of Canada (NSERC), funding reference numbers RGPIN-2017-03987 and RGPIN 418517. The James Clerk Maxwell Telescope has historically been operated by the Joint Astronomy Centre on behalf of the Science and Technology Facilities Council of the United Kingdom, the National Research Council of Canada and the Netherlands Organisation for Scientific Research. We wish to recognize and acknowledge the significant cultural role and deep reverence that the summit of Maunakea has always had within the indigenous Hawaiian

community. We are truly grateful for the opportunity to conduct observations from this mountain. In addition to software cited in the paper, we also made use of the ASTROPY (Astropy Collaboration et al., 2013) and MATPLOTLIB (Hunter, 2007) software packages. The Dominion Radio Astrophysical Observatory is a National Facility operated by the National Research Council Canada. The Canadian Galactic Plane Survey is a Canadian project with international partners, and is supported by the Natural Sciences and Engineering Research Council of Canada (NSERC).

Chapter 3

Characterizing Outflows in the Cygnus X Region

This chapter is published as Deb et al. 2021: "Characterizing outflows in the Cygnus X region", Monthly Notices of the Royal Astronomical Society, Volume 503, Issue 1, May 2021, Pages 1264–1275.

3.1 abstract

In this paper, we perform an analysis of 13 outflows in the Cygnus X star-forming region. We use the James Clerk Maxwell Telescope observations of ^{13}CO(3-2) and C^{18}O(3-2) molecular emission lines combined with archival ^{12}CO(3-2) data. Using these new observations, we measure the mechanical properties of the outflows, and identify the associated protostars, finding their properties consistent with previous surveys of outflows throughout the Milky Way. Finally, we develop and test a method to measure the same properties using the existing ^{12}CO(3-2) line data alone, finding the properties agree to within a factor of 2.

3.2 Introduction

Star formation shapes structure and evolution of a galaxy by consuming gas and injecting feedback into the interstellar medium (ISM). A significant amount of feedback comes from the momentum and energy from the winds of massive stars but also some fraction of

feedback comes from protostellar outflows.

All accreting astronomical objects tend to have bipolar outflows or collimated jets, resulting from the interaction between the gravitational potential of the central rotating object and the magneto-centrifugal potential arising from the accretion disk (Krumholz, 2015; Bally, 2016). Accreting neutron stars, quasars, active galactic nuclei, and young stellar objects (YSO) all show bipolar outflows at some point in their lives. While the bipolarity, degree of collimation, and morphology of these outflows are similar regardless of their origin, some outflow properties depend on the central object. For example, for outflows generated by protostars, the ejecta velocities can vary from 1 to 100 km s^{-1}, whereas neutron stars can produce outflow velocities at a significant fraction of the speed of light.

Outflows set in as soon as the accretion disks around collapsing protostars are formed. The outflows associated with young stellar objects (protostars) provide useful information about the evolutionary stages of forming stars as well as the condition of the parent clouds, since the size, velocity, mass and momentum of the ejecta depend on the generating YSO (protostar) and the cloud environment (Bally, 2016).

Most YSOs show two components: a high-speed, relatively low-mass collimated jet of atomic or ionized matter, and a wide angled, slow-moving, massive molecular component. The bipolar atomic/ionized jet is emitted orthogonal to the plane of the accretion disk reaching large distances. The molecular component appears more closely connected to the rotating core. Outflows inject mass and momentum into the protostellar environment in opposite directions perpendicular to the plane of accretion, and the mass injection rate increases with the accretion rate (Ellerbroek et al., 2013). During the early stages of protostellar evolution, molecular outflows are the dominant sources of momentum and energy injection to the natal cloud. Additionally, the physical characteristics continuously evolve with the YSOs. In the early stages of class 0 YSOs, outflows are predominantly molecular and become progressively more atomic and ionized with increasing velocities as the YSOs evolve into class I.

Because of the multiple ionization states for outflowing material, several tracers are required for revealing all the different features of outflows. The atomic and ionized components of the jet are observed with radio and x-ray continuum emission and the (semi-) forbidden line transitions of atomic species in the optical and UV. While the molecular component can be traced through the infrared lines of H_2, the low-J rotational transition lines of CO molecules are the most commonly used tracers because of their brightness and their observability. The lines are bright because of the relatively high fractional abundance of CO and the high likelihood of collisions with H_2 and He that populate the low-J states. The low J transitions can be observed in the millimetre/submillimetre regimes with ground-based facilities. In addition, high spectral resolution observations can measure the Doppler broadening of the spectral line profile, which reveals the characteristic line wing features in outflows. These line wings extend 10 to 100 km s^{-1} from the line centre.

With molecular spectroscopy we can measure several properties of the outflows using bipolar wings. The standard properties inferred are size, morphology, mass, momentum, energy, and mechanical luminosity. By comparing these quantities with the proto-stellar luminosity, we constrain the accretion time, the efficiency of outflow launching, and the momentum and energy injection rates into the ISM. For low-mass cores this feedback is conjectured to play a significant role in providing turbulence and maintaining virial balance against the core gravitational energy in collapsing clouds. For massive cores, outflow feedback can potentially disrupt and shred the cloud (Bally, 2016). However, the impact of outflow feedback and its coupling to the parent clouds remains uncertain. Some studies have argued that outflows provide a minimal contribution of feedback (e.g., Hansen et al., 2012a) and may not be effective at driving local cloud turbulence (Swift & Welch, 2008; Duarte-Cabral et al., 2012; Drabek-Maunder et al., 2016). However, these estimates rely on careful characterization of outflow properties over a large region within the host molecular cloud. The impact of outflows could be larger than previously considered. Dunham et al. (2014) argued that outflow mass, momentum estimated from low-J CO lines only

provide lower limits on those quantities given the standard assumptions about opacity and line excitation.

Most outflow studies have focused on the nearest star-forming regions, which are mostly relatively quiescent. The Orion molecular cloud is the nearest site of high-mass star formation and remains the case study for outflows and feedback from newly forming O and B stars (Bally, 2016). However, on Galactic scales, Orion is a relatively small molecular cloud and more distant regions contain larger molecular clouds and a wealth of outflow activity. In this work, we study the Cygnus X region, a massive molecular cloud complex associated with the spiral arm. Cygnus X is the most active star-forming region within 2 kpc and shows a range of outflow behaviour across the region.

This work is a follow-up of a survey of the Cygnus X region in ^{12}CO(3 − 2) emission made with the James Clerk Maxwell telescope (JCMT) by Gottschalk et al. (2012, hereafter G12). The G12 work identified 47 molecular outflows in the ^{12}CO emission. In this work, we present ^{13}CO(3 − 2) and C^{18}O(3 − 2) observations of 13 of these outflows to measure their properties. This work extends the analysis presented in Deb et al. (2018, hereafter D18), which studied one object in detail in the context of triggered star formation. Here, we use standard approaches to measure the outflow properties for the combined sample of 13 outflows.

In addition, we also develop a procedure to measure the properties of outflows using only the ^{12}CO(3 − 2) emission line. This method is motivated because we have carried out a wide area survey of the Cygnus X region in ^{12}CO(3 − 2) emission using the JCMT that will be presented in forthcoming work (Deb et al. in preparation). As part of that survey, we have identified hundreds of protostellar outflows. Measuring the properties using multiple CO tracers of those outflows would require a heavy investment of telescope time. Hence, validating the methods for a single-tracer measurement of outflow properties is important for studying outflows in the context of feedback.

Specifically, we detail our observational techniques and data extraction in Section 4.5.

In Section 3.4.3, we discuss the properties of all three CO rotational lines and assuming a constant excitation temperature among all species we determine the optical depths and column densities of the optically thin lines as functions of position and velocity offsets from the line centre. Section 3.4.4 shows how we calculate mass, momentum, and energy of the molecular outflows using all three tracers following a similar approach as D18. Finally, in section 3.5 we present a model for extracting outflow properties from ^{12}CO(3-2) line alone and compare the results to the three-line estimates.

3.3 Observations

Here, we have used rotational transition lines ^{13}CO(3-2) and C^{18}O(3-2) observed in the bands centered at 330.58 and 329.33 GHz, respectively, using the JCMT at the summit of Mauna Kea in Hawai'i, using the Heterodyne Array Receiver Program (HARP) instrument and the Auto Correlation Spectral Imaging System (ACSIS) spectrometer (see also D18). In Table 3.1, we summarize some of the observational details of the 13 outflow sources, including project codes, weather bands and mean atmospheric opacity values at 225 GHz during the observational runs (March 2010, and July 2011) at the JCMT. Most sources were observed using "jiggle" mapping but the largest source was observed using a raster map. We configured the receivers and ACSIS correlator to provide 61 kHz spectral resolution in simultaneous observations across the two spectral lines.

The 13 outflows presented here were part of the larger sample of outflows identified in G12. For this project the brightest outflows from G12 were selected. While we planned to observe more outflows, we only obtained data on these 13 targets based on the constraints set of observational feasibility (telescope scheduling and weather). Thus, our actual sample is not designed to statistically represent the parent outflow population.

For data reduction, we used the observatory-maintained STARLINK software package (Currie et al., 2014) and the standard reduction and calibration recipes developed for the JCMT. The observatory provides calibrated data on the $T_{\rm A}^{*}$ scale (antenna temperature corrected

for atmospheric opacity, but not for source-beam coupling). We convert the data to the main beam temperature scale by assuming a beam efficiency based on observatory recommendations of $\eta_{\rm MB} = 0.64$[1] and setting $T_{\rm MB} = T_A^*/\eta_{\rm MB}$. We grid these data into position-position-velocity spectral line data cube with a beam size of 14.6″ (pixel size of 7.3″) and velocity resolution of 0.055 km s^{-1}. The central spatial coordinates of each cube are shown in Table 3.1 (refer to D18 for more details). For each position, we defined an emission-free region of the baseline by-eye and then subtracted a linear baseline. Additionally, we have archival ^{12}CO(3-2) line data from G12, which we re-sampled and aligned to match the same coordinate grid as the ^{13}CO(3-2) and C^{18}O (3-2) data. The median values of RMS noise in the final ^{13}CO(3-2) and C^{18}O(3-2) data cubes are 0.31 K and 0.38 K in 0.055 km s^{-1} channels, respectively. The noise values for the archival ^{12}CO(3-2) data at the same velocity resolution are larger (typically 0.4 to 0.8 K) but this line is always strongly detected. All three lines are detected at $> 5\sigma$ at some position in each of the targets.

The locations of the 13 observed outflows are shown in Figure 3.1 with a background of 8 μm PAH emission, which highlights the regions of star formation in Cygnus X (Crocker et al., 2011; Peeters et al., 2004). The large cavities in the 8 μm emission surround regions where molecular gas was destroyed by newly formed stars giving the popular "Swiss cheese" appearance (Bally et al., 1999a). The observed outflows are all located near the DR21 region, with eight in the active star-forming region and five outflows in satellite clouds, including the region studied in D18.

3.4 Results

Here, we present the observations of the individual outflows and describe how we measure their physical properties.

[1] https://www.eaobservatory.org/jcmt/instrumentation/heterodyne/harp/

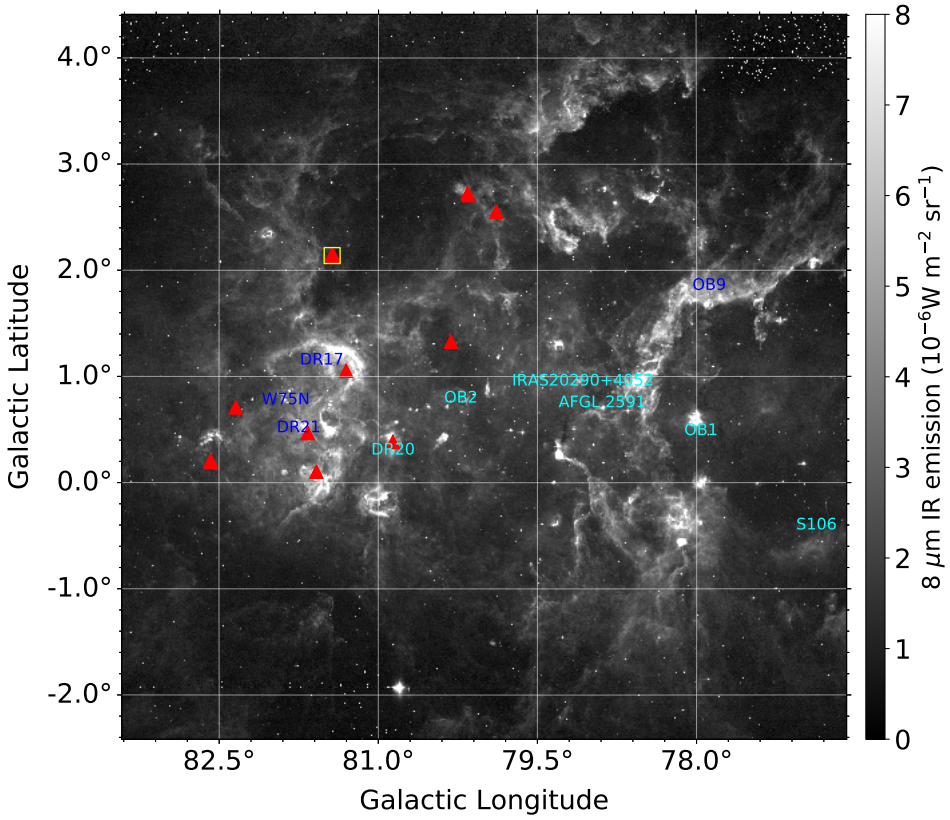

Figure 3.1: Dust thermal emission at 8 μm reveals molecular clouds in Cygnus X, with the major star-forming regions labeled (blue and cyan). Locations of the outflows discussed in this work are marked with red triangles. The yellow square denotes the location of the cometary feature discussed in Deb et al. (2018).

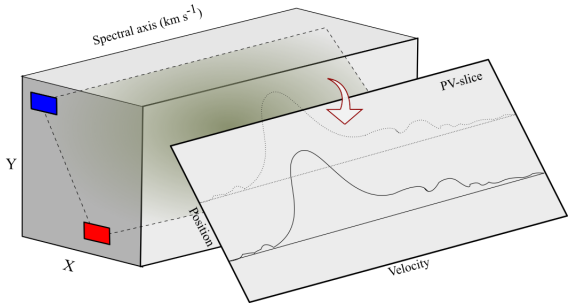

Figure 3.2: A position-velocity (PV) slice out of a data cube. The $x-y$ plane defines the plane of sight. The third axis is for frequency or equivalently velocity, along which spectral line profiles at each spatial pixel along the $x-y$ line as shown in the PV-slice.

3.4.1 Atlas of Outflows

Our primary data product is a multi-tracer atlas of these 13 outflows. In Figure 3.3 we show one of the molecular outflows, G79.886+2.552, from three complementary perspectives. We have included similar three-panel figures for the rest of the 12 sources in a supplemental document that is available online.

By eye, we extract a position-velocity (PV) slice from the data cube (Figure 3.2) that is centred on middle of the outflow and oriented so that the slice goes through the brightest part of the red- and blueshifted outflow lobes. We extract the property outflows from this PV slice. The PV-slice is one beam (14.6″) in width and the emission is spatially averaged perpendicular to the slice direction. We experimented with changing the slice widths but found that the results were most stable for the chosen width, acting as a compromise between including all emission from the outflow and including background emission from the molecular cloud.

The first panel of the atlas (Panel a) displays the spectrum for each of the three CO isotopologues averaged over the red- and blue-shifted sides of the PV slice as the red and blue curves, respectively. The spectrum shows the contrasts in the different line structure of the three species. The strong wing features are visible in the high opacity ^{12}CO(3-2) emission but the optically thin C^{18}O(3-2) emission is symmetric and useful for determining the line centre. The shaded bands in blue and red mark the regions we identify, again by eye, as belonging to the blue- and redshifted wings. We give the values for these boundaries in Table 3.1.

Panel (b) displays the integrated intensity maps of the ^{12}CO(3-2) emission, which reveal the spatial distribution (size and morphology) of the outflowing molecular gas. Red and blue contours represent the red- and blueshifted wings of the outflow, plotted over the background of total emission (gray-scale). The gray-scale shows the integration over the entire spectral line, but the blue and red contour sets indicate emission over the velocity ranges indicated in panel (a). Yellow stars show the positions of protostellar sources in the

region according to the catalogue of Kryukova et al. (2014a), which was generated from *Spitzer*-IRAC survey of the region. We have identified the infrared source that is driving the outflow, marked by a cyan star, by finding the protostar that best matches the position of the centre of the outflow.

Finally, in panel (c) we display the PV slice for the outflow. This panel shows the spatially-averaged contour lines of ^{12}CO(3 − 2) emission along the PV-slice against the background of spatially-averaged ^{13}CO(3 − 2) emission. The velocity offsets distributed over position offsets indicate the strength of bipolarity in the outflowing gas.

Table 3.1: Observational Summary. The Project ID is the designation from the JCMT. The last five columns give ranges for the blue- and redshifted wings of the outflow and the line centre.

Outflow	RA (J2000)	Dec (J2000)	Proj. ID	Atm. Opacity @225GHz	Min. blue Vel. (km s^{-1})	Max. blue vel. (km s^{-1})	Line centre vel. (km s^{-1})	Min. red vel. (km s^{-1})	Max. red vel. (km s^{-1})
G79.886+2.552	$20^h24^m31.6^s$	$+42°04'20.0''$	M10AC12	0.070	-20	0	6.3	12	+20
G81.435+2.147	$20^h31^m12.5^s$	$+43°05'42.0''$	M10AC12	0.069	-16	-5	-2.8	12.5	+15
G81.424+2.140	$20^h31^m12.3^s$	$+43°04'53.0''$	M10AC12	0.069	-14	-6	-3.1	-1.5	+10
G81.302+1.055	$20^h35^m33.5^s$	$+42°20'17.0''$	M10AC12	0.083	+8	14.5	15.4	17	+24
G80.314+1.330	$20^h31^m12.3^s$	$+41°42'30.0''$	M11AC10	0.062	-40	-33.5	-32.2	-29.5	-27
G80.862+0.385	$20^h37^m00.6^s$	$+41°35'00.0''$	M10AC12	0.060	-15	-5	-1.8	0	+8
G81.663+0.468	$20^h39^m15.9^s$	$+42°16'15.0''$	M10AC12	0.075	+10	16.5	19.3	23	+44
G81.551+0.098	$20^h40^m28.7^s$	$+41°57'21.0''$	M10AC12	0.061	-14.5	-8.5	-6	-4.5	+1.8
G81.582+0.104	$20^h40^m33.3^s$	$+41°59'05.0''$	M10AC12	0.082	-15	-8.5	-6.2	-4.5	+2
G82.581+0.203	$20^h43^m27.8^s$	$+42°49'58.0''$	M10AC12	0.120	-10.5	6.5	10.2	15.5	+32
G82.571+0.194	$20^h43^m27.9^s$	$+42°49'11.0''$	M10AC12	0.120	-4	7.5	11.0	13.5	+23

3.4.2 Distances

We determine the distances to each outflow based on their mean line-of-sight velocity. Referring to Rygl et al. (2012) and Gottschalk et al. (2012) we associate the outflows here with four different major star-forming regions in Cygnus X. The range of local standard of rest velocities ($v_{\rm LSR}$) of the 13 outflows are included in Table 3.1. Using water masers Rygl et al. (2012) determined the average proper motion velocities of the two star-forming regions W 75N and DR 21 to be 9 km s^{-1} and -3 km s^{-1}, along with their parallax distances. Hence we consider an outflow with a slightly positive velocity ($0 < v_{\rm LSR}/({\rm km\ s^{-1}}) < 8$) towards Cygnus X to be at the same distance as Cygnus Rift, which is at a mean distance of 650 pc from the sun (Gottschalk et al., 2012) and one with a low negative velocity ($-10 < v_{\rm LSR}/({\rm km\ s^{-1}}) < 0$ to be associated with DR 21, at 1.5 kpc. We associate outflows with positive LSR velocities ($v_{\rm LSR}/({\rm km\ s^{-1}}) > 8$) with W 75N, at 1.3 kpc. Outflows G81.435+2.147 and G81.435+2.147 are part of the cometary feature mentioned in Deb et al. (2018) and are being irradiated by Cygnus OB2 hence we assumed a distance of 1.4 kpc for them.

3.4.3 CO line emission: Column Density

To measure the physical properties of the outflows, we extend the work of D18 to determine the outflow column density as a function of velocity from the CO lines. The column density estimates are controlled by the opacity of the underlying tracer (Oosterloo et al., 2017), so we measure the opacity of the spectral line as a function of position using the three molecular rotational transitions (^{12}CO(3-2), ^{13}CO(3-2) and C^{18}O(3-2)). Using the radiative transfer equation and the emission model from Mangum & Shirley (2015), we express the spectral line emission in terms of radiation temperature as a function of optical depth τ_ν, $T_R = [J_\nu(T_{\rm b}) - J_\nu(T_{\rm bg})](1 - e^{-\tau_\nu})$, where $J_\nu(T) = \frac{c^2}{2k\nu^2}B_\nu(T)$ and $T_{\rm bg}$ is the constant background temperature, taken to be the cosmic microwave background ($T_{\rm bg} \approx 2.73$ K).

We assume local thermodynamic equilibrium (LTE) in the molecular gas, and use a

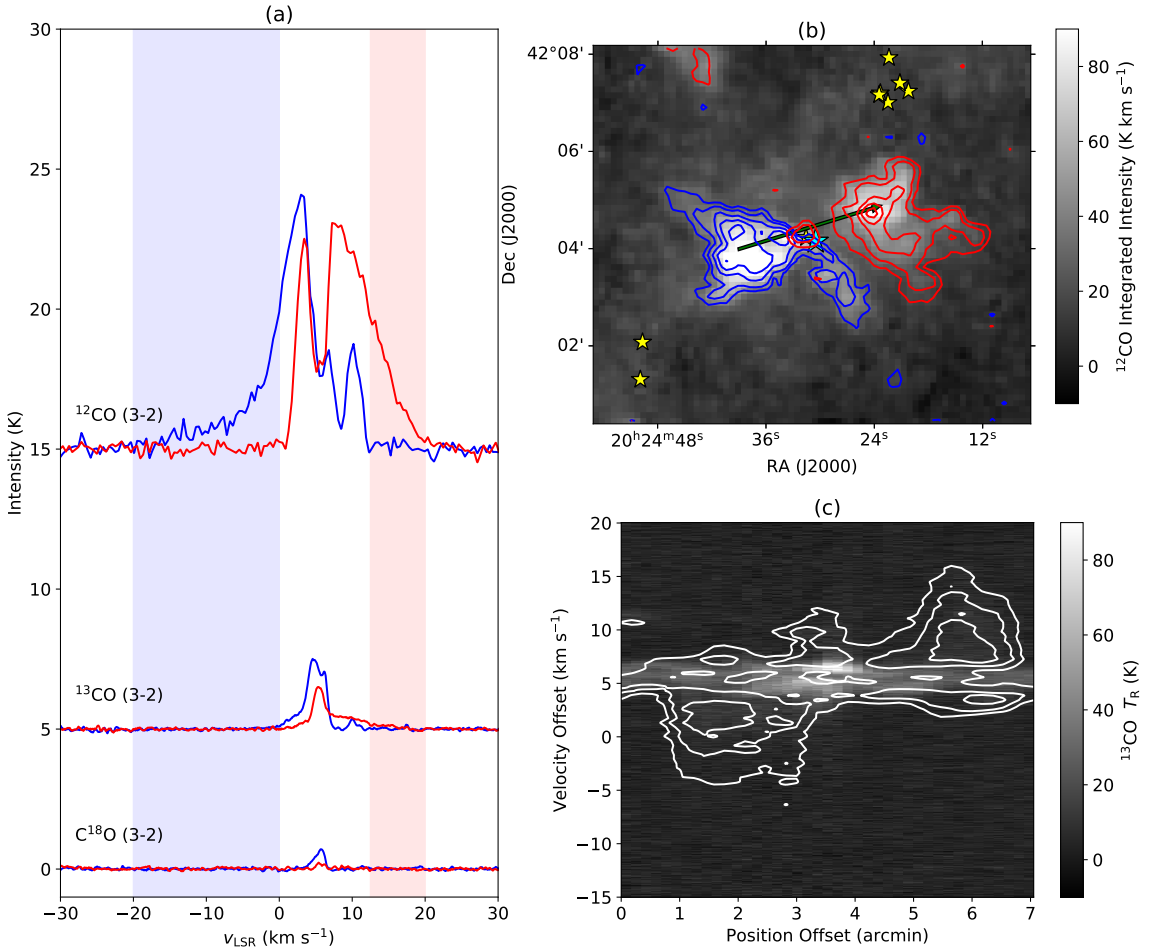

Figure 3.3: Outflow G79.886+2.552 : (a) Average spectral intensity in blue- and red-shifted outflow regions are shown in ^{12}CO(3-2) (offset +15 K), ^{13}CO(3-2) (offset +5 K), and C^{18}O(3-2) lines. The wing feature is present in ^{12}CO(3-2) line, which is self-absorbed in the line centre caused by the foreground Cygnus Rift. (b) Integrated intensity of ^{12}CO(3-2) line emission highlights the spatial distribution of molecular gas. Red and blue contours represent the red- and blueshifted wings, plotted over the background of total emission (gray-scale). Blue and red contours are obtained by integrating over velocity ranges of $v = -20$ to 0 km s^{-1} and $v = 12.5$ to 20 km s^{-1} respectively. Contour lines are drawn at levels (5, 10, 20, 30, 40) K km s^{-1} and (4, 8, 15, 20, 25) K km s^{-1} respectively. Yellow stars indicate protostars in Kryukova et al. (2014a) catalouge, with the driving IR source marked in cyan. (c) Spatial and spectral distribution of outflowing gas along the PV-slice marked by the green arrow in panel (b). Contours are drawn at levels (3, 5, 7.5, 9.5, 11) K.

constant molecular excitation temperature $T_{\rm ex}$ (corresponding to the rotational transition $J = 3 \rightarrow 2$) as the characteristic brightness temperature $T_{\rm b}$ associated with emission from all three species. We model the main beam temperature $T_{\rm MB}$, as

$$T_{\rm MB} = f[J_\nu(T_{\rm ex}) - J_\nu(T_{\rm bg})](1 - e^{-\tau_\nu}). \tag{3.1}$$

Here, f is the beam-filling factor and is assumed to be 1. We assume the ^{12}CO(3-2) line is optically thick, particularly near the line centre, so the excitation temperature can be approximated as

$$T_{\rm ex} = \frac{h\nu/k}{\ln\left[1 + \frac{h\nu/k}{T_{\rm max} + J_\nu(T_{\rm bg})}\right]}, \tag{3.2}$$

where $T_{\rm max}$ is the peak of the ^{12}CO(3-2) spectral distribution along each line of sight. Following Mangum & Shirley (2015), we have the column density of the top state of the transition for ^{13}CO(3-2) and C^{18}O(3-2) expressed in terms of their optical depth integrated over the Doppler-broadened spectral profile for every position (e.g., D18),

$$N_u = \frac{8\pi\nu_0^3}{c^3 A_{ul}} \frac{1}{e^{\frac{h\nu_0}{kT_{\rm ex}}} - 1} \int \tau_\nu dv. \tag{3.3}$$

Here, ν_0 is the equivalent rest frequency and A_{ul} is the Einstein coefficient for the $u = 3$ to $l = 2$ transition. We extrapolate total column density of the species using the partition function Q, which is well approximated as

$$Q \approx \frac{kT}{hB_0} \exp\left(\frac{hB_0}{3kT}\right). \tag{3.4}$$

With these assumptions, the total column density is

$$\begin{aligned} N_{\rm tot} &= \frac{Q}{g_u} \exp\left(\frac{E_u}{kT_{\rm ex}}\right) N_u \\ &= \frac{Q}{g_u} \exp\left(\frac{E_u}{kT_{\rm ex}}\right) \frac{8\pi\nu_0^3}{c^3 A_{ul}} \frac{1}{e^{\frac{h\nu_0}{kT_{\rm ex}}} - 1} \int \tau_\nu dv. \end{aligned} \tag{3.5}$$

For the C^{18}O line, the Einstein coefficient $A_{ul} = 6.011 \times 10^{-7}$ s^{-1}, $\nu_0 = 330.588$ GHz and the rotational constant $B_0 = 54891.42$ MHz. These values are obtained from LAMDA [2] (Schöier et al., 2005) and NIST[3] databases.

[2] http://home.strw.leidenuniv.nl/~moldata/

[3] https://physics.nist.gov/PhysRefData/MolSpec/

In star-forming clouds, $C^{18}O$ has a low abundance relative to ^{12}CO ($N_{C^{18}O}/N_{^{12}CO} \approx 1.5 \times 10^{-3}$) and ^{13}CO ($N_{C^{18}O}/N_{^{13}CO} \sim 0.1$) (Wilson & Rood, 1994), so it's often reasonable to assume the $C^{18}O$ emission is optically thin. However, the line can be optically thick in some regions of star formation as some authors have suggested (White et al., 2015). In our case, we verify this by following the approach outlined in (White et al., 2015; Ladd et al., 1998) to estimate the line-of-sight maximum optical depth of $C^{18}O$ (3-2) emission. This approach compares the brightness ratio of $T_{^{13}CO}/T_{C^{18}O}$ to an assumed abundance ratio of 8. Finding a brightness ratio significantly smaller than the abundance ratio would imply significant opacity in the $C^{18}O$ line. We estimate the $C^{18}O$ optical depth for the outflows for every pixel in the regions of significant emission. Then we compute medians of these values for each outflow. The median varies from 0.23 to 0.65 with corresponding standard deviation from 0.04 to 0.28. This may justify the treatment of $C^{18}O$ (3-2) line as optically thin. In this case, the optical depths for the two species are derived from Equation 3.1, in terms of their main beam temperatures,

$$C^{18}O : \tau_\nu = \frac{T_{MB}}{J_\nu(T_{ex}) - J_\nu(T_{bg})} \tag{3.6}$$

$$^{13}CO : \tau_\nu = -\ln\left[1 - \frac{T_{MB}}{J(T_{ex}) - J(T_{bg})}\right] \tag{3.7}$$

3.4.4 Physical properties of the outflows

We estimate the mass, momentum, and kinetic energy of each outflow given the CO column density measured as a function of line-of-sight velocity. We use the ^{13}CO(3-2) spectral line as the primary tracer of column density, since the optically thick low-J transition lines of ^{12}CO is subject to self absorption and will provide an underestimate of the mass near the line centre. The ^{13}CO(3-2) line has low signal-to-noise ratio in outflow wings. At large velocity offsets, it can be too weak to extract any useful information. Hence, we implement an extrapolation technique, adopted from Arce & Goodman (2001), for inferring ^{13}CO(3-2) emission from the brighter ^{12}CO(3-2) line. Using Equation 3.5, we express the column density of ^{13}CO(3-2) as a function of position offset (spatial pixel) and velocity along the

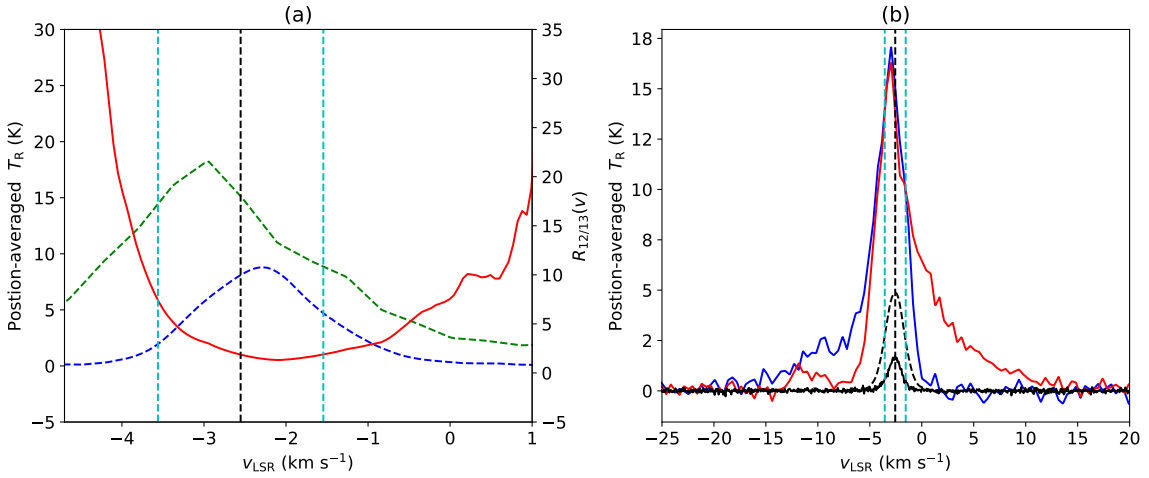

Figure 3.4: (a) Parabolic shape of $R_{12/13}(v)$ (red), plotted along with ^{12}CO(3-2) (green),^{13}CO(3-2) (blue) emissions. Local minimum occurs near the emission peak.(b) Spectral line profiles of ^{12}CO(3-2) (blue,red),^{13}CO(3-2) (dotted), and C^{18}O (3-2)(solid) show relative brightness values around the line centre that is best identified by C^{18}O. Bipolar outflow is best visible in ^{12}CO(3-2) line, where ^{13}CO(3-2) emission is insignificant. Vertical dotted lines in both panels denote velocity centroid (black) and 4σ limits (cyan) of the fitted Gaussian. Both diagrams are constructed from the data associated with outflow G81.435+2.147.

spectral axis in a position-velocity (PV) slice (D18),

$$N_{^{13}\mathrm{CO}}(x,y,v) = \frac{8\pi\nu_0^3 Q_{\mathrm{rot}}}{7c^3 A_{ul}} \frac{e^{\frac{E_u}{kT_{\mathrm{ex}}}}}{e^{\frac{h\nu_0}{kT_{\mathrm{ex}}}} - 1} \tau_\nu(\mathbf{x}, v)\, \delta v. \tag{3.8}$$

For calculating outflow properties we separate the asymmetric blue- and red-shifted wings of the spectral profile from the symmetric central components. As a first step, we estimate the velocity centroid v_0 of the line by fitting a Gaussian model to the C^{18}O(3-2) data, along with line width σ_v. We use C^{18}O(3-2) because it is optically thin and has a symmetric profile that is bright only around the line centre (Figure 3.4). We repeat this fitting process for every spatial pixel along the PV-slice (Figure 3.2). After fixing the line centre, we fit a quadratic function to the observed emission ratio of ^{12}CO(3-2)/^{13}CO(3-2), denoted by $R_{12/13}(v)$ since the line ratio typically resembles a parabola around v_0:

$$R_{12/13}(v) \;\hat{=}\; C_0 + C_2\,(v - v_0)^2.$$

This is done separately for each of the blue- and red-shifted lobes. We also set an upper limit of 65 for the ratio, based on the relative abundance of the two molecular species in molecular clouds (Wilson & Rood, 1994). The fitted ratio ranges between this value and a minimum at the velocities where the ^{13}CO(3-2) line is the brightest (Figure 3.4). Using the main beam temperature of ^{12}CO(3-2) (T_{12}) and the fitted ratio $R_{12/13}$, we can infer the ^{13}CO(3-2) main beam temperature ($\hat{T}_{13}$) where the signal is undetectable. Following a strategy adapted from Arce & Goodman (2001), we estimate $\hat{T}_{\mathrm{R},13}(x, y, v)$ in three regimes based on the signal-to-noise ratio of the two emission lines:

$$\hat{T}_{13}(x, y, v) = \begin{cases} T_{13} & \text{if } T_{13} \geqslant 5\,\sigma_{13} \\ \frac{T_{12}}{R_{12/13}} & \text{if } T_{13} < 2\,\sigma_{13},\ T_{12} \geqslant 2\,\sigma_{12} \\ 0 & \text{if } T_{13} < 2\,\sigma_{13},\ T_{12} < 2\,\sigma_{12}. \end{cases}$$

Here, the noise levels of the two lines are given as σ_{12} and σ_{13}. The last condition states that ^{13}CO(3-2) main beam temperature cannot be estimated when both emission lines are undetectable.

Using the optical depth (Equation 3.6) and the column density (Equation 4.2), we determine the H_2 column density $N_{H_2}(x, y, v)$ as $N_{H_2} = N_{^{13}CO}/X_{CO}$ by assuming a fixed abundance ratio $X_{CO} = 10^{-6}$ of ^{13}CO(3-2) relative to H_2 (Wilson & Rood, 1994). For the total mass in the outflow, we integrate $N_{H_2}(x, y, v)$ over blue- and red-shifted segments of the spectral axis at each position along the PV-slice and then sum over all such positions,

$$\begin{aligned} M_{\mathrm{outflow}} &= \mu_{H_2} \int_{\mathbf{x}} \int_{\mathrm{wing}} N_{H_2}(x, y, v)\, dv\, d\mathbf{x} \\ &\approx \mu_{H_2} \sum_{\mathbf{x},\mathrm{wing}} N_{H_2}(x, y, v)\, \delta v\, \delta A_{\mathrm{pix}}. \end{aligned} \tag{3.9}$$

Here, we have assumed a mean molecular mass per H_2 as μ_{H_2} =2.4 m_H (m_H assuming a 10% atomic He abundance by number. We determine the physical pixel areas by projecting the angular size of each pixel to the assumed distance of the outflow (Section 3.4.2; Table 3.2).

We also estimate the projected outflow momentum and energy using

$$p = p_0 \cos\theta = \sum M(x, y, v)|v - v_0| \tag{3.10}$$

$$E = E_0 \cos^2\theta = \frac{1}{2} \sum M(x, y, v)(v - v_0)^2 \tag{3.11}$$

where θ is the unknown inclination angle with respect to the line of sight and p_0 and E_0 indicated the unprojected momentum and energy. The results are summarized in Table 3.2. Table 3.3 includes the protostellar sources that generate the outflows, identified by searching the Kryukova et al. (2014a) catalogue, along with their infrared (IR) luminosity, except the source NOMAD1 1323-0477179 for which we were unable to find the spectral index value and IR luminosity.

We exclude the source G80.314+1.330 from further analysis. We were unable to find a protostar associated with the object G80.314+1.330 in existing catalogues. Gottschalk et al. (2012) identified this object as an outflow, which we also have confirmed using spectral distribution, contour, and PV plots (Figure 3.12). However, the high negative velocity (Table 3.1) and weak emission suggest that this outflow is unlikely to be located in Cygnus X but is likely located further away along the line of sight, likely in the Perseus arm. Hence, a protostar is too distant to be detected.

Table 3.2: Dynamical properties of the 12 outflows: mass, momentum, and energy columns for estimates from all three CO lines, discussed in section 3.4.4, along with corresponding estimates from ^{12}CO alone, discussed in section 3.5.

Outflow	Distance (kpc)	T_{ex} (K)	Mass ($M_\odot$)	^{12}CO-only Mass ($M_\odot$)	Momentum ($M_\odot$) km s^{-1}	^{12}CO-only Momentum ($M_\odot$) km s^{-1}	Energy (10^{45}ergs)	^{12}CO-only Energy (10^{45}ergs)
G79.886+2.552	0.65 ± 0.15	16	0.72 ± 0.16	0.42 ± 0.33	3.86 ± 0.89	1.82 ± 1.10	0.34 ± 0.08	0.15 ± 0.10
G81.435+2.147	1.4 ± 0.08	25	5.12 ± 0.29	1.42 ± 0.63	27.01 ± 1.55	6.40 ± 1.27	1.95 ± 0.11	0.40 ± 0.23
G81.424+2.140	1.4 ± 0.08	22	1.36 ± 0.06	0.70 ± 0.31	5.70 ± 0.29	2.31 ± 0.40	0.30 ± 0.02	0.09 ± 0.05
G81.302+1.055	1.3 ± 0.07	36	9.68 ± 0.52	5.18 ± 0.59	30.20 ± 1.62	18.72 ± 2.06	1.15 ± 0.06	0.97 ± 0.11
G80.862+0.385	1.5 ± 0.08	31	4.65 ± 0.24	4.70 ± 0.54	31.8 ± 1.66	22.31 ± 2.51	1.48 ± 0.11	1.34 ± 0.13
G81.663+0.468	1.3 ± 0.07	19	2.90 ± 0.17	1.56 ± 0.14	21.30 ± 1.15	14.58 ± 1.30	2.06 ± 0.16	1.50 ± 0.14
G81.551+0.098	1.5 ± 0.08	17	1.43 ± 0.08	0.33 ± 0.04	2.94 ± 0.16	0.80 ± 0.09	0.08 ± 0.004	0.05 ± 0.002
G81.582+0.104	1.5 ± 0.08	24	3.68 ± 0.20	1.41 ± 0.15	7.50 ± 0.40	8.00 ± 0.85	1.69 ± 0.01	0.47 ± 0.05
G82.581+0.203	1.3 ± 0.07	20	2.13 ± 0.11	1.27 ± 0.14	12.84 ± 0.68	8.21 ± 0.94	1.48 ± 0.08	0.74 ± 0.08
G82.571+0.194	1.3 ± 0.07	18	1.16 ± 0.06	0.33 ± 0.04	3.38 ± 0.18	1.25 ± 0.14	0.22 ± 0.01	0.08 ± 0.01
G80.158+2.727	0.65 ± 0.07	16	1.50 ± 0.16	0.32 ± 0.07	6.22 ± 0.68	1.21 ± 0.23	0.43 ± 0.05	0.06 ± 0.01
G80.149+2.710	0.65 ± 0.07	27	0.18 ± 0.02	0.36 ± 0.08	1.13 ± 0.12	1.10 ± 0.23	0.13 ± 0.01	0.08 ± 0.01

3.5 Estimation of outflow properties based on ^{12}CO(3-2) data

Outflows are ubiquitous in wide-area surveys of molecular emission (Gottschalk et al., 2012; Drabek-Maunder et al., 2016), and the feedback from outflows into the molecular ISM is best understood in the context of these large surveys. However, a full determination of outflow properties requires multiple isotopologues (Section 3.4.3) and, ideally, multiple rotational transitions from those isotopologues to measure both opacity and excitation temperature (Dunham et al., 2014). While ideal, observing all these transitions is expensive in terms of telescope time, so approximate methods are needed to interpret survey data.

To analyze outflows in the wide area survey of Cygnus X (Deb et al. in preparation), we need to estimate outflow mass and other dynamical properties without ^{13}CO(3-2). A common approximation is to estimate an optical depth correction factor, $\frac{\tau_{12}}{1-e^{-\tau_{12}}}$, to measure out mass from the ^{12}CO(3-2) line alone (Zhang et al., 2020; Plunkett et al., 2015; Dunham et al., 2014; Ginsburg et al., 2011). However, even with the correction factor the mass estimate from ^{12}CO(3-2) alone could still be an underestimate by 0.5 to 1 dex (Ginsburg et al., 2011), because the assumption of ^{13}CO(3-2) to be optically thin in the outflow wings may not be valid for lower velocity offsets from the line centre (refer to section 3.6.2).

Here, we use our in-hand data on ^{13}CO emission to calibrate empirical relationships between the observed ^{12}CO(3-2) emission (T_{12}) and the outflow properties as characterized from the full analysis of the ^{13}CO(3-2) data (section 3.4.3). Specifically, we empirically estimate the opacity that would be seen in the ^{13}CO line, which we infer based on the brightness of the ^{12}CO emission. The empirical estimate avoids using the (unobserved) $T_{\rm MB}$ for ^{13}CO and scales the ^{12}CO brightness directly to the ^{13}CO optical depth. We also estimate the line centroid and width so we can define the velocity ranges that correspond to the wings of the outflow and the velocities relative to the line centre.

Our empirical relationship between ^{12}CO brightness and ^{13}CO optical depth is shown in Figure 3.5, where we fit a linear relationship between the log of both quantities. Since the

Table 3.3: Protostellar sources associated with the 12 outflows, as identified in Kryukova et al. (2014a).

Outflow	Distance (kpc)	IR Source	Angular Separation	Spectral Index	L_{IR} $\log(L/L_{\odot})$
G79.886+2.552	0.65 ± 0.15	J202430.49+420409.19	16.42″	0.16	1.87
G81.435+2.147	1.4 ± 0.1	J203111.82+430521.66	21.70″	2.12	0.84
G81.424+2.140	1.4 ± 0.1	J203112.70+430457.56	6.30″	0.91	0.45
G81.302+1.055	1.3 ± 0.1	J203534.44+422006.80	14.58″	1.23	1.95
G80.862+0.385	1.5 ± 0.1	J203702.60+413440.97	8.76″	1.34	1.72
G81.663+0.468	1.3 ± 0.1	J20391672+4216090.00	10.94″	−0.05	2.39
G81.551+0.098	1.5 ± 0.1	J204028.48+415711.97	9.36″	1.64	2.04
G81.582+0.104	1.5 ± 0.1	J204033.48+415900.63	4.81″	1.87	0.95
G82.581+0.203	1.3 ± 0.1	J204322.87+425022.76	59.64″	0.93	−0.58
G82.571+0.194	1.3 ± 0.1	J204328.27+424900.09	11.64″	0.82	2.28
G80.158+2.727	0.65 ± 0.15	J202434.18+422331.60	19.28″	0.84	1.56
G80.149+2.710	0.65 ± 0.15	NOMAD1 1323-0477179	17.51″	···	···

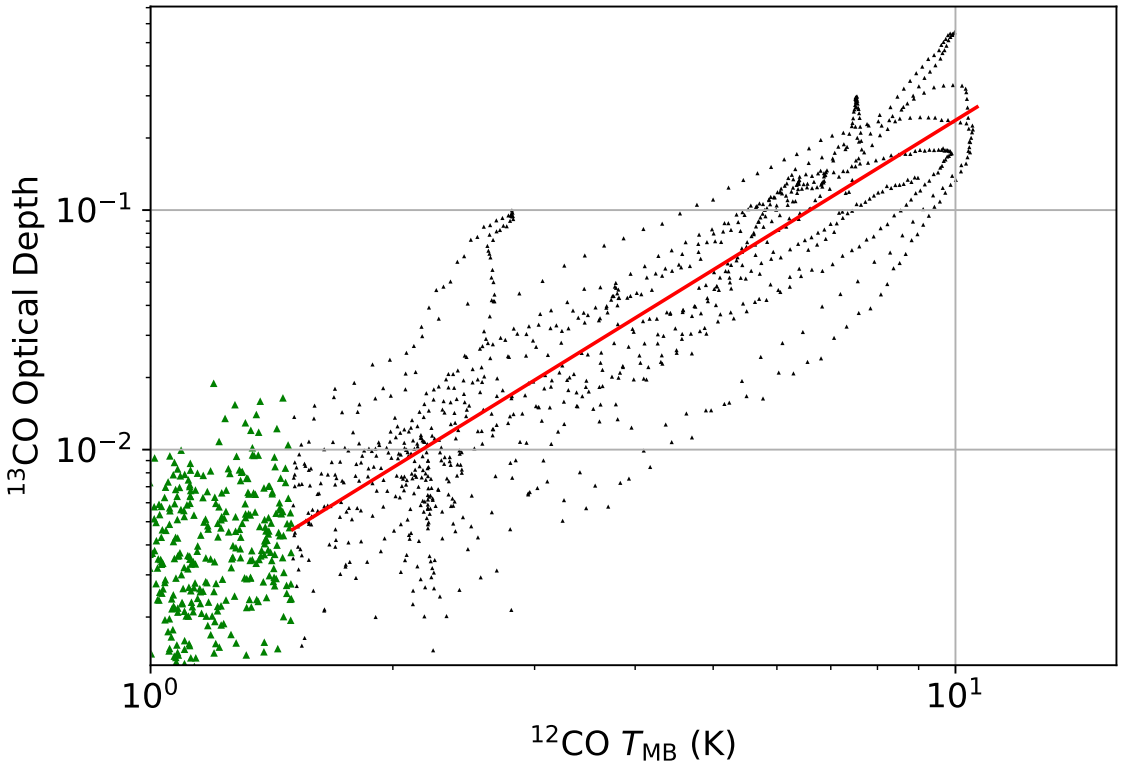

Figure 3.5: Scatter plot shows the association between ^{12}CO(3-2) emission in terms of position-averaged main beam temperature in K and ^{13}CO(3-2) optical depth. The raw data set is divided into detectable signal (in black) and noise ($< 2\sigma_{12}$, in green). The straight line (in red) denotes the line of best fit.

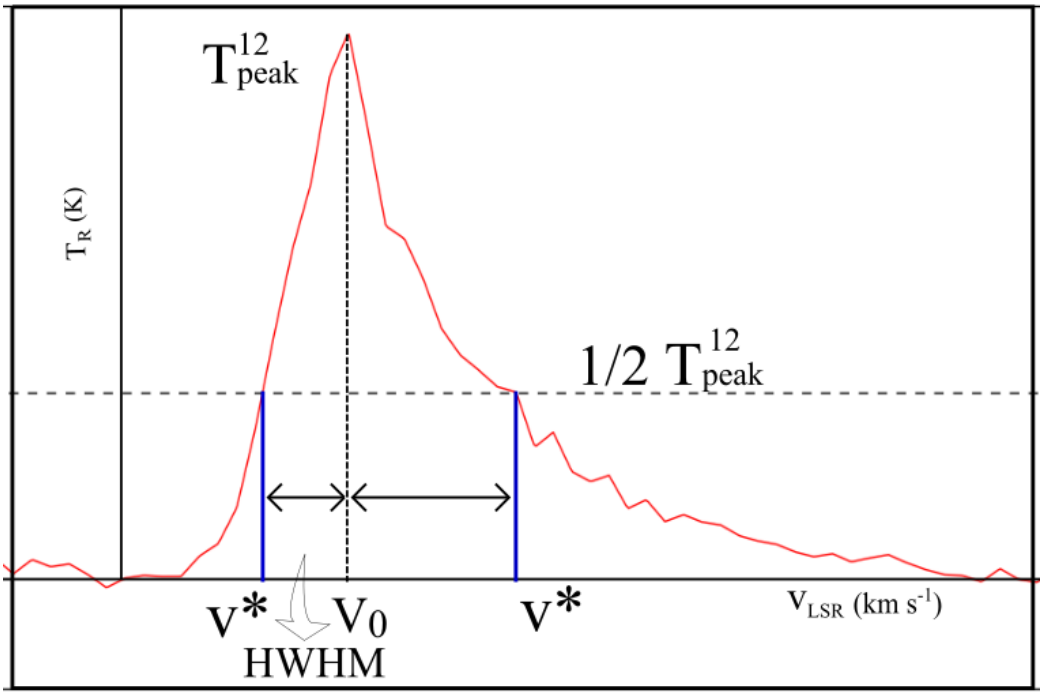

Figure 3.6: A schematic view of HWHM estimation technique from a spectral line profile

^{12}CO(3-2) line observations were stored as a data cube (Figure 3.2), we average the value $T_{12}(x, y, v)$ over the position coordinate. Similarly, our estimate of $\tau_{\nu,13}$ is from the full analysis in 3.4.3, and we again average$\tau_{\nu,13}(x, y, v)$ over position coordinates. Figure 3.5 shows the scatter plot of $(\tau_{\nu,13}, T_{12})$, for all outflows included in Table 3.2. We perform a linear regression on the bivariate set, with adjusted-R^2 = 0.8 and F-statistic= 3538 demonstrating a strong relationship. The best fit in log-space is given by,

$$\log_{10}\tau_{\nu,13} = -2.69 \pm 0.02 + (2.07 \pm 0.04) \times \log_{10} T_{12}. \tag{3.12}$$

Using this fitted equation, we estimate ^{13}CO column density as a function of position and velocity in a PV-slice, again by assuming a mean particle mass of $\mu_{H_2} = 2.4 m_H$ and using distances of the outflows from the sun.

To estimate the wing mass, we also estimate the profile line centre v_0 and velocity width σ_v. Unlike in Section 3.4.4, here we assume we do not have access to ^{13}CO(3-2) and C^{18}O(3-2) data, so we approximate the ^{12}CO(3-2) spectral line with a Gaussian profile. We then estimate the line centre by leaving v_0 as a free parameter and minimizing the outflow

kinetic energy along each line of sight in the PV slice.

Next, we calculate σ_v by measuring the half width at half maximum (HWHM) of the line profile, where for a Gaussian, HWMW = $\sqrt{2 \ln 2}\,\sigma_v$. Since the line profile is asymmetric, we measure the HWHM on both sides of v_0 and take the minimum width as the line width as shown in the schematic Figure 3.6. We measure the HWHM by finding the velocity channels v^* corresponding to the brightness $\frac{1}{2}T^{12}_{\rm peak}$ where $T^{12}_{\rm peak}$ denotes the maximum of $T_{\rm MB}$ for a spectral profile. In that case, referring to figure 3.6, we can write,

$$\text{HWHM} = \min_{v^*} |v^* - v_0|.$$

There is foreground absorption observed in the outflow spectra (Figure 3.3), which is possibly caused by the foreground Cygnus Rift. This absorption feature, however, does not alter the estimation of v_0 and σ_v because the outflow wings are unaffected by the absorption. The inferred value of σ_v can be up to a factor of two larger than the value measured directly from the observed ^{13}CO(3-2) line.

We define the outflow velocity wings as spectral regions with $|v - v_0| > 2\sigma_v$. The mass estimate is obtained by summing over such velocity channels and position offsets along the PV-slice. The estimated values of mass, projected momentum and projected energy are included in Table 3.2. Similar to section 3.4.4, momentum and energy values estimated from ^{12}CO alone contain unknown projection angle with respect to the line of sight. In Figure 4.7, we compare the property estimates for the ^{12}CO-only method vs those derived from using all three lines. Considering the small sample size, there is good correlation between the fitted the estimated values but some measurable systematic differences. Table 3.4 summarizes the typical differences. The mean mass from ^{12}CO alone is typically 0.31 dex (a factor of 0.48) smaller than the estimates from all CO lines. The momentum and energy values are also a factor of 0.47 and 0.53 smaller than the corresponding estimates from all CO lines. The consistent slight underestimation of outflow energetics is attributed to the larger inferred ^{12}CO(3-2) value of σ_v mentioned before. Table 3.4 also notes the width of the distribution, which is comparable to the offset that we measure. We do not apply any

$\log_{10}$(^{12}CO-only / All lines) quantities	Mean	Standard deviation
Mass	−0.31	0.26
Momentum	−0.32	0.23
Energy	−0.28	0.31

Table 3.4: Comparison between outflow properties from the approximations using the ^{12}CO(3-2) line alone and those estimated from all three CO lines. On average, this approach systematically underestimates dynamical properties by ∼ 0.3 dex, which should be included in an error budget.

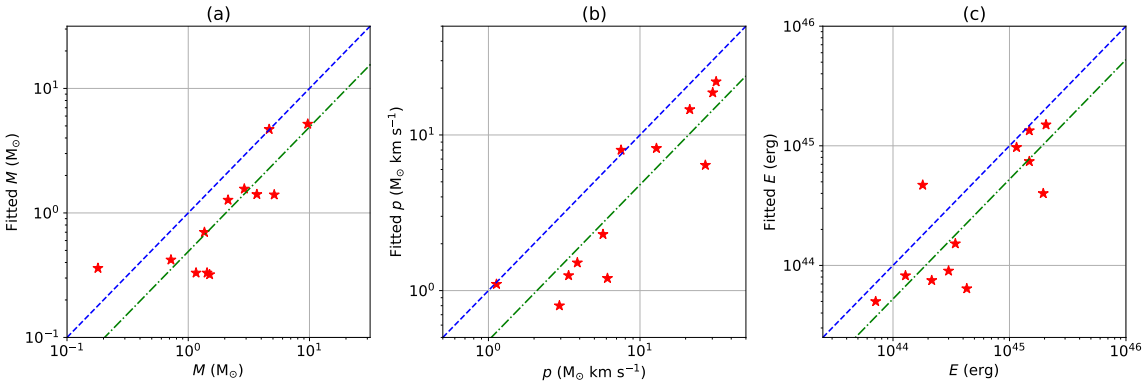

Figure 3.7: Scatter plots show comparison between outflow mass (M), projected momentum (p) and projected energy (E) estimated from ^{13}CO(3-2), ^{12}CO(3-2) and C^{18}O(3-2) data (x-axis) and those estimated from ^{12}CO(3-2) alone (y-axis). Blue dashed lines denote perfect correlation. Green dash-dotted lines denote the relationship between three-line estimated values ^{12}CO-only values. A comparison between the two sets of lines shows a consistent underestimation of the outflow properties.

ad hoc scalings at this point to the ^{12}CO-only estimates to bring them into agreement with the full analysis, but we will consider the offsets and spread in Table 3.4 as part of our error budget.

3.6 Discussion

3.6.1 Outflow Properties and Protostellar Sources

We have estimated several dynamical properties of 12 outflows and identified their infrared sources using the Kryukova et al. (2014a) catalogue. Based on the spectral index (α) value,

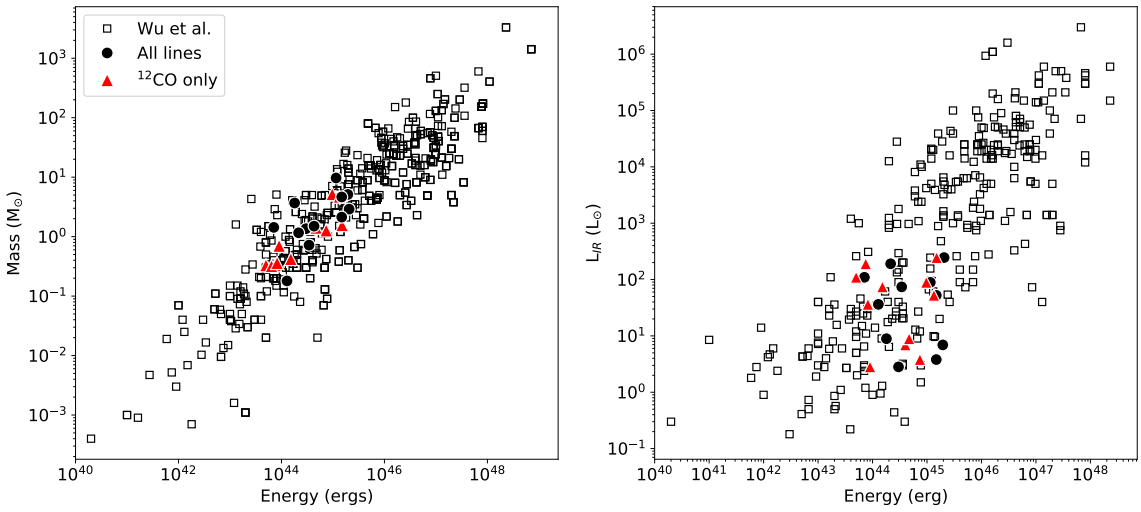

Figure 3.8: (left) Scatter plots show outflow mass plotted against energy. Red triangles denote quantities estimated from only ^{12}CO(3-2) data. (right) Infrared luminosity plotted against outflow energy. Colour scheme is the same as in (left). The Cygnus X outflows are consistent with the broader population irrespectrive of the method used for property estimation.

we categorize J202430.49+420409.19 and J20391672+4216090.00 as flat-spectrum protostars. All of the remaining protostars have spectral index values (defined as α in $F_\nu \propto \nu^{-\alpha}$) greater than 0.3. These values imply they are in their early stages of evolution and belong to either class 0 or class I. The early evolutionary stages also implies the bolometric luminosity is approximately the same as infrared luminosity ($L_{\rm IR}$), included in Table 3.2. We were unable to find luminosity and spectral index value for NOMAD1 1323-0477179, which was referred as the IR source associated with the outflow G80.149+2.710 in Gottschalk et al. (2012). It is likely that the IR source of this outflow is a deeply embedded class 0 protostar in its early stages of evolution.

As suggested from previous analyses (Bally, 2016, and references therein), we examined the correlation between mechanical luminosity $L_{\rm mech}$, or infrared luminosity $L_{\rm IR}$ and spectral index. As defined, a lower value of spectral index indicates a more evolved protostar. Outflow energy, IR and mechanical luminosities nominally decrease as the protostar evolves, the highest being achieved in the early stages, we would expect a positive correlation of these outflow properties with increasing spectral index. In our sample such

correlation is observed but is extremely weak with large scatter. We attribute this to having a small, heterogeneous sample of outflows at various distances and the narrow range of spectral index that is recovered. We will revist these scalings in the context of the larger outflow survey (Deb et al., in preparation).

For context, we compare our sample with the catalogue of Wu et al. (2004), which assembles a meta-analysis of outflow properties from the literature. The 12 outflows are broadly consistent with the population of outflows with respect to all their measured properties. In particular, we find that the mechanical luminosity $L_{\rm mech}$ is, on average $\sim 10^{-3} L_{\rm IR}$, which traces the accretion power, consistent with other sources.

3.6.2 Uncertainties in Parameter Estimates

We have used CO lines for estimating outflow mass, momentum and energy, which are subject to significant uncertainties based on our assumptions. Even so, CO molecules remain the best species for studying the molecular outflows because of their high line intensity, low critical density, near-LTE excitation modes, and their relatively large abundances relative to other molecules.

Our estimates of outflow properties from a single ^{12}CO line is similar to other approaches forwarded in the literature. Among early work involving CO lines, Bontemps et al. (1996) estimated outflow momentum flux from ^{12}CO (2-1) emission using $p \propto \int_{\rm wings} T_{\rm R}^{12}(v) dv A(r, dr) v^2$, r denotes the radius of a projected annulus orthogonal to the outflow direction and dr is the width of such annulus. This is comparable to the approach discussed here, with modifications since the authors estimated momentum from ^{12}CO emission in terms of radiation temperature and integrating over the spectral and spatial spread of the outflowing gas. Another common assumption found in the literature is that outflow wings are optically thick in the ^{12}CO line (Bally et al., 1999b; Arce & Goodman, 2001; Dunham et al., 2014; Wilson et al., 2013). An optically thick tracer only reflects the conditions of the surface of the cloud, thus results in an underestimation of mass, and

subsequently of momentum and energy. We use the optically thinner ^{13}CO(3-2) line for tracing H_2 column density in the outflow wings, although we have not made any explicit assumption that $\tau_{13} \ll 1$. Instead, we rely on the assumption of a constant excitation temperature for all lines and for all species. Bally et al. (1999b) suggested a similar method for estimating wing column density from ^{13}CO (1-0) line. The authors used the observed ^{13}CO emission when it was above the RMS noise level and extrapolated from ^{12}CO (1-0) using a second-order fitted polynomial ratio $R_{12/13}$ when ^{13}CO was below the noise level. However, the authors used a different intrinsic abundance ratio, which provides a corresponding limit for the fitted brightness ratios ($R_{12/13} \leqslant 89$).

Some authors suggested estimating mass from ^{12}CO(3-2) brightness by using an opacity correction factor $\frac{\tau_{12}}{1-e^{-\tau_{12}}}$ (Dunham et al., 2014). This is done by assuming ^{13}CO(3-2) is optically thin, thereby numerically solving τ_{12} from the observed ratio $R_{12/13}$ using Equation 3.1 under LTE, and here using a ^{12}CO/^{13}CO abundance ratio of 65 (Wilson & Rood, 1994),

$$R_{12/13} = \frac{T_{12}}{T_{13}} = \frac{1 - e^{-\tau_{12}}}{1 - e^{-\tau_{13}}} \approx 65 \frac{1 - e^{-\tau_{12}}}{\tau_{12}} \tag{3.13}$$

$\frac{\tau_{12}}{1-e^{-\tau_{12}}}$ compensates for ^{12}CO(3-2) being optically thick in line wings,

$$\hat{T}_{12} \sim 65\, T_{13} = \frac{\tau_{12}}{1 - e^{-\tau_{12}}} T_{12}. \tag{3.14}$$

The factor $\frac{\tau_{12}}{1-e^{-\tau_{12}}} \sim \tau_{12}$. Wilson et al. (2013) note that Equation 3.14 would overestimate the ratio $R_{12/13}$ in Equation 3.13 by an amount that scales with τ_{12}, resulting in an underestimation of the opacity correction factor. This underestimate arises because the assumption that ^{13}CO(3-2) is optically thin may not be true near the line centre. The opacity profile can vary from one outflow to another. This ambiguity motivated our empirical model for determining the gas column density in outflow wings using the conditional estimation technique described in section 3.4.4.

Our primary assumption is that all three CO lines are in LTE and have the same thermal excitation temperature $T_{\rm ex}$. Ginsburg et al. (2011) caution that while lower-J transition lines of ^{12}CO might be in LTE, ^{12}CO(3-2) may not be in LTE because of its high critical

density value (27× greater than $J = 1 \rightarrow 0$ line). In this case, the ^{12}CO(3-2) line may be subthermally excited ($T_{\rm ex} < T_{\rm K}$), which following the expression for ^{13}CO(3-2) optical depth and Equation 4.2, implies the gas column density is underestimated. The mass and other dynamical properties would also then be lower limits. However, the authors mentioned their sample sizes were small and their claim of ^{12}CO(3-2) being a poor tracer for column density in outflows is more relevant for later stages of evolution with warmer gas. By comparing the rotational transition lines of ^{12}CO Ginsburg et al. (2011) showed that the $J = 3 \rightarrow 2$ line produces lower estimates of column density than the $J = 2 \rightarrow 1$ and $J = 1 \rightarrow 0$ lines for gas at higher excitation temperatures ($T_{\rm ex} > 20$K). In contrast, Plunkett et al. (2015) measured mass and other dynamical properties by adopting specific fixed values of $T_{\rm ex}$ as well as a functional form of $T_{\rm ex}$ that varied from pixel to pixel. This may be generally better than our method of estimating column density $T_{\rm peak}$ of ^{12}CO(3-2) emission in LTE as described in section 3.4.4. However, the pixel-by-pixel $T_{\rm ex}$ profile does not produce significantly different values, unless the gas is warm ($T_{\rm ex}$ >50 K) (Plunkett et al., 2015). In our case, the estimated excitation temperature ranges from 16 K to 36 K which, following the argument of Plunkett et al. (2015), should produce results in good agreement with that from a more generalized temperature profile.

We also developed a model for extrapolating H_2 column density from the ^{12}CO(3-2) line alone. Bally & Lada (1983) estimated outflow mass of 12 sources from ^{12}CO(3-2) and ^{13}CO(3-2) lines by determining an assumed common excitation temperature by imposing a different 12-to-13 CO abundance ratio. The authors used a functional dependence of column density $N_{13}(v)$ on T_{ex} and τ_{13}. For the sources with missing ^{13}CO(3-2) data, they constrained $\tau_{12} \ll 1$ and $T_{ex} > 10$ K to estimate ^{12}CO(3-2) column density, and used a fixed ^{12}CO(3-2) to H_2 ratio. In contrast, we have not imposed restrictions on τ_{12} and T_{ex} for measuring H_2 column density. Instead, we used a direct approach of least square fitting to establish a functional relation between τ_{13} and ^{12}CO(3-2) brightness. Since the two CO line species have approximately the same abundance ratio in all star-forming clouds, and

^{12}CO(3-2) transition is ubiquitous in outflows of class 0 and I protostars, the advantage of our approach is that Equation 4.1 may be applicable in any outflow study that lacks ^{13}CO(3-2) line data.

This approach establishes a direct relationship between the two CO lines in the outflow wings with more generality. Figure 4.7 and Table 3.4 summarize the small sample correlation between the fitted ^{13}CO model and estimates based on all lines. There is a systematic underestimate of outflow properties, which may be caused by unaccounted for opacity in the ^{12}CO line. Since we have a small sample size of 12, we place our estimates in context by comparing them to the catalogue presented in Wu et al. (2004), which shows 391 high-velocity molecular outflows from various sources in different evolutionary stages. The larger catalogue contains sources that are both low and high mass protostars. We plot our estimated values along with the values calculated by (Wu et al., 2004) (Figure 3.8). Specifically, we compare with the Wu et al. (2004) results for (a) outflow mass vs energy and (b) IR luminosity of the central sources vs outflow energy. Both plots show significant correlations, but this can be primarily attributed to all the axes scaling with d^2, where d is the distance to the source. In comparing the Wu et al. (2004) data with our two sets of our results (i.e., estimates from all lines and those from ^{12}CO alone), we see that both sets of estimates follow the general trends and scales from the population as a whole. Furthermore, the margin between the ^{12}CO-only estimates and the multi-line estimates (Table 3.4) is small compared to the distribution of the broader population.

The similarity of the distribution of both sets of estimated values to the larger population of outflows indicates our estimates and regression model are providing good estimates of outflow properties suitable for survey analysis. Overall, we estimate that the projected outflow properties have a 0.3 dex uncertainty and the unknown inclination of the angle suggests a further factor of 2 underestimate for the momentum and a factor of 2 underestimate for the energy assuming a uniform distribution of angles on the sky.

3.7 Conclusions

In this paper, we have studied 13 molecular outflows in the Cygnus X region identified by (G12), using JCMT observations of the ^{12}CO(3-2), ^{13}CO(3-2), and CO^{18}(3-2) spectral lines. We have calculated various properties of the outflows, identified associated infrared sources, and evaluated a new method to estimate gas column density from ^{12}CO(3-2) line alone.

1. We present each of 13 molecular outflows in an atlas, displaying the extent of bipolarity, spatial and spectral extent of outflowing gas, along with the velocity distribution in PV-slices. All outflows except for G80.314+1.330 appear to be associated with clouds in the Cygnus X region. The outflow G80.314+1.330 has a relatively larger negative LSR velocity and is likely associated with the Perseus Arm.

2. Assuming LTE and uniform excitation temperature among the three CO lines we estimate mass, momentum, and energy of the remaining 12 outflows by following the method descried in (D18). The results are summarized in Table 3.2. Our estimated values are comparable with those of a larger population study of outflows (Wu et al. (2004)) and shown in Figure 3.8. In particular, we find the mechanical luminosity of the outflows is $L_{\rm mech} \sim 10^{-3} L_{\rm IR}$.

3. We also test a method of estimating of outflow properties from only ^{12}CO(3-2) line data. We compare our ^{12}CO(3-2)-only estimates with the three-line estimates. A relatively small but consistent underestimation (0.3 dex) is present in all three properties (mass, momentum, and energy; Figure 4.7) and is likely due to projected linewidth of ^{13}CO(3-2) being larger than the observed ^{13}CO(3-2) line width so less emission is included in the outflow wings. Since our sample is small, we compare the values with a compilation of properties from Wu et al. (2004). In this context, the outflow properties we measure are consistent with the general population and the uncertainties are within the scatter in the broader population (Figure 3.8).

After comparing the projected and estimated outflow properties we conclude that our ^{12}CO-only optical depth model produces a fairly close correlation between estimated and projected values. Therefore we can utilize this model in our next work which will present a large survey of outflows in Cygnus X.

Acknowledgements

The James Clerk Maxwell Telescope has historically been operated by the Joint Astronomy Centre on behalf of the Science and Technology Facilities Council of the United Kingdom, the National Research Council of Canada and the Netherlands Organisation for Scientific Research. The authors wish to recognize and acknowledge the significant cultural role and reverence that the summit of Maunakea has always had within the indigenous Hawaiian community. We are most fortunate to have the opportunity to conduct observations from this mountain. The authors acknowledge support from the Natural Sciences and Engineering Research Council of Canada, funding reference numbers RGPIN-2017-03987 and RGPIN 418517.

Data Availability: The data underlying this article are available in the Canadian Astronomy Data Centre, at https://dx.doi.org/10.11570/21.0001. [4]

[4]Data hosted during review at https://www.canfar.net/storage/list/eros/OUTFLOWS_FITS

3.8 Atlas of Molecular Outflows in Cygnus X

Figures 3.9 to 3.20 show maps of the remaining 12 outflows analysed in the main text.

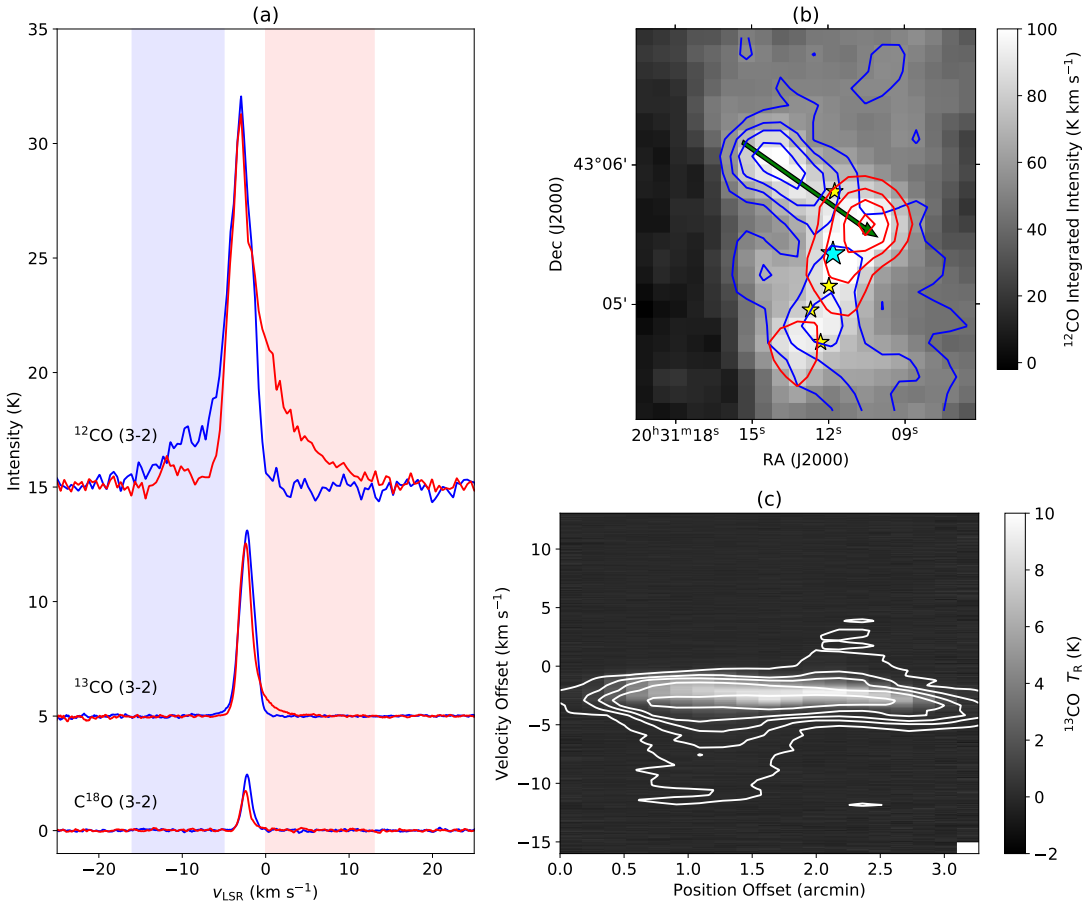

Figure 3.9: Outflow G81.435+2.147: (a) Blue- and redshifted outflow regions are shown in ^{12}CO(3-2) (offset +15 K), ^{13}CO(3-2) (offset +5 K), and C^{18}O(3-2) lines (b) Blue and red contour lines are obtained by integrating over velocity ranges from $v = -16$ to -5 km s^{-1} and $v = 0$ to 13 km s^{-1}, and drawn at levels (7, 13, 20, 30, 40, 50) K km s^{-1} and (10, 20, 30, 40, 50) K km s^{-1} respectively. (c) Contours are drawn at levels (2, 5, 7.5, 10, 15, 20) K.

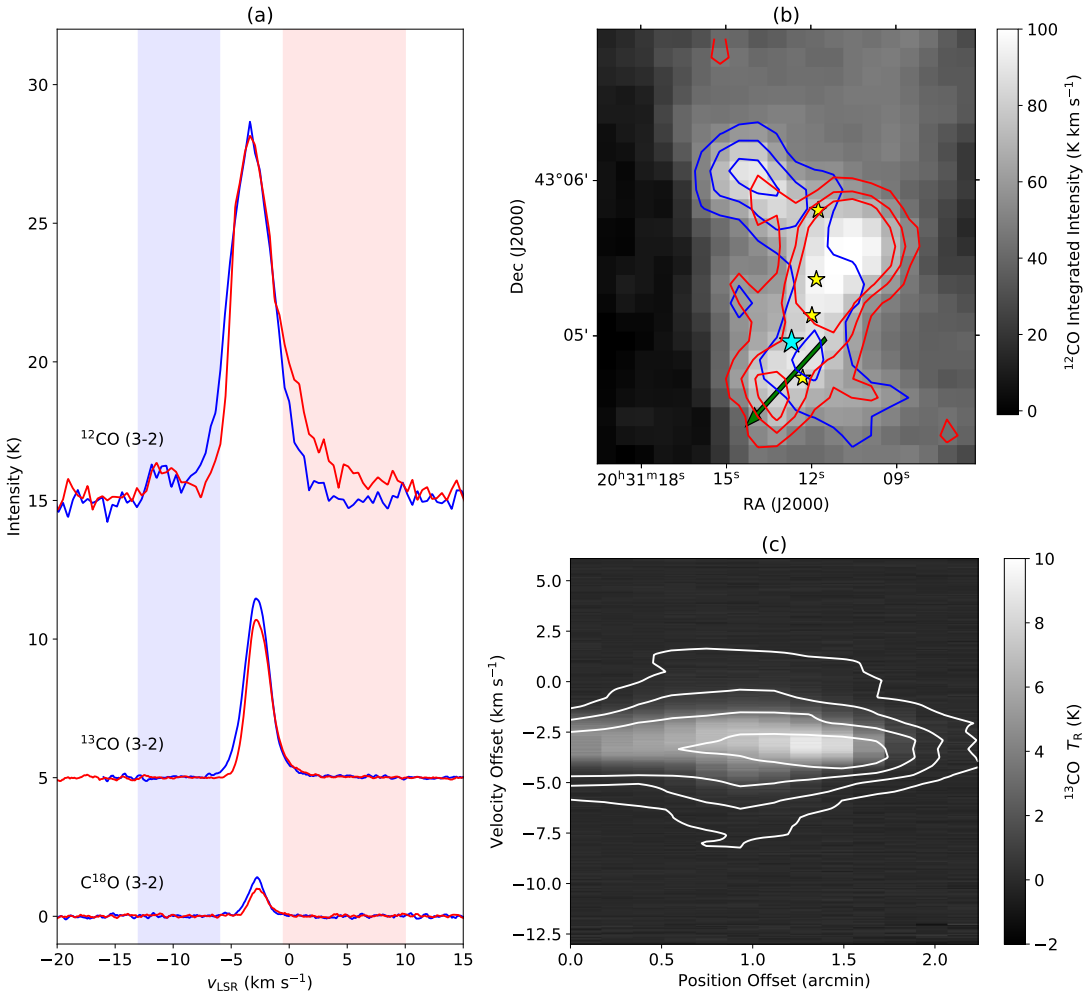

Figure 3.10: Outflow G81.424+2.140: (a) Blue- and redshifted outflow regions are shown in ^{12}CO(3-2) (offset +15 K), ^{13}CO(3-2) (offset +5 K), and C^{18}O(3-2) lines (b) Blue and red contour lines are obtained by integrating over velocity ranges from $v = -14$ to -6 km s^{-1} and $v = -1.5$ to 6 km s^{-1}, and drawn at levels (6, 13, 22) K km s^{-1} and (4, 10, 24) K km s^{-1} respectively. (c) Contours are drawn at levels (4, 10, 16) K.

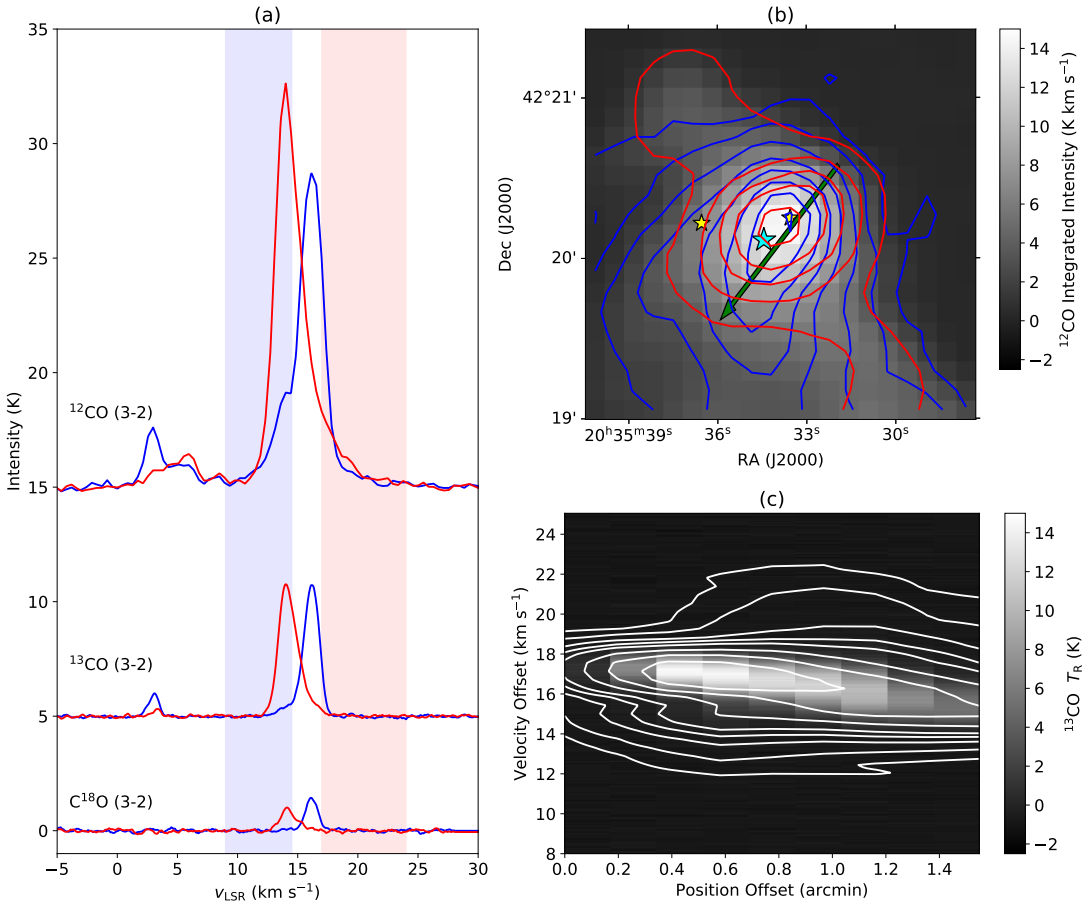

Figure 3.11: Outflow G81.302+1.055: (a) Blue- and redshifted outflow regions are shown in ^{12}CO(3-2) (offset +15 K), ^{13}CO(3-2) (offset +5 K), and C^{18}O(3-2) lines (b) Blue and red contour lines are obtained by integrating over velocity ranges from v = 9 to 14.5 km s^{-1} and v = 17 to 24 km s^{-1}, and drawn at levels (0.45, 1, 2.5, 5, 7.5, 10, 12.5, 15, 20, 25, 28) K km s^{-1} and (1, 3, 5, 7, 10, 15, 23) K km s^{-1} respectively. (c) Contours are drawn at levels (1.2, 2.5, 5, 7.5, 10, 15, 20, 25) K.

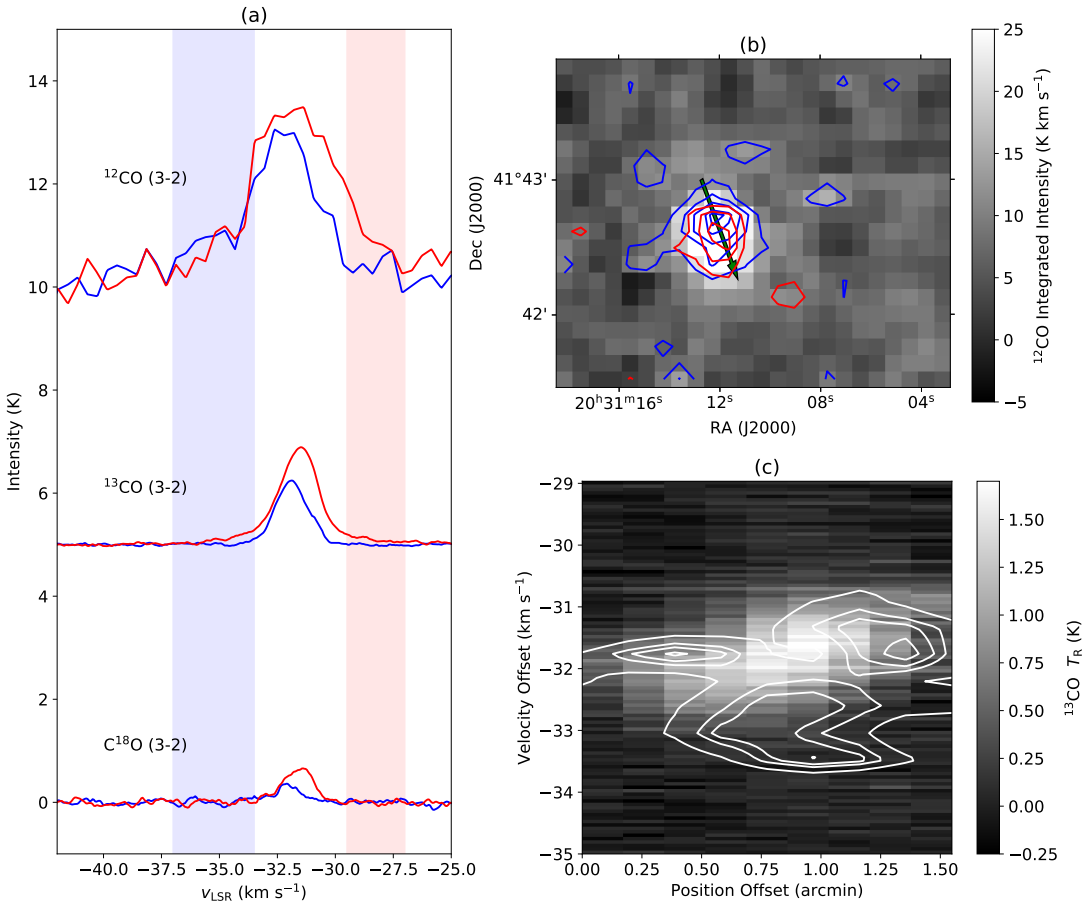

Figure 3.12: Outflow G81.424+2.140: (a) Blue- and redshifted outflow regions are shown in ^{12}CO(3-2) (offset +10 K), ^{13}CO(3-2) (offset +5 K), and C^{18}O(3-2) lines (b) Blue and red contour lines are obtained by integrating over velocity ranges from $v = -37$ to -33.5 km s^{-1} and $v - 29.5$ to -27 km s^{-1}, and drawn at levels (3, 7, 11, 16, 18) K km s^{-1} and (3, 5, 7) K km s^{-1} respectively. (c) Contours are drawn at levels (2, 2.6, 2.9, 3.3) K.

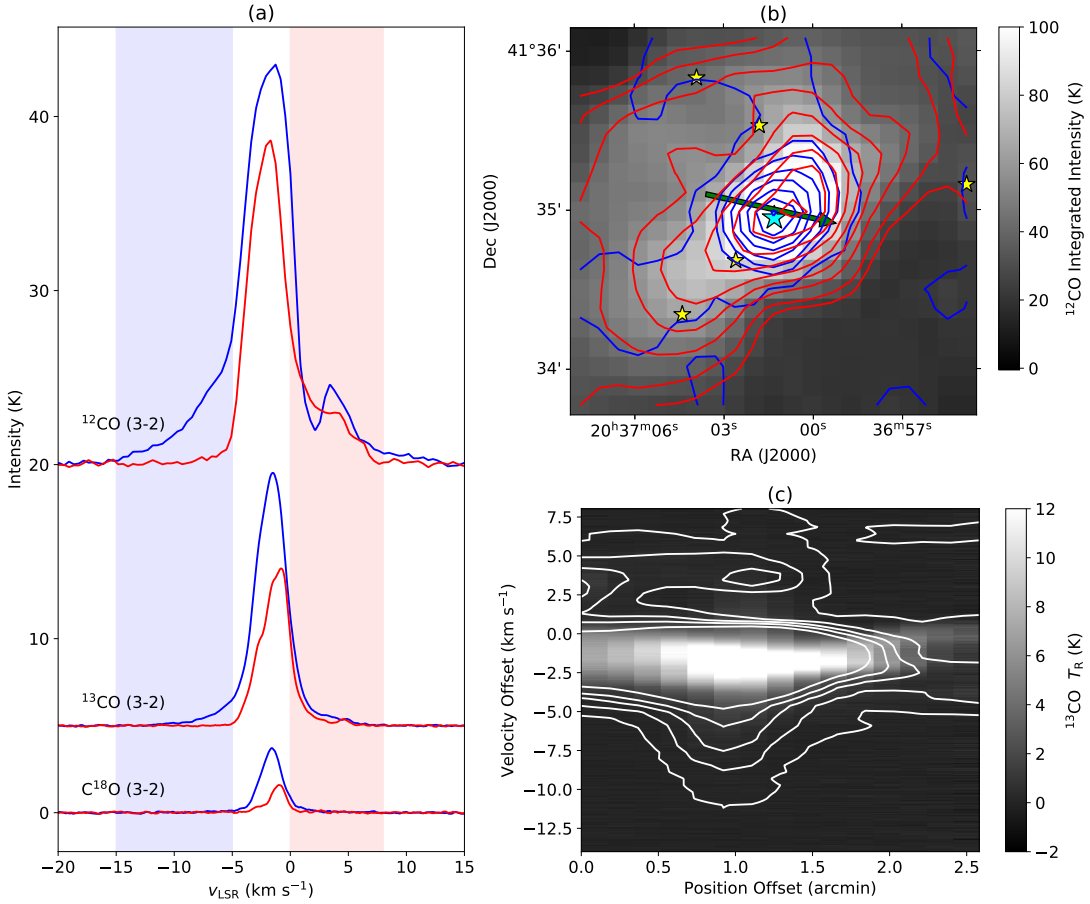

Figure 3.13: Outflow G80.862+0.385: (a) Blue- and redshifted outflow regions are shown in ^{12}CO(3-2) (offset +20 K), ^{13}CO(3-2) (offset +5 K), and C^{18}O(3-2) lines (b) Blue and red contour lines are obtained by integrating over velocity ranges from $v = -15$ to -5 km s^{-1} and $v = 0$ to 8 km s^{-1}, and drawn at levels (7, 12, 16, 22, 30, 40, 50, 63) K km s^{-1} and (15, 20, 30, 40, 50, 60, 70, 80, 90) K km s^{-1} respectively. (c) Contours are drawn at levels (1.2, 3, 5, 7, 10) K.

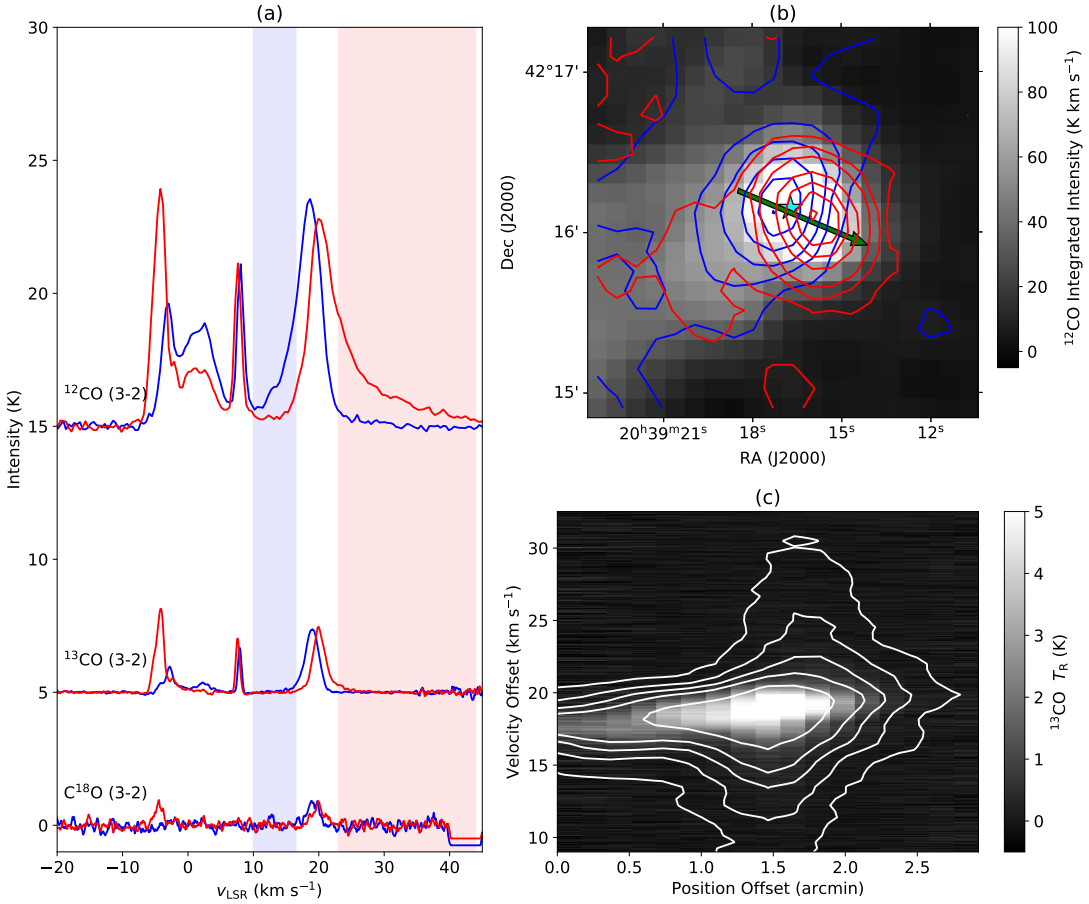

Figure 3.14: Outflow G81.663+0.468: (a) Blue- and redshifted outflow regions are shown in ^{12}CO(3-2) (offset +15 K), ^{13}CO(3-2) (offset +5 K), and C^{18}O(3-2) lines (b) Blue and red contour lines are obtained by integrating over velocity ranges from v = 10 to 16.5 km s^{-1} and v = 23 to 44 km s^{-1}, and drawn at levels (3, 7, 12, 20, 30, 40) K km s^{-1} and (1.5, 5, 10, 25, 40, 55, 75) K km s^{-1} respectively. (c) Contours are drawn at levels (1.2, 3, 5, 7, 10) K.

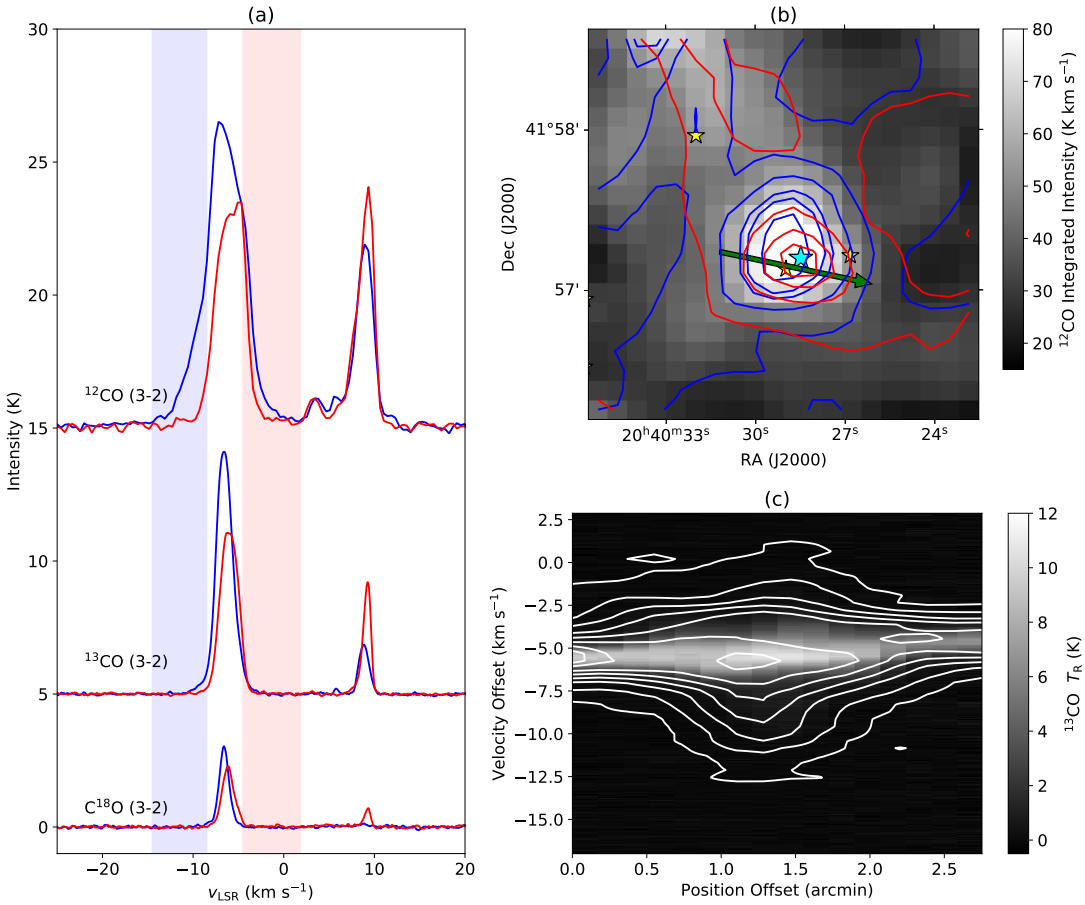

Figure 3.15: Outflow G81.551+0.098: (a) Blue- and redshifted outflow regions are shown in ^{12}CO(3-2) (offset +15 K), ^{13}CO(3-2) (offset +5 K), and C^{18}O(3-2) lines (b) Blue and red contour lines are obtained by integrating over velocity ranges from $v = -14.5$ to -8.5 km s^{-1} and $v = -4.5$ to 1.8 km s^{-1}, and drawn at levels (4, 12, 20, 28, 32, 40) K km s^{-1} and (1, 8, 18, 25, 30, 35) K km s^{-1} respectively. (c) Contours are drawn at levels (0.6, 2, 4, 6, 8, 10, 12, 13, 14) K.

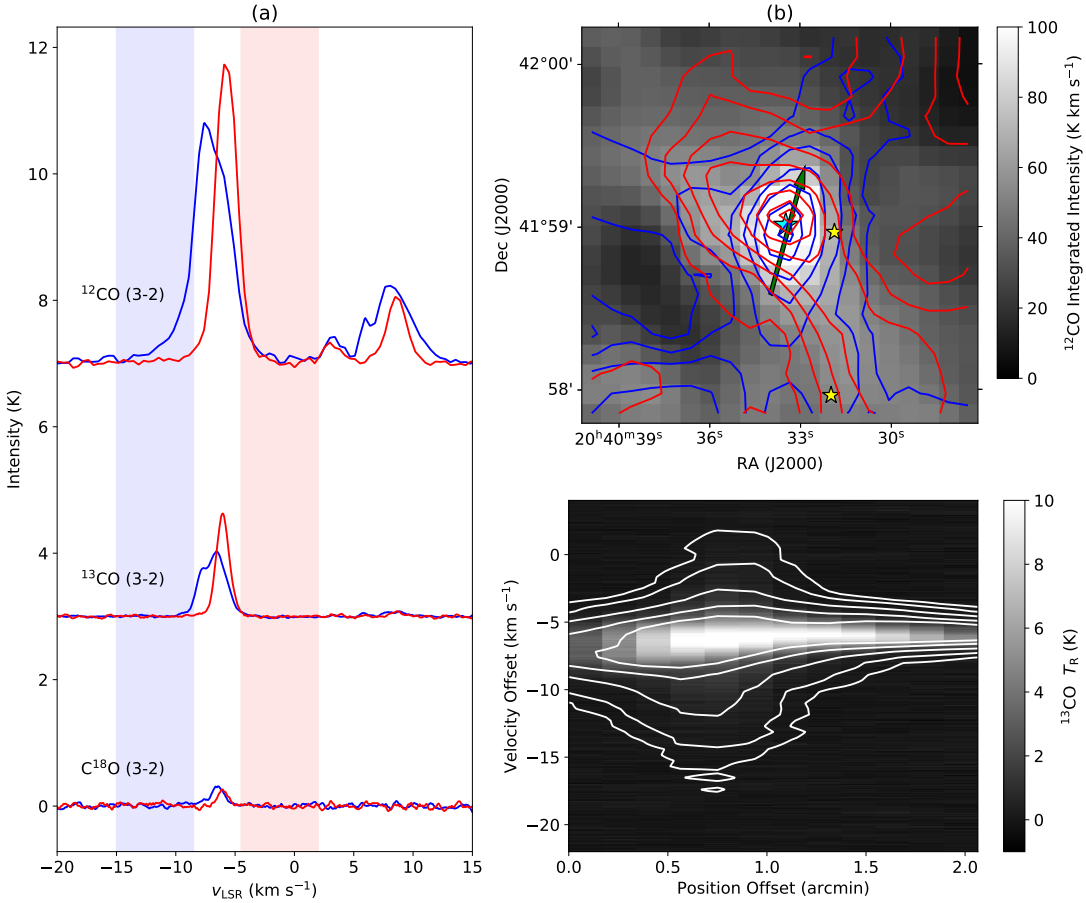

Figure 3.16: Outflow G81.582+0.104: (a) Blue- and redshifted outflow regions are shown in ^{12}CO(3-2) (offset +7 K), ^{13}CO(3-2) (offset +3 K), and C^{18}O(3-2) lines (b) Blue and red contour lines are obtained by integrating over velocity ranges from $v = -15$ to -8.5 km s^{-1} and $v = -4.5$ to 2 km s^{-1}, and drawn at levels (2.5, 4.5, 8, 16, 25, 38, 48, 53) K km s^{-1} and (3, 5, 8, 12, 18, 25, 31, 35) K km s^{-1} respectively. (c) Contours are drawn at levels (1.7, 3, 6, 10, 13, 17, 21) K.

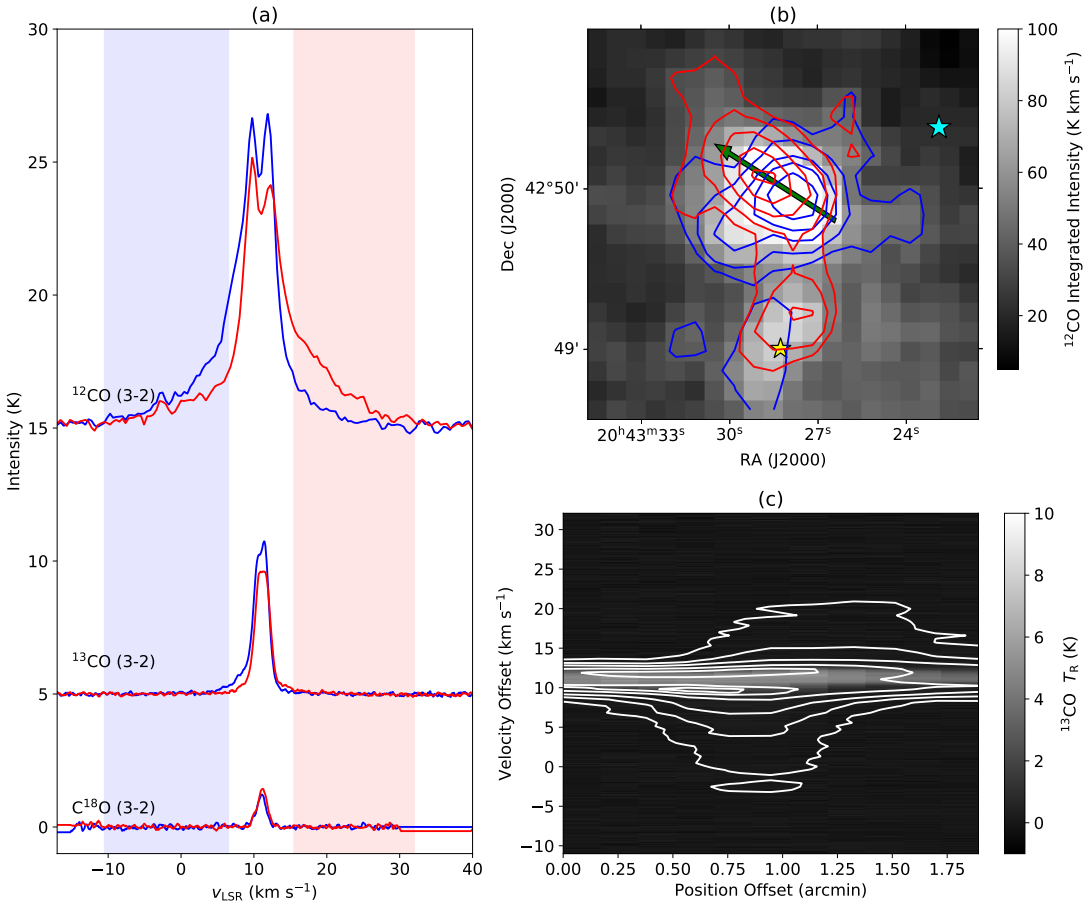

Figure 3.17: Outflow G82.581+0.203: (a) Blue- and redshifted outflow regions are shown in ^{12}CO(3-2) (offset +15 K), ^{13}CO(3-2) (offset +5 K), and C^{18}O(3-2) lines (b) Blue and red contour lines are obtained by integrating over velocity ranges from $v = -10.5$ to 6.5 km s^{-1} and $v = 15.5$ to 32 km s^{-1}, and drawn at levels (5, 10, 20, 30, 45, 68, 77) K km s^{-1} and (5, 10, 20, 32, 42) K km s^{-1} respectively. (c) Contours are drawn at levels (1.5, 3, 5, 8, 10, 11, 12) K.

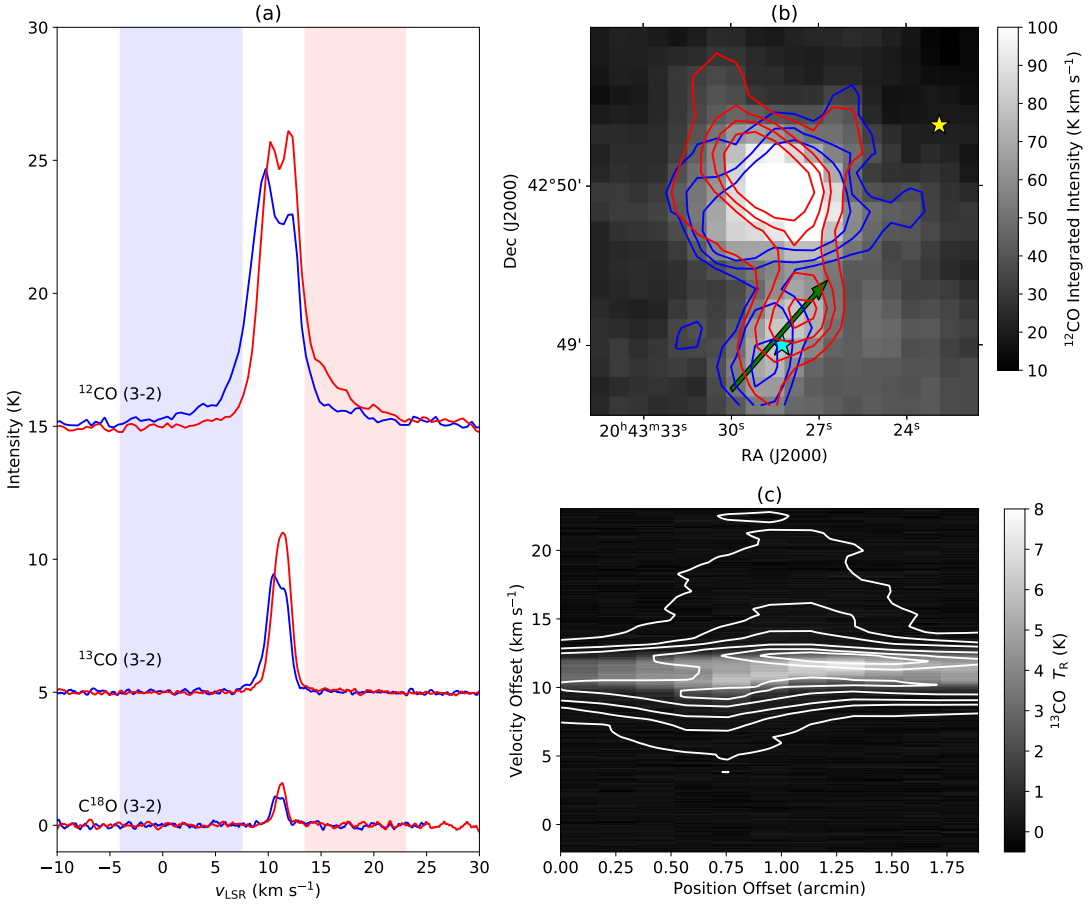

Figure 3.18: Outflow G82.571+0.194: (a) Blue- and redshifted outflow regions are shown in ^{12}CO(3-2) (offset +15 K), ^{13}CO(3-2) (offset +5 K), and C^{18}O(3-2) lines (b) Blue and red contour lines are obtained by integrating over velocity ranges from $v = -4$ to 7.5 km s^{-1} and $v = 13.5$ to 23 km s^{-1}, and drawn at levels (4, 7, 12) K km s^{-1} and (5, 10, 15, 22) K km s^{-1} respectively. (c) Contours are drawn at levels (1, 3, 5, 8, 10, 11, 12) K.

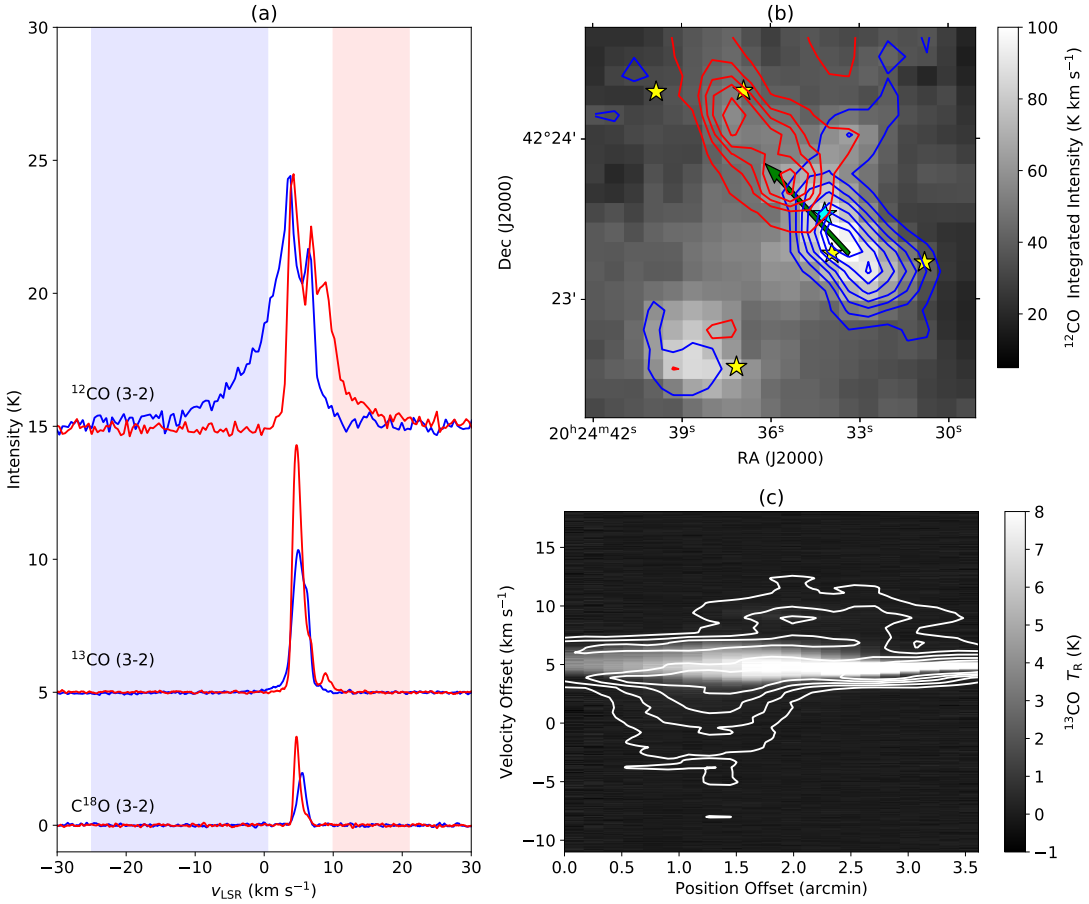

Figure 3.19: Outflow G80.158+2.727: (a) Blue- and redshifted outflow regions are shown in ^{12}CO(3-2) (offset +15 K), ^{13}CO(3-2) (offset +5 K), and C^{18}O(3-2) lines (b) Blue and red contour lines are obtained by integrating over velocity ranges from $v = -25$ to 0.5 km s^{-1} and $v = 10$ to 21 km s^{-1}, and drawn at levels (4, 9, 14, 19, 25, 30, 34) K km s^{-1} and (5, 8, 10, 12, 15) K km s^{-1} respectively. (c) Contours are drawn at levels (1.9, 4, 6, 8, 10) K.

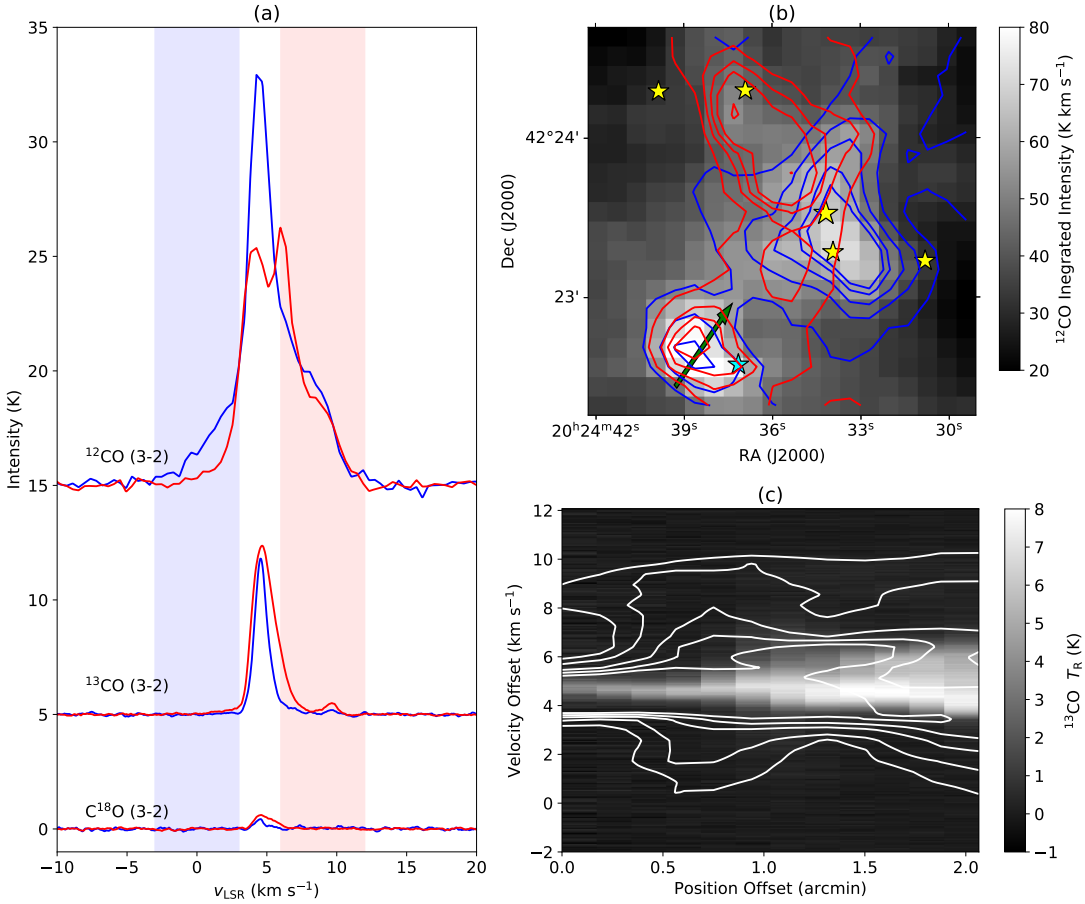

Figure 3.20: Outflow G80.149+2.710: (a) Blue- and redshifted outflow regions are shown in ^{12}CO(3-2) (offset +15 K), ^{13}CO(3-2) (offset +5 K), and C^{18}O(3-2) lines (b) Blue and red contour lines are obtained by integrating over velocity ranges from $v = -3$ to 3 km s^{-1} and $v = 6$ to 12 km s^{-1}, and drawn at levels (4, 9, 14, 19, 22) K km s^{-1} and (8, 11, 13, 15, 25) K km s^{-1} respectively. (c) Contours are drawn at levels (2, 3.5, 6, 8, 10) K.

Chapter 4

A Large Scale Survey of Protostellar Outflows in the Cygnus X Region

This chapter has been submitted to Monthly Notices of the Royal Astronomical Society as Deb et al. 2022: "A Large Scale Survey of Protostellar Outflows in the Cygnus X Region".

4.1 abstract

In this paper, we perform a large scale analysis of protostellar outflows in Cygnus X, representing the first untargeted search for outflows in this region. We identify outflows in new and previously published JCMT observations of ^{12}CO(3-2) spectral line emission. We implement the linear regression model described in Deb et al. (2021) to estimate outflow properties using only a single emission line. We associate these outflows with previously surveyed protostars, and we use a machine learning approach to infer the properties of unobserved protostars. We find outflow power is 0.1% of protostellar luminosity and that outflow dynamical times are 15 times shorter than associated molecular core free-fall times. By comparing outflow power to turbulent dissipation power, we conclude that single-generational outflows cannot provide enough energy support for the surrounding molecular clouds. Finally, we search for evidence of large-scale triggering of star formation in the region by ionization fronts but find no evidence that the association with ionized gas emission leads to an increase in star formation rates in molecular gas.

4.2 Introduction

Star formation in galaxies occurs in giant molecular clouds. The internal conditions of molecular clouds set the initial conditions for star formation and essentially controls the secular evolution of galaxies. The internal structure of molecular clouds, in turn, is continuously regulated by various physical factors including magnetic fields, self-gravity, turbulence, shocks, heating and cooling mechanisms, and radiation (Chevance et al., 2022). Since the first molecular clouds were discovered in the Orion Nebula (Wilson et al., 1970), there have been several models developed in order to shed light on the structure and dynamics of molecular clouds. In early models, cloud evolution was dominated by magnetic fields (Shu et al., 1987) or gravitational free-fall collapse alone (Bastien et al., 1991; Klessen et al., 1998). Recently, observational improvements suggest both gravity and magnetohydrodynamic (MHD) turbulence as the primary drivers behind molecular cloud dynamics and associated star formation (Krumholz & McKee, 2005; Hennebelle & Chabrier, 2008). Although gravity is the single most important factor is the interstellar gas evolution, sub-cloud scale inhomogeneities are more likely to be caused by turbulence. Local turbulence can lead to small-scale virially unstable cloud formation in otherwise gravitationally bound giant molecular clouds (Clarke et al., 2017).

Large-scale virial equilibrium in the interstellar medium (ISM) is achieved by a balance between gravity and turbulent gas flow (e.g., Sun et al., 2020). Turbulence is short-lived and requires a constant source of energy injection. One of the proposed mechanisms for turbulent driving is protostellar outflows (e.g., Miesch & Bally, 1994). Feedback in the initial phase of protostellar accretion, as jets and outflows, originating from the protostellar disk, can inject high energy into the cloud. The relative importance of this contribution to the overall GMC turbulence is disputed. For example, Henning (1989) has suggested most of the energy deposit goes into the lower density gas in the ISM but Nakamura & Li (2007) suggest that these outflows can drive local turbulence. Outflow feedback can also be a contributing source for disrupting local clouds (Matzner & McKee, 2000) or

triggering star formation but these effects are challenging to distinguish in regions also shaped by radiative feedback from newly formed stars. Ionizing radiation from young massive stars, which are often formed in clusters, interact with the molecular and atomic gas in the ISM creating expanding HII bubbles. These expanding HII regions can drive turbulence or trigger local collapse in dense molecular cores via "collect and collapse" model (Elmegreen & Lada, 1977; Miesch & Bally, 1994). Overall, the role of protostellar feedback, particularly through outflows is thought to be significant but likely subdominant source of turbulent driving in clouds (Arce et al., 2010; Frank et al., 2014), but they play a central role in shaping the process of star formation and the resulting initial mass function (Guszejnov et al., 2021).

However, the observational basis for these studies has predominantly focused on the nearest clouds, all of which are relatively low-mass cloud complexes such as the Perseus molecular cloud $\sim 10^4$ $M_\odot$ (Padoan et al., 1999; Arce et al., 2010) or Taurus (Narayanan et al., 2012). Such clouds only rarely have radiative feedback from high mass stars, except for the Orion molecular cloud complex (Goicoechea et al., 2015; Berné et al., 2022). In this work, we explore the dynamical influence of outflows in the context of the Cygnus X star forming region and associated molecular clouds.

Cygnus X, located in the spiral arm the Orion Spur, hosts one of the most massive ($\sim 5 \times 10^6$ $M_\odot$), gas-rich molecular clouds known in the galaxy (Schneider et al., 2006). It is also one of the most active star forming cloud complexes. Additionally, molecular rings around expanding HII regions, an observational signature of triggered star formation driven by radiative feedback, are often spotted in Cygnus X (Figure 4.1). One such case of triggering was studied in detail in Deb et al. (2018).

Thanks to a wide-area JCMT survey (Section 2), we have the opportunity to identify outflows in the cloud and measure their properties (Section 3). We can explore, for the first time, a large population of molecular outflows in a GMC, especially in the context of radiative triggering. We use previous work (Deb et al., 2021, hereafter D21) to estimate

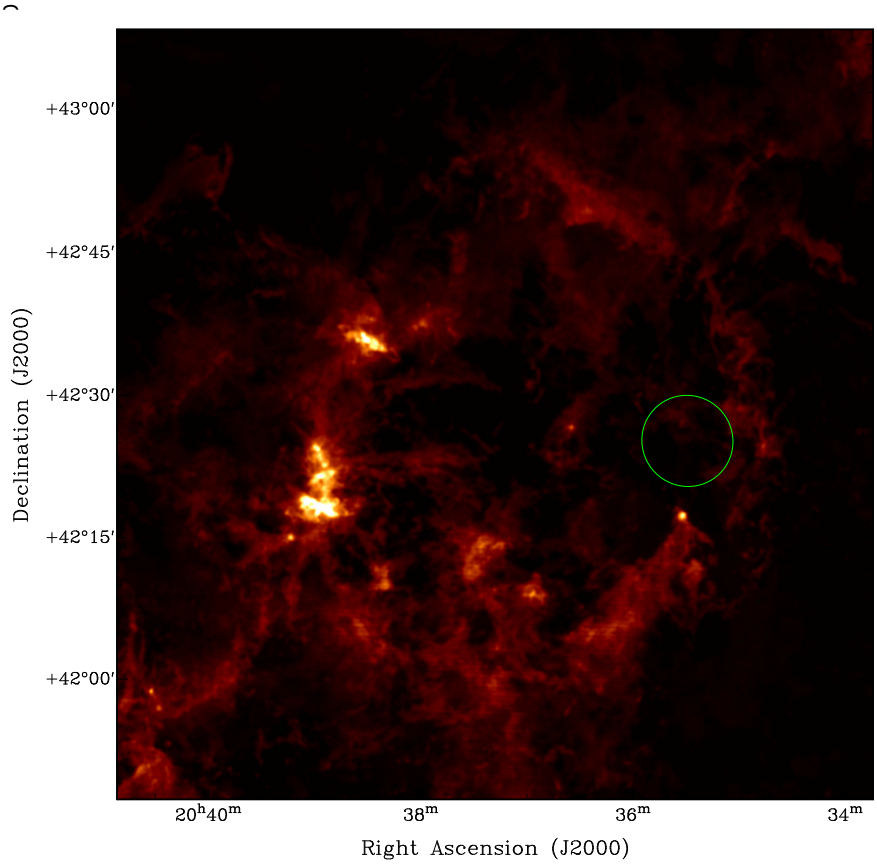

Figure 4.1: Molecular gas ring structure with pillars and globules around young stellar cluster C114 (green circle) in Cygnus X north revealed in ^{12}CO(3-2) emission (Gottschalk et al., 2012). The molecular gas shows several cometary features where the radiative feedback has blown away molecular gas around a dense core (Gottschalk et al., 2012).

outflow properties from ^{12}CO(3-2) spectral line data alone (Section 4.1). As new outflows are identified in this work, we estimate the missing protostellar luminosity values using a machine learning approach (Section 4.2). We explore the contribution of outflows towards the turbulent support of Cygnus X in Section 4.3. Finally, in Section 4.4, we investigate the possibility of large-scale triggered star formation in Cygnus X via a supervised classification method.

4.3 Observations

4.3.1 JCMT ^{12}CO(3-2) observations

The observations for the Cygnus X ^{12}CO(3-2) survey were carried out using the Heterodyne Array Receiver (HARP) system (Buckle et al., 2009) on the James Clerk Maxwell Telescope (JCMT) in Hawai'i. In addition to the Cygnus X pathfinder survey (Gottschalk et al., 2012) we observed 10 additional fields. Characteristics of those fields, such as centre coordinate, date of observation, and the rms noise, are listed in Table 4.1. For data reduction, we used the observatory-maintained STARLINK software package (Currie et al. 2014) and the standard reduction and calibration recipes developed for the JCMT. The observatory provides calibrated data on the $T_{\rm A}^*$ scale (antenna temperature corrected for atmospheric opacity, but not for source-beam coupling). We convert the data to the main beam temperature scale by assuming a beam efficiency based on observatory recommendations of $\eta_{\rm MB} = 0.64$[1] and setting $T_{\rm B} = T_{\rm A}^*/\eta_{\rm MB}$. We follow the same approach as adopted in Gottschalk et al. (2012) for the preparation of the fields and their mosaicking into a single large position-position-velocity data cube. The final mosaic which contains the pathfinder data and the newly observed fields is shown as moment maps in Figure 4.2.

Gottschalk et al. (2012) found three different "layers" of ^{12}CO(3-2) emission along the velocity dimension in the pathfinder survey. Those layers can easily be separated in velocity space and are connected to different star forming cores and compact HII regions, such as DR 21 and IRAS 23350+4126 in the negative velocity layer and DR 17 and W51N in the layer with high positive velocities. The low positive velocity layer is supposed to be connected to the so-called "Great Cygnus Rift," a large molecular cloud and dust complex, which is revealed by a large jump in observed visual extinction of stars at a distance of about 500 to 800 pc in the direction of Cygnus X (Schneider et al., 2006, and references therein). This layer does not contain much star formation activity, and most of the outflows are located in the negative and high positive velocity layers.

[1] https://www.eaobservatory.org/jcmt/instrumentation/heterodyne/harp/

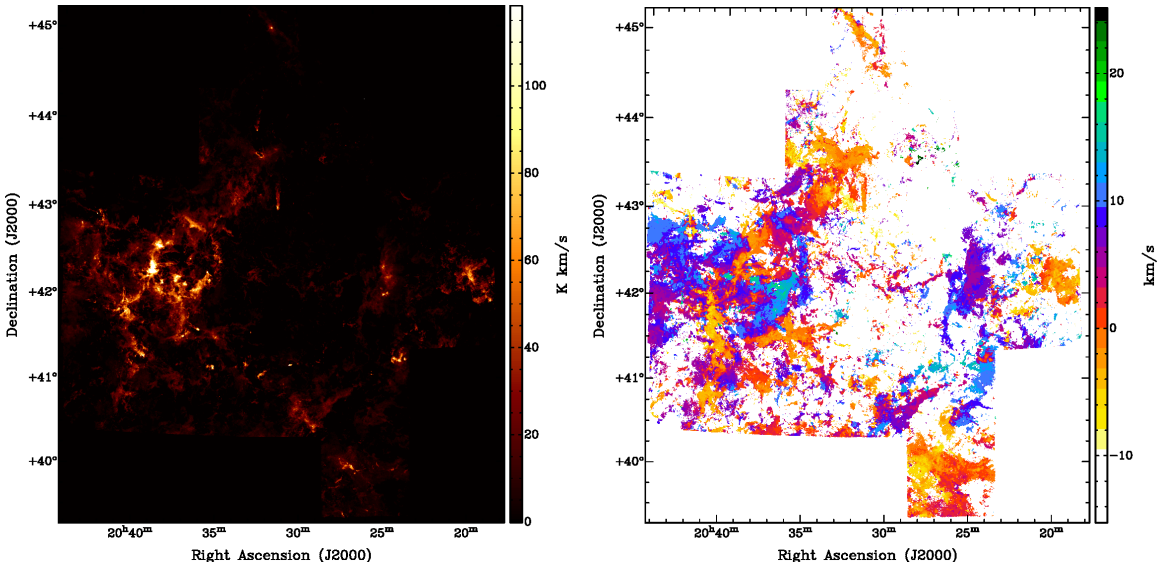

Figure 4.2: 0th and 1st moment maps of our entire Cygnus X ^{12}CO(3-2) survey calculated over a velocity range of −20 to +25 km s^{-1}.

Table 4.1: Centre positions, dates of observation, and rms noise for the extension fields for the Cygnus X survey.

Field	R.A.(J2000)	DEC(J2000)	Date	Noise [K]
9	$20^h\,33^m\,23.7^s$	43° 55′ 12”	Aug 2010	0.89
10	$20^h\,27^m\,54.0^s$	43° 55′ 04″	Sep 2010	0.79
11	$20^h\,30^m\,49.0^s$	44° 54′ 45″	Nov 2010	1.06
12	$20^h\,20^m\,19.7^s$	42° 55′ 04″	Sep 2010	0.77
13	$20^h\,20^m\,26.5^s$	41° 55′ 20″	Sep 2010	0.75
15	$20^h\,25^m\,48.6^s$	40° 55′ 50″	Aug 2011	1.12
16	$20^h\,31^m\,04.2^s$	40° 55′ 30″	Aug 2011	0.95
17	$20^h\,36^m\,21.8^s$	40° 55′ 50″	Aug 2011	0.97
18	$20^h\,49^m\,38.4^s$	40° 55′ 50″	Aug 2011	1.11
19	$20^h\,25^m\,54.6^s$	39° 56′ 00″	Aug 2011	1.12

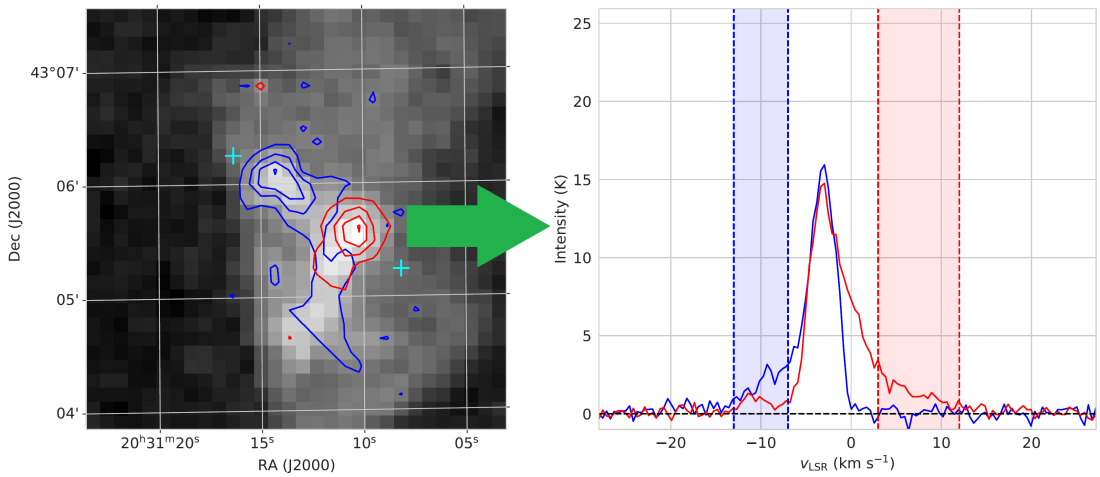

Figure 4.3: (left) Spatial location of an outflow object G81.435+2.147 from the JCMT survey in ^{12}CO(3-2) map. Blue and red contour lines show how the gas is distributed in velocity space (spectral axis) at each pixel in the neighborhood of the local region (marked in cyan). (right) Spectral distribution of gas corresponding to the pixels of highest levels of blue and red contours is associated with blue- and redshifted wings respectively. This characteristic wings seen in spectral distribution is an indicator of a molecular outflow.

The moment maps displayed in Figure 4.2 reveal the complexity of this area of the Galactic plane of our Galaxy. It is only because of the high spatial and velocity resolution of our JCMT observations, that we are able to separate the different layers and study individual outflows in detail.

4.3.2 Ancillary Data

We use the wide area survey of the 21 cm radio continuum data to trace the thermal radio emission in the Cygnus X region. These data were taken from the Canadian Galactic Plane Survey (CGPS, Taylor et al., 2003c). In this area of the Galactic plane, the CGPS provides 1420 MHz images with a sensitivity of about 100 mK and a resolution of about $75'' \times 50''$ at a position angle of -90° for the major beam, measure counterclockwise from west.

4.4 Outflow Identification and Characterization

To find outflows in the JCMT Cygnus X survey, we manually search the spectral-line data cube of ^{12}CO(3-2) emission over the entire area in Cygnus X. At some point in its evolution,

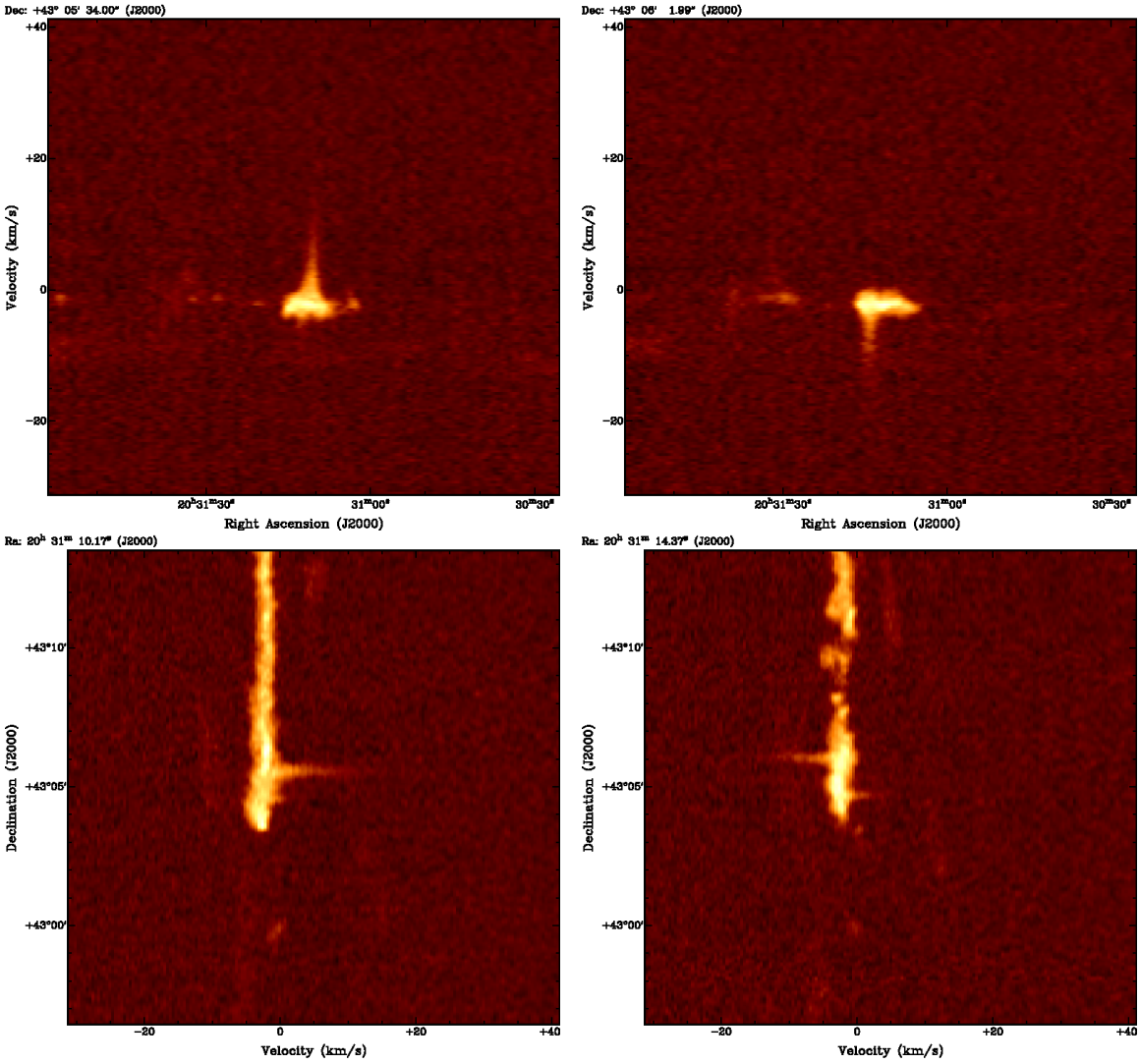

Figure 4.4: R.A.-velocity (top) and velocity-DEC (bottom) diagrams for the outflow shown in Figure 4.3. The redshifted wing is shown on the left and the blueshifted on the right.

every protostar is thought to generate a molecular gas outflow (Shu et al., 1987). The outflowing gas from the rotating central disk and protostar, is ejected in opposite directions, hence appears to have blue- and red-shifted components to the observer, unless orthogonal to the line of sight. This spectral bipolarity will be captured in the velocity axis of the data cube. To identify an outflow, we locate bright emission regions in the spatial plane of the map and manually investigate whether the area has either of the pixels with associated blue- or red-shifted emission, also known as line wings. This inspection was done field by field. Figures 4.3 and 4.4 illustrate this strategy, in which we select an emission region and the pixels display the signature of the 'wing' feature in the spectral distribution along the velocity-axis. This characteristic feature confirms this location has a molecular outflow. Manual inspection has several limitations and will not necessarily detect all outflows. One limitation of this approach might lie in the relative angle the spectral axis of the outflowing gas makes with respect to the line of sight, i.e., when they are perpendicular to each other we may not be able to detect an outflow. Additionally, when they are perfectly aligned, the emission spectrum may appear symmetric precluding the identification of line features based on asymmetry. We also include outflows detected in Gottschalk et al. (2012) and those analyzed in D21.

The inspection procedure was done by authors SD and RK independently for all new fields and the resulting lists of outflows were inspected for common sources, which then were added to our final list of new outflows. All 82 molecular outflows that were detected in the Cygnus X pathfinder and the extension areas are shown in Figure 4.5, which is colour-coded for the three different layers. The outflows are also listed in Table 4.6.

We assign a distance to each outflow based on the mean line of sight the velocity (v_c), and comparing it with velocities of the different layers of Cygnus X. The strategy is described in D21. Essentially, we estimate local standard of rest velocities ($v_{\rm LSR}$), included in Tables 4.6 and associate the outflows with 3 different major star-forming regions in Cygnus X (Rygl et al., 2012; Gottschalk et al., 2012). We consider an outflow with a slightly pos-

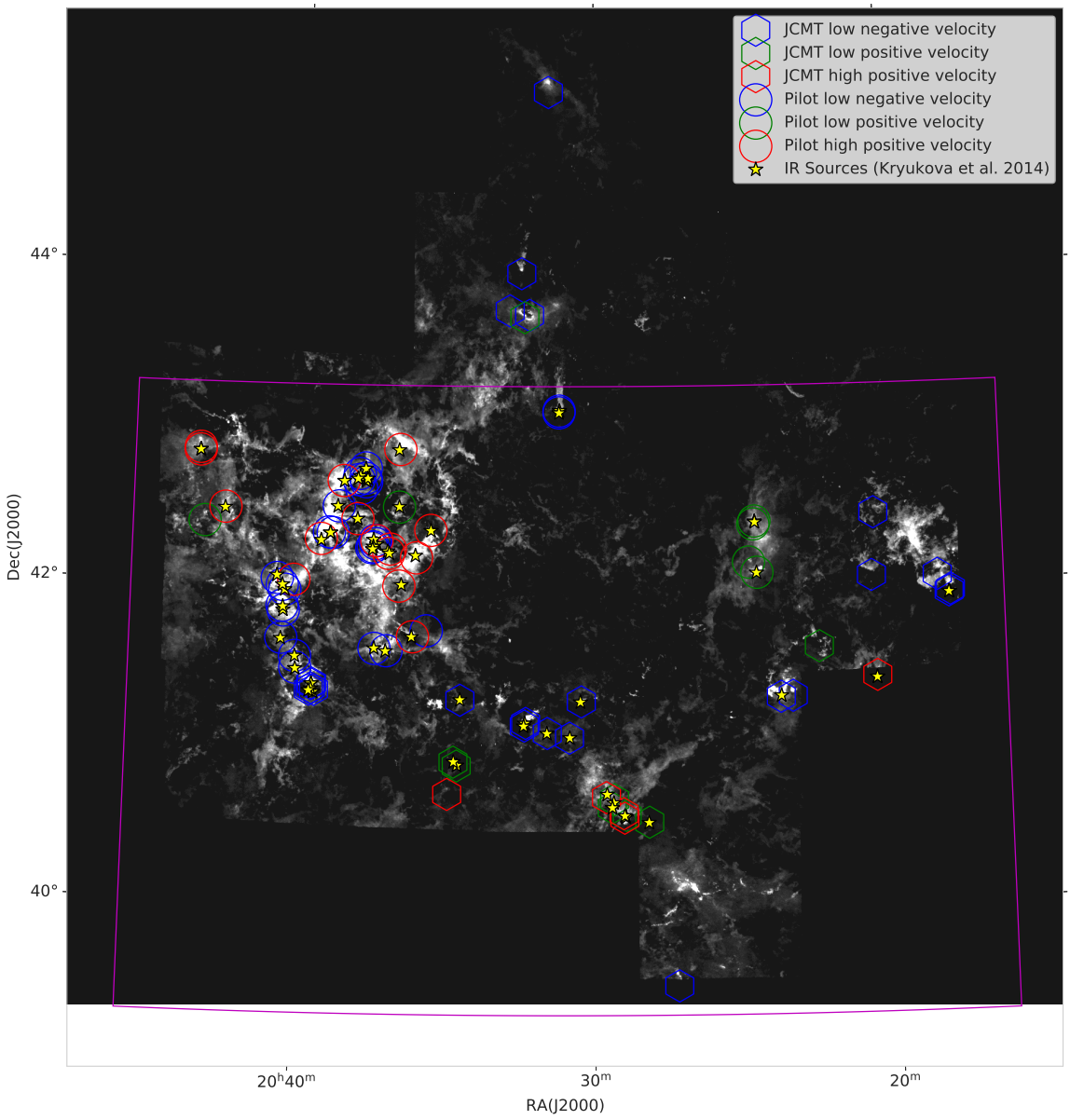

Figure 4.5: Locations of molecular outflows in Cygnus X at different LSR velocities (color-coded) are shown in ^{12}CO(3-2) integrated intensity map. Outflows from the Pilot survey (circles) have their associated infrared sources (yellow stars). Protostars corresponding to the newly-found outflows from the JCMT observations (hexagons) are not identified yet. The IR sources are identified from Kryukova et al. (2014a), the range of the survey is shown by a magenta rectangle.

itive velocity ($0 < v_{\rm LSR}/({\rm km\ s^{-1}}) < 8$) towards Cygnus X to be at the same distance as Cygnus Rift, which is at a mean distance of 650 pc from the sun (Gottschalk et al., 2012) and one with a low negative velocity ($-10 < v_{\rm LSR}/({\rm km\ s^{-1}}) < 0$ to be associated with DR 21, at 1.5 kpc. We associate outflows with positive LSR velocities ($v_{\rm LSR}/({\rm km\ s^{-1}}) > 8$) with W 75N, at 1.3 kpc.

4.5 Results

In this section, we present our four main results. First, we infer the properties of the molecular outflows using the model of D21 that allows us to extrapolate the mass, momentum and power of an outflow based only on its single line emission (Section 4.5.1). We then compare the outflow powers to their associated protostellar luminosities to assess the efficiency of outflow generation (Section 4.5.2). Next, we explore the global evolution of star formation in Cygnus X. First, we estimate the importance of outflows in driving turbulence in the Cygnus X GMC (Section 4.5.3), and then we assess the roles of triggering by an ionized radiation front (Section 4.5.4).

4.5.1 Outflow properties from ^{12}CO(3-2) data

We work with the single spectral line data from the Cygnus X ^{12}CO(3-2) survey for estimating outflow properties using a regression model. In order for a complete determination of outflow properties requires multi-line observations using optically thinner traces such as lines from ^{13}CO or C^{18}O (D21). Using ^{12}CO(3-2) as the primary tracer of line-of-sight column density of molecular hydrogen gas tends to underestimate mass contributions near the line center (D21). Unfortunately, observing multiple rotational transition lines of more than one CO isotopologue is not often possible due to limited telescope time and resources. Thus D21 built an empirical relationship between the brightness of the ^{12}CO emission and the opacity of ^{13}CO(3-2),

$$\log_{10}\tau_{v,13} = -2.69 \pm 0.02 + (2.07 \pm 0.04) \times \log_{10}(T_{12}/1\ {\rm K}). \quad (4.1)$$

where T_{12} is the brightness temperature of the ^{12}CO(3-2) emission. Using this fitted equation, we estimate ^{13}CO(3-2) column density according to (details in Deb et al. (2021),

$$N_{^{13}\mathrm{CO}}(x, y, v) = \frac{8\pi\nu_0^3 Q_{\mathrm{rot}}}{7c^3 A_{ul}} \frac{\exp\left(\frac{E_u}{kT_{\mathrm{ex}}}\right)}{\exp\left(\frac{h\nu_0}{kT_{\mathrm{ex}}}\right) - 1} \tau_\nu(\mathbf{x}, v)\, \delta v. \tag{4.2}$$

as a function of position and velocity. Subsequently, the H_2 column density is obtained as $N_{\mathrm{H_2}} = N_{^{13}\mathrm{CO}}/X_{\mathrm{CO}}$ by using a fixed abundance ratio $X_{\mathrm{CO}} = 10^{-6}$ of ^{13}CO relative to H_2 (Wilson & Rood, 1994). Finally we estimate molecular mass as a function of velocity and position by assuming a mean particle mass of $\mu_{\mathrm{H_2}} = 2.4 m_{\mathrm{H}}$ and using distances of the outflows from the Sun.

We developed an approach to estimate the wing mass in the absence of observations on other spectral lines (D21). We begin by extracting a position-velocity (PV) slice from the ^{12}CO(3-2) data cube mentioned in Section 4.3 along the line connecting blue- and redshifted lobes of an outflow identified in Section 4.4. To estimate outflow energetics, we need to find the line center and line width for every spatial pixel along the PV-slice. We obtain the line center by fitting a Gaussian profile to the ^{12}CO(3-2) spectral line and minimizing the outflow kinetic energy along each line-of-sight (spectral axis) belonging to the PV-slice. We estimate line width by measuring the half width at half maximum (HWHM) of the line profile for each pixel. For outflow contribution via velocity wings we only consider spectral regions with $|v - v_0| > 2\ \sigma_v$. In Table 4.6, we present the properties of our identified outflows. All estimates for outflow mass, momentum, and energy are obtained by summing over all velocity channels satisfying this condition, for all pixels along the PV-slice,

$$M_{\mathrm{outflow}} = \sum_{x,y} \sum_{v \in \mathrm{wing}} M(v, y, x), \tag{4.3}$$

$$p_{\mathrm{outflow}} \cos\theta_i = \sum_{x,y} \sum_{v \in \mathrm{wing}} M(v, y, x) |v - v_0|, \tag{4.4}$$

$$E_{\mathrm{outflow}} \cos^2\theta_i = \frac{1}{2} \sum_{x,y} \sum_{v \in \mathrm{wing}} M(v, y, x)(v - v_0)^2. \tag{4.5}$$

It is to noted that the momentum and energy are projected quantities, where θ_i denotes the

Table 2. Outflows: estimated energetics and observed protostellar (IR sources) association

Outflow	RA (deg)	Dec (deg)	Distance (kpc)	V_c (km s^{-1})	Mass ($M_\odot$)	Momentum ($M_\odot$ km s^{-1})	Energy (10^{44}erg)	Dyn. Time (10 kyr)	Separation (arcsec)	$\log_{10}(L_{IR}/L_\odot)$	Spectral Index
G78.905+2.778★	305.133	41.396	0.65	7.5	3.466	17.356	13.350	12.656	7.0	0.8	1.4
G78.914+2.796★	305.121	41.414	1.30	10.4	0.420	0.800	0.160	20.300	72.0	0.8	1.4
G79.012+1.084★	307.051	40.510	0.65	5.1	0.620	0.010	0.995	13.600	18.0	0.3	0.0
G79.079+3.464★	304.506	41.926	1.50	-3.9	5.060	10.060	2.330	21.600	19.0	1.5	0.5
G79.085+3.477★	304.495	41.938	1.50	-2.6	0.130	0.410	0.140	11.700	68.0	1.1	0.4
G79.125+0.973★	307.256	40.537	1.30	8.2	7.710	13.970	3.000	46.100	42.0	0.8	1.0
G79.130+0.994★	307.237	40.553	0.65	7.0	0.140	0.340	0.110	11.600	48.0	0.8	1.0
G79.151+0.985★	307.263	40.565	0.65	7.7	0.130	0.190	0.030	13.600	61.0	0.1	0.7
G79.164+2.219★	305.942	41.290	1.50	-1.4	12.900	27.760	6.870	53.200	24.0	0.5	1.1
G79.224+0.947★	307.360	40.602	0.65	7.0	0.200	0.480	0.150	13.600	8.0	0.3	1.9
G79.257+0.989★	307.340	40.653	0.65	6.2	0.230	0.360	0.070	2.100	79.0	0.3	1.9
G79.298+0.955★	307.408	40.666	1.30	9.6	0.200	0.520	0.150	10.200	73.0	0.8	0.3
G79.737+0.989★	307.714	41.041	1.50	-3.2	0.160	0.990	0.700	3.900	11.0	2.4	1.9
G79.843+0.893★	307.899	41.070	1.50	-3.0	0.320	0.880	0.310	11.100	13.0	0.7	0.6
G79.877+1.183★	307.615	41.269	1.50	-5.0	2.190	12.550	7.850	9.400	27.0	1.9	0.8
G79.886+2.552	306.127	42.072	0.65	6.6	0.380	1.980	1.510	9.000	11.0	1.9	0.2
G79.966+0.804★	308.091	41.116	1.50	-13.6	0.980	2.260	0.840	6.400	23.0	0.1	1.2
G79.974+0.821★	308.080	41.133	1.50	-13.8	5.140	11.590	3.800	14.400	29.0	2.4	1.7
G80.047+0.309★	308.682	40.886	0.65	4.9	2.890	19.357	17.019	6.400	8.0	2.3	0.1
G80.149+2.710	306.154	42.376	0.65	6.0	0.190	0.630	0.230	5.700	64.0	1.2	2.0
G80.158+2.727	306.144	42.394	0.65	6.0	0.230	0.900	0.510	5.100	10.0	1.2	0.8
G80.336+0.573★	308.630	41.276	1.50	-5.0	0.100	0.230	0.060	14.800	5.0	1.7	1.1
G80.832+0.570	309.034	41.671	1.30	11.5	2.450	5.720	1.550	9.100	37.0	0.9	0.8
G80.862+0.385	309.254	41.580	1.50	-1.4	6.070	28.010	14.870	11.700	26.0	1.7	1.3
G80.916+0.331	309.356	41.594	1.50	-1.3	0.720	2.420	1.010	15.600	8.0	1.7	0.1
G80.933-0.130★	309.856	41.328	1.50	-1.4	11.940	27.880	6.830	19.800	58.0	1.7	0.8
G80.952-0.140★	309.882	41.337	1.50	-2.2	2.000	7.430	2.840	5.200	11.0	1.6	0.9
G80.952-0.155★	309.898	41.328	1.50	-2.8	2.870	8.150	2.570	15.700	19.0	1.3	0.2
G80.973-0.115★	309.873	41.368	1.50	-1.1	0.980	2.650	1.040	21.600	19.0	0.5	0.3
G80.973-0.122★	309.880	41.364	1.50	-2.5	5.500	10.690	2.510	31.500	10.0	0.5	0.3
G81.117-0.140	310.017	41.465	1.50	-4.2	2.170	6.740	2.720	22.100	22.0	2.0	0.3
G81.140+0.687	309.155	41.988	1.30	12.3	0.210	0.920	0.500	5.700	73.0	-0.4	1.4
G81.175-0.100	310.022	41.538	1.50	-3.8	0.720	2.590	1.080	10.700	5.0	1.5	2.3
G81.218+0.877	309.009	42.167	1.30	13.6	0.440	1.670	0.740	4.800	59.0	-0.6	0.3
G81.302+1.055	308.891	42.341	1.30	14.6	7.660	33.790	17.590	7.300	11.0	1.7	1.3
G81.317-0.103	310.142	41.650	1.50	-5.1	0.290	1.130	0.510	12.600	18.0	0.7	2.1
G81.340+0.755	309.244	42.192	1.30	15.7	0.140	1.230	1.200	3.200	11.0	1.8	1.6
G81.365+0.781	309.232	42.220	1.30	16.6	0.790	3.290	1.860	7.600	96.0	-0.1	0.2
G81.424+2.140	307.803	43.085	1.50	-1.7	0.310	1.400	0.700	11.100	7.0	0.5	0.9
G81.435+0.702★	309.378	42.232	1.50	0.0	8.940	36.780	15.760	15.100	5.0	2.0	1.2
G81.435+2.147	307.801	43.096	1.50	-2.4	2.600	11.180	5.580	15.100	8.0	0.8	1.8
G81.436+0.692★	309.390	42.226	1.50	0.0	26.400	97.410	37.960	16.100	41.0	2.1	1.7
G81.437+0.728	309.357	42.252	1.50	-1.3	1.440	4.370	1.540	7.400	27.0	0.2	0.7
G81.450+0.016	310.127	41.822	1.50	-4.7	2.930	8.410	2.640	9.400	15.0	0.5	1.8
G81.460+0.735	309.363	42.272	1.50	-1.3	16.790	94.830	58.320	13.100	47.0	0.2	0.8
G81.462+0.736	309.348	42.270	1.30	17.4	3.645	16.734	12.210	14.600	76.0	0.2	0.7
G81.476+0.020	310.138	41.852	1.50	-4.7	2.550	6.900	2.190	18.800	31.0	0.1	0.5
G81.539+0.983	309.161	42.484	0.65	2.6	0.280	1.470	0.850	4.800	4.0	1.2	1.7
G81.551+0.098	310.118	41.952	1.50	-5.9	4.290	17.360	7.890	8.700	5.0	2.0	1.6
G81.582+0.104	310.140	41.983	1.50	-5.9	2.350	14.220	9.750	9.400	5.0	1.0	1.9
G81.632+0.102	310.185	42.025	1.50	-6.8	1.850	3.950	0.950	20.400	66.0	0.5	0.1
G81.634+0.726	309.512	42.407	1.30	8.5	0.370	1.180	0.430	4.000	8.0	0.8	0.2
G81.663+0.468	309.820	42.278	1.30	19.9	1.710	8.620	4.650	1.600	32.0	2.4	-0.1
G81.673+0.536★	309.752	42.320	1.50	0.0	33.570	341.270	382.340	3.600	35.0	2.1	1.6
G81.681+0.540	309.720	42.316	1.50	-3.0	11.920	145.990	193.030	4.100	83.0	2.1	1.6
G81.773+0.687	309.674	42.484	1.50	-3.8	0.780	1.830	0.470	25.200	32.0	0.1	1.2
G81.794+0.910	309.445	42.640	1.50	-0.4	1.700	5.490	2.100	26.200	19.0	2.1	1.5
G81.813+0.919	309.451	42.662	1.50	-0.8	0.110	0.630	0.400	6.600	62.0	-0.4	0.3
G81.829+1.195	309.158	42.846	1.30	13.6	0.190	0.440	0.100	12.800	39.0	2.0	1.2
G81.831+0.880	309.510	42.652	1.50	-2.1	1.290	5.460	2.470	10.500	33.0	1.5	1.0
G81.857+0.905	309.500	42.691	1.50	-3.0	0.350	1.760	1.030	8.300	59.0	0.9	1.7
G81.861+0.959	309.450	42.726	1.50	-0.8	0.240	0.740	0.260	11.800	15.0	-0.2	0.3
G81.867+0.780	309.637	42.645	1.30	10.6	14.340	50.180	19.730	23.000	19.0	0.6	0.9
G82.187+0.105★	310.639	42.463	1.30	8.1	0.030	0.240	0.250	2.400	20.0	1.8	2.1
G82.571+0.194	310.868	42.816	1.30	11.1	0.140	0.450	0.160	9.600	4.0	2.3	0.8
G82.581+0.203	310.867	42.833	1.30	11.1	2.430	15.600	12.500	4.500	38.0	2.3	0.8

★ Newly discovered in this work. Other outflows are from Gottschalk et al. (2012).

Figure 4.6

inclination angle of the outflow with respect to the line of sight. Throughout this paper, we will omit the projection factor, for the sake of our ignorance of θ_i and notational convenience. Assuming isotropic distributions of inclinations on the sky, the true values of momentum and energy of an outflow will be on average larger by factors of 2 or 3 respectively.

Following the approach described above we estimate mass, momentum, kinetic energy, and dynamical time as

$$T_{\rm dyn} = \frac{R_{\rm lobe}}{\sigma_v}, \tag{4.6}$$

for 82 outflows in Cygnus X (Table 4.6). The variable $R_{\rm lobe}$ denotes the size of blue- or redshifted lobe of an outflow. We have identified the infrared (IR) sources or the associated protostars of 66 outflows from the catalogue of Kryukova et al. (2014a), including their observed infrared luminosity values and spectral indices. We make the spatial association by identifying the closest catalogued protostars within two beam widths (30″) of the outflow position, defined as the convergent point of outflow wings as listed in Table 4.6. Except for protostars G79.886+2.552 and G81.861+0.959, all of these sources are either class 0 or class I protostars as identified in Kryukova et al. (2014a).

Similar to the small sample comparison in D21, we plot estimated values of mass and kinetic energy for the 82 sources against a larger population of 391 outflows from a variety of different sources and evolutionary stages presented in the Wu et al. (2004) catalogue (Fig. 4.7). There are scopes for errors regarding underestimation, discussed in D21, and uncertainties due to projection angle and outflow activity cycle (Section 4.5.3). However, since the two distributions of outflows overlap, we contend that our method of estimating outflow properties based on ^{12}CO(3-2) alone provides reasonable results for wide-area surveys that lack multi-line observations.

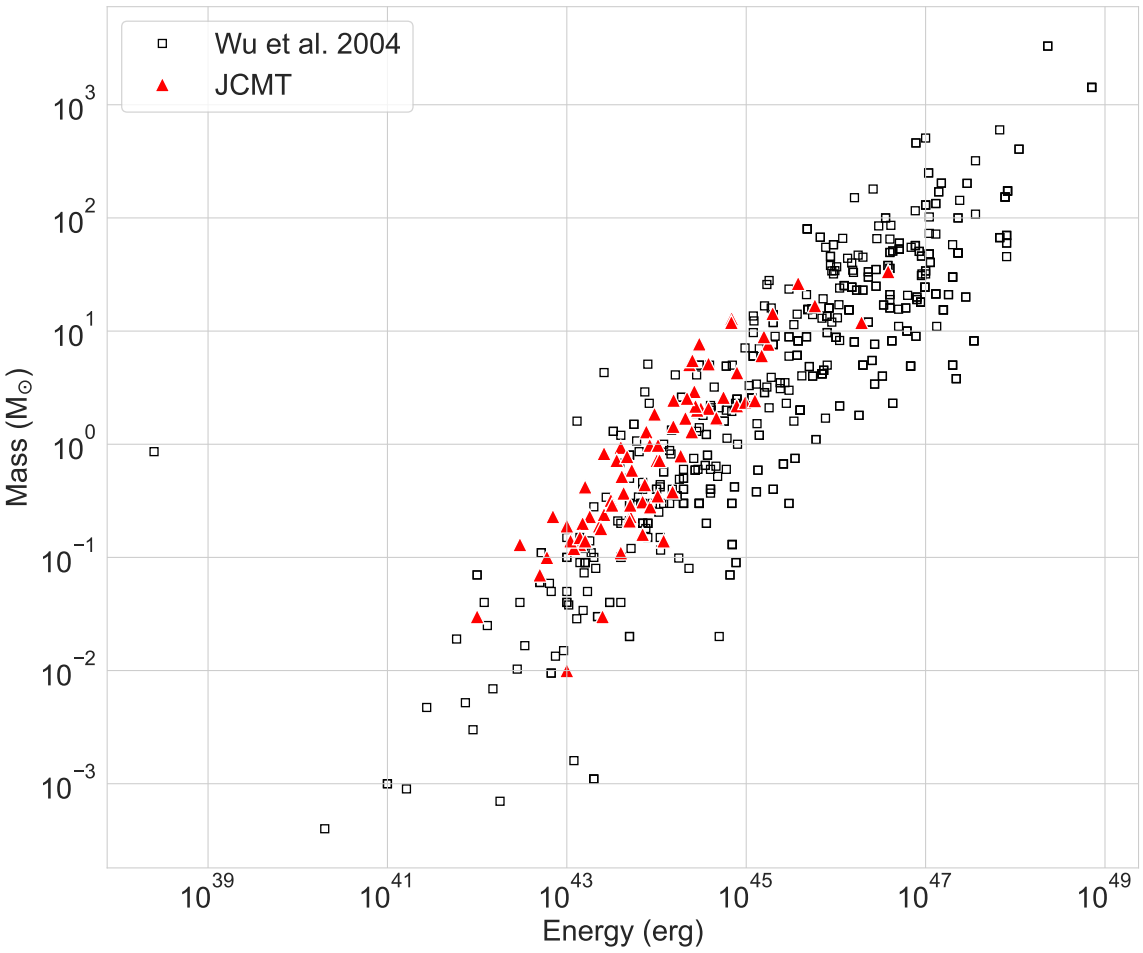

Figure 4.7: Scatter plot of outflow mass and energy. Values estimated from ^{12}CO(3-2) line alone for Cygnus X observations are shown with red triangles. These values compare closely with a broader population (Wu et al., 2004) with respect to the same properties estimated using different methods.

4.5.2 Outflow Efficiency

Here, we estimate the efficiency of outflow driving by comparing the infrared luminosities of protostars to the power required to drive the outflows. The infrared luminosity is a proxy for accretion power, so this estimates the fraction of accretion power that is converted into feedback. We estimate the outflow power as

$$L_{\rm mech} = \frac{E_{\rm outflow}}{T_{\rm dyn}}. \tag{4.7}$$

In Figure 4.9, we show the estimated values of mass and kinetic energy for the entire list of 82 sources. This figure includes 66 sources with associated sources in the Kryukova et al. (2014a) catalogue. For the remaining 16 sources without associated, catalogued protostars, we do find infrared sources in some of the survey data covering the region. However, the full set of their properties are unknown, in particular luminosity and protostellar classification and they were not covered in enough bands to infer their properties. Instead, we estimate the missing protostellar luminosity values with supervised machine learning. We use the existing values of 66 outflows (Table 4.6) as the (labeled) training data to infer the empirical relation between the IR luminosity of a source and its mass, momentum, and energy.

A common approach for such a problem is the least square regression, which estimates regression coefficients ($\vec{\beta}$) by minimizing the mean squared error (MSE) on training data. However, we impose regularization on our regression model. This is done by minimizing the MSE in a constrained parametric space $||\vec{\beta}|| \leq c$. The benefit of this approach is that it still minimizes error but makes sure $\vec{\beta}$ does not get too large. In other words, regularization reduces model complexity and overfitting that may arise from sampling bias with a simple least square regression.

The most common regularization methods are *Lasso* and *Ridge* regression (Hastie et al., 2009). Both minimize

$$||\vec{y} - \mathbf{X}\vec{\beta} - \beta_0||_2^2 + \alpha||\vec{\beta}||, \tag{4.8}$$

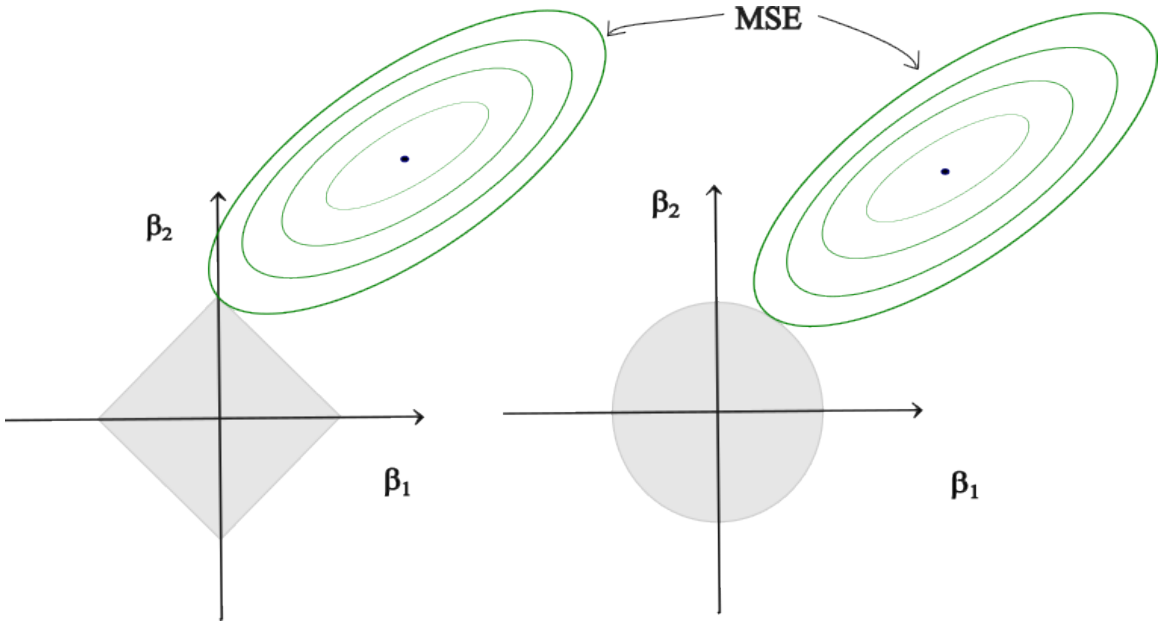

Figure 4.8: 2D schematic of *Lasso* (left) and *Ridge* regression (right) in parametric space. Regions of constraint are denoted by solid areas in gray. Contour lines (green) denote level curves of constant MSEs. *Lasso* is defined with l_1 norm causing the constraint area to have corners on parameter axes. *Ridge* is defined with Euclidean norm causing the constraint area to be circular. The goal of the optimization is to find the level curve, corresponding to the smallest MSE, among all the level curves that intersect the constraint area. The difference in geometry implies that for *Lasso*, this minimum level curve can intersect within or at the boundary on one of the parameter-axes meaning one of the coefficients vanishes completely. This is not the case for *Ridge*. The parameters shrink altogether but none of them completely vanishes. This makes *Lasso* better for removing redundant predictor variables, and *Ridge* better for reducing model complexity (diagram adopted from Hastie et al. 2009).

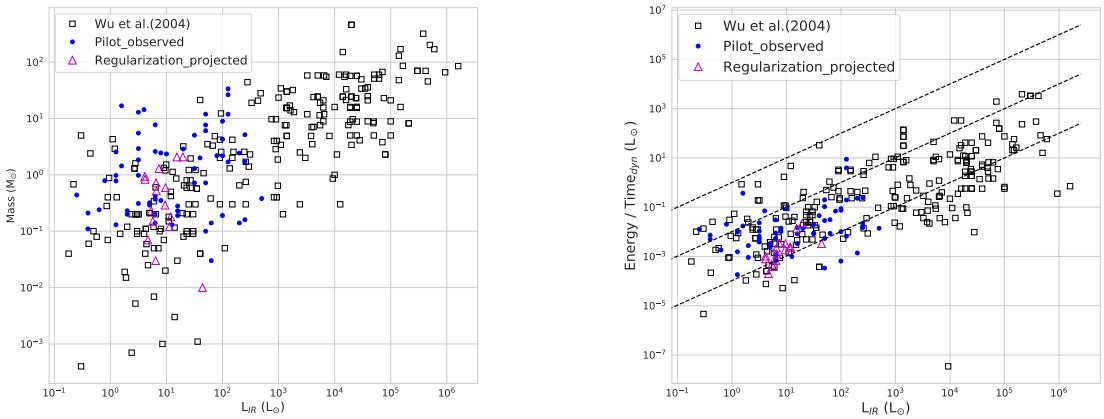

Figure 4.9: Correlation between infrared luminosity and outflow mass (left) and outflow power (right). The data include observed values (blue circles) and values inferred from the machine learning model described in the text (triangles). For reference, the heterogeneous survey of outflows from Wu et al. (2004) is also shown in the data. We find that the typical efficiency for outflow driving is $\sim 10^{-3}$.

for some constant $\alpha \in \mathbb{R}$. The difference is *Lasso* uses l_1 norm $\|\cdot\|_1$ whereas *Ridge* uses Euclidean norm $\|\cdot\|_2$. This impacts the geometry of the regions of constraint, and leads to different estimation of regression coefficients. *Lasso* performs better in removing redundancy in predictor variables, but *Ridge* handles potential multicollinearity in the data much better. This difference is illustrated schematically in Fig. 4.8.

In practice, often the best model is one in between *Lasso* and *Ridge*. The technique to do so is known as *Elastic Net* (Hastie et al., 2009). This regularization regression method estimates regression coefficients by minimizing

$$MSE + r\alpha \|\beta\|_1 + \frac{1-r}{2}\alpha \|\beta\|_2^2 , \quad r \in [0,1], \tag{4.9}$$

where MSE is based on training data,, r and α are the hyperparameters of the model. Without mathematical details, the meaning of α and r here is that as we increase the value, the constraint space shrinks. We vary the values of these hyperparameters and select the model that minimizes the above expression.

To implement these methods, we apply *Elastic net* regression to infer the missing protostellar luminosity associated with the newly discovered outflows that lack protostellar

associations. The results are given in Table 4.2, where the last column gives the projected IR luminosity. Based on the observed data and the inferred results from the regression model, we also find that the mechanical luminosity $L_{\rm mech}$ is, on average, 10^{-3} $L_{\rm IR}$ which traces the accretion power. This yields the efficiency with which the accretion power is converted into outflow power: 10^{-3} for our sample. This result is consistent with the larger population in Wu et al. (2004), as shown in Fig.4.9.

Table 4.2: Outflow results: estimated energetics and projected inferred luminosity.

Outflow	RA	Dec	Distance	Vc	Mass	Momentum	Energy	Dynamical Time	Log(L_{IR}) (projected)
	(deg)	(deg)	(kpc)	(km s^{-1})	($M_\odot$)	($M_\odot$km s^{-1})	(10^{45}erg)	(10 kyr)	($L_\odot$)
G78.070+0.629⋆	306.817	39.479	1.50	-0.6	0.10	0.30	0.10	4.4	1.1
G79.125+2.283⋆	305.842	41.295	1.50	-2.5	2.10	7.80	3.10	18.9	1.2
G79.208+3.465⋆	304.602	42.033	1.50	-3.9	1.30	3.00	0.80	18.9	0.9
G79.279+2.599⋆	305.614	41.602	0.65	5.9	0.03	0.04	0.01	1.2	0.8
G79.447+3.127⋆	305.158	42.040	1.50	-3.8	0.80	1.40	0.30	21.0	0.6
G79.761+3.367⋆	305.131	42.434	1.50	-1.8	0.20	0.60	0.20	31.5	0.7
G79.906+0.157⋆	308.731	40.683	1.30	8.2	0.10	0.20	0.00	20.6	0.7
G79.962+2.556	306.188	42.136	0.65	5.5	0.00	0.10	0.10	2.5	1.6
G80.815+0.661	308.918	41.709	1.50	-3.0	0.20	0.40	0.10	30.0	0.8
G81.559+0.183	310.044	42.016	1.30	9.3	0.30	0.90	0.30	14.3	1.0
G81.770+0.851	309.486	42.597	1.50	-0.4	0.50	1.30	0.40	27.3	0.8
G82.031+2.353⋆	308.058	43.697	1.50	-1.1	0.90	1.80	0.40	42.0	0.6
G82.037+2.321⋆	308.099	43.683	0.65	1.2	0.70	1.40	0.40	13.6	0.8
G82.189-0.042	310.813	42.374	0.65	7.2	0.20	0.60	0.20	8.5	1.1
G82.272+2.467⋆	308.128	43.959	1.50	-6.1	0.60	1.70	0.50	13.3	1.0
G83.096+3.272⋆	307.899	45.098	1.50	-1.5	2.10	8.30	3.80	14.0	1.3

⋆ Newly discovered in this work. Other outflows are from Gottschalk et al. (2012).

4.5.3 Outflow Duty Cycle and Energy Support

In this section, we investigate the scales on which molecular outflows could contribute to the turbulent support of the Cygnus X clouds. This is important because both observational data and numerical simulations indicate turbulence-driven filamentary gas flow plays a significant role in formation of giant molecular clouds (GMC) as well as controlling the star formation rate (SFR) in molecular clouds (Chevance et al., 2022).

The gas flow in a typical molecular cloud is supersonic due to high Mach numbers ($\mathcal{M} > 20$) and turbulent due to high Reynolds numbers ($\mathcal{R}e \sim 10^9$) (Krumholz, 2015; Heyer & Dame, 2015). Supersonic turbulence dissipates rapidly, typically in less than a crossing time $T_{\rm cross} = \ell/\Delta v$, Δv being the average velocity dispersion in the cloud of size ℓ (Stone et al., 1998). For most molecular clouds, $T_{\rm ff} \sim 2 - 3\, T_{\rm cross}$, which implies two things. First, although turbulence is thought to provide support against gravitational collapse particularly at larger length scales, clouds require constant energy injection to maintain turbulence. Second, supersonic turbulence in cloud cores is capable of driving local and isolated star formation at smaller scales by rapidly creating density fluctuations via shocks, which can provoke gravitational collapse. Since turbulence dissipates on scales that are comparable to but shorter than the free-fall time, this can in turn further facilitate star formation. The presence of turbulence in the later phase of collapse otherwise could have disrupted the process. However, for the same reason the star formation process in a turbulent core is inefficient as compared to large-scale clustered star formation that happens in the absence of turbulence (Mac Low & Klessen, 2004; Guszejnov et al., 2021).

Molecular outflows in star-forming cloud cores are a byproduct of the efficient accretion of material onto the associated protostars. Fast-moving collimated jets and low-velocity wide-angled outflows exist in the very early phases of protostellar formation (Frank et al., 2014). These jets and bipolar outflows inject kinetic energy far into the surrounding cloud. Any energy into molecular clouds is advected as supersonic turbulence and dissipated as heat energy. Moreover, supersonic turbulence in molecular clouds might favor a momen-

tum cascade structure (Matzner, 2007). Such a structure would make molecular outflows more important than high-velocity collimated jets.

Several authors have attempted to address the question whether outflow feedback is important in cloud dynamics. Some authors have argued molecular outflow energy is not significant in providing turbulence support (Hansen et al., 2012b; Narayanan et al., 2012). On the other hand, using numerical simulations, Norman & Silk (1980); Nakamura & Li (2007); Wang et al. (2010) showed outflows can contribute to the ambient gas evolution, in terms of driving turbulence and influencing the local SFR, particularly if there are preexisting strong magnetic fields and sufficiently large amount of initial turbulence (Cunningham et al., 2009), all of which support against gravitational instability. Banerjee et al. (2007) showed collisional interaction among outflows associated with multiple protostars can provide a considerable amount of turbulent energy into the parent cloud. Furthermore, Arce et al. (2010) and Frank et al. (2014) argue that some of the discrepancies between simulation and observational estimates can arise from differences in the scales probed.

Given the lack of a clear consensus and an expected dependence on the physical scales being probed, we estimate the contribution of outflow driving to molecular cloud support as a function of scale in Cygnus X. In particular, we measure the kinetic energy in the ambient cloud around an outflow and compare that to the energy coming from an outflow during the single observed duty cycle. We begin by considering an area around the outflow that is 8 times larger than the outflow extent ($R_{\rm lobe}$); and for each spatial pixel in the area, we estimate the line center of the spectral axis following the same formalism described in D21. Then we estimate the energy using

$$E_{\rm cloud} = \frac{3}{2} \sum_{x,y} \sum_{v_0-2\sigma_v}^{v_0+2\sigma_v} M(v,y,x)(v-v_0)^2 \tag{4.10}$$

and compare the result to the outflow kinetic energy, shown in Fig. 4.10. The peak of the histogram shows $E_{\rm outflow}$ is 10 to 15 times smaller than $E_{\rm outflow+cloud}$ which would naively suggest outflows are insufficient to support the cloud kinetic energy.

Such a simple picture does not account for the episodic nature of protostellar outflows,

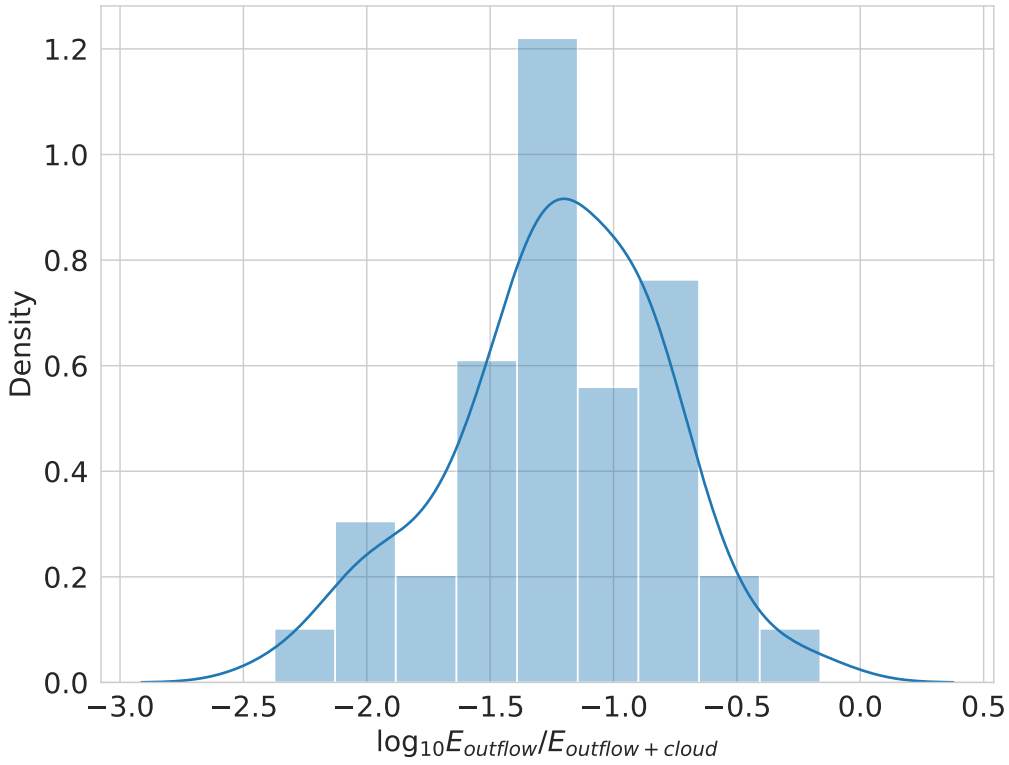

Figure 4.10: Distribution of outflow energy relative to the cloud energy

including the reality that several protostars in the survey area are associated with molecular line outlows. For a single YSO, outflow activity varies dramatically over time depending on the density structure of the accreting gas. Outflows are episodic and multiple outflow duty cycles are thought to occur during the class 0/I phase of an YSO (Frank et al., 2014). We have estimates of the dynamical time of the outflows: $T_{\rm dyn}$ essentially denotes the time scale of an individual outflow activity. The outflow driving is then subject to some duty cycle including times where the protostar is accreting without visible molecular outflow activity. We compare the dynamical times of outflows to the free-fall time of the associated clump (measured on scale of $\sim 40''$ to $1.5'$):

$$T_{\rm ff} = \sqrt{\frac{\pi^2 R^3}{8GM}}. \tag{4.11}$$

We interpret the latter as the characteristic time to form a star, since the gravitational collapse timescale in a magnetically supercritical core is of the order of free-fall time (Kim et al., 2021). For our sample of outflow-clump combination, we find the average value of the ratio $T_{\rm dyn}/T_{\rm ff} \approx 15$. This implies during the lifetime of a protostar, ≈ 15 duty cycles of outflow activity can occur while some of these cycles can be quiescent.

We note that the number of duty cycles could make up for the deficit between in cloud energy and outflow driving energy in Figure 4.10. This comes at no surprise that energy from a single duty cycle is not significant to the overall turbulence energy budget required for the cloud because of the variability in outflow activity the energies may not be comparable. It is clear there is a timescale difference. Additionally, energy injected during each duty cycle adds to the turbulent support on a global scale for the entire cloud, but, as discussed earlier, may allow local isolated gravitational collapse at smaller scales.

To look into the significance of outflow feedback in Cygnus X, we thus compare the outflow energy injection rate, or the mechanical luminosity, to the power in turbulent energy loss in the cloud as a function of spatial scale, ℓ. We use Equation 4.7 to calculate $L_{\rm mech}$ for

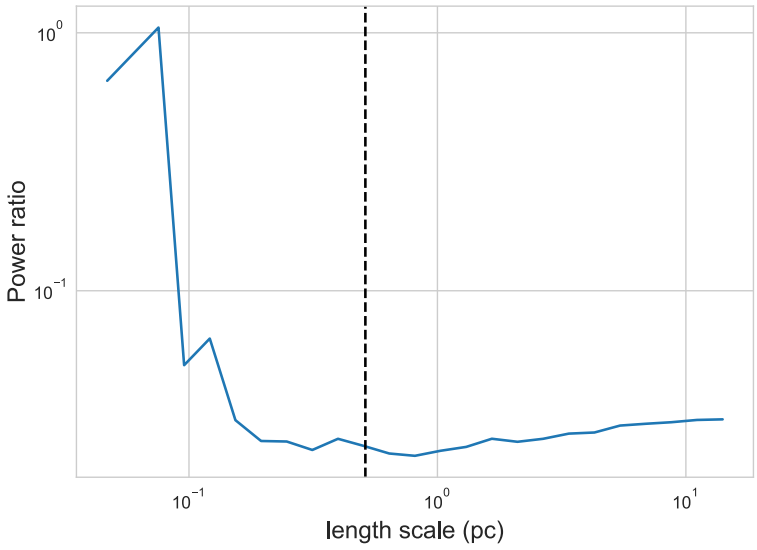

Figure 4.11: Contribution of outflow power to cloud turbulence as a function of spatial scales.

each outflow and sum the total energy contribution. The turbulent energy is given as

$$L_{\rm turb} = \frac{E_{\rm cloud}}{T_{\rm cross}}. \tag{4.12}$$

We calculate the turbulent dissipation power as a function of spatial scale ℓ:

$$L_{\rm turb} = \frac{3}{2}\frac{\sum_{(x,y)<\ell}\sum M(v,y,x)(v-v_0)^2}{T_{\rm cross}(\ell)}. \tag{4.13}$$

where $T_{\rm cross}(\ell) = \ell/\sigma_{v,{\rm cloud}}(\ell)$ and $\sigma_{v,{\rm cloud}}(\ell)$ is the velocity dispersion measured in the data cube over a region with spatial scale ℓ:

$$\sigma_{v,{\rm cloud}}(\ell) = \frac{\sum_{(x,y)<\ell}\sum M(v,y,x)(v-v_0)^2}{\sum_{(x,y)<\ell}\sum M(v,y,x)}. \tag{4.14}$$

The factor of 3 in Equation 4.13 arises because we assume isotropy of the turbulent motions in three dimensions. The sum is carried out over spatial area, which is computed for all pixels within a distance of ℓ of *any* protostellar outflow.

Since the driving scale of the turbulence is important in local collapse, we plot the power ratio $L_{\rm mech}/L_{\rm lum}$ against cloud scale ℓ in Figure 4.11. We find outflow energy might contribute significantly towards the total turbulence at local scale ($\ell < 0.2$ pc), thus impacting

local star formation but the relative contribution declines sharply with increasing length scales such that, at ℓ = 1pc the observed driving power is < 3% of the turbulent energy losses on this scale. It is to be noted that we observe many YSOs without associated outflows potentially due to their quiescent phase, so there is some room for error in the estimation of outflow energy, but the overall result should still be valid since some outflows will turn off while the quiescent stars will turn on. These results are broadly consistent with the results seen in the Taurus cloud by Narayanan et al. (2012), where outflows can be locally important but are unlikely to be important globally. However, this study of Cygnus X extends the result to significantly higher mass molecular clouds.

4.5.4 Outflows and Triggered Star Formation

Observations indicate that star formation can be influenced by previous generation of high-luminosity stars through the role of stellar feedback. However, it can be challenging to uniquely identify evidence for triggering of star formation by that feedback (Dale et al., 2015). Here, we use the wide-area mapping of the region in CO, radio continuum, and the mid-infrared to investigate whether there is evidence for large-scale triggering of star formation in the region. Cygnus X is a site for many young stars and a rich deposit of molecular gas and we have a rich set of data that can trace the reservoir of material for star formation (from the new CO data), the influence of triggering through high mass stars (through the radio continuum tracing the presence of ionized gas) and the current star formation (using protostar catalogs derived from infrared observations). Our approach is to assess whether molecular gas overlapping with significant ionized gas emission shows enhanced or suppressed star formation rates relative to a similar mass of gas without associated ionized gas.

The expanding hot HII regions are associated with active star formation in two ways, they surround young stars, and their expansion could induce formation of new generations of stars. A dense HII region around a young massive star or stellar cluster can drive com-

pressed ionizing radiation fronts. The shockwave preceding the ionization front can provide enough surface pressure facilitating star-formation in collapsing molecular clouds or even initiating the collapse. This is known as triggering by positive feedback. Internal feedback in a molecular cloud can also disrupt star formation by dispersing and shredding already collapsing gas, known as negative feedback. This is particularly true for high-mass stellar clusters that produce overwhelming number of ionizing photons capable of ionizing cloud material making it gravitationally unbound. Such a case in Carina Nebula is discussed by Smith (2008).

Local triggering by positive feedback is difficult to confirm, particularly for a small sample of protostars. Using numerical simulations, Dale et al. (2015) argued typical signatures for potential triggering, including proximity to an ionization front and HII regions, proximity to bright rims enclosing the cloud, and cometary or pillar structure of the collapsing cloud, used in the literature may not always be sufficient for inferring triggering scenarios. This is because gravitational instability in the compressed shells driven by ionizing fronts is also greatly influenced by factors such as local turbulence and magnetic fields. Cases of spontaneous and triggered star formation are often found in the same region. Following the virial equation, without knowing all the components involving in cloud instability in details, it is extremely hard to conclusively build a case for triggering on the molecular cloud length-scales. However, sites that have multiple signatures of triggering, occurring simultaneously, are more likely to be the actual cases of triggered star formation. One such case of triggering is discussed in Deb et al. (2018).

Since molecular hydrogen gas (traced by the ^{12}CO line) is essential for star formation, we expect a higher number of protostars in regions where both the molecular gas deposit and the signatures of ionizing fronts are relatively high, if the regions are indeed cases of triggered star formation. In this section, we explore whether the two factors increase the number of outflows and protostars as a potential signpost for triggering.

Cygnus X has 145 individually known HII regions (Paladini et al., 2003). Free-free or

thermal bremsstrahlung emission can provide significant cooling for these regions, which can be observed at 1420 MHz or 21-cm radio continuum (Vasquez et al., 2010). Although, there is non-thermal synchrotron emission present also observed in the same continuum band as the thermal bremsstrahlung, the spectral energy distribution of free-free emission is characteristically flatter over the frequency range. On the other hand, the SED of synchrotron emission has a much steeper profile and can be distinguished by using the spectral index in a multi-frequency technique for thermal and non-thermal separation (Xu et al., 2013). Using low frequency data to estimate the non-thermal contribution, Landecker et al. (2010) estimate that most of the radio continuum emission from Cygnus X region is dominated by thermal emission. Moreover, several authors have indicated there is no large enough supernova remnant present around Cygnus X (Green, 2009, 2019; Xu et al., 2013) that could contribute significantly to the observed radio continuum emission. We thus treat the radiocontinuum emission as tracing the photoionized gas associated with high mass stars in the region.

We examine the spatial correlation between protostars (in the infrared catalogue or through protostellar outflows) and the joint distribution of the radio continuum (tracer for stellar feedback) from the Canadian Galactic Plane Survey (CGPS) (Taylor et al., 2003c) and the ^{12}CO(3-2) line data (proxy for molecular hydrogen). We divide the common observational area of these studies (Figure 4.5) into a 7×7 equally spaced spatial grid structure. We count the number of outflows or protostars and compute the average of the integrated intensity of ^{12}CO(3-2) (K km/s), and the average surface brightness of the 21-cm radio continuum (in Kelvins), over all pixels in each grid. In essence, we construct 49 observations of data triplets { ^{12}CO(3-2), 21-cm, number of outflows}. As we have discussed in section 4.3, outflows are episodic and they are not often observed during the quiescence of accretion. For this reason, we also completed the analysis using the number of flat-spectrum IR sources as a tracer of star formation, using the protostars listed in the Kryukova et al. (2014a) catalogue.

For a regression model based on generalized linear model, a good assumption for the underlying probability distribution for numbers of discrete sources is that the data follow the Poisson distribution, since the number of outflows is a discrete quantity ranging from 0 to 20 per grid. Our small sample has a high data imbalance, i.e., there are 18 occurrences of grid boxes with zero protostars or outflows. Given the small simple size our predictive model is unlikly to be highly reliable and we are more interested in investigating the general trend in the data, if any, rather than an actual quantitative prediction.

To address the imbalance in the data, the technique we implement is to look at the problem two ways. First, we explore fitting a decision boundary in a 2D hyperplane consisting of ^{12}CO(3-2) and 21-cm data, that separates values that are more likely to lack any protostars and the values that are more likely to produce non zero number of protostars in the corresponding region. We then find if there is a pattern in the data following an increasing number among the non-zero values.

We implemented *Support Vector Machine* with a Gaussian Kernel for this purpose, to fit a decision boundary as described above. The results are shown in Figure 4.12. The solid black contour line marks the boundary between star forming and non-star forming grids. We see most of the regions with no protostars are inside the boundary, associated with low values of gas and ionizing radiation intensity. On the other hand, protostars are forming outside the boundary, the region associated with higher values of the two quantities. Moreover, it is evident from the figure that there is a clear increasing pattern of greater number of protostars being associated with larger values of both the ^{12}CO(3-2) and 21-cm. Visibly, this pattern is slightly off-diagonal favoring ^{12}CO(3-2). Also quantitatively, the correlation coefficient between ^{12}CO(3-2) and the number of protostars is 0.63 as compared to that between 21-cm and the number of protostars is 0.55. We thus conclude that ^{12}CO(3-2) is a slightly better individual predictor of the presence of outflows (protostars), although the difference is not very big.

So, we find a trend of higher number of flat-spectrum protostars being associated with

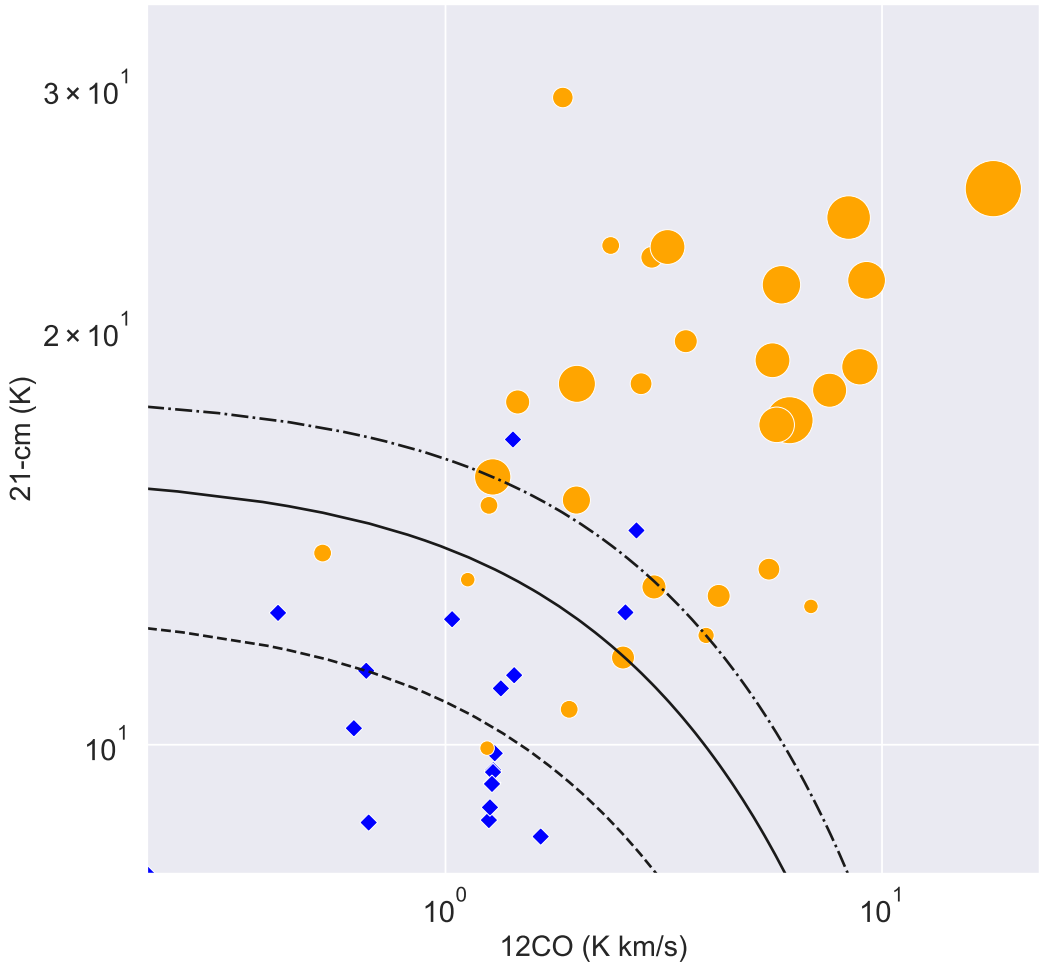

Figure 4.12: Protostellar association with gas distribution in 49 regions of equal area, marked by orange filled-circles and blue filled-diamonds. The regions marked in orange contain protostars, and the ones marked in blue do not, with the circle area being proportional to the number of protostars (1 to 50) in that region. The contour lines are fitted using *Support Vector Machine* algorithm, solid line marking the decision boundary inside which the joint distribution of ^{1}2CO(3-2) and 21-cm emission is not sufficient to produce protostars

more gas and stronger radiation. Also, 21-cm emission alone does not correlate with protostellar number well where ^{12}CO(3-2) is weak or missing. This is consistent with the fact that star formation requires molecular gas as the primary material. Overall, this result may indicate an ionization front can perhaps trigger local star formation where molecular gas emission is high but there is no evidence that this effect is strong. While this approach provides a statistical framework for assessing whether the influence of triggering separate from the amount of molecular gas in a region, it suffers from our small sample size. This method could be applied to other wide area surveys of molecular gas and protostar data in other regions in the Milky Way.

4.6 Summary

This paper presents a wide-field survey of the Cygnus X star-forming region using spectral line and radio-continuum data. Using new and previously published (Gottschalk et al., 2012) JCMT observations of ^{12}CO(3-2) we have identified 82 molecular outflows, many of which were previously unknown. We have also identified associated protostars of 66 outflows. The main findings of this paper are that

1. We have estimated the outflow mass, momentum, energy from ^{12}CO(3-2) alone. This technique has applications in molecular gas surveys that lack multi-line observations.

2. We have implemented a machine learning method to predict luminosity values for outflows that do not have protostars in the catalogue. We compared our prediction with an independent outflow catalogue with observed values. We find our estimated values are consistent. This, again may be useful for studies that are missing observed luminosity. Using these methods, we find that the outflow power is 0.1% that of an associated protostars infrared luminosity. We further estimate that outflow dynamical times are 15× shorter than the local gas free-fall time.

3. We have compared outflow energy contribution to their ambient cloud for turbulent

support. We found this contribution is significant for smaller length scales (< 0.2 pc) and declines with increasing cloud size to become insignificant on > 1 pc scales.

4. We have investigated for possible large-scale triggered star formation in Cygnus X by modifying a machine learning classification technique. We found there is marginal evidence for such triggering but our method can be robustly applied to larger studies.

Acknowledgements

The James Clerk Maxwell Telescope has historically been operated by the Joint Astronomy Centre on behalf of the Science and Technology Facilities Council of the United Kingdom, the National Research Council of Canada and the Netherlands Organisation for Scientific Research. The authors wish to recognize and acknowledge the significant cultural role and reverence that the summit of Maunakea has always had within the indigenous Hawaiian community. We are most fortunate to have the opportunity to conduct observations from this mountain. The authors acknowledge support from the Natural Sciences and Engineering Research Council of Canada, funding reference numbers RGPIN-2017-03987 and RGPIN 418517.

Data Availability: The data underlying this article are available in the Canadian Astronomy Data Centre, at https://dx.doi.org/10.11570/21.0001. [2]

[2]Data hosted during review at https://www.canfar.net/storage/list/eros/OUTFLOWS_FITS

Chapter 5

Conclusions and Future Work

5.1 Conclusions

In this thesis, I present a study of the molecular clouds in the Cygnus X star-forming region. This work is a collection of three separate projects studying different aspects of triggered star formation and protostellar feedback. I provided an overall understanding of the internal structure and gas dynamics of the molecular clouds in one of the most active star-forming regions in the galaxy. There are two main topics this work aimed to understand, the role of protostellar feedback in terms of outflow kinetic energy in cloud dynamics, and the influence of radiative feedback from young stars on the ongoing star formation in Cygnus X.

In Chapter 2, I discussed a particular molecular structure, in the shape of comet, located at 50 parsec north of Cyg OB2 stellar cluster, and investigate a possible case of triggering. Using mainly multi-line observations of ^{12}CO(3-2), ^{13}CO(3-2), and C^{18}O(3-2) from the JCMT Hawaii, I estimated the mass, momentum, energy of the two molecular outflows found in the 'cometery feature'. I also built a case for potential triggering scenario. The geometry of the structure, proximity to highly luminous stellar cluster OB2 complex, molecular gas in the cometary feature surrounded by a rim of 21-cm radio continuum emission, and a time-scale analysis altogether indicate the star formation in the cometary feature is very likely to be triggered by a radiation front from the OB2 complex.

In Chapter 3, I extended the work of outflow property estimation to 13 new outflows

found in Cygnus X, again, using multi-line data. These estimates are consistent with previous surveys of outflows throughout the galaxy. I also identified the associated protostars. Additionally, I developed and tested a method of estimating the same outflow properties using ^{12}CO(3-2) line alone. The two sets of estimation agree within a factor of two. This method can be applied to many surveys that lack multi-line observations.

In Chapter 4, I conducted a large-scale study of new and previously published JCMT ^{12}CO(3-2) line data, identifying 82 outflows. Since this study lacks ^{13}CO(3-2) and C^{18}O(3-2) observations, I implemented the method developed in the previous part to estimate outflow properties. I identified associated protostars for 66 of the outflows, and inferred protostellar luminosity for the object for which I did not find existing protostars. This inference was done using machine learning. I computed the relative contribution of outflows to their parent cloud for turbulent support as a function of length scale, and find that outflows are important at smaller scales but unlikely to provide turbulent support for larger scales ($>$ 1 pc). Finally, using machine learning in order to find support for large-scale triggering, I find there is some evidence of triggered star formation by radiation front where molecular gas deposit is high.

5.2 Future Work

There remains a great deal of exploration to be done using the JCMT Cygnus X data set, which is one of the highest-quality studies of a giant molecular cloud. In the future, I would like to explore a few areas to have a more complete picture of the outflow activity and star formation in Cygnus X. Our case study of triggering (Deb et al., 2018) investigated the influence of radiative feedback on star formation, but a crucial component missing from our analysis is the magnetic field. In the context of the Eagle Nebula, Pattle et al. (2018) has shown magnetic fields can play a central role in interpreting triggered regions. For this reason, we proposed measurement of the magnetic field and geometry using the dust polarization in the SCUBA-2 continuum observations with the POL-2 instrument.

Although approved, the observing window would not provide adequate data quality for that specific study. In the future, I would like to conduct a similar magnetic field polarimetry study to build a spatial map of the magnetic field structure in the Cygnus X region, which will help understand the importance of magnetic fields in a radiatively driven "triggered" star formation scenario. Particularly, I would use the Davis-Chandrasekhar-Fermi method (Davis, 1951; Chandrasekhar & Fermi, 1953) to evaluate the geometry and field strength. This will complement our large-scale study of star formation in Cygnus X and confirm the possibility of magnetic support.

The machine learning method I have developed in this work to assess the importance of triggering can be used in a broader sample. The relatively small sample used here is not nearly enough to extract a data-driven insight into the interaction between ionization fronts and molecular gas in the context of radiatively-driven star formation. With the JCMT data set, I can identify and create a larger catalogue of outflows. Predicting star formation, specifically triggered star formation is a very complex task. With a large sample of observations along with data on the magnetic field structure, molecular gas, radiation, and turbulence energy, it is possible to build a multi-variable and more reliable predictive model of star formation in Cygnus X. There are several ways to achieve this goal, including ensemble learning of classification and regression models, as well as prediction with an *Artificial Neural Network (ANN)* architecture.

In addition to the statistical model, I can conduct direct searches for triggering and cometary features observed in the molecular spectral line data. This has two benefits, the first being creating a catalogue of detailed observational records of star formation history in Cygnus X, particularly triggering scenarios, and secondly, the observational study might serve as a test data set for a machine learning model to predict triggered star formation.

BIBLIOGRAPHY

Arce H. G., Goodman A. A., 2001, ApJ, 554, 132

Arce H. G., Borkin M. A., Goodman A. A., Pineda J. E., Halle M. W., 2010, ApJ, 715, 1170

Astropy Collaboration et al., 2013, A&A, 558, A33

Bally J., 2016, ARA&A, 54, 491

Bally J., Lada C. J., 1983, ApJ, 265, 824

Bally J., Reipurth B., Lada C. J., Billawala Y., 1999a, AJ, 117, 410

Bally J., Reipurth B., Lada C. J., Billawala Y., 1999b, AJ, 117, 410

Banerjee R., Klessen R. S., Fendt C., 2007, ApJ, 668, 1028

Barentsen G., et al., 2014, MNRAS, 444, 3230

Bastien P., Arcoragi J.-P., Benz W., Bonnell I., Martel H., 1991, The Astrophysical Journal, 378, 255

Beerer I. M., et al., 2010, ApJ, 720, 679

Berné O., et al., 2022, PASP, 134, 054301

Bik A., et al., 2012, ApJ, 744, 87

Bodenheimer P. H., 2011, Principles of Star Formation

Bontemps S., Andre P., Terebey S., Cabrit S., 1996, A&A, 311, 858

Boulanger F., Cox P., Jones A. P., 2000, in Casoli F., Lequeux J., David F., eds, Springer Conference Series Vol. 70, Infrared Space Astronomy, Today and Tomorrow. p. 251

Buckle J. V., et al., 2009, MNRAS, 399, 1026

Chandrasekhar S., Fermi E., 1953, ApJ, 118, 113

Chevance M., Krumholz M. R., McLeod A. F., Ostriker E. C., Rosolowsky E. W., Sternberg A., 2022, arXiv e-prints, p. arXiv:2203.09570

Churchwell E., et al., 2009, PASP, 121, 213

Clarke S. D., Whitworth A. P., Duarte-Cabral A., Hubber D., 2017, Monthly Notices of the Royal Astronomical Society, 468, 2489

Comerón F., Pasquali A., 2012, A&A, 543, A101

Comerón F., et al., 2002, A&A, 389, 874

Commercon B., Levrier F., Maury A., Henning T., Launhardt R., Dullemond C., 2013, in Protostars and Planets VI Posters.

Condon J. J., Cotton W. D., Greisen E. W., Yin Q. F., Perley R. A., Taylor G. B., Broderick J. J., 1998, AJ, 115, 1693

Corradi R. L. M., et al., 2008, VizieR Online Data Catalog, pp J/A+A/480/409

Crocker A. F., Calzetti D., Thilker D. A., KINGFISH Team 2011, in American Astronomical Society Meeting Abstracts #217. p. 112.03

Crutcher R. M., 2012, Annual Review of Astronomy and Astrophysics, 50, 29

Cunningham N. J., Moeckel N., Bally J., 2009, ApJ, 692, 943

Currie M. J., Berry D. S., Jenness T., Gibb A. G., Bell G. S., Draper P. W., 2014, in Astronomical Data Analysis Software and Systems XXIII. p. 391

Dale J. E., Ercolano B., Bonnell I. A., 2013, MNRAS, 430, 234

Dale J. E., Haworth T. J., Bressert E., 2015, MNRAS, 450, 1199

Davis L., 1951, Physical Review, 81, 890

Deb S., Kothes R., Rosolowsky E., 2018, MNRAS, p. 2262

Deb S., Kothes R., Rosolowsky E., 2021, MNRAS, 503, 1264

Dickel H. R., Wendker H., Bieritz J. H., 1969, A&A, 1, 270

Drabek-Maunder E., Hatchell J., Buckle J. V., Di Francesco J., Richer J., 2016, MNRAS, 457, L84

Draine B. T., 2011, Physics of the Interstellar and Intergalactic Medium

Draine B. T., Lazarian A., 1997, in American Astronomical Society Meeting Abstracts. p. 51.19

Duarte-Cabral A., Chrysostomou A., Peretto N., Fuller G. A., Matthews B., Schieven G., Davis G. R., 2012, A&A, 543, A140

Dunham M. M., Arce H. G., Mardones D., Lee J.-E., Matthews B. C., Stutz A. M., Williams J. P., 2014, ApJ, 783, 29

Ellerbroek L. E., Podio L., Kaper L., Sana H., Huppenkothen D., de Koter A., Monaco L., 2013, A&A, 551, A5

Elmegreen B. G., 1998, in Woodward C. E., Shull J. M., Thronson Harley A. J., eds, Astronomical Society of the Pacific Conference Series Vol. 148, Origins. p. 150 (arXiv:astro-ph/9712352)

Elmegreen B. G., Lada C. J., 1977, ApJ, 214, 725

Evans Neal J. I., et al., 2009, The Astrophysical Journal Supplement Series, 181, 321

Frank A., et al., 2014, in Beuther H., Klessen R. S., Dullemond C. P., Henning T., eds, Protostars and Planets VI. p. 451 (arXiv:1402.3553), doi:10.2458/azu˙uapress˙9780816531240-ch020

Ginsburg A., Bally J., Williams J. P., 2011, MNRAS, 418, 2121

Goicoechea J. R., et al., 2015, ApJ, 812, 75

Gottschalk M., Kothes R., Matthews H. E., Landecker T. L., Dent W. R. F., 2012, A&A, 541, A79

Green D. A., 2009, Bulletin of the Astronomical Society of India, 37, 45

Green D. A., 2019, Journal of Astrophysics and Astronomy, 40, 36

Guszejnov D., Grudić M. Y., Hopkins P. F., Offner S. S. R., Faucher-Giguère C.-A., 2021, MNRAS, 502, 3646

Haffner L. M., Reynolds R. J., Tufte S. L., 1998, ApJ, 501, L83

Hansen C. E., Klein R. I., McKee C. F., Fisher R. T., 2012a, ApJ, 747, 22

Hansen C. E., Klein R. I., McKee C. F., Fisher R. T., 2012b, ApJ, 747, 22

Hastie T., Tibshirani R., Friedman J., 2009, The elements of statistical learning: data mining, inference and prediction, 2 edn. Springer, http://www-stat.stanford.edu/~tibs/ElemStatLearn/

Hennebelle P., Chabrier G., 2008, The Astrophysical Journal, 684, 395

Henning T., 1989, Astronomische Nachrichten, 310, 363

Hester J. J., et al., 1996, AJ, 111, 2349

Heyer M., Dame T. M., 2015, ARA&A, 53, 583

Hildebrand R. H., 1983, QJRAS, 24, 267

Hollenbach D. J., Tielens A. G. G. M., 1999, Reviews of Modern Physics, 71, 173

Hunter J. D., 2007, Computing in Science and Engineering, 9, 90

Kennicutt R. C., Evans N. J., 2012, Annual Review of Astronomy and Astrophysics, 50, 531

Kim J.-G., Ostriker E. C., Filippova N., 2021, The Astrophysical Journal, 911, 128

Klein R. I., McKee C. F., Colella P., 1994, ApJ, 420, 213

Klessen R. S., Burkert A., Bate M. R., 1998, The Astrophysical Journal, 501, L205

Knödlseder J., 2000, A&A, 360, 539

Kogut A., Banday A. J., Bennett C. L., Gorski K. M., Hinshaw G., Reach W. T., 1996, ApJ, 460, 1

Königl A., 1991, ApJ, 370, L39

Krumholz M. R., 2015, arXiv e-prints, p. arXiv:1511.03457

Krumholz M. R., McKee C. F., 2005, ApJ, 630, 250

Kryukova E., Megeath S. T., Gutermuth R. A., Pipher J., Allen T. S., Allen L. E., Myers P. C., Muzerolle J., 2012, AJ, 144, 31

Kryukova E., et al., 2014a, AJ, 148, 11

Kryukova E., et al., 2014b, AJ, 148, 11

Kuiper R., Klahr H., Beuther H., Henning T., 2011, ApJ, 732, 20

Ladd E. F., Fuller G. A., Deane J. R., 1998, ApJ, 495, 871

Landecker T. L., et al., 2000, A&AS, 145, 509

Landecker T. L., et al., 2010, A&A, 520, A80

Lefloch B., Lazareff B., 1994, A&A, 289, 559

Mac Low M.-M., Klessen R. S., 2004, Reviews of Modern Physics, 76, 125

Machida M. N., Hosokawa T., 2013, Monthly Notices of the Royal Astronomical Society, 431, 1719

Madsen G. J., Haffner L. M., Reynolds R. J., 2001, arXiv e-prints, pp astro–ph/0112232

Makin S. V., Froebrich D., 2018, The Astrophysical Journal Supplement Series, 234, 8

Mangum J. G., Shirley Y. L., 2015, Publications of the Astronomical Society of the Pacific, 127, 266

Matzner C. D., 2007, ApJ, 659, 1394

Matzner C. D., McKee C. F., 2000, ApJ, 545, 364

Miesch M. S., Bally J., 1994, ApJ, 429, 645

Molinari S., et al., 2016, A&A, 591, A149

Nakamura F., Li Z.-Y., 2007, ApJ, 662, 395

Narayanan G., Snell R., Bemis A., 2012, MNRAS, 425, 2641

Norman C., Silk J., 1980, ApJ, 238, 158

Oosterloo T., Raymond Oonk J. B., Morganti R., Combes F., Dasyra K., Salomé P., Vlahakis N., Tadhunter C., 2017, A&A, 608, A38

Osterbrock D. E., Ferland G. J., 2006, Astrophysics of gaseous nebulae and active galactic nuclei

Padoan P., Bally J., Billawala Y., Juvela M., Nordlund Å., 1999, The Astrophysical Journal, 525, 318

Paladini R., Burigana C., Davies R. D., Maino D., Bersanelli M., Cappellini B., Platania P., Smoot G., 2003, A&A, 397, 213

Pattle K., et al., 2018, ApJ, 860, L6

Peeters E., Spoon H. W. W., Tielens A. G. G. M., 2004, ApJ, 613, 986

Piddington J. H., Minnett H. C., 1952, Australian Journal of Scientific Research A Physical Sciences, 5, 17

Plunkett A. L., Arce H. G., Corder S. A., Dunham M. M., Garay G., Mardones D., 2015, ApJ, 803, 22

Rybicki G. B., Lightman A. P., 1986, Radiative Processes in Astrophysics

Rygl K. L. J., et al., 2012, A&A, 539, A79

Sale S. E., et al., 2014, VizieR Online Data Catalog, p. J/MNRAS/443/2907

Schneider N., Bontemps S., Simon R., Jakob H., Motte F., Miller M., Kramer C., Stutzki J., 2006, A&A, 458, 855

Schneider N., Simon R., Bontemps S., Comerón F., Motte F., 2007, A&A, 474, 873

Schneider N., et al., 2016, A&A, 591, A40

Schöier F. L., van der Tak F. F. S., van Dishoeck E. F., Black J. H., 2005, A&A, 432, 369

Shu F. H., Adams F. C., Lizano S., 1987, ARA&A, 25, 23

Shu F., Najita J., Ostriker E., Wilkin F., Ruden S., Lizano S., 1994, ApJ, 429, 781

Smith N., 2008, Nature, 455, 201

Stahler S. W., Palla F., 2004, The Formation of Stars

Sternberg A., Hoffmann T. L., Pauldrach A. W. A., 2003, ApJ, 599, 1333

Stone J. M., Ostriker E. C., Gammie C. F., 1998, The Astrophysical Journal, 508, L99

Sun J., et al., 2020, ApJ, 892, 148

Swift J. J., Welch W. J., 2008, ApJS, 174, 202

Taylor A. R., et al., 2003a, AJ, 125, 3145

Taylor A. R., et al., 2003b, AJ, 125, 3145

Taylor A. R., et al., 2003c, AJ, 125, 3145

Tenorio-Tagle G., Bodenheimer P., 1988, ARA&A, 26, 145

Uyanıker B., Fürst E., Reich W., Aschenbach B., Wielebinski R., 2001, A&A, 371, 675

Vaidya B., Fendt C., Beuther H., 2009, ApJ, 702, 567

Vasquez J., Cappa C. E., Pineault S., Duronea N. U., 2010, MNRAS, 405, 1976

Walsh D., Brown R. H., 1955, Nature, 175, 808

Wang P., Li Z.-Y., Abel T., Nakamura F., 2010, ApJ, 709, 27

Wendker H. J., Higgs L. A., Landecker T. L., 1991, A&A, 241, 551

Westpfahl D. J., 1999, in Taylor G. B., Carilli C. L., Perley R. A., eds, Astronomical Society of the Pacific Conference Series Vol. 180, Synthesis Imaging in Radio Astronomy II. p. 201

White G. J., et al., 2015, MNRAS, 447, 1996

Wilson T. L., Rood R., 1994, Annual Review of Astronomy and Astrophysics, 32, 191

Wilson R. W., Jefferts K. B., Penzias A. A., 1970, ApJ, 161, L43

Wilson T. L., Rohlfs K., Hüttemeister S., 2013, Tools of Radio Astronomy, doi:10.1007/978-3-642-39950-3.

Wright N. J., Drew J. E., Mohr-Smith M., 2015, MNRAS, 449, 741

Wu Y., Wei Y., Zhao M., Shi Y., Yu W., Qin S., Huang M., 2004, A&A, 426, 503

Xu W. F., Gao X. Y., Han J. L., Liu F. S., 2013, A&A, 559, A81

Zhang S., et al., 2020, ApJS, 248, 15